KU LEUVEN

ARENBERG DOCTORAL SCHOOL
Faculty of Science

Laser spectroscopy of radioactive molecules for future searches of new physics

Michail Athanasakis-Kaklamanakis

Supervisor:
Prof. dr. G. Neyens
Co-supervisor:
Prof. dr. Á. Koszorús

Dissertation presented in partial
fulfillment of the requirements for the
degree of Doctor of Science (PhD):
Physics

September 2023

Laser spectroscopy of radioactive molecules for future searches of new physics

Michail ATHANASAKIS-KAKLAMANAKIS

Examination committee:
Prof. dr. E. Janssens, chair
Prof. dr. G. Neyens, supervisor
Prof. dr. Á. Koszorús, cosupervisor
Prof. dr. T. E. Cocolios
Prof. dr. R. P. de Groote
Prof. dr. J. Loreau
Prof. dr. R. F. Garcia Ruiz
(Massachussetts Institute of Technology)
Prof. dr. M. R. Tarbutt
(Imperial College London)

Dissertation presented in partial fulfillment of the requirements for the degree of Doctor of Science (PhD): Physics

September 2023

Uitgegeven in eigen beheer, Michail Athanasakis-Kaklamanakis, Office 26/1-007, CERN, 1 Esplanade des Particules, Meyrin 1217, Switzerland, B-3001 Leuven (Belgium)

Acknowledgments

First and foremost, I would like to thank my PhD supervisor Gerda Neyens for giving me the chance to be part of her group. Gerda, you gave me the opportunity to work on such an interesting topic and the freedom to approach it in my own way, always believing that I can produce interesting results when I was in doubt. I could not have had a better PhD supervisor.

Secondly, I would like to thank my PhD co-supervisor Ági Koszorús, who was undoubtedly a catalyst in the growth of my technical and scientific skills.

Thirdly, I would like to thank the CRIS group. Shane, Sarina, Quanjun, Louis, Jordan, Miranda, Yongchao, Bram, Julius, Sonja, Kieran, Ruben, Thomas, Xiaofei, Ronald, Dag, and more people than I can list: I am thankful for all the guidance, assistance, and support. This work is a collective, rather than personal, achievement, and I am deeply thankful for everyone's presence in the past 3 years.

I am deeply thankful for all the friends and colleagues at ISOLDE. I am especially thankful for Mia, Lukas, Maxime, Sebastian, and all other colleagues from the TISD and ISOLTRAP teams, whose work on the production of molecular beams at ISOLDE was a critical aspect of completing this work.

I would also like thank Alex, Anastasia, Sasha, Robert, Konstantin, Carsten, Timur, Leonid, Thomas and all the people who supported our molecular experiments with their work on molecular theory and spectroscopic interpretation.

Most importantly, I want to thank my family. My mother Elena, my siblings Marina and Giorgos, my aunt Tatiana and her family, and my late grandparents Michail and Kaiti.

Lastly, I am thankful for Olga, James, and Laura from CERN's EP Safety team for keeping us safe and always being there for us, standing proud for all of our progress.

Abstract

This work presents theoretical, experimental, and technical progress on the spectroscopy of short-lived radioactive molecules that have been identified for their great promise as probes for fundamental, nuclear, chemical, and astrophysical research. The presented doctoral work includes the study of the nuclear charge radius in molecular spectra through the derivation of the molecular King-plot analysis. Moreover, new measurements from the broadband laser spectroscopy of radium monofluoride (RaF) and actinium monofluoride (AcF) are analyzed and presented, which have been proposed for their exceptional sensitivity to nuclear, hadronic, and leptonic moments that violate parity and time-reversal symmetries. The measurements were obtained with the Collinear Resonance Ionization Spectroscopy (CRIS) experiment at ISOLDE, CERN's radioactive ion beam facility. In the case of AcF, this thesis stands as the first work that reports spectroscopic results on the molecule, which is of interest also for research in physical chemistry and nuclear medicine. Lastly, technical developments in the form of a voltage-scanning setup and a new laser-ablation ion source for the CRIS experiment are outlined, aimed at performing faster and more sensitive molecular spectroscopy of radioactive and non-radioactive molecules in the future.

The results of this work are of high importance for the development of accurate and precise molecular theory, which in turn is crucial for the future endeavors of precision spectroscopy to test the limits of the Standard Model and to search for new physics using short-lived radioactive molecules.

Beknopte samenvatting

Dit werk presenteert theoretische, experimentele en technische vooruitgang op het gebied van spectroscopie van kortlevende radioactieve moleculen die zijn geïdentificeerd vanwege hun grote potentieel als sondes voor fundamenteel, nucleair, chemisch en astrofysisch onderzoek. Het gepresenteerde doctoraatswerk omvat de studie van de kernladingsstraal in moleculaire spectra door middel van de afleiding van de moleculaire King-plot analyse. Bovendien zijn nieuwe metingen van de breedbandlaserspectroscopie van radium monofluoride (RaF) en actinium monofluoride (AcF) geanalyseerd en gepresenteerd, die zijn voorgesteld vanwege hun uitzonderlijke gevoeligheid voor nucleaire, hadronische en leptonische momenten die pariteit en tijdreversale symmetrieën schenden. De metingen zijn verkregen met de Collinear Resonance Ionization Spectroscopy (CRIS) experiment in ISOLDE, de faciliteit voor radioactieve ionenbundels in CERN. In het geval van AcF, is dit proefschrift het eerste werk dat spectroscopische resultaten over het molecuul rapporteert, dewelke ook van belang zijn voor onderzoek in de fysische chemie en nucleaire geneeskunde. Ten slotte zijn er technische ontwikkelingen gepresenteerd in de vorm van een voltagescanneropstelling en een nieuwe laser-ablatie ionenbron voor het CRIS experiment, gericht op het sneller en gevoeliger uitvoeren van moleculaire spectroscopie van radioactieve en niet-radioactieve moleculen in de toekomst.

De resultaten van dit werk zijn van groot belang voor de ontwikkeling van nauwkeurige en precieze moleculaire theorie, wat weer cruciaal is voor de toekomstige inspanningen naar precisiespectroscopie om de grenzen van het van het Standaard Model te testen en naar nieuwe fysica te zoeken

met behulp van kortlevende radioactieve moleculen.

Contents

List of Figures

List of Tables

Chapter 1

Introduction

1.1 General context

This thesis presents theoretical, experimental, and technical work on the intersection of nuclear and molecular physics, focused on the emerging research prospects of gas-phase studies of short-lived radioactive molecules.

The study of nuclear observables through high-precision measurements of atomic electrons has been a staple of nuclear-structure research with laser spectroscopy for many decades [7, 8]. Thanks to the electromagnetic field created by the nucleus at the center of the atom, the energy levels of the atomic electrons can be influenced by the various nuclear properties, such as the nuclear electromagnetic moments, the nuclear spin, and the nuclear charge radius. As the atomic Hamiltonian is well-understood down to the quantum electrodynamics level, spectroscopy of the hyperfine structure of atoms that contain short-lived radioactive nuclei has been highly successful in the study of properties of nuclei with extreme proton-to-neutron ratios and tests of *ab initio* nuclear theory [8, 7].

Molecules possess additional degrees of freedom compared to atoms, which significantly complicates the description of their energy levels and their substructure due to the internal dynamics. Even diatomic molecules, composed of just two atoms, possess rich substructures in their electronic spectra that stem from the different vibrations and rotations of the chemical bond around its equilibrium length and orientation. These additional degrees of freedom, however, also offer to the molecular structure an enhanced sensitivity to a number of key observables for fundamental, nuclear, and chemical physics studies. For example, it is now understood that molecular structure can be leveraged to study the limits of the Standard Model (SM) of particle physics and candidate theories that extend it with greater precision than possible in atomic studies [9].

Despite its success at describing the Universe, a number of cosmological observations are inconsistent with the SM, such as the existence of dark matter and the overwhelming imbalance of matter over antimatter. The latter problem is understood to be intimately linked to the level of time-reversal (T) violation in the Universe [10]. While T symmetry is violated to a small extent in the SM [11], a yet unknown, significantly stronger source of T violation is required to solve the baryon asymmetry problem (also known as the baryogenesis problem).

Precision spectroscopy of diatomic molecules has emerged as the foremost approach to search for the permanent electric dipole moments (EDMs) of nuclei and the electron, the very existence of which violates T symmetry [12]. Consequently, a successful measurement of the electron EDM (eEDM) would provide an exceptionally stringent benchmark of the limits of the SM and its extensions, by comparing the measurement with the predicted magnitudes. Measurements of nuclear EDMs, on the other hand, would provide new information on currently unknown symmetry-violating nucleon-nucleon interactions [13].

Searches for the eEDM with molecular spectroscopy utilize the precession of an EDM around the direction of an electric field, similar to the more familiar magnetic counterpart. Analogous to the Larmor frequency for magnetic dipoles, the EDM precession frequency is proportional to the strength of the electric field, and so using a molecule with as strong of an internal electric field as possible is crucial for an optimal measurement of the eEDM.

In heavy polar molecules, the effective electric field formed along the internuclear axis due to the large charge difference of the heavy nucleus and the light ligand can reach the GV/cm range, far surpassing what can be applied in the laboratory by several orders of magnitude. Moreover, contrary to atoms, polar molecules can be polarized along a laboratory axis of choice with relatively weak applied fields. As a result, weak applied electric fields can direct the exceedingly stronger internal effective electric field E_{eff} of heavy polar molecules along a well-defined laboratory axis, about which the eEDM precession can then be measured, for instance in the form of relative quantum-state populations that can be measured efficiently [14].

Beyond the eEDM, molecular spectroscopy is also at the forefront of precision searches for the nuclear Schiff, anapole, and magnetic quadrupole moments in nuclei with non-zero spin, all of which violate parity (P) and/or T symmetries, and which would predominantly emerge from currently unknown P, T-violating nucleon-nucleon interactions. The molecular benefit in this case stems from the presence of opposite-parity electronic states with much smaller spacing than in atoms. Core-penetrating molecular electrons that have a non-zero spatial overlap with a nucleus interact with the P, T-violating intranuclear fields, resulting in mixing of opposite-parity electronic states. Since the unmixed electronic states lie a lot closer in energy in molecules than in atoms, the resulting P, T-violating mixing is a lot stronger for the molecular structure, and thus the nuclear properties are more easily measurable.

For both the eEDM and symmetry-odd nuclear moments, a strong enhancement in the measurable signal of the target observable is expected when studying molecules that contain a heavy and deformed nucleus. The molecular sensitivity to the moments of interest scales with the charge of the heavy nucleus, as it leads to a stronger E_{eff}. In the case of the nuclear moments, a second source of enhancement is expected; the static octupole deformation that many heavy nuclei possess [15, 16, 17] leads to an enhancement of the P, T-violating nuclear moments [18, 19, 20, 21], as the reflection-asymmetric shape of an octupole-deformed nucleus results in close-lying opposite-parity rotational doublets at low energy that are therefore more easily mixed by the P, T-violating nucleon-nucleon interactions.

However, almost all such heavy and deformed nuclei above ^{208}Pb are unstable and have short half-lives. Therefore, the spectroscopy of such molecules is only known theoretically and prior to this work, only one experimental study on the spectroscopy of such radioactive molecules has been published, performed by our collaboration [5].

Beyond the fundamental-physics motivation, the study of short-lived radioactive molecules is also of interest for nuclear, chemical, and astrophysical studies that are not possible with atoms [22, 23]. However, to harness the benefits of molecules that contain heavy radioactive nuclei, spectroscopy of radioactive molecules needs to be developed at radioactive ion beam (RIB) facilities, where the nuclei are studied as they are being produced.

For nuclear structure research, molecular spectroscopy can offer higher sensitivity to the nuclear charge radius and the nuclear magnetic dipole and electric quadrupole moments. Measurements of changes in the nuclear charge radius across an isotopic chain can be used to probe the magicity of nucleon numbers [24], test the ability of nuclear theory to elucidate correlation effects and the odd-even staggering [25], uncover complex nuclear effects manifesting in the charge radius [26], and highlight the role of three-nucleon interactions [27]. The nuclear moments, on the other hand, provide insights into the balance between single-particle and collective behavior in the structure of a nucleus [28]. The nuclear magnetic dipole moment gives access to the nuclear g-factor, which is distinct for each orbital that the unpaired nucleons in a nuclear state can occupy and quantifies the purity of a single-particle description of a nuclear state. The electric quadrupole moment, on the other hand, quantifies the departure of a nucleus from sphericity and the emergence of a static oblate or prolate quadrupole-deformed shape.

Studying a nucleus as part of a molecule allows for engineering – to a certain extent – the electronic structure of the studied species by choosing a suitable ligand such that the molecular states have a high sensitivity to the nuclear observables of interest. As an example, the electric field gradient (EFG) in atomic K is weak, resulting in a very small hyperfine splitting due to the nuclear electric quadrupole moment for all atomic states and thus a lack of quadrupole-moment measurements for short-lived isotopes. On the contrary, the EFG in the KF molecule is significantly stronger, and thus the most accurate values for the electric quadrupole moments of the naturally abundant $^{39-41}$K have been determined from the spectroscopy of KF [29, 30].

In general, molecular spectroscopy at RIB facilities can enable the study of species that cannot be efficiently extracted as atoms from RIB sources. Isotopes of several elements can be produced intensely within the targets of RIB facilities, but as they form reactive or refractory atoms, their atomic extraction rates are very weak, prohibiting their study with laser spectroscopy. By forming molecules of the species of interest, refractory atoms can be extracted as part of volatile molecules, and reactive atoms can be bound to a compound of choice in a controlled manner [31, 32, 33].

Experiments on radioactive molecules are also of interest as benchmarks of *ab initio* quantum chemistry. In the heavy region, the understanding of actinide chemistry remains incomplete despite progress [34, 35] and more experimental data is necessary, while the role of $5f$ electrons in chemical bonding remains a topic of active research [36, 37, 38]. Due to the size of the systems, a fully relativistic *ab initio* treatment that accurately captures electron correlation has been prohibitively challenging until recently. Studies of pre- and early-actinide molecules, where the $5f$ orbital is not yet occupied, are necessary for the development and benchmark of the computational implementations that can tackle the $5f$ region in the future.

Lastly, the detection of molecular spectral lines in the millimeter range has emerged as a highly sensitive pathway to determining the isotopic composition of matter in celestial objects [39]. Such knowledge is necessary to understand nucleosynthesis in the core of stars [40, 41, 42], which for decades has been studied with γ-ray spectroscopy. However, γ-ray spectroscopy does not have the necessary sensitivity and resolution for isotopic-ratio studies in high-mass stars or supernova explosions. Millimeter-wave spectroscopy, on the other hand, was recently used with great success to identify the presence of ^{26}AlF in stellar-merger remnants [43], demonstrating for the first time the high sensitivity and resolution of the approach for the astrophysical detection of a radioactive nuclide.

In the absence of direct laboratory measurements of a radioactive molecule's millimeter-wave spectrum on Earth, its lines can be searched for in space through extrapolations of the spectral lines of stable isotopomers of the same molecule, as in the case of AlF [43, 44]. This approach relies on a mass-independent analysis of the Dunham parametrization (as an example, see Ref. [45]), which is not valid for triatomic or polyatomic molecules and whose resulting uncertainty is prohibitively large for radioactive isotopomers more than 1 amu away from the analyzed stable isotopomers. Therefore, direct measurements of radioactive molecules in the millimeter-wave range on Earth are necessary for the astrophysical detection of the majority of radioactive molecules.

Despite the wide interest in radioactive molecules research across many scientific areas, molecular spectroscopy had until recently not been demonstrated at an RIB facility, and only compounds of the primordial uranium and thorium isotopes had been studied in the gas phase. The main limitation for molecular spectroscopy at RIB facilities has been the low production rates of the species of interest that are available for study. The richness of molecular spectra, with hundreds of energy levels populated at room temperature, leads to a significantly lower spectroscopic efficiency compared to the study of atoms. In combination with the already weak production rates of radioactive beams, these characteristics deemed the spectroscopy of radioactive molecules at RIB facilities unfeasible in the past.

With the development of the collinear resonance ionization spectroscopy (CRIS) experiment at CERN-ISOLDE (see Section 2.4), which combines the resolution of fast-beam collinear laser spectroscopy (CLS) [46] with the sensitivity and selective detection of resonance ionization spectroscopy [47, 48], the sensitivity limit of CLS at ISOLDE has significantly advanced down to 20 atoms per second [49]. This allowed the first study of a short-lived radioactive molecule in 2018, with the broadband laser spectroscopy of radium monofluoride (RaF) at CRIS [5].

Since the first study of RaF at CRIS, research in radioactive molecules has gained significant momentum. More efforts are being devoted at ISOLDE for the production of a variety of radioactive molecules while other RIB facilities, such as FRIB, TRIUMF, and IGISOL [23], are also developing controlled molecular production. Furthermore, the possibility of implementing precision-control techniques at RIB facilities is being explored, and challenges and next steps are being identified [23, 22, 50].

1.2 Outline of the thesis

As expressed in Ref. [23], a significant amount of work is still necessary in order to harness the full potential of radioactive molecules research. The doctoral work presented in this thesis is focused on progress in the study of short-lived radioactive molecules along three directions: theory, experiment, and technical developments. The thesis is structured around 3 papers and complemented with relevant information not included in any publication so far.

Chapter 1 gives an introduction to this work and an outline of how the manuscript is structured, along with a list of co-authored papers that are not described in the following chapters.

Chapter 2 provides an overview of concepts from nuclear, atomic, and molecular physics that are necessary to understand the research presented in this thesis, as well as an introduction to the CRIS experiment that was used to obtain the presented measurements.

In Chapter 3, a link between the well-known King-plot analysis of atomic spectra and isotope shifts in diatomic molecules is made, which can accelerate the study of nuclear charge radii through molecular spectroscopy and illuminates the role of nuclear size effects in molecular structure. Following an extended motivation for the work, the results are presented in Article 1:

- **Article 1:** M. Athanasakis-Kaklamanakis, S. G. Wilkins, A. A. Breier, G. Neyens, *King-plot analysis of isotope shifts in simple diatomic molecules* Physical Review X **13**, 011015 (2023). doi

In Chapters 4 & 5, the analysis of new laser spectroscopy experiments on RaF is presented, reporting measurements of the high-lying electronic structure and spectroscopy of short-lived isotopomers from ^{210}RaF to ^{230}RaF. The resulting excited electronic levels are reported in Article 2, which is included in Chapter 4:

- **Article 2:** M. Athanasakis-Kaklamanakis, S. G. Wilkins, L. V. Skripnikov, Á. Koszorús, A. A. Breier, M. Au, I. Belošević,

R. Berger, M. L. Bissell, A. Borschevsky, A. Brinson, K. Chrysalidis, T. E. Cocolios, R. P. de Groote, A. Dorne, C. M. Fajardo-Zambrano, K. T. Flanagan, S. Franchoo, R. F. Garcia Ruiz, K. Gaul, S. Geldhof, T. F. Giesen, D. Hanstorp, R. Heinke, T. Isaev, A. A. Kyuberis, S. Kujanpää, L. Lalanne, G. Neyens, M. Nichols, L. F. Pašteka, H. A. Perrett, J. R. Reilly, S. Rothe, S.-M. Udrescu, B. van den Borne, Q. Wang, J. Wessolek, X. F. Yang, C. Zülch, and the ISOLDE Collaboration, *Pinning down electron correlations in RaF via spectroscopy of excited states* Under review (2023) arXiv:2308.14862

In Chapter 6, the first spectroscopy of the AcF molecule is presented. The experiment performed on this new radioactive molecule is introduced, along with a motivation for this work and the analysis of the results. A publication on this work is currently in preparation, but the details are not finalized and thus not presented here.

Finally, in Chapter 7, technical developments at the CRIS experiment for efficient and sensitive spectroscopy of radioactive molecules are described. The bulk of these developments were presented at the 19th International Conference on Electromagnetic Isotope Separators and related topics (EMIS) in 2022, and a resulting paper was published in the conference proceedings and is included in this chapter as Article 3:

- **Article 3**: M. Athanasakis-Kaklamanakis, J. R. Reilly, Á Koszorús, S. G. Wilkins, L. Lalanne, S. Geldhof, M. Nichols, Q. Wang, B. van den Borne, D. Chorlton, T. E. Cocolios, K. T. Flanagan, R. F. Garcia Ruiz, R. P. de Groote, D. Hanstorp, G. Neyens, A. J. Smith, A. R. Vernon, X. F. Yang, *Voltage scanning and technical upgrades at the Collinear Resonance Ionization Spectroscopy experiment* Nuclear Instruments and Methods in Physics Research Section B: Beam Interactions with Materials and Atoms 541, 86-89 (2023)

A fourth article is added to the appendix, which is discussed in Chapter 5:

- **Article 4**: T. A. Isaev, S. G. Wilkins, M. Athanasakis-Kaklamanakis, *On the Feasibility of Rovibrational Laser Cooling of Radioactive RaF^+ and RaH^+ Cations* Atoms 9, 101 (2021)

1.3 Co-authored papers not included in the thesis

The work included in this thesis has given rise to several publications in peer-reviewed scientific journals. A list of the co-authored publications that are not discussed in this thesis is given below:

1. **M. Athanasakis-Kaklamanakis** and G. Neyens, *Nuclear matter radii from molecular rotations using ultra-high-resolution spectrometers* Under review (2023)
2. G. Arrowsmith-Kron *et al.* (69 authors), *Opportunities for Fundamental Physics Research with Radioactive Molecules*, Submitted to *Reports on Progress in Physics* (2023) arXiv:2302.02165

   – Wrote a section on the CRIS experiment and contributed to the general section for ISOLDE.
3. L. V. Skripnikov, A. V. Oleynichenko, A. Zaitsevskii, N. S. Mosyagin, **M. Athanasakis-Kaklamanakis**, M. Au, G. Neyens, *Ab initio study of electronic states and radiative properties of the AcF molecule* Accepted at Journal of Chemical Physics (2023) arXiv:2305.06932

   – Provided the motivation for the study and assisted with manuscript preparation.
4. S.-M. Udrescu, S. G. Wilkins, **M. Athanasakis-Kaklamanakis**, R. F. Garcia Ruiz, *et al.*, *Precision spectroscopy and laser cooling scheme of a radium-containing molecule* Accepted at Nature Physics (2023) preprint

   – Had a major role in preparing and performing the experiment.
5. M. Au, ..., **M. Athanasakis-Kaklamanakis** *et al.*, *Developments at ISOLDE's OFFLINE 2 mass separator facility for studies of molecular ion beams*, proceedings of the International Conference on Electromagnetic Isotope Separators and related topics (EMIS Conference), South Korea, October 2022. Nuclear Instruments and Methods in Physics Research Section B (2023) doi

   – Participated in the experimental efforts.

6. M. Au, **M. Athanasakis-Kaklamanakis**, L. Nies, *et al.*, *In-source and in-trap formation of molecular ions in the actinide mass range at CERN-ISOLDE*, proceedings of the International Conference on Electromagnetic Isotope Separators and related topics (EMIS Conference), South Korea, October 2022. Nuclear Instruments and Methods in Physics Research Section B (2023) doi

   – Participated in the experimental efforts.

7. S. Kraemer, J. Moens, ..., **M. Athanasakis-Kaklamanakis** *et al.*, *Observation of the radiative decay of the* ^{229}*Th nuclear clock isomer* Nature **617** (7962), 706-710 (2023). doi

   – Participated in the experimental efforts.

8. M. Au, **M. Athanasakis-Kaklamanakis** *et al.*, *Production of neptunium and plutonium nuclides from uranium carbide using 1.4-GeV protons* Physical Review C, **107**, 064604 (2023) doi

   – Participated in the experimental efforts.

9. L. Nies, ..., **M. Athanasakis-Kaklamanakis**, *et al.*, *Isomeric excitation energy for* $^{99}In^{m}$ *from mass spectrometry reveals contrasting trends next to doubly magic* ^{100}Sn Physical Review Letters, **131**, 022502 (2023) doi

   – Participated in the experimental efforts.

10. **M. Athanasakis-Kaklamanakis**, D. Manara *et al.*, *Identifying Thermodynamic Mechanisms Affecting Reactor Pressure Vessel Integrity During Severe Nuclear Accidents Simulated by Laser Heating at the Laboratory Scale* Nuclear Science and Engineering **197** 3 (2022) 1-17. doi

    – Had a major role in the design of the experiment, led the experimental efforts, analyzed the data, and wrote the manuscript.

11. S. Kujanpää, ..., **M. Athanasakis-Kaklamanakis** *et al.*, *RAPTOR: a new collinear laser ionization spectroscopy and laser-radiofrequency double-resonance experiment at the IGISOL facility*, proceedings of the International Conference on Electromagnetic Isotope Separators and related topics (EMIS Conference), South

Korea, October 2022. Nuclear Instruments and Methods in Physics Research Section B (2023). doi

– Participated in the experimental efforts.

12. M. Nichols, ..., **M. Athanasakis-Kaklamanakis** *et al.*, *Investigating radioactive negative ion production via double electron capture*, proceedings of the International Conference on Electromagnetic Isotope Separators and related topics (EMIS Conference), South Korea, October 2022. Nuclear Instruments and Methods in Physics Research Section B (2023) doi

    – Assisted in the preparation of the experiment and participated in the experimental efforts.

Lastly, three documents were authored, submitted, and defended to the ISOLDE and n_TOF Committee (INTC) at CERN to secure radioactive beam time at ISOLDE for the study of radioactive molecules:

1. Radioactive molecules ISOLDE (2021), CERN-INTC-2021-017, INTC-I-227, cds.cern.ch/record/2748712
2. Laser ionization spectroscopy of AcF (2021), CERN-INTC-2021-053, INTC-P-615, cds.cern.ch/record/2782407
3. IS663: Rotational and hyperfine spectroscopy of RaF (2023), CERN-INTC-2023-037, INTC-P-555-ADD-1, cds.cern.ch/record/2856444

All three documents were successfully accepted in full by the INTC, and a total of 48 shifts (144 hours) of experimental time at ISOLDE were secured.

Chapter 2

Prior concepts

2.1 Nuclear physics

The atomic nucleus is one of the most complex structures known in the Universe. The protons and neutrons (collectively referred to as nucleons) that comprise the nucleus interact with each other through the electromagnetic, weak nuclear, and strong nuclear forces, resulting in a sensitive balance between attraction and repulsion. The protons and neutrons are thus strongly correlated, as each of their dynamics have great impact on the overall inter-nucleon potential, which in turn determines the quantum state of the individual nucleons.

One of the earliest and most successful approaches to treating the complexity of such a correlated many-body problem was the conception of a nuclear shell model [51]. The basis of the nuclear shell model is a simplified treatment of the nuclear many-body problem where the nucleons behave as independent particles in a mean, effective potential; each nucleon's behavior is thus seen as governed by the potential created by all other nucleons [52]. The neglected nucleon correlations can then be treated as a perturbation of the Hamiltonian in the form of a residual interaction. Through this approach, the nucleons acquire a set of quantum states (orbitals) that they can occupy, each orbital with a maximum occupation, energy, and angular momentum. As nucleons are added to the nucleus, they occupy the available orbitals in the order that results in the lowest energy configuration and thus the most energetically stable nuclear state. The orbitals become inert when they are fully occupied, and the properties of the nucleus is seen as determined solely by the behavior of the valence nucleons in the partially occupied orbitals.

This treatment is known as the nuclear shell model because, as in the atomic counterpart, certain numbers of protons and neutrons result in sets of fully occupied nucleon orbitals comprising well-bound nuclei. These numbers are known as *magic*, and early experimental studies showed that they are 2, 8, 20, 28, 50, 82, and 126 for protons and neutrons, separately. One of the major arguments in favor of the nuclear shell model is its ability to predict the emergence of these magic numbers, for which the nuclear spin-orbit coupling is a necessary component [53]. When a nucleus has a magic number of protons or neutrons, adding more nucleons beyond magicity places them in orbitals whose energy has a significant gap from the energy of the lower-lying, fully occupied orbitals. The presence of these gaps thus also infers the existence of "shells" of energy levels that are formed between the gaps.

Of course, the nuclear shell structure is not a realistic treatment in all regions of the nuclear chart, as the nucleon correlations can be strong enough to not justify their inclusion as just a perturbation in the potential. Close to magic (both protons and neutrons at magic numbers) and semi-magic (either protons or neutrons at magic numbers) nuclei, however, the shell model has proven to be an accurate description of the observed nuclear structure [51]. The intuitive justification for the success of the shell structure close to magicity is that magic nuclei behave as especially well-bound inert cores, and thus adding few particles or holes results in a pure single- or few-particle picture that follows closely an independent particle behavior.

In certain cases, this single-particle picture fails to account for the observed nuclear structure even in regions of magicity. This is commonly attributed to the emergence of collective behavior, where nucleon correlations play a critical role and lead to the nucleus behaving more as a collective entity rather than as a combination of independent nucleons. Moreover, as experimental techniques in nuclear physics are becoming more efficient and sensitive and nuclei farther from stability are coming within reach, the emergence of new magic numbers and the disappearance of the traditional ones has become evidence that the shell structure is not static, and instead evolves as a function of proton and neutron numbers (and their imbalance) across the chart of the nuclides [54]. These observations bring into light two major questions in nuclear structure. Firstly, what is the interplay between single-particle behavior and collective structure? Secondly, how do the single-particle and collective behaviors evolve as a function of proton and neutron numbers?

The nuclear electromagnetic moments and the nuclear charge radii are especially informative observables in terms of tackling these questions, and they are discussed in the following subsections.

2.1.1 Nuclear spin, moments, and radii

All nuclei with an even number of protons and an even number of neutrons have been observed to have a ground-state wavefunction of even parity and 0 total nuclear angular momentum (referred to as the nuclear spin I). This maybe surprising observation points to the fact that the angular momenta of the nucleons tend to pair to a total angular momentum of 0, when possible. As a consequence, when either or both protons and neutrons are odd-numbered, the nuclear spin is determined by the angular momentum j of the unpaired proton and neutron, and, in odd-odd nuclei,the coupling between them (following Paar's rule [55]). Consequently, the nuclear spin is often the first piece of information about the quantum state occupied by the unpaired nucleons, and systematic studies of the evolution of the nuclear spin as a function of protons and neutrons can provide information on shell evolution.

Nuclei with $I > 0$ have a lab-frame magnetic dipole moment, while nuclei with $I > \frac{1}{2}$ also have a lab-frame electric quadrupole moment. These moments arise from the distribution and movement of the nucleons within the nucleus. The protons carry positive electric charge and as they are distributed within the nucleus, so is the nuclear charge. Additionally, the proton motions create magnetic fields, as do the intrinsic nucleon spins. These nuclear properties are most commonly analyzed and discussed in the form of the 2^k-pole electromagnetic moments that emerge from the multipole expansion of the nuclear electromagnetic potential.

From symmetry considerations, only the even-k electric and odd-k magnetic moments conserve parity and are allowed. The magnitude of the allowed moments decreases for increasing k, and thus the magnetic dipole moment μ ($k = 1$) and the electric quadrupole moment Q ($k = 2$) are the most commonly studied nuclear moments [28]. Higher-order moments, such as the magnetic octupole moment [56, 57] and the electric hexadecapole moment [58] are occasionally also studied.

The magnetic dipole moment μ is defined as the expectation value of the z-axis component of the rank-1 magnetic dipole operator for the nuclear state that has the maximum spin-momentum projection $m_I = I$. Commonly, it has the form:

$$\mu = gI\mu_N \tag{2.1}$$

where g is called the g-factor, I is the nuclear spin, and $\mu_N = \frac{e\hbar}{2m_p}$ is called the nuclear magneton.

The importance of the magnetic dipole moment is that it can be shown that [28], at the single-particle limit, the g-factor of the nuclear state is equal to the g-factor of a single unpaired nucleon in a partially occupied orbital (called the Schmidt moments), while also being subject to straightforward additivity rules for the case of few particles (or holes) on top of an inert core. This means that measurements of the magnetic dipole moment in nuclei are excellent probes of the wavefunction of the unpaired nucleons, as well as the extent that the single-particle behavior accurately describes the structure of the nucleus. Deviations of the magnetic dipole moment from the Schmidt values indicate that mixing is present in the nuclear wavefunction [59], which is a signature of collectivity.

The electric quadrupole moment provides information on the deformation of the nuclear shape and its deviation from sphericity. The electric quadrupole operator is defined as:

$$\hat{Q} = e\sum_{k=1}^{A}\left(3z_k^2 - r_k^2\right) \tag{2.2}$$

where e is the fundamental charge and z_k and $r_k = \sqrt{x_k^2 + y_k^2 + z_k^2}$ are the coordinates of the kth nucleon [28]. The electric quadrupole moment that can be measured in the laboratory is the spectroscopic one (Q_s), which is the expectation value of the z-component of the quadrupole operator (Eq. 2.2). For well-deformed nuclei, the spectroscopic quadrupole moment can be related to the intrinsic electric quadrupole moment Q_0 in the body-fixed axis system of the nucleus by [28, 60]:

$$Q_s = \frac{3K^2 - I(I+1)}{(I+1)(2I+3)} Q_0 \tag{2.3}$$

where K is the projection of the nuclear spin I on the intrinsic deformation axis of the nucleus. The intrinsic electric quadrupole moment is of high interest, as it can be related (through the liquid drop model) to the nuclear quadrupole deformation parameter β_2, which quantifies the deviation of the nuclear shape from sphericity, as:

$$Q_0 = \frac{3}{\sqrt{5\pi}} eZR^2\beta_2 \left\{ 1 + \pi^2 \left(\frac{\alpha}{R}\right)^2 + \frac{2}{7}\sqrt{\frac{5}{\pi}}\beta_2 \right\} \tag{2.4}$$

where Z is the atomic number, R is the nuclear radius, and α is a surface thickness correction factor ($\alpha = 0.54$ fm for the Pb region).

Eq. 2.4 also brings the nuclear radius into the discussion. Nuclei have two radii that are of high interest for nuclear-structure studies: the matter radius, which takes into account the radial spread of both protons and neutrons, and the charge radius, which arises only from the proton distribution. With laser spectroscopy, we can only observe the second radial moment of the nuclear charge distribution, which is commonly referred to as the mean-squared nuclear charge radius:

$$\langle r_{\mathrm{ch}}^2 \rangle = \frac{1}{Ze} \int r^2 \rho_{\mathrm{ch}} dV \tag{2.5}$$

where ρ_{ch} is the nuclear charge density distribution. Other radial moments of order N can be calculated by substituting r^2 for r^N in Eq. 2.5, while the corresponding radial moments of the matter radius can be extracted by using ρ_{mat} instead.

2.1.2 Intrinsic moments, octupole deformation, and Schiff moment

In the intrinsic nuclear frame, which is a body-fixed axis system of the nucleus, transitions of any multipolarity can be observed between nuclear states.

While intrinsic nuclear moments are not observable with laser spectroscopy, other techniques, such as nuclear reactions and decay spectroscopy, are sensitive to them. Using Coulomb excitation, electric octupole deformation has been observed in the low-lying states of the radioactive nuclei ^{220}Rn and ^{222,224,228}Ra ($I^{\pi} = 0^{+}$ ground state) [15, 61]. Octupole collectivity has been observed in several long-lived heavy nuclei as well [62], including ^{226}Ra for which there is evidence of electric hexadecapole deformation in the low-lying structure as well [63].

Electric octupole (E3) moments in ^{220}Rn and ^{222,224,228}Ra, or the electric dipole moment (E1) in ^{228}Th [64], are only observed in the intrinsic frame, and they do not manifest in the laboratory frame. One reason is the spin requirement following the Wigner-Eckart theorem, while the nuclei under question all have $I = 0$ ground states. A second important reason is that the E1 and E3 operators violate parity symmetry, and thus the E1 and E3 moments would manifest in the laboratory frame as a result of symmetry-violating mechanisms in the fundamental forces.

In the Standard Model of particle physics (and all other realistic particle physics theories), the simultaneous action of charge conjugation (C), parity (P), and time reversal (T) is a good symmetry, but the individual C, P, and T symmetries can be violated in different fundamental interactions. The weak nuclear force, for example, is known to be P, T-violating [65]. Several cosmological observations, however, such as the existence of dark matter and the imbalance of matter over antimatter, indicate that the level of T violation in the fundamental forces must be greater than that considered in the Standard Model. To trace the level of T violation in the Universe and to explore the limits of the Standard Model and its extension theories (commonly referred to as Beyond-the-Standard-Model theories, BSM), global experimental efforts are concentrating on searching for the laboratory-frame P, T-violating moments of the proton, the neutron, and the electron, as well as nuclei.

Permanent electric dipole moments (EDMs) have received the most focus of all P, T-violating moments as probes for new physics [66, 12]. Several experimental campaigns are ongoing around the world[1] to measure the neutron EDM using ultracold neutron sources, reaching a sensitivity of 10^{-26} e cm [67], to be compared to the Standard Model value of 10^{-34} e cm [68]. The electron EDM (eEDM) is at the center of precision measurements with atomic, diatomic, and polyatomic beams, with the current best sensitivity reported between 10^{-29} and 10^{-30} e cm [69, 70], while the Standard Model prediction is below 10^{-38} e cm [71]. In nuclei, the permanent EDM cannot be reliably studied within atoms or molecules due to the complete or partial electronic screening, which is known as the Schiff theorem [72]. Instead, experimental campaigns aim to measure a different but related observable, the nuclear Schiff moment.

The intrinsic nuclear Schiff moment is defined as the expectation value of the Schiff operator for the nuclear substate with maximal spin projection $m_I = I$, where the Schiff operator is:

$$\hat{S}_{\text{int}} = \frac{e}{10}\sqrt{\frac{4\pi}{3}}\sum_i^Z\left(r_i^3 - \frac{5}{3}\langle r_{\text{ch}}^2\rangle r_i\right)Y_0^1(i) + ... \tag{2.6}$$

where the index i runs over all protons, $\langle r_{\text{ch}}^2\rangle$ is the mean-squared nuclear charge radius, r_i is the radial coordinate of the ith proton.

If we consider the P, T-violating interaction between two nuclear states of equal spin but opposite parity $|I^\pi, m_I = I\rangle = |\Psi\rangle$ and $|I^{-\pi}, m_I = I\rangle = |\bar{\Psi}\rangle$, then the laboratory-frame nuclear Schiff moment can be written as [73]:

$$S_{\text{lab}} \approx -2\frac{\langle\Psi|\hat{S}_{\text{int}}|\bar{\Psi}\rangle\langle\bar{\Psi}|\hat{V}_{P,T}|\Psi\rangle}{\Delta E} \tag{2.7}$$

where ΔE is the difference in excitation energy between the two opposite-parity nuclear states, and $\hat{V}_{P,T}$ is the P, T-violating nuclear potential that mixes the two opposite-parity states, a convenient expression of which is given in Ref. [73] following the chiral effective field theory treatment in Ref. [74].

---

[1] https://www.psi.ch/en/nedm/edms-world-wide

By measuring the laboratory-frame Schiff moment of a nucleus, the aspiration is to extract $\langle\bar{\Psi}|\hat{V}_{P,T}|\Psi\rangle$ through Eq. 2.7. For this purpose, it is necessary to know the intrinsic-frame Schiff moment as precisely as possible, which can only be deduced from nuclear theory. This poses a challenge and a dilemma: heavy nuclei are preferred [13, 73, 9] as they have large mean-squared charge radii and their octupole deformation results in closely spaced opposite-parity doublets at low energy which enhance the symmetry-violating mixing, but their theoretical description is not tractable with *ab initio* methods, and only nuclear density functional theory, whose precision is unclear and to a certain extent limited, is possible. A similar dilemma stands for searches of other symmetry-violating nuclear moments as well, where heavy nuclei are beneficial as well. For nuclear-spin-dependent parity violation, molecules containing light nuclei are under consideration [75, 76], as their structure can be investigated with the *ab initio* No Core Shell Model [77].

2.2 Atomic physics

2.2.1 Atomic hyperfine structure

Laser spectroscopy of radioactive atoms is focused, for the most part, on extracting the electromagnetic moments and changes in mean-squared charge radii of the unstable atomic nuclei by systematic measurements of the hyperfine structure and isotope shift in atomic transitions [8, 7].

As elaborated in the previous section, a nucleus with non-zero spin I possesses a magnetic dipole moment in the laboratory frame, while if $I \geq 1$, the nucleus also possesses a spectroscopic electric quadrupole moment. These nuclear properties couple with the electromagnetic fields induced by the motion of atomic electrons to give rise to very small splittings of atomic states. Because the splitting due to the electron-nucleus interaction is smaller than the fine-structure splitting, it is referred to as the hyperfine structure (hfs).

The atomic hfs can be derived starting from the expression of the nuclear electromagnetic properties as a collection of 2^k-pole electric and magnetic terms of a scalar and vector potential, and the interaction Hamiltonian of an electron in the presence of the nuclear potential [78]. In the absence of parity- and time-reversal-violating electron-nucleus interactions, the hfs Hamiltonian consists of only even-k electric and odd-k magnetic terms, with decreasing importance for increasing k. Therefore, the magnetic dipole and electric quadrupole terms dominate the atomic hfs, while in certain cases the magnetic octupole term has also been measured (see Refs. [56, 57] and reference therein).

The splitting of an atomic state due to the interaction of the nuclear magnetic dipole moment μ and the magnetic field at the location of the nucleus due to the electronic motion is parametrized by the hfs A factor, according to:

$$\Delta E_\mu = -\frac{AK}{2} \tag{2.8}$$

where

$$K = F(F+1) - I(I+1) - J(J+1) \tag{2.9}$$

and

$$A = \frac{\mu B}{IJ} \tag{2.10}$$

In Eq. 2.9, I is the total nuclear angular momentum (nuclear spin), J the total electronic angular momentum, and F is the total atomic angular momentum that arises from the LS coupling of I and J. In Eq. 2.10, μ is the nuclear magnetic dipole moment and I the nuclear spin, while B is the magnetic field at the location of the nucleus due to the atomic electrons and J the total angular momentum of the atomic state.

A shift that is usually smaller than the dipole splitting in Eq. 2.8 is caused by the interaction of the nuclear electric quadrupole moment and the atomic electric field gradient at the nuclear volume, which is parametrized by the hfs B factor and has the form:

$$\Delta E_Q = B\frac{3(K(K+1) - 4I(I+1)J(J+1))}{8I(2I-1)J(2J-1)} \tag{2.11}$$

where K is given by Eq. 2.9 as for the dipole splitting and

$$B = eQ_s\frac{\partial^2 V}{\partial z \partial z} \tag{2.12}$$

where e is the elementary charge, $\frac{\partial^2 V}{\partial z \partial z}$ is the atomic electric field gradient at the location of the nucleus, and Q_s is the spectroscopic nuclear electric quadrupole moment.

2.2.2 Isotope shifts

When the same atomic transition is measured in different isotopes of the same element, the center of gravity of the measured structure (whether hfs is present or not) appears shifted. The isotope-dependent change in the transition frequency is called the *isotope* shift and has two components: the field shift and the mass shift.

The field shift emerges from the difference in the nuclear charge radius between the two isotopes. As electrons in atomic orbitals with non-zero spatial overlap with the nucleus (such as s and p orbitals) penetrate the nuclear volume, their binding energy is perturbed by the radius of the nuclear charge. This is quantified by the transition-specific atomic field-shift factor F (units of GHz fm^{-2}), which takes the analytical first-order form [79]:

$$F = \pi\Delta|\psi(0)|^2\frac{\alpha_0^3}{Z}\zeta N\langle r^2\rangle^{\sigma-1} \tag{2.13}$$

where $\Delta|\psi(0)|^2$ is the change (between lower and upper electronic states) in the non-relativistic probability density of the electron cloud at the location of the nucleus including electron screening effects, α_0 is the Bohr radius, Z is the atomic number, and ζ, N, and σ are nuclear functions quantifying the deviation of a real nucleus from a point-like model. The analytical form of the nuclear factors is elaborated on in Ref. [79].

The mass shift, on the other hand, stems from the slight change in the center of mass of the atomic system due to the change in the nuclear mass between isotopes. Two terms contribute to the mass shift, the normal mass shift (NMS) and the specific mass shift (SMS), with the SMS depending on the total electron correlation energy across all electron pairs in the atom. Overall, the mass shift is quantified by the transition-specific atomic mass-shift factor K (units of GHz amu), which has the form:

$$K = k_{\text{NMS}} + k_{\text{SMS}} \tag{2.14}$$

where the k_{NMS} and k_{SMS} constants are calculated from relativistic one-body and two-body operators, respectively, described in Eqs. 2 and 3 of Ref. [80].

Overall, the isotope shift $\delta\nu^{A,A'}$ between an isotope A and a reference isotope A' for a specific atomic transition takes the form of [79]:

$$\delta\nu^{A,A'} = F\delta\langle r^2\rangle^{A,A'} + K\frac{M_{A'} - M_A}{M_{A'}M_A} \tag{2.15}$$

where $\delta\langle r^2\rangle^{A,A'}$ is the change in mean-squared nuclear charge radius between isotopes A and A', M_A, $M_{A'}$ are the isotopic masses, and K involves the mass of the reference isotope in Eq. 2.14[2]. Thus, knowledge of the isotope-shift factors F and K and measurements of $\delta\nu^{A,A'}$ means that Eq. 2.15 can be used to extract the change in mean-squared nuclear charge radius between isotope A and the reference isotope A' (assuming the masses are known precisely enough), which is a cornerstone of atomic laser spectroscopy for nuclear structure research.

Bringing together the hfs and the isotope shift, the transition energy in an isotope A for the angular momentum components F and F' of the lower and upper electronic states, respectively (not to be mistaken with the field-shift factor), can be expressed as:

$$hv_A(F,F') = h\nu_{0,A'} + \Delta E_\mu(F) + \Delta E_Q(F) + \Delta E_\mu(F') + \Delta E_Q(F') + \delta\nu^{A,A'} \tag{2.16}$$

---

[2] An optical parameter $\lambda^{A,A'}$ that takes into accounts higher-order radial moments has been omitted from Eq. 2.15. More information on $\lambda^{A,A'}$ can be found in Ref. [81].

where $\nu_{0,A'}$ is the frequency of the nominal, unperturbed transition in the reference isotope A'.

2.2.3 Atomic King-plot analysis of isotope shifts

The isotope-shift factors F and K can be calculated from first principles using Eq. 2.13 and 2.14, through *ab initio* calculations of the electronic wave function. Alternatively, if values of $\delta\langle r^2\rangle^{A,A'}$ are known from non-optical experiments, such as electron scattering or muonic-atom spectroscopy, then measurements of $\delta\nu^{A,A'}$ and Eq. 2.15 can be used to deduce F and K.

In certain situations, isotope-shift measurements between the same set of isotopes are available for two or more atomic transitions, but F and K are not known for all measured transitions. A manipulation of Eq. 2.15 that is known as an atomic King-plot analysis can then be used to extract F and K for any atomic transition if they are known for any other transition.

Consider two sets of isotope-shift measurements $\delta\nu_i^{A,A'}$ and $\delta\nu_j^{A,A'}$, corresponding to atomic transitions i and j, respectively, measured on the same set of isotopes. For transitions i and j, a separate isotope-shift equation according to Eq. 2.15 holds, but $\delta\langle r^2\rangle^{A',A}$ and $\frac{M_{A'}-M_A}{M_{A'}M_A}$ are common in both. As a result, the two isotope-shift equations can be combined to yield an expression that relates F_i and K_i to F_j and K_j:

$$\tilde{M}^{A,A'}\delta\nu_i^{A,A'} = \frac{F_i}{F_j}\tilde{M}^{A,A'}\delta\nu_j^{A,A'} + K_i - K_j\frac{F_i}{F_j} \tag{2.17}$$

where $\tilde{M}^{A,A'} = \frac{M_{A'}M_A}{M_{A'}-M_A}$.

As per Eq. 2.17, in a linear fit between $\tilde{M}^{A,A'}\delta\nu_i^{A,A'}$ and $\tilde{M}^{A,A'}\delta\nu_j^{A,A'}$ (called the modified isotope shifts), the slope relates the unknown F_j to the known F_i, and then the y-intercept relates the unknown K_j to the known K_i, F_i, and F_j (known through the slope).

Notably, Eq. 2.17 relies on the assumption that Eq. 2.15 contains purely atomic (F and K) and purely nuclear (radii and masses) factors. This is an assumption that is correct only through a first-order approximation. Specifically, F has a nuclear-distribution dependence (Eq. 2.13) and K a nuclear-mass (through the atomic mass M) dependence (Eq. 2.14). This means that F and K are, in reality, not fully isotope-independent, and thus Eq. 2.17 is not fully linear. The (Standard Model) non-linearity of the King-plot expression in Eq. 2.17 is a field of active study (see, for example, Ref. [82] and references therein), in support of the experimental studies of King-plot non-linearity as a probe of physics beyond the Standard Model [83, 84, 85, 86].

2.3 Molecular physics

2.3.1 Vibrations and rotations of a diatomic molecule

Compared to their constituent atoms, even diatomic molecules, which have the simplest molecular geometry, possess a significantly richer energy level structure. The reason is that the molecular bonds vibrate and rotate and these extra degrees of freedom lead to additional vibrational and rotational energy on top of the electronic.

The vibrational and rotational spectra of diatomic molecules can be described very accurately through the treatment of the anharmonic vibrating rotor. This semi-classical picture treats molecular vibrations as akin to two masses M_A and M_B attached to the ends of a spring. In the harmonic approximation, the potential energy curve of this picture is parabolic and can be expressed as $V(r) = \frac{1}{2}k(r - r_e)^2$, where k is the characteristic restoration force constant and r is the displacement from the equilibrium position r_e. By solving the time-independent Schrödinger equation (TISE) for this potential, the vibrational energy levels for the harmonic vibrator model are given by:

$$E_v = \omega\hbar\left(v + \frac{1}{2}\right) \tag{2.18}$$

where $\omega = \sqrt{\frac{k}{\mu}}$ is the harmonic vibrational frequency and $v = 0, 1, 2, ...$ is the vibrational quantum number, $\mu = \frac{M_A M_B}{M_A + M_B}$ is the molecule's reduced mass, and M_A and M_B the atomic masses. Notably, as per Eq. 2.18, molecules possess non-zero vibrational energy even in their lowest vibrational state, as $E_0 = \frac{1}{2}\omega \neq 0$.

Eq. 2.18 leads to a vibrational energy level series that is equidistant. That is, each vibrational level has an energy that is greater than the preceding vibrational level by exactly ω. Observed vibrational spectra, however, do not exhibit this feature [87]. Instead, at high vibrational quantum numbers, the vibrational states begin to converge and once a molecule's vibrational energy reaches the convergence limit, the molecule enters the dissociation limit. This observation thus demands a revision of the vibrational potential that is used in the TISE, such that the resulting level series exhibits a loss of harmonicity for high v and a dissociation limit at the continuum.

Thus, the Morse potential is more common:

$$V(r) = D_e \left(1 - e^{-\alpha(r-r_e)}\right)^2 \tag{2.19}$$

where D_e is the equilibrium dissociation energy, $\alpha = \sqrt{\frac{k_e}{2D_e}}$, and r_e is the internuclear distance at the minimum of the Morse potential well. The Morse potential is compared to the harmonic oscillator in Fig. 2.1.

The energy of the vibrational levels for the Morse potential [88] is given by:

$$E_v = \omega_e \left(v + \frac{1}{2}\right) - x_e\omega_e \left(v + \frac{1}{2}\right)^2 + ... \tag{2.20}$$

where $\omega_e = \frac{\alpha}{2\pi c}\sqrt{\frac{2D_e}{\mu}}$ and $x_e = \frac{h\omega_e c}{4D_e}$, and corrections at powers of $\left(v + \frac{1}{2}\right)$ greater than 2 are omitted due to their negligible contribution.

The vibrational progression given by Eq. 2.20 indeed exhibits the features seen in real spectra; the vibrational spacing is approximately constant for low v and decreases as v increases, until the energy reaches a convergence limit that corresponds to the dissociation energy.

In terms of the rotational energy, the measured spectra of diatomic molecules do not exhibit a converging series but instead a gradually

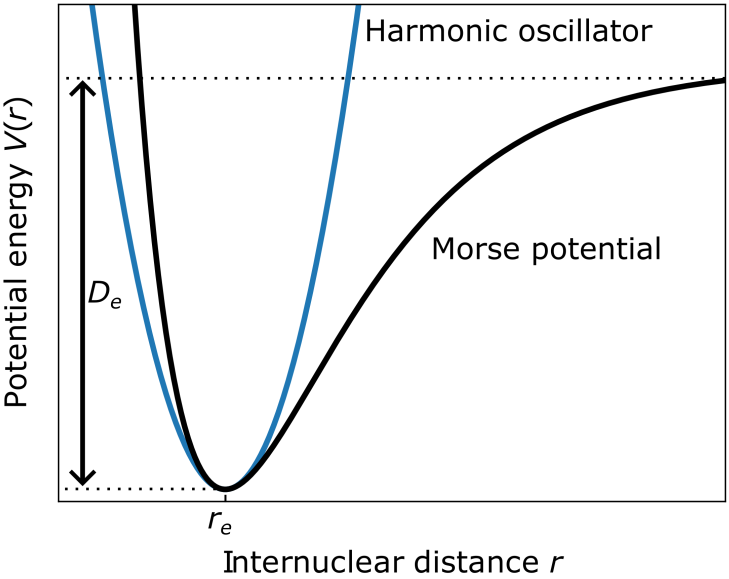

Figure 2.1: Comparison of vibrational potential energy curves for diatomic molecules.

diverging one [87]. Treating the diatomic molecule as two point nuclei separated by the bond distance r_e and with a reduced mass μ, the energy of a rotational level of quantum number J is expressed in the rotor picture [87] as:

$$E_J = BJ(J+1) + DJ^2(J+1)^2 + ... \tag{2.21}$$

where B is called the rotational constant, D is the centrifugal distortion constant (not to be confused with the dissociation energy), and corrections at higher orders of $J(J+1)$ are neglected, even though they can be defined and are relevant in rotational spectroscopy of sufficient resolution [89]. The rotational constant is defined as $B = \frac{h^2}{8\pi^2 I}$, where I is the moment of inertia about an axis perpendicular to the internuclear axis. Invariably, the moment of inertia is expressed for the point-nucleus approximation, as $I = \mu r_e^2$. The anharmonicity constant D is defined as $D = -\frac{h^3}{128\pi^6\mu^3\omega_e^2c^3r_e^6}$ [88].

The molecular rotations are affected by the vibrational mode of the system, as the vibrational mode determines the average molecular bond distance, which in turn determines the rotational constant. Thus, a more accurate definition of the rotational constant needs an explicit dependence on the vibrational quantum number v. Most commonly, the v-dependent rotational constant B_v is defined as:

$$B_v = B_e - \alpha_e \left(v + \frac{1}{2}\right) \tag{2.22}$$

where $\alpha_e = \frac{3h^2\omega_e}{16\pi^2\mu r_e^2 D_e}\left(\frac{1}{\alpha r_e} - \frac{1}{\alpha^2 r_e^2}\right)$ [88] (here, α and D_e are the Morse potential constants from Eq. 2.19) and B_e is called the *equilibrium* rotational constant. A similar v-dependent expression also holds for the anharmonic D constant, but its dependence on v is very weak, so for the resolution that is typically achieved in laser spectroscopy, D can be assumed to be independent of v.

Combining Eqs. 2.20 and 2.21, the energy of a molecule in a rovibrational (that is, rotational plus vibrational) level with quantum numbers v and J is:

$$E_{v,J} = \omega_e\left(v + \frac{1}{2}\right) - x_e\omega_e\left(v + \frac{1}{2}\right)^2 + B_vJ(J+1) + DJ^2(J+1)^2 \tag{2.23}$$

The quantum numbers and molecular constants in Eq. 2.23 hold only within a specific electronic state. Laser spectroscopy, however, probes transitions between rovibrational states belonging to different electronic states. In that case, the *rovibronic* (electronic, vibrational, and rotational) transition energy between a lower state whose quantum numbers and constants are denoted by a double prime ($''$) and an upper state, denoted by a single prime ($'$), is:

$$E_{\mathrm{el,v,J}} = T'_{\mathrm{el}} - T''_{\mathrm{el}} + E'_{v',J'} - E''_{v'',J''} \tag{2.24}$$

where T'_{el} and T''_{el} are the electronic excitation energies of the upper and the lower electronic states, respectively.

2.3.2 Angular-momentum coupling: Hund's cases

Eq. 2.24 captures the vibrational and rotational structure of the electronic states involved in a transition probed by laser spectroscopy. Depending on the spectroscopic resolution, however, higher-order angular-momentum coupling effects have to also be considered, and a choice has to be made in terms of the effective Hamiltonian to be considered in the analysis.

Depending on the structure of the electronic states in question, the angular momenta whose projections are good quantum numbers have to be determined. Afterwards, the effective Hamiltonian can be constructed as a sum of terms arising from the angular momentum interactions, each with a molecular constant that determines the interaction strength. Brown and Carrington [89] provide an excellent introduction into the different types of angular momentum couplings and their relative importance in different electronic states.

Generally, four angular momenta need to be considered in molecular spectroscopy: (a) the rotational angular momentum $\boldsymbol{R}$ of the molecule about a molecular axis defined by the molecule's symmetry, (b) the electronic orbital angular momentum $\boldsymbol{L}$, (c) the electronic spin angular momentum $\boldsymbol{S}$, and (d) the nuclear spin angular momentum $\boldsymbol{I}$. The four angular momenta can interact pair-wise in all combinations, and any of them can be part of the effective Hamiltonian if the projections of the angular momenta that play a role in the interaction are good quantum numbers. In most cases, the interactions have direct and indirect components. Often, the total angular momentum excluding electronic spin $\boldsymbol{N}$ is also used in the formulation of effective Hamiltonians.

To determine which angular momenta should be involved in the effective Hamiltonian, Hund's cases provide a very useful starting point. Hund's cases are idealized situations of electronic states whose structure can be fully described by considering specific interactions as dominating over all others. Hund proposed five distinct cases [90], referred as Hund's case (a)-(e), a description of which can be found in most molecular spectroscopy textbooks, such as Brown and Carrington's [89]. Often, Hund's cases (a) and (b) are most relevant to the observed spectra, as in the case of the RaF and AcF spectra presented in this thesis. Therefore, only these two cases are elaborated upon.

2.3.3 Hund's case (a)

In Hund's case (a) states, the projection Λ of the electronic orbital angular momentum on the internuclear axis is a good quantum number. Through the spin-orbit interaction that couples the electronic spin angular momentum to the orbital one, the projection Σ of the electronic spin on the internuclear axis is also a good quantum number. Therefore, the projection Ω of the total electronic angular momentum (combined orbital and spin) is also a good quantum number.

The electron can orbit about the internuclear axis in two different ways (clockwise and anti-clockwise) with opposite-sign projections, leading to pairs of degenerate states referred to as Λ-doubling. The coupling between the total electronic angular momentum and the rotational angular momentum of the molecule, however, lifts the degeneracy of the Λ-doubling pairs, giving rise to a splitting of the rotational levels to opposite-parity sublevels.

The (partial) Hamliltonian for Hund's case (a) states is expressed as:

$$\begin{aligned}\hat{H} = {} & B\boldsymbol{R}^2 + D\boldsymbol{R}^4 + A\boldsymbol{L}_z\boldsymbol{S}_z + o\frac{1}{2}\left(\boldsymbol{S}_+^2 e^{-2i\phi} + \boldsymbol{S}_-^2 e^{+2i\phi}\right) \\ & - p\frac{1}{2}\left(\boldsymbol{N}_+\boldsymbol{S}_+ e^{-2i\phi} + \boldsymbol{N}_-\boldsymbol{S}_- e^{+2i\phi}\right) + q\frac{1}{2}\left(\boldsymbol{N}_+^2 e^{-2i\phi} + \boldsymbol{N}_-^2 e^{+2i\phi}\right) \qquad (2.25)\end{aligned}$$

where B is the rotational constant, D is the anharmonic rotational constant, A is the spin-orbit constant, o, p, and q are the Λ-doubling constants, ϕ is the azimuthal angle of the orbital precession of the electron about the internuclear axis, and the operators subscripted with $+$ or $-$ denote the ladder operators of the denoted angular momentum. The o constant is relevant to states with two valence electrons or more, p is relevant to states with at least 1 valence electron, while q can arise also in states with no unpaired valence electrons.

The Π and Δ states presented in the following chapters were thus analyzed according to Hund's case (a). Further information on the effective Hamiltonian for Hund's case (a) states, including the hyperfine interaction, can be found in Brown and Carrington [89].

2.3.4 Hund's case (b)

Hund's case (b) states exhibit no or very weak spin-orbit coupling, and thus this case is fitting for Σ states that have no projection of the electronic orbital angular momentum, and therefore no spin-orbit coupling. In this case, Ω cannot be defined.

The electronic spin angular momentum $\boldsymbol{S}$ is instead coupled to $\boldsymbol{N} = \boldsymbol{R}+\boldsymbol{L}$ to form the total angular momentum $\boldsymbol{J}$. Due to the strong coupling between the electronic spin and the molecular rotation, a spin-rotation coupling effect is also present, such that each rotational line is split into a doublet $J_{\pm} = N \pm \frac{1}{2}$.

The (partial) Hamiltonian in this case is:

$$\hat{H} = B\boldsymbol{N}^2 + D\boldsymbol{N}^4 + \gamma \boldsymbol{N} \cdot \boldsymbol{S} \tag{2.26}$$

The Σ states presented in the following chapters were thus analyzed according to Hund's case (b). More information on the effective Hamiltonian and excluded terms can be found in Brown and Carrington [89].

2.3.5 Molecular isotope shifts

As with atomic transitions, the energy of molecular transitions also shows a gradual shift as a result of isotopic change in one or more of the constituent atoms. Contrary to atoms, however, isotope shifts are not limited to electronic transitions in molecules; iso-electronic vibrational and iso-vibronic rotational transitions also show isotope shifts.

A molecular mass shift was the first contribution to the isotope shift that received attention in molecular spectroscopy [91], and its emergence was rationalized as a breakdown of the Born-Oppenheimer approximation. A molecular field shift was also identified soon after, and several molecules have been analyzed and demonstrated a sizeable effect [92, 93, 94, 95, 96, 97, 98, 99, 100]. Molecular field-shift studies, however, have so far received a very small fraction of the research focus that similar studies in atoms have received.

The most common approach to analyzing molecular isotope shifts is through the mass-independent parametrization of the molecular states based on the Dunham expansion. The Dunham expansion [101] expresses the energy of a molecular rovibronic level as a series of factors and expressions of the vibrational v and rotational J quantum numbers [101]:

$$E = \sum_{(k,l)\geq(0,0)} Y_{kl} \left(v + \frac{1}{2}\right)^k [J(J+1)]^l \tag{2.27}$$

Y_{kl} are the Dunham coefficients and are unique to each electronic state; in general, they are also specific to each isotopomer of a molecule, too. Early on, it was noticed that the ratio of the values of a Dunham coefficient in two isotopomers was approximately equal to a power of the inverse ratio of their reduced masses (see Ref. [102] and references therein). The approximate nature of the equality led to expressing the Dunham coefficients as a product of the reduced mass of the isotopomer in question, an isotope-independent factor, and a term that depends separately on the masses and the nuclear radii of the constituent atoms in the isotopomer in question [93]:

$$Y_{kl} = \mu^{-(l+k/2)} \tilde{U}_{kl} \left[1 + m_e \left(\frac{\Delta^A_{kl}}{M_A} + \frac{\Delta^B_{kl}}{M_B}\right) + V^A_{kl}\langle r^2\rangle_A + V^B_{kl}\langle r^2\rangle_B\right] \tag{2.28}$$

In Eq. 2.28, μ is the reduced mass of the isotopomer, $\tilde{U}_{kl}$ is the isotope-independent term of the Dunham coefficient, m_e, M_A, and M_B are the masses of the electron, atom A, and atom B, respectively, and $\langle r^2\rangle_A$ and $\langle r^2\rangle_B$ are the mean-squared nuclear charge radii for atoms A and B, respectively. The remaining terms, specifically $\Delta^A_{kl}/\Delta^B_{kl}$ and V^A_{kl}/V^B_{kl}, are the molecular-structure parameters that quantify the sensitivity of the state energy to the mass and nuclear charge radius of the constituent atoms, respectively. Therefore, Δ_{kl} and V_{kl} in Eq. 2.28 function in a manner similar the atomic mass- and field-shift factors.

Eq. 2.28 is thus often used in conjunction with measurements in multiple isotopomers to determine the parameters Δ_{kl} and V_{kl} in different electronic states of interest. Substituting the mass and nuclear charge radius of the atoms for specific isotopomers can then reproduce the experimentally measured transition energies, or make predictions for the transition energies in isotopomers that have not been experimentally studied. Examples of such analyses for astrophysical searches using molecular spectroscopy can be found in Ref. [44] and references therein.

2.4 Collinear Resonance Ionization Spectroscopy

The Collinear Resonance Ionization Spectroscopy (CRIS) experiment is a permanent laser spectroscopy setup at ISOLDE, CERN's radioactive ion beam (RIB) facility [103, 104]. CRIS was constructed with the purpose of measuring the electromagnetic moments and charge radii of nuclei far from stability [105, 106, 25], and throughout the years has expanded its activities to include works on nuclear decay spectroscopy [107], molecular physics [5, 4, 2], and atomic physics with neutral [108] and anionic species [109].

Laser spectroscopy has been a cornerstone of ground- and isomeric-state nuclear structure studies for several decades [8, 7], where the systematic measurement of the hfs in isotopic chains is used to trace the evolution of the nuclear magnetic dipole and electric quadrupole moments and the nuclear charge radius. Systematic studies of these observables as a function of Z and N provide detailed information on the evolution of shell structure and the changing interplay between collective and single-particle degrees of freedom. Laser spectroscopy for nuclear structure can be generally categorized along two approaches: in-source laser spectroscopy [47] and collinear laser spectroscopy (CLS) [46].

In-source laser spectroscopy utilizes resonance ionization spectroscopy (RIS) that takes place as close to the point of production of the radioactive atoms as possible. In the ISOL (isotope separation on-line) method at accelerator facilities with proton beams above 0.5 GeV, the radioactive atoms are formed by the energetic proton bombardment of a (thick) solid target of non-radioactive material, such as UC_x, LaC_x, CaO, and others. By heating the target material to temperatures close to or above 2000 °C, the radioactive atoms formed within the matrix of the target material diffuse to the surface of the target and then effuse as a neutral vapor, at which point they find their way to a narrow transfer line.

In in-source laser spectroscopy, a series of pulsed lasers illuminate the vapor of radioactive atoms in the transfer line, such that the valence atomic electrons of the element of choice are step-wise excited from their initial state (the atomic ground state or a low-lying metastable state) to above the ionization potential following a series of resonant transitions up to an auto-ionizing state, or with a final non-resonant ionization step. After ionization, the radioactive ions are accelerated to kinetic energies (KE) of a few tens of keV and sent to different experimental stations that can perform sensitive and selective detection of the resonantly produced ions, such as a decay spectroscopy station or a mass measurement setup. The resonantly produced ion rate is measured as a function of the frequency of one of the resonant steps in the RIS scheme, resulting in a nearly background-free hfs spectrum. As a result, the spectroscopic efficiency and selectivity of in-source laser spectroscopy is very high, placing nuclei with production rates far less than 1 per second within reach, and thus several isotopes at the extremes of the nuclear landscape have been measured with this approach, such as ^{96}Ag [110] and ^{177}Hg [48].

Because in-source spectroscopy is performed on a hot atomic vapor, however, the achievable spectroscopic resolution is Doppler-limited to several GHz. This places a strict requirement on the atomic cases that are compatible with the technique, as large field-shift factors and magnetic dipole hfs splittings are required for the successful extraction of nuclear observables within the achievable resolution. In the last decade, the development of a laser ion source and trap (LIST) [111] and in particular its perpendicular-illumination variant (PI-LIST) [112, 113] at ISOLDE, CERN have delivered promising results on high-resolution in-source spectroscopy, but significant improvements in these techniques are still necessary.

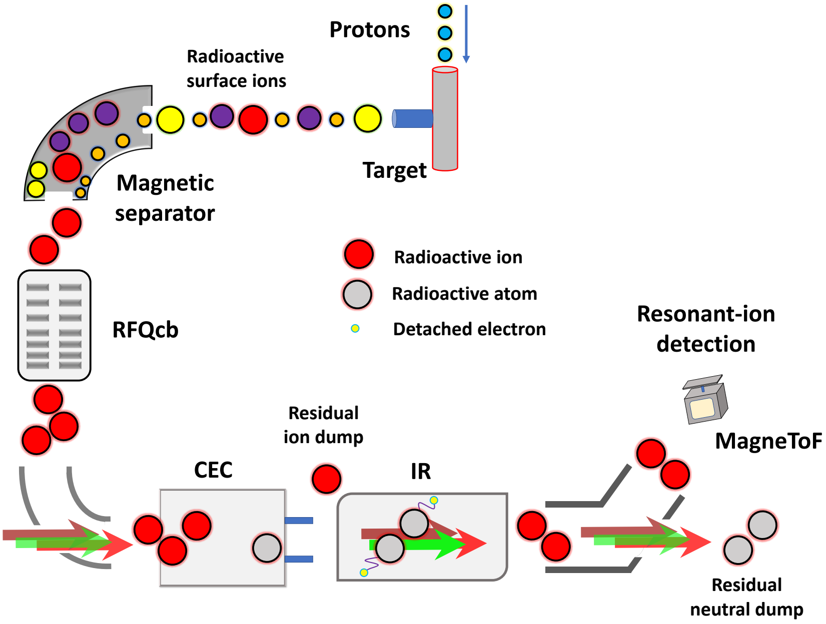

Figure 2.2: Schematic representation of the CRIS technique at CERN-ISOLDE, including cooling and bunching in the RFQcb (radiofrequency quadrupolar cooler-buncher), neutralization in the CEC (charge-exchange cell), and resonance ionization in the IR (interaction region).

On the contrary, in CLS the spectroscopy is performed on fast beams of a few tens of keV by overlapping the laser(s) and the atomic beam in a collinear geometry. The central benefit of CLS is that the spread in KE of the hot beam is significantly compressed when translated to a velocity spread at higher energies. As a result, the Doppler-limited resolution achievable in CLS of fast beams is typically at least two orders of magnitude better than in in-source spectroscopy, typically reaching the natural linewidth of the transition.

Traditionally, CLS experiments utilize laser-induced fluorescence (LIF) for the detection of atomic resonance. Using a single, continuous-wave (CW) laser, CLS experiments tune the excitation wavelength observed by the fast atoms in their rest frame while monitoring the photon count rate with a photomultiplier tube (PMT), detecting the de-excitation photons after successfully driving a resonant transition. This approach benefits from the technical simplicity of having to overlap only one laser beam with the fast atoms while evading temporal mismatches thanks to the use of a CW laser. However, LIF-based CLS faces significant limitations due to the laser-induced photon background on the PMT, and thus the resulting signal-to-noise ratio is orders of magnitude lower than in in-source laser spectroscopy that is based on ion detection.

The CRIS experiment was thus commissioned in 2012 as a merger between the LIF-based CLS and the RIS-based in-source spectroscopy [105]. At CRIS, the fast (30-50 keV) beams of radioactive ions are firstly neutralized in a charge-exchange cell (CEC) filled with hot K ($>$100 °C) or Na ($>$180 °C) vapor. After the CEC, the residual ions are deflected onto a beam dump and only the neutral species continue into the interaction region (IR), where they are spatially and temporally overlapped in a collinear geometry, as in CLS, with a series of pulsed lasers that stepwise excite the valence electrons from their initial state to above the ionization potential, as in in-source spectroscopy. Following RIS, the resonantly ionized species are deflected away from the residual neutral beam onto an ETP MagneToF single-ion detector. A schematic of the CRIS technique is shown in Fig. 2.2. A key component of the CRIS technique is the ISCOOL radiofrequency quadrupolar cooler-buncher (RFQcb) of ISOLDE [114], which accumulates the continuously produced radioactive ions into a high-capacity linear Paul trap filled with helium buffer gas, and releases them in short (width of few microseconds) uniform bunches cooled to room temperature. The bunched structure delivered by ISCOOL ensures no duty cycle loss due to the pulsed structure of the CRIS lasers.

By probing fast beams, CRIS takes advantage of the suppressed Doppler broadening of CLS, achieving the record resolution for CLS of 20 MHz in Fr [106], while by performing RIS and ion detection for spectroscopy, CRIS has also achieved a record sensitivity and selectivity in CLS with the high-resolution spectroscopy of ^{78}Cu that has a production rate of 20 ions per second [49].

Fig. 2.3 shows an example CRIS laser scheme, used for the spectroscopy of neutron-rich K isotopes [1]. The hfs of the K atoms is measured by

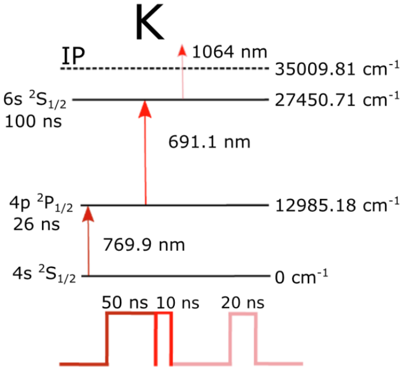

Figure 2.3: Example CRIS laser scheme used for the spectroscopy of K. Appears in Ref. [1], reproduced with permission from the authors.

scanning the wavelength of the first transition (769.9 nm), which is driven by the fundamental output of a pulsed injection-seeded titanium:sapphire (Ti:Sa) laser with a linewidth of ∼17 MHz [115], whose cavity is stabilized to maximize the circulation of the CW seed (Sirah Matisse) at the target output wavelength.

The second step (691.1 nm) also corresponds to a resonant transition, but as its purpose is not to measure the hfs, it is driven by a broadband pulsed laser with a linewidth of at least 3 GHz. If the wavelength allows, pulsed dye lasers are preferable for such steps, as they deliver more pulse energy than Ti:Sa lasers and their grating-based cavities are widely and continuously tunable. Lastly, the fundamental harmonic of a Nd:YAG laser at 1064 nm is used to non-resonantly ionize the resonantly excited atoms.

In 2018, CRIS performed laser spectroscopy of a molecule for the first time, studying the electronic and vibrational structure of $^{223-226,228}$RaF during the IS657 experiment [5]. This experiment produced a momentum for the study of radioactive molecules with laser spectroscopy, which is the topic of the following chapters.

Chapter 3

Extending the King-plot analysis to diatomic molecules

3.1 Motivation

In atomic spectroscopy, the small shift in the energy of an electronic transition between different isotopes of the same atom is well-understood (see Section 2.2). In its most common expression, the isotope shift $\delta\nu^{A,A'}$ in the transition energy between two isotopes A and A' is related to the difference in the mean-squared nuclear charge radii and the (reduced) difference in their mass as

$$\delta\nu^{A,A'} = F\delta\langle r^2\rangle^{A,A'} + K\frac{M_{A'} - M_A}{M^{A'}M^A} \tag{3.1}$$

In Eq. 3.1, isotope A' is used as a reference; that is, we relate the properties of isotope A with respect to those of A'.

As discussed in Chapter 1, the factors F and K are called the isotope-shift factors and they quantify the sensitivity of the electronic transition in question to the nuclear size and nuclear mass, respectively. In atomic spectroscopy, F and K can be calculated with *ab initio* atomic theory [80], or for elements that possess 3 or more stable isotopes, they can be extracted from non-optical measurements of the nuclear radius, such as muonic X-ray spectroscopy or electron scattering experiments [116].

Atomic measurements of $\delta\nu^{A,A'}$ can then be used along with the F and K factors (and the nuclear masses) to extract the relative difference in the nuclear radius, as per Eq. 3.1.

The presence of isotope shifts in electronic transitions is not an exclusive feature of atomic spectroscopy, however. Isotopic effects have been noticed in molecular spectra for a long time, with one of the earliest mentions dating almost a century ago [87]. In the 1980s, the first systematic works on isotope shifts in diatomic molecules were performed on molecules with multiple stable isotopes. The initial studies involved Pb isotopes in the heavy diatomic molecules PbO and PbS, along with developments in the theoretical understanding of the measurements [95, 92, 94, 91, 117]. More recently, the first systematic attempts to calculate the field shift in molecular isotope shifts with *ab initio* quantum chemistry were published [118, 4], especially after the identification of strong isotope shifts in the isotopomers of RaF [4].

However, the existing theoretical framework of molecular isotope shifts [44] lacks a complete derivation from first principles. As a result, while *ab initio* quantum chemistry could calculate the field shift in diatomic molecules of Pb and Ra, albeit with limited accuracy, no *ab initio* calculation of the molecular mass shift has been attempted to date. Therefore, any study based on a multi-isotopomer analysis, such as those relevant in astrophysics [45], requires prior measurements of isotope shifts across many isotopomers of the molecule of interest, and a subsequent fit of the measurements to phenomenological expressions.

Shifts in the energies of electronic states in different isotopomers of diatomic molecules have so far been investigated with the aid of a parametrization known as the Dunham expansion [101]

$$\begin{aligned} E^{\Lambda}_{v,J} = \sum_{(k,l)\geq(0,0)} & \mu^{-(l+k/2)}\left(v+\frac{1}{2}\right)^{k}[J(J+1)]^{l}\,\tilde{U}^{\Lambda}_{kl} \\ & \times\left[1+m_e\left(\frac{\Delta^{\Lambda,A}_{kl}}{M_A}+\frac{\Delta^{\Lambda,B}_{kl}}{M_B}\right)+V^{\Lambda,A}_{kl}\left\langle r^2\right\rangle_A+V^{\Lambda,B}_{kl}\left\langle r^2\right\rangle_B\right] \end{aligned} \tag{3.2}$$

where Λ identifies a specific electronic state, v, and J are the vibrational and rotational quantum numbers respectively of the rovibrational substate in question, and μ is the reduced mass of the molecule, $\tilde{U}_{kl}^{\Lambda}$ is a generic factor that encompasses all non-isotopic dependencies of the energy state, m_e is the mass of the electron, M_A and M_B are the masses of the constituent atoms A and B (including the electrons) of the diatomic molecule, $\langle r^2 \rangle_A$ and $\langle r^2 \rangle_B$ are the mean-squared charge radii of the constituent atomic nuclei, $\Delta_{kl}^{\Lambda,A}$ and $\Delta_{kl}^{\Lambda,B}$ are factors that quantify the change in the electronic energy per unit mass of the constituent atom, and $V_{kl}^{\Lambda,A}$ and $V_{kl}^{\Lambda,B}$ are factors that quantify the change in the electronic energy per unit radius-squared of the constituent atomic nuclei. The indices k, l determine the level of higher-order correction that is desired.

While Eq. 3.2 is widely used in multi-isotopomer studies of diatomic molecules, there are limitations to it. Firstly, it contains several factors that lack a first-principles derivation, and thus molecular isotope shifts cannot be calculated with *ab initio* quantum chemistry. These factors are $\tilde{U}_{kl}^{\Lambda}$, as well as Δ_{kl}^{Λ} and V_{kl}^{Λ}, despite the last two playing the role of the molecular analogs to the atomic mass- and field-shift factors. Secondly, while the Δ_{kl}^{Λ} and V_{kl}^{Λ} factors are present in Eq. 3.2 as part of an expansion of indices k, l, they do not depend on the vibrational and rotational quantum numbers v and J. That is, even though Eq. 3.2 includes v and J in its parametrization of the energies of the rovibrational substates of an electronic state, the way the energies of these rovibrational substates shift as a result of isotopic substitution is common for all. As far as one can tell, this assumption is a simplification without a rigorous first-principles justification.

To improve our intuitive understanding of the molecular isotope shift, it would be preferable that Eq. 3.2 is expressed in a form similar to that of atomic isotope shifts. If such an algebraic manipulation of Eq. 3.2 is possible, then in principle a King plot could be constructed between isotope shifts in atoms and molecules that contains the same nuclei (and thus the same values for the masses and radii).

The King-plot analysis of isotope shifts, as described in Chapter 2, relates the isotope-shift factors of different electronic transitions in atoms and ions of the same element. Combining molecular and atomic isotope shifts in a King-plot analysis would then allow one to relate the molecular isotope-shift factors Δ_{kl}^{Λ} and V_{kl}^{Λ}, which lack an *ab initio* derivation, to the atomic counterparts, which can be fully described by theory. Therefore, more information could be obtained towards answering the questions about the vibrational and rotational dependence and complete analytical form of molecular isotope-shift factors. It must be clarified, however, that *ab initio* calculations of atomic isotope-shift factors often compute these parameters by repeating the calculation of electronic-state energies for different values of the nuclear mass and radius (often including unphysical values) and estimating the sensitivity of each electronic state to the nuclear properties. Therefore, atomic calculations of isotope-shift factors often do not make use of the first-principles relations to the electronic wavefunction.

In the course of the doctoral studies covered in this dissertation, theoretical work was undertaken to explore the possibility of expressing the isotope shifts in diatomic molecules in a form that resembles the atomic expression. By introducing the approximation that the reduced mass is the same for all isotopomers of a molecule, Eq. 3.2 leads to an isotope-shift expression of familiar form.

Using an atomic-like expression for the molecular isotope shift, where *atomic-like* means that the molecular isotope shift is expressed as the sum of a field and a mass shift, isotope shifts in atoms, molecules, and their ions that contain nuclei of the same element can be inter-related using a King-plot analysis.

The consequence of this development is that the molecular isotope-shift factors that lack an *ab initio* derivation can be extracted from measurements in the laboratory and, for elements with less than 3 stable isotopes, knowledge of the atomic isotope-shift factors. This development can lead to progress in nuclear and molecular physics, as well as astrophysics.

The algebraic operations that enable a King-plot analysis of molecular isotope shifts, as well as a demonstration of the validity of the approach with literature measurements in YbF, ZrO, and SnH, led to an article that was published in *Physical Review X*. The original article can be found on the next page.

Nuclear- and molecular-physics implications of the molecular King-plot analysis can be found in the *Discussion* section of the article.

3.2 Article 1: King-plot Analysis of Isotope Shifts in Simple Diatomic Molecules

PHYSICAL REVIEW X **13,** 011015 (2023)

King-Plot Analysis of Isotope Shifts in Simple Diatomic Molecules

Michail Athanasakis-Kaklamanakis[*]
Experimental Physics Department, CERN, CH-1211 Geneva 23, Switzerland
and KU Leuven, Instituut voor Kern- en Stralingsfysica, B-3001 Leuven, Belgium

Shane G. Wilkins
Department of Physics, Massachusetts Institute of Technology, Cambridge, Massachusetts 02139, USA
and Laboratory for Nuclear Science, Massachusetts Institute of Technology,
Cambridge, Massachusetts 02139, USA

Alexander A. Breier
Laboratory for Astrophysics, Institute of Physics, University of Kassel, 34132 Kassel, Germany

Gerda Neyens
KU Leuven, Instituut voor Kern- en Stralingsfysica, B-3001 Leuven, Belgium

(Received 8 April 2022; accepted 19 December 2022; published 9 February 2023)

We demonstrate that the isotope shift in isotopomers of diatomic molecules, where the nucleus of one of its constituent atoms is replaced by another isotope, can be expressed as the sum of a field shift and a mass shift similar to the atomic case. We show that a linear relation holds between atomic and molecular isotopes shifts, thus extending the King-plot analysis to molecular isotope shifts. Optical isotope shifts in YbF and ZrO and infrared isotope shifts in SnH are analyzed with a molecular King-plot approach utilizing Yb^+ and Zr^+ ionic isotope shifts and charge radii of Sn obtained with nonoptical methods. The changes in the mean-squared nuclear charge radii $\delta\langle r^2\rangle$ of $^{170\text{–}174,176}\mathrm{Yb}$ and $^{90\text{–}92,94,96}\mathrm{Zr}$ extracted from the molecular transitions are found to be in excellent agreement with the values from the spectroscopy of Yb^+ and Zr^+, respectively. On the contrary, in the case of the vibrational-rotational transition in SnH, no sensitivity to the nuclear volume can be deduced within the experimental resolution, which makes it unsuitable for the extraction of nuclear charge radii but provides insights into the molecular electronic wave function not accessible via other methods. The new opportunities offered by the molecular King-plot analysis for research in nuclear structure and molecular physics are discussed.

DOI: 10.1103/PhysRevX.13.011015

Subject Areas: Atomic and Molecular Physics,
Nuclear Physics

I. INTRODUCTION

When the same atomic transition is measured with high-enough precision in atoms (or ions) containing two different isotopes of the same element, a small change in the transition frequency is observed called the isotope shift being the sum of the field shift and the mass shift [1]:

$$\delta\nu_{\mathrm{IS}}^{A,A'} = \delta\nu_{\mathrm{FS}}^{A,A'} + \delta\nu_{\mathrm{MS}}^{A,A'}. \tag{1}$$

The field shift (FS) $\delta\nu_{\mathrm{FS}}^{A,A'}$ originates from the change in the electromagnetic field experienced by core-penetrating electrons and is thus linked to the change in the mean-squared nuclear charge radius $\delta\langle r^2\rangle^{A,A'}$, which gives information about the proton distribution in the nucleus. For this reason, isotope shifts have been measured for a large number of elements and isotopes, both stable and radioactive, as they provide key information on the evolution of nuclear charge radii across the nuclear chart [2]. The nuclear charge radius is being actively studied as a quantity through which a number of unique nuclear phenomena can manifest, and whose systematic study can provide direct insights into the strong nuclear interaction and shell structure [3–5].

The mass shift $\delta\nu_{\mathrm{MS}}^{A,A'}$, on the other hand, arises from the difference in mass between the two isotopes and has two contributions: a shift due to the slight change to the center of nuclear mass with respect to the electrons (normal mass shift, NMS) and a shift due to the change in the correlation energy between electrons (specific mass

---

[*] m.athkak@cern.ch

shift, SMS). Overall, the isotope shift can be expressed in terms of the difference in the mean-squared nuclear charge radii of the two isotopes and the relative difference of their atomic masses:

$$\begin{aligned}\delta\nu_{\mathrm{FS}}^{A,A'} &= F\delta\langle r^2\rangle^{A,A'},\\ \delta\nu_{\mathrm{MS}}^{A,A'} &= (K_{\mathrm{NMS}}+K_{\mathrm{SMS}})\frac{M_{A'}-M_A}{M_{A'}M_A},\\ \therefore\ \delta\nu_{\mathrm{IS}}^{A,A'} &= F\delta\langle r^2\rangle^{A,A'}+K\frac{M_{A'}-M_A}{M_{A'}M_A},\end{aligned}\tag{2}$$

where F and K are called the field-shift and mass-shift factors, respectively, and are specific to the electronic transition that is studied. While the NMS factor K_{NMS} can be calculated exactly due to its classical form, the field-shift factor F and the SMS factor K_{SMS} require atomic-structure calculations that include two-body interactions between all electrons [1]. Such calculations can be challenging or impossible with state-of-the-art methods, depending on the atomic structure.

To overcome this problem, the atomic factors for a transition i that cannot be accurately calculated are often derived from the calculated ones in a transition j using a King-plot analysis [1]. It makes use of the linear relationship between the isotope shifts in two transitions in the same element as

$$\begin{aligned}\tilde{M}^{A,A'}\delta\nu_i^{A,A'} &= \tilde{M}^{A,A'}F_i\delta\langle r^2\rangle^{A,A'}+K_i,\\ \tilde{M}^{A,A'}\delta\nu_j^{A,A'} &= \tilde{M}^{A,A'}F_j\delta\langle r^2\rangle^{A,A'}+K_j,\\ \therefore\ \tilde{M}^{A,A'}\delta\nu_i^{A,A'} &= \frac{F_i}{F_j}\tilde{M}^{A,A'}\delta\nu_j^{A,A'}+K_i-\frac{F_i}{F_j}K_j,\end{aligned}\tag{3}$$

where $\tilde{M}^{A,A'}=(M_{A'}M_A/M_{A'}-M_A)$. The relationship between $\tilde{M}^{A,A'}\delta\nu_i^{A,A'}$ and $\tilde{M}^{A,A'}\delta\nu_j^{A,A'}$ in Eq. (3) is linear, and therefore, in a plot of $\tilde{M}^{A,A'}\delta\nu_i^{A,A'}$ against $\tilde{M}^{A,A'}\delta\nu_j^{A,A'}$, the slope and y intercept of the linear fit will relate the isotope-shift factors of the two transitions [1]. Importantly, the King-plot analysis can also be applied to transitions in different charge states of the same atom (for example, see Ref. [6]), allowing further optimization of the experimental conditions, such as favorable chemistry.

Because of the relation between the isotope shift and the difference in mean-squared charge radii of the two isotopes, isotope-shift measurements with high-precision atomic spectroscopy have been a cornerstone of nuclear-structure studies with laser spectroscopy at radioactive ion-beam (RIB) facilities [2,7].

By tracing the evolution of the isotope shift across an isotopic range, the changes in mean-squared nuclear charge radii can be studied with high accuracy. The nuclear charge radius is a nuclear-structure observable of importance, as precision measurements across the nuclear chart continue to challenge the predictive ability of *ab initio* nuclear theory [5,8–10], and by extension our understanding of the observable. Such precision studies in nuclei with extreme proton-to-neutron ratios are a key pathway to obtaining new insights into the strong nuclear interaction.

While in previous decades, models of the nucleon-nucleon interaction used to be derived empirically, progress in nuclear theory has nowadays led to *ab initio* derivations from quantum chromodynamics using chiral effective field theory [11]. In combination with modern methods to solve the many-body Schrödinger equation and growing computational power [12–16], *ab initio* calculations of nuclear observables are now available not only for light nuclei, where rare nuclear phenomena such as nucleon superfluidity [17], nucleon clustering and bubble structures [18–20], many-body currents and continuum effects [21,22], and many-body nuclear forces [21,23,24] have been investigated, but also for nuclei as heavy as ^{208}Pb [25]. However, extending the measurements of nuclear charge radii to more weakly bound isotopes or to new isotopic chains is often challenging due to the atomic structure of the species of interest [2]. For example, the high reactivity and the predominance of extreme-ultraviolet electronic transitions from the ground state have hindered the study of most atomic chains in the oxygen region, while many heavier nuclei form refractory atoms, preventing their production and study at traditional RIB facilities [2].

In several cases, studying the nucleus as part of a diatomic molecule could provide a solution to this problem. In the past, radioactive molecular beams containing a reactive or refractory element have been observed at isotope-separation on-line ISOL facilities, including as a method to extract a particular element more easily from the target and/or to separate it from its isobars more effectively [26,27]. Recently, laser-spectroscopic studies of short-lived radioactive molecules were performed for the first time [28,29], and the potential benefit of studying the spectra of radioactive molecules for a number of scientific areas has also been recognized [30], such as astrophysics, medical-isotope production, fundamental physics, and nuclear structure. To be beneficial for nuclear-structure studies, molecular laser spectroscopy should be capable of providing access to the nuclear moments and changes in mean-squared charge radii with a comparable or higher precision compared to atomic spectroscopy. While the study of the molecular hyperfine structure with laser spectroscopy is well established for molecules containing stable isotopes [31–33], the influence of nuclear-size effects on the molecular isotope shifts has received less attention. Early works on molecular isotope shifts focused on the presence of the mass shift [34,35], with later studies also establishing the presence of a field shift in the isotope shifts in PbS and PbO [36–38]. Recently, the first optical isotope shifts in short-lived isotopomers of a molecule were reported for RaF [29]. However, in all molecular studies so far, measurements of $\delta\langle r^2\rangle^{A,A'}$ from atomic laser spectroscopy have been used as input in the analysis to compare the extracted electronic density around the nuclear volume with computational predictions. To the knowledge of the authors, no study so far has focused on $\delta\langle r^2\rangle^{A,A'}$ as an observable to be extracted from the molecular isotope shifts for cases where a value is not already available from other methods. One of the reasons is that the accuracy of mass-shift calculations in molecules has not been sufficiently benchmarked. Therefore, any experimental progress in the study of nuclear-size effects in molecules would require extensive theoretical work.

In this work, a different approach is proposed: We demonstrate that the King-plot analysis framework for atomic spectroscopy can be extended to diatomic molecules. This is demonstrated here for simple diatomic molecules having a Σ electronic ground state with few valence electrons. However, the presented formalism to express the molecular isotopomer shift as the sum of a field and a mass shift where only one of the two atoms is modified is generally applicable. By then relating the well-studied atomic field- and mass-shift factors with the molecular counterparts, rapid experimental progress in studying size effects in unstable nuclei with molecular laser spectroscopy could be enabled. The validity of the method is tested, as first examples, with literature optical isotope-shift measurements in YbF and ZrO, for Yb and Zr containing multiple stable isotopes. It is shown that the values of $\delta\langle r^2\rangle^{A,A'}$ extracted from the molecular isotope shifts following a King-plot analysis with atomic (ionic) data are consistent with the charge radii extracted from atomic (ionic) spectroscopy. The molecular King-plot approach is also explored for vibrational-rotational transitions in SnH. From the analysis of YbF, ZrO, and SnH, it is observed that the molecular King-plot analysis can also be a sensitive tool to study the electronic wave function in diatomic molecules, providing a versatile tool to obtain molecular-structure insights.

II. THE MOLECULAR ISOTOPE SHIFT

Molecular electronic states possess vibrational and rotational substructure, typically leading to very rich spectra. In simplistic terms, for each electronic state in a diatomic molecule, an associated series of energy levels due to vibrations of the atomic bond is added on top of the electronic energy, with further, smaller energy contributions to each vibrational substate stemming from the rotational energy of the molecule. Further splittings due to the fine and the hyperfine structure are also present. The simplified description of the rovibronic (rotational, vibrational, and electronic) and hyperfine structure is shown pictorially in Fig. 1.

The energy of a diatomic molecular level can be parametrized according to the Dunham expansion [39]:

$$E^{\Lambda}_{\nu,J} = \sum_{(k,l)\geq(0,0)} Y^{\Lambda}_{kl}\left(\nu+\frac{1}{2}\right)^k [J(J+1)]^l, \qquad (4)$$

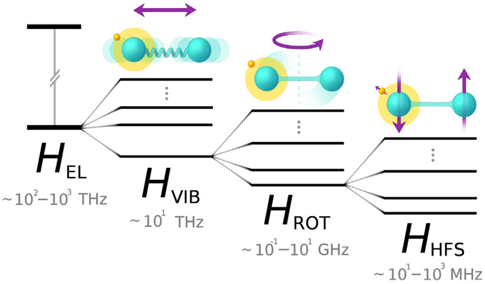

FIG. 1. Vibrational, rotational, and hyperfine structures of an electronic state in a simple diatomic molecule. The substructure splittings are schematic and are not representative of physical scales, but typical frequency scales are given under each term.

where the $\hat{N}^2$ notation is used in the present work; thus, Λ denotes some electronic state, and ν and J are the vibrational and rotational quantum numbers, respectively. Y_{kl} are the Dunham parameters [40], and they are related to the usual molecular parameters, such that Y_{00} corresponds to the electronic term energy T_e, Y_{10} corresponds to the harmonic frequency ω_e, Y_{01} to the rotational constant B_e, etc. The powers k and l quantify the order of vibrational and rotational correction to the energy, respectively.

Almost a century ago, it was noticed that the ratio of the values of a Dunham parameter in two isotopomers X' and X'' of the same molecule is almost equal to the ratio of their reduced masses raised to the power of $l + k/2$. Because of the presence of higher-order corrections, however, the equivalence is not exact [39,41]:

$$\frac{Y^{\Lambda,X'}_{kl}}{Y^{\Lambda,X''}_{kl}} \approx \left(\frac{\mu_{X''}}{\mu_{X'}}\right)^{l+k/2},$$

where $\mu = (M_A M_B / M_A + M_B)$ is the reduced mass of the diatomic molecule with A and B being its constituent atoms.

The ratio can be made exact with the introduction of a parameter U^{Λ}_{kl} that groups the higher-order corrections in the Dunham parameters [42,43] as

$$Y^{\Lambda}_{kl} = \mu^{-(l+k/2)} U^{\Lambda}_{kl}, \qquad (5)$$

and so Eq. (4) can be written as

$$E^{\Lambda}_{\nu,J} = \sum_{(k,l)\geq(0,0)} \mu^{-(l+k/2)} U^{\Lambda}_{kl}\left(\nu+\frac{1}{2}\right)^k [J(J+1)]^l. \qquad (6)$$

Additionally, U^{Λ}_{kl} can be further decomposed into an isotope-independent parameter $\tilde{U}^{\Lambda}_{kl}$, and terms that depend on the masses and the extended nuclear volumes of the atomic constituents [44]

$$U_{kl}^{\Lambda} = \tilde{U}_{kl}^{\Lambda}\left[1 + m_e\left(\frac{\Delta_{kl}^{\Lambda,A}}{M_A} + \frac{\Delta_{kl}^{\Lambda,B}}{M_B}\right) + V_{kl}^{\Lambda,A}\langle r^2\rangle_A + V_{kl}^{\Lambda,B}\langle r^2\rangle_B\right], \tag{7}$$

where m_e is the electron mass, M_A and M_B are the masses of atoms A and B, respectively, and $\langle r^2\rangle$ is the mean-squared nuclear charge radius.

The parameters $\Delta_{kl}^{\Lambda,A}$ and $\Delta_{kl}^{\Lambda,B}$ are specific to each atom A and B in the diatomic molecule but invariant under isotopic substitution, and they quantify the sensitivity of the electronic, vibrational, and rotational (hence, rovibronic) state energy to the corresponding atomic mass, in the form of corrections to the Born-Oppenheimer approximation. Similarly, the isotope-independent parameters $V_{kl}^{\Lambda,A}$ and $V_{kl}^{\Lambda,B}$ quantify the sensitivity of the state energy to the extended volume of the corresponding atomic nucleus, and they are independent of the nuclear mass. Therefore, overall, the energy of a rovibronic state Λ in a diatomic molecule can be expressed with explicit dependence on the atomic masses and the extended nuclear volumes of the constituent atoms as

$$E_{\nu,J}^{\Lambda} = \sum_{(k,l)\geq(0,0)} \mu^{-(l+k/2)}\left(\nu + \frac{1}{2}\right)^k [J(J+1)]^l \tilde{U}_{kl}^{\Lambda} \times \left[1 + m_e\left(\frac{\Delta_{kl}^{\Lambda,A}}{M_A} + \frac{\Delta_{kl}^{\Lambda,B}}{M_B}\right) + V_{kl}^{\Lambda,A}\langle r^2\rangle_A + V_{kl}^{\Lambda,B}\langle r^2\rangle_B\right]. \tag{8}$$

A detailed discussion and definition for the field parameters $V_{kl}^{\Lambda,A/B}$ is given in Ref. [43] (in this text, A/B denotes "A or B" and not a numerical ratio). The field parameters are dependent on the nuclear charge $Z^{\alpha/\beta}$ of atom A/B containing isotope α/β, the fundamental charge e, the vacuum permittivity ϵ_0, the molecular force constant k_e, the electron density $E_{\mathrm{el}}^{\Lambda,A/B}$ at the nucleus of A/B for state Λ, the equilibrium internuclear distance R_e, and the second expansion coefficient of the Dunham potential α_1 [43]. Almoukhalalati *et al.* [43] demonstrated that, while further improvements are required to accurately match the values fitted from experiment, calculations of the field parameters are tractable with *ab initio* theory, and the parameter definitions derived in their work are generally accurate.

On the other hand, the mass-related parameters $\Delta_{kl}^{\Lambda,A/B}$ are defined by Eq. (8) [34] and, although Watson provided theoretical justification for the addition of these parameters [35], several problems with the formulation of Eq. (8) were later identified by Le Roy [45]. Instead, it was proposed [45] that a multi-isotopomer analysis in molecules is used instead, which incorporates isotope referencing in the Dunham expansion as

$$E_{\nu,J}^{\Lambda,X'} = \sum_{(k,l)\neq(0,0)} \left(\frac{\mu_{X''}}{\mu_{X'}}\right)^{l+k/2}\left(\nu + \frac{1}{2}\right)^k [J(J+1)]^l Y_{kl}^{\Lambda,X''} + \sum_{(k,l)\geq(0,0)} \left(\frac{\mu_{X''}}{\mu_{X'}}\right)^{l+k/2}\left(\nu + \frac{1}{2}\right)^k [J(J+1)]^l \times \left(\frac{\Delta M_A^{X'}}{M_A^{X'}}\delta_{kl}^{\Lambda,A} + \frac{\Delta M_B^{X'}}{M_B^{X'}}\delta_{kl}^{\Lambda,B} + \delta\langle r^2\rangle_A^{X'} f_{kl}^{\Lambda,A} + \delta\langle r^2\rangle_B^{X'} f_{kl}^{\Lambda,B}\right), \tag{9}$$

where X is a diatomic molecule containing atoms A and B, X' is some isotopomer with isotopes α' and β' for the two atoms, respectively, X'' is the reference isotopomer with isotopes α'' and β'', $\Delta M_A^{X'} = M_A^{\alpha''} - M_A^{\alpha'}$ is the difference in atomic mass between the reference isotope and the isotope in question for atom A, and $\delta\langle r^2\rangle_A^{X'} = \langle r^2\rangle_{\alpha'} - \langle r^2\rangle_{\alpha''}$ is the change in the mean-squared charge radius of the nucleus in atom A. Identical expressions for $\Delta M_A^{X'}$ and $\delta\langle r^2\rangle_A^{X'}$ also hold for atom B. As seen in Eq. (9), the energy of the rovibronic state Λ in isotopomer X' is expressed as a series of isotopomer-specific corrections to the Dunham parameters of the reference isotopomer X''.

The modified mass parameters $\delta_{kl}^{\Lambda,A/B}$ introduced by Le Roy are related to the mass parameters $\Delta_{kl}^{\Lambda,A/B}$ defined by Ross *et al.* [34] (the relation is described in Ref. [45]) while preventing the complications created by the latter. The modified field parameters $f_{kl}^{\Lambda,A/B}$ are also related to the volume parameters analyzed by Almoukhalalati *et al.* [43] in a similar fashion. As the Le Roy formalism is fully equivalent with that of Eq. (8) [45], the work of Almoukhalalati *et al.* [43], which is based on Eq. (8), is also fully consistent with Eq. (9) and their results are equally relevant to the Le Roy formalism.

Since the Le Roy formalism allows for more straightforward algebra when dealing with isotopomer shifts, the remainder of this work follows the Le Roy formalism for clarity, although the results of this section can also be derived starting from Eq. (8) with equal validity.

Using Eq. (9), the transition energy between a lower state Λ'', ν'', J'' and an upper state Λ', ν', J' (the transition is hence identified as $\Lambda' \leftarrow \Lambda''$) in isotopomer X' can thus be expressed as

$$\begin{aligned}
(E^{\Lambda',X'} - E^{\Lambda'',X'}) = h\nu^{X'}_{\Lambda'\leftarrow\Lambda''} = {} & \sum_{(k,l)\neq(0,0)} \left(\frac{\mu_{X''}}{\mu_{X'}}\right)^{l+k/2} \left(\nu' + \frac{1}{2}\right)^k [J'(J'+1)]^l Y^{\Lambda' X''}_{kl} \\
& + \sum_{(k,l)\geq(0,0)} \left(\frac{\mu_{X''}}{\mu_{X'}}\right)^{l+k/2} \left(\nu' + \frac{1}{2}\right)^k [J'(J'+1)]^l \left(\frac{\Delta M^{X'}_A}{M^{X'}_A}\delta^{\Lambda',A}_{kl} + \frac{\Delta M^{X'}_B}{M^{X'}_B}\delta^{\Lambda',B}_{kl} + \delta\langle r^2\rangle^{X'}_A f^{\Lambda',A}_{kl} + \delta\langle r^2\rangle^{X'}_B f^{\Lambda',B}_{kl}\right) \\
& - \sum_{(k,l)\neq(0,0)} \left(\frac{\mu_{X''}}{\mu_{X'}}\right)^{l+k/2} \left(\nu'' + \frac{1}{2}\right)^k [J''(J''+1)]^l Y^{\Lambda'' X''}_{kl} - \sum_{(k,l)\geq(0,0)} \left(\frac{\mu_{X''}}{\mu_{X'}}\right)^{l+k/2} \left(\nu'' + \frac{1}{2}\right)^k [J''(J''+1)]^l \\
& \times \left(\frac{\Delta M^{X'}_A}{M^{X'}_A}\delta^{\Lambda'',A}_{kl} + \frac{\Delta M^{X'}_B}{M^{X'}_B}\delta^{\Lambda'',B}_{kl} + \delta\langle r^2\rangle^{X'}_A f^{\Lambda'',A}_{kl} + \delta\langle r^2\rangle^{X'}_B f^{\Lambda'',B}_{kl}\right). \qquad (10)
\end{aligned}$$

In a spectroscopic experiment, which measures transition frequencies between molecular states, the highest order of correction in Eq. (10) (that is, the maximum k and l in the summation series) is defined by the spectroscopic precision. Thus, the maximum (k, l) is common to all summations in Eq. (10).

Based on Eq. (10), the isotope shift (of some isotopomer X' with respect to the reference isotopomer X'', as per the definition) in the transition frequency between the two molecular states can be expressed as

$$\begin{aligned}
& (E^{\Lambda',X'} - E^{\Lambda'',X'}) - (E^{\Lambda',X''} - E^{\Lambda'',X''}) \\
& = h\delta\nu^{X'\leftarrow X''}_{\Lambda'\leftarrow\Lambda''} = \sum_{(k,l)\neq(0,0)} \left(\frac{\mu_{X''}}{\mu_{X'}}\right)^{l+k/2} \left(\nu' + \frac{1}{2}\right)^k [J'(J'+1)]^l Y^{\Lambda' X''}_{kl} + \sum_{(k,l)\geq(0,0)} \left(\frac{\mu_{X''}}{\mu_{X'}}\right)^{l+k/2} \left(\nu' + \frac{1}{2}\right)^k [J'(J'+1)]^l \\
& \times \left(\frac{\Delta M^{X'}_A}{M^{X'}_A}\delta^{\Lambda',A}_{kl} + \frac{\Delta M^{X'}_B}{M^{X'}_B}\delta^{\Lambda',B}_{kl} + \delta\langle r^2\rangle^{X'}_A f^{\Lambda',A}_{kl} + \delta\langle r^2\rangle^{X'}_B f^{\Lambda',B}_{kl}\right) - \sum_{(k,l)\neq(0,0)} \left(\frac{\mu_{X''}}{\mu_{X'}}\right)^{l+k/2} \left(\nu'' + \frac{1}{2}\right)^k [J''(J''+1)]^l Y^{\Lambda'' X''}_{kl} \\
& - \sum_{(k,l)\geq(0,0)} \left(\frac{\mu_{X''}}{\mu_{X'}}\right)^{l+k/2} \left(\nu'' + \frac{1}{2}\right)^k [J''(J''+1)]^l \left(\frac{\Delta M^{X'}_A}{M^{X'}_A}\delta^{\Lambda'',A}_{kl} + \frac{\Delta M^{X'}_B}{M^{X'}_B}\delta^{\Lambda'',B}_{kl} + \delta\langle r^2\rangle^{X'}_A f^{\Lambda'',A}_{kl} + \delta\langle r^2\rangle^{X'}_B f^{\Lambda'',B}_{kl}\right) \\
& - \sum_{(k,l)\neq(0,0)} \left(\frac{\mu_{X''}}{\mu_{X''}}\right)^{l+k/2} \left(\nu' + \frac{1}{2}\right)^k [J'(J'+1)]^l Y^{\Lambda' X''}_{kl} - \sum_{(k,l)\geq(0,0)} \left(\frac{\mu_{X''}}{\mu_{X''}}\right)^{l+k/2} \left(\nu' + \frac{1}{2}\right)^k [J'(J'+1)]^l \\
& \times \left(\frac{\Delta M^{X''}_A}{M^{X''}_A}\delta^{\Lambda',A}_{kl} + \frac{\Delta M^{X''}_B}{M^{X''}_B}\delta^{\Lambda',B}_{kl} + \delta\langle r^2\rangle^{X''}_A f^{\Lambda',A}_{kl} + \delta\langle r^2\rangle^{X''}_B f^{\Lambda',B}_{kl}\right) + \sum_{(k,l)\neq(0,0)} \left(\frac{\mu_{X''}}{\mu_{X''}}\right)^{l+k/2} \left(\nu'' + \frac{1}{2}\right)^k [J''(J''+1)]^l Y^{\Lambda'' X''}_{kl} \\
& + \sum_{(k,l)\geq(0,0)} \left(\frac{\mu_{X''}}{\mu_{X''}}\right)^{l+k/2} \left(\nu'' + \frac{1}{2}\right)^k [J''(J''+1)]^l \left(\frac{\Delta M^{X''}_A}{M^{X''}_A}\delta^{\Lambda'',A}_{kl} + \frac{\Delta M^{X''}_B}{M^{X''}_B}\delta^{\Lambda'',B}_{kl} + \delta\langle r^2\rangle^{X''}_A f^{\Lambda'',A}_{kl} + \delta\langle r^2\rangle^{X''}_B f^{\Lambda'',B}_{kl}\right). \qquad (11)
\end{aligned}$$

The energy terms in Eq. (11) that correspond to the reference isotopomer can be simplified due to the definition of the relative terms. It is noticed that $(\mu_{X''}/\mu_{X''})^{l+k/2} = 1$. Additionally, $\Delta M^{X''}_A = 0$ and $\Delta M^{X''}_B = 0$ by definition, and so the modified mass terms vanish from Eq. (11). Similarly, the changes in the mean-squared charge radii $\delta\langle r^2\rangle^{X''}_A$ and $\delta\langle r^2\rangle^{X''}_A$ for the reference isotopomer are by definition 0. Therefore, Eq. (11) becomes

$$\begin{aligned}
h\delta\nu^{X'\leftarrow X''}_{\Lambda'\leftarrow\Lambda''} = {} & \sum_{(k,l)\neq(0,0)} \left(\frac{\mu_{X''}}{\mu_{X'}}\right)^{l+k/2} \left(\nu' + \frac{1}{2}\right)^k [J'(J'+1)]^l Y^{\Lambda' X''}_{kl} + \sum_{(k,l)\geq(0,0)} \left(\frac{\mu_{X''}}{\mu_{X'}}\right)^{l+k/2} \left(\nu' + \frac{1}{2}\right)^k [J'(J'+1)]^l \\
& \times \left(\frac{\Delta M^{X'}_A}{M^{X'}_A}\delta^{\Lambda',A}_{kl} + \frac{\Delta M^{X'}_B}{M^{X'}_B}\delta^{\Lambda',B}_{kl} + \delta\langle r^2\rangle^{X'}_A f^{\Lambda',A}_{kl} + \delta\langle r^2\rangle^{X'}_B f^{\Lambda',B}_{kl}\right) - \sum_{(k,l)\neq(0,0)} \left(\frac{\mu_{X''}}{\mu_{X'}}\right)^{l+k/2} \left(\nu'' + \frac{1}{2}\right)^k [J''(J''+1)]^l Y^{\Lambda'' X''}_{kl} \\
& - \sum_{(k,l)\geq(0,0)} \left(\frac{\mu_{X''}}{\mu_{X'}}\right)^{l+k/2} \left(\nu'' + \frac{1}{2}\right)^k [J''(J''+1)]^l \left(\frac{\Delta M^{X'}_A}{M^{X'}_A}\delta^{\Lambda'',A}_{kl} + \frac{\Delta M^{X'}_B}{M^{X'}_B}\delta^{\Lambda'',B}_{kl} + \delta\langle r^2\rangle^{X'}_A f^{\Lambda'',A}_{kl} + \delta\langle r^2\rangle^{X'}_B f^{\Lambda'',B}_{kl}\right) \\
& - \sum_{(k,l)\neq(0,0)} \left(\nu' + \frac{1}{2}\right)^k [J'(J'+1)]^l Y^{\Lambda' X''}_{kl} + \sum_{(k,l)\neq(0,0)} \left(\nu'' + \frac{1}{2}\right)^k [J''(J''+1)]^l Y^{\Lambda'' X''}_{kl}. \qquad (12)
\end{aligned}$$

At this stage, the approximation that the reduced masses of the two isotopomers are equal needs to be introduced: $\mu_{X'} = \mu_{X''}$. As a result of this approximation, it follows that $(\mu_{X''}/\mu_{X'})^{l+k/2} = 1$ and Eq. (12) becomes

$$\begin{aligned} h\delta\nu^{X'\leftarrow X''}_{\Lambda'\leftarrow\Lambda''} = {} & \sum_{(k,l)\neq(0,0)} \left(\nu' + \frac{1}{2}\right)^k [J'(J'+1)]^l Y^{\Lambda' X''}_{kl} + \sum_{(k,l)\geq(0,0)} \left(\nu' + \frac{1}{2}\right)^k [J'(J'+1)]^l \\ & \times \left(\frac{\Delta M_A^{X'}}{M_A^{X'}} \delta_{kl}^{\Lambda',A} + \frac{\Delta M_B^{X'}}{M_B^{X'}} \delta_{kl}^{\Lambda',B} + \delta\langle r^2\rangle_A^{X'} f_{kl}^{\Lambda',A} + \delta\langle r^2\rangle_B^{X'} f_{kl}^{\Lambda',B}\right) \\ & - \sum_{(k,l)\neq(0,0)} \left(\nu'' + \frac{1}{2}\right)^k [J''(J''+1)]^l Y^{\Lambda'' X''}_{kl} - \sum_{(k,l)\geq(0,0)} \left(\nu'' + \frac{1}{2}\right)^k [J''(J''+1)]^l \\ & \times \left(\frac{\Delta M_A^{X'}}{M_A^{X'}} \delta_{kl}^{\Lambda'',A} + \frac{\Delta M_B^{X'}}{M_B^{X'}} \delta_{kl}^{\Lambda'',B} + \delta\langle r^2\rangle_A^{X'} f_{kl}^{\Lambda'',A} + \delta\langle r^2\rangle_B^{X'} f_{kl}^{\Lambda'',B}\right) \\ & - \sum_{(k,l)\neq(0,0)} \left(\nu' + \frac{1}{2}\right)^k [J'(J'+1)]^l Y^{\Lambda' X''}_{kl} + \sum_{(k,l)\neq(0,0)} \left(\nu'' + \frac{1}{2}\right)^k [J''(J''+1)]^l Y^{\Lambda'' X''}_{kl}, \end{aligned} \tag{13}$$

and therefore, in Eq. (13), the terms containing the Dunham parameters of the reference isotopomer $Y_{kl}^{\Lambda X''}$ cancel out, leading to

$$\begin{aligned} h\delta\nu^{X'\leftarrow X''}_{\Lambda'\leftarrow\Lambda''} = {} & \sum_{(k,l)\geq(0,0)} \left(\nu' + \frac{1}{2}\right)^k [J'(J'+1)]^l \left(\frac{\Delta M_A^{X'}}{M_A^{X'}} \delta_{kl}^{\Lambda',A} + \frac{\Delta M_B^{X'}}{M_B^{X'}} \delta_{kl}^{\Lambda',B} + \delta\langle r^2\rangle_A^{X'} f_{kl}^{\Lambda',A} + \delta\langle r^2\rangle_B^{X'} f_{kl}^{\Lambda',B}\right) \\ & - \sum_{(k,l)\geq(0,0)} \left(\nu'' + \frac{1}{2}\right)^k [J''(J''+1)]^l \left(\frac{\Delta M_A^{X'}}{M_A^{X'}} \delta_{kl}^{\Lambda'',A} + \frac{\Delta M_B^{X'}}{M_B^{X'}} \delta_{kl}^{\Lambda'',B} + \delta\langle r^2\rangle_A^{X'} f_{kl}^{\Lambda'',A} + \delta\langle r^2\rangle_B^{X'} f_{kl}^{\Lambda'',B}\right). \end{aligned} \tag{14}$$

Without loss of generality, it can be considered that only one atom in the diatomic molecule undergoes isotopic substitution, while the other atom is kept at its reference isotope (a reference isotopomer that differs in just one of the two atoms can always be chosen). Therefore, considering atom A as undergoing isotopic substitution, then $\Delta M_B^{X'} = 0$ and similarly $\delta\langle r^2\rangle_B^{X'} = 0$. Therefore, the isotope shift in a diatomic molecule where only one atom undergoes isotopic substitution, can be expressed as

$$\begin{aligned} h\delta\nu^{X'\leftarrow X''}_{\Lambda'\leftarrow\Lambda''} = {} & \sum_{(k,l)\geq(0,0)} \left(\nu' + \frac{1}{2}\right)^k [J'(J'+1)]^l \left(\frac{M_A^{\alpha''} - M_A^{\alpha'}}{M_A^{\alpha'}} \delta_{kl}^{\Lambda',A} + \delta\langle r^2\rangle_A^{X'} f_{kl}^{\Lambda',A}\right) \\ & - \sum_{(k,l)\geq(0,0)} \left(\nu'' + \frac{1}{2}\right)^k [J''(J''+1)]^l \left(\frac{M_A^{\alpha''} - M_A^{\alpha'}}{M_A^{\alpha'}} \delta_{kl}^{\Lambda'',A} + \delta\langle r^2\rangle_A^{X'} f_{kl}^{\Lambda'',A}\right). \end{aligned} \tag{15}$$

With a simple rearrangement, the isotope shift for a molecular transition $\Lambda' \leftarrow \Lambda''$ between isotopomers X' and X'' where atom A contains isotopes α' and α'', respectively, can be finally expressed in a linear form with respect to the change in mean-squared nuclear charge radius:

$$\delta\nu^{X'\leftarrow X''}_{\Lambda'\leftarrow\Lambda''} = \Psi\delta\langle r^2\rangle_A^{\alpha',\alpha''} + \Xi\frac{M_A^{\alpha''} - M_A^{\alpha'}}{M_A^{\alpha''} M_A^{\alpha'}}, \tag{16}$$

where

$$\Psi = \frac{1}{h} \sum_{(k,l)\geq(0,0)} \left\{\left(\nu' + \frac{1}{2}\right)^k [J'(J'+1)]^l f_{kl}^{\Lambda',A} - \left(\nu'' + \frac{1}{2}\right)^k [J''(J''+1)]^l f_{kl}^{\Lambda'',A}\right\}$$

and

$$\Xi = \frac{M_A^{\alpha''}}{h} \sum_{(k,l)\geq(0,0)} \left\{\left(\nu' + \frac{1}{2}\right)^k [J'(J'+1)]^l \delta_{kl}^{\Lambda',A} - \left(\nu'' + \frac{1}{2}\right)^k [J''(J''+1)]^l \delta_{kl}^{\Lambda'',A}\right\}$$

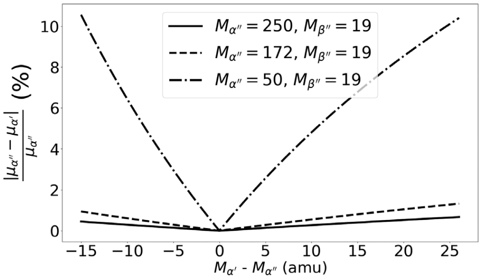

FIG. 2. Percentage residual error for the approximation of constant reduced mass for molecules with different atomic-mass combinations in the medium-mass and heavy regions.

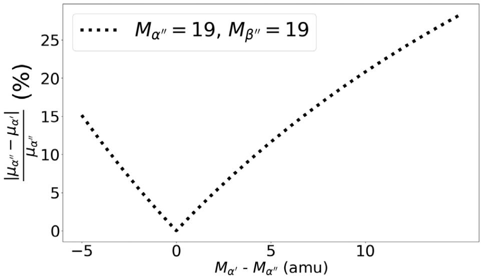

FIG. 3. Percentage residual error for the approximation of the constant reduced mass for a representative light molecule.

are isotope-independent constants. For the linearized isotope-shift equation in diatomic molecules [Eq. (16)], Ψ is the field-shift factor and Ξ is the mass-shift factor analogous to the atomic counterparts. The definition of Ξ contains the atomic mass of the reference isotope of atom A; the term is added such that Eq. (16) is expressed in terms of $M_A^{\alpha''} - M_A^{\alpha'}/M_A^{\alpha''}M_A^{\alpha'}$, as in the atomic case [Eq. (2)]. Therefore, when a change of reference isotopomer is performed, the mass-shift factor should be scaled accordingly for the new reference mass.

Combining Eqs. (2) and (16), a King-plot analysis using atomic and molecular isotope shifts can be performed in the same manner as the analysis containing only atomic transitions, ultimately arriving at an expression identical to Eq. (3) that relates the atomic and molecular isotope-shift factors.

The approximation $\mu_{X'} = \mu_{X''}$ that is used to arrive at Eq. (16) introduces an error to the extracted Ψ and Ξ proportional to $\mu_{X'} - \mu_{X''}$, that is, the deviation of $\mu_{X''}/\mu_{X'}$ from unity. In Figs. 2 and 3, the percentage residual error of the approximation is shown for different atomic masses in diatomic molecules. For medium-mass and heavy diatomic molecules, the residual error remains below 10% even up to 20 amu from the reference isotope, which is lower or comparable to the typical error in atomic isotope-shift factors [46,47].

For light molecules, the error quickly rises above 10%. While such a level can be comparable to the uncertainty in calculated atomic isotope-shift factors for complex atoms (especially for the specific mass shift) [46], it is recommended that the analysis of light molecules with the King-plot method is segmented. That is, the isotopic chain should be separated in smaller regions of only few amu each, and a separate King-plot analysis is performed in each, yielding a set of Ψ and Ξ for each segment of the isotopic chain.

III. ANALYSIS OF MOLECULAR ISOTOPE SHIFTS

A. Optical isotope shifts in YbF

To demonstrate the validity of Eq. (16), the high-resolution laser-spectroscopic data of the optical isotope shifts in $^{170–174,176}$YbF in the literature [48] are analyzed with the molecular King-plot method along with the high-resolution atomic measurements in Yb$^+$ in the literature [49]. YbF possesses a simple electronic structure, with a single unpaired electron outside a closed shell, similar to the structure of group II monofluorides [50], while the Yb

TABLE I. Parameter values (in cm^{-1}) and isotope shifts (in GHz) for the 369.4-nm transition in Yb$^+$ [49], and the T_0 fitted parameter [51], the $^OP_{12}(3)(2 \rightarrow 2)_{A,0\leftarrow X,0}$, and the $^OP_{12}(9)(8 \rightarrow 9)_{A,0\leftarrow X,0}$ branch features in YbF [48].

A	T_0	$^OP_{12}(3)$	$^OP_{12}(9)$	$\delta\nu^{A,172}_{\mathrm{Yb}^+,369.4}$ [a]	$\delta\nu^{A,172}_{T_0}$	$\delta\nu^{A,172}_{^OP_{12}(3)}$	$\delta\nu^{A,172}_{^OP_{12}(9)}$
170	18 788.6634(39)	18 103.9508(15)	18 098.7484(15)	+1.6223(8)	+1.058(121)	+1.019(77)	+0.878(77)
171	18 788.6502(4)			+1.0343(8)	+0.663(32)		
172	18 788.6281(10)	18 103.9168(21)	18 098.7191(21)	0(0)	0(0)	0(0)	0(0)
173	18 788.6145(7)			−0.5699(7)	−0.408(37)		
174	18 788.5985(11)	18 103.8891(23)	18 098.6982(23)	−1.2753(7)	−0.887(45)	−0.830(93)	−0.627(93)
176	18 788.5702(10)	18 103.8626(22)	18 098.6779(22)	−2.4928(10)	−1.736(42)	−1.625(91)	−1.235(91)

[a] There is a sign change in the isotope shifts in Yb$^+$ with respect to Ref. [49] due to a difference in the subtraction convention.

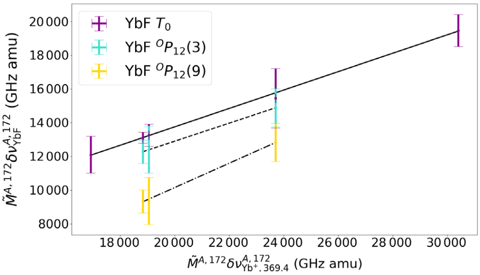

FIG. 4. King plots for the isotope shifts in the $A^2\Pi_{1/2}$ T_0 values and the ${}^{O}P_{12}(3)$ $(F' = 2, F'' = 2)_{A,0\leftarrow X,0}$ and ${}^{O}P_{12}(9)$ $(F' = 8, F'' = 9)_{A,0\leftarrow X,0}$ branch features in YbF, and the 369.4-nm transition in Yb$^+$. All error bars arise from the 1σ uncertainties of the isotope shifts and the uncertainties of the mass measurements taken from the 2020 Atomic Mass Evaluation [52].

element possesses multiple stable isotopes. Therefore, YbF is a suitable first test case to explore the validity of Eq. (16) in a diatomic molecule.

The YbF data are taken from Ref. [48] and Table 1 of its Supplemental Material. King-plot analyses are performed using the fitted values of T_0 for the $A^2\Pi_{1/2}$ $(\nu = 0)$ state in ${}^{170\text{–}174,176}$YbF [51], as well as the branch feature ${}^{O}P_{12}(3)$ $(F' = 2,\ F'' = 2)$ and the branch feature ${}^{O}P_{12}(9)$ $(F' = 8,\ F'' = 9)$ in the $A^2\Pi_{1/2}$ $(\nu = 0) \leftarrow X^2\Sigma^+$ $(\nu = 0)$ transition in ^{170,172,174,176}YbF (Table I).

Using the mass values listed in the 2020 Atomic Mass Evaluation [52], three King plots are constructed for the YbF and Yb$^+$ transitions (Fig. 4). Evidently, the best-fit lines obtained using an orthogonal-distance-regression (ODR) routine, pass through the error bars for all data points, demonstrating the linearity of the isotope-shift expression both in the molecule and in the ion.

As per Eq. (3), using which the field and mass shift of the molecule [Eq. (16)] are related to those of the ionic system, the slope m of the best-fit line $y = mx + b$ in the King plot is equal to F_i/F_j and the y intercept to $b = K_i - (F_i/F_j)K_j$. The slopes and intercepts of the best-fit lines in Fig. 4 are

$$\begin{aligned} m_{T_0} &= +0.546(9), \\ b_{T_0} &= +2830(180), \\ m_{P_{12}(3)} &= +0.535(2), \\ b_{P_{12}(3)} &= +2200(50), \end{aligned}$$

and

$$\begin{aligned} m_{P_{12}(9)} &= +0.722(22), \\ b_{P_{12}(9)} &= -4300(400), \end{aligned}$$

including the 1σ errors from the ODR fit.

TABLE II. Field- (Ψ, in GHz fm^{-2}) and mass-shift (Ξ, in GHz amu) factors for the isotope shifts in the fitted $A^2\Pi_{1/2}$ $(\nu = 0)$ T_0 parameter and the $A^2\Pi_{1/2}$ $(\nu = 0) \leftarrow X^2\Sigma^+$ $(\nu = 0)$ ${}^{O}P_{12}(3)$ $(F' = 2,\ F'' = 2)$ and $A^2\Pi_{1/2}$ $(\nu = 0) \leftarrow X^2\Sigma^+$ $(\nu = 0)$ ${}^{O}P_{12}(9)$ $(F' = 8,\ F'' = 9)$ branch features in YbF, from the King-plot analyses with the isotope shifts in the 369.4-nm transition in Yb$^+$.

	T_0^{YbF}	${}^{O}P_{12}(3)^{\mathrm{YbF}}$	${}^{O}P_{12}(9)^{\mathrm{YbF}}$
Ψ	−7.75(17)	−7.59(11)	−10.24(34)
Ξ	+2350(310)	+1720(240)	−4900(600)

The field- and mass-shift parameters for the 369.4-nm transition in Yb$^+$ are known from Ref. [49] (with adjusted sign for the reference convention):

$$\begin{aligned} F_{369.4} &= -14.185(190)\ \mathrm{GHz\,fm^{-2}}, \\ K_{369.4} &= -890(445)\ \mathrm{GHz\,amu}. \end{aligned}$$

The deduced molecular Ψ and Ξ are given in Table II.

Using the factors in Table II, the changes in the mean-squared nuclear charge radii of the Yb isotopes can be extracted from the isotope shifts in YbF using Eq. (16). The results, along with the values of $\delta\langle r^2\rangle^{A,172}$ extracted from the isotope shifts in the 369.4-nm transition in Yb$^+$ using $F_{369.4}$ and $K_{369.4}$ listed above are presented in Table III and Fig. 5 [53].

For all three sets of isotope shifts, the changes in mean-squared charge radii extracted from the molecule are consistent with the results from atomic spectroscopy within 1σ of the molecular value. The residual errors are shown in Fig. 6.

B. Optical isotope shifts in ZrO

To further explore the applicability of Eq. (16), a King-plot analysis is also performed on the optical isotopes shifts in the $P(1)$, $R(1)$, $P(20)$, and $R(20)$ rotational lines of the $C^1\Sigma^+ - X^1\Sigma^+$ transition in ZrO from the literature [56] and the 327-nm transition in Zr$^+$ [57]. The molecular and

TABLE III. Changes in the mean-squared nuclear charge radii of Yb isotopes (in fm^2) extracted from the isotope shifts in the 369.4-nm transition in Yb$^+$ [49] and from the isotope shifts in YbF analyzed with the King-plot method.

A	$\delta\langle r^2\rangle^{A,172}_{369.4}$	$\delta\langle r^2\rangle^{A,172}_{P_{12}(3)}$	$\delta\langle r^2\rangle^{A,172}_{P_{12}(9)}$	$\delta\langle r^2\rangle^{A,172}_{T_0}$
170	−0.119(3)	−0.119(11)	−0.119(9)	−0.116(16)
171	−0.075(1)			−0.075(5)
172	0(0)	0(0)	0(0)	0(0)
173	+0.042(1)			+0.043(5)
174	+0.094(2)	+0.094(13)	+0.093(10)	+0.094(7)
176	+0.184(5)	+0.184(13)	+0.184(13)	+0.184(9)

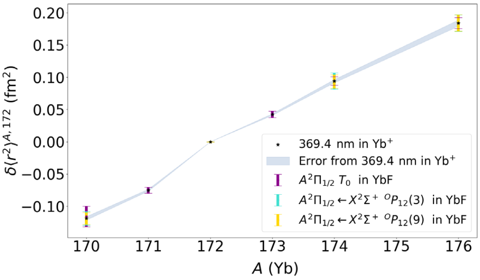

FIG. 5. Changes in the mean-squared nuclear charge radii of $^{170\text{–}174,176}$Yb extracted from isotope shifts in YbF [48] using the King-plot method [Eq. (16)] compared with those extracted from isotope-shift measurements in the 369.4-nm transition in Yb$^+$ [49]. The uncertainties (also given in Table III) stem from the experimental uncertainties in the isotope shifts and the molecular isotope shift factors extracted from the King plot (Table II) using Eq. (2). The reference errors (gray band) are taken from Ref. [49].

atomic (ionic) isotope shifts for $^{90\text{–}92,94,96}$Zr are shown in Table IV. Simard *et al.* [56] did not report uncertainties for the observed wave numbers appearing in Ref. [56]. For the purpose of this demonstrative analysis, an uncertainty of 50 MHz is associated with each isotope-shift value, since the present analysis aims to explore the applicability of the molecular King-plot method, rather than the rigorous extraction of charge radii.

The four King plots and a schematic comparison of $\delta\langle r^2\rangle^{A,90}_{\mathrm{Zr}}$ are shown in Figs. 7 and 8, respectively. The isotope-shift factors Ψ and Ξ for the molecular transitions extracted from the King-plot analysis are shown in Table V. As evident from Fig. 8 and Table VI, the changes in mean-squared charge radii for $^{90\text{–}92,94,96}$Zr extracted from the four molecular transitions are consistent with the values extracted from the spectroscopy of Zr$^+$, falling within 1σ of the values extracted from atomic spectroscopy.

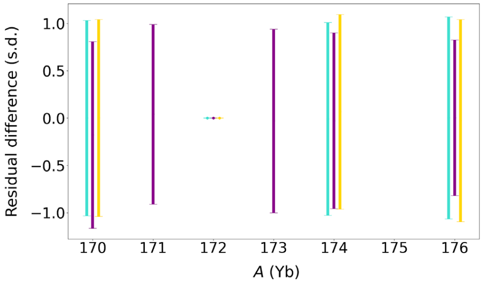

FIG. 6. Residual difference of $\delta\langle r^2\rangle^{A,172}_{\mathrm{Yb}}$ extracted from the molecular isotope shifts compared with the values extracted from high-resolution atomic spectroscopy [49], in units of the error in the molecular values. Magenta, T_0; cyan, $^OP_{12}(3)$; gold, $^OP_{12}(9)$. An arbitrary horizontal offset between the different sets of molecular isotope shifts is applied for visual clarity. The error bars represent the uncertainties in the radii (Table III) extracted using the molecular isotope shifts divided by the uncertainties in the radii using the atomic isotope shifts.

TABLE IV. Isotope shifts $\delta\nu^{A,90}$ (in GHz) for the 327-nm transition in Zr$^+$ [57] and the $P(1)$, $R(1)$, $P(20)$, and $R(20)$ rotational lines of the $C^1\Sigma^+ - X^1\Sigma^+$ transition in ZrO [56] for $^{90\text{–}92,94,96}$Zr.

A	327 nm	$P(1)$	$R(1)$	$P(20)$	$R(20)$
90	0(0)	0(0)	0(0)	0(0)	0(0)
91	−0.192(3)	1.091(50)	0.971(50)	2.221(50)	0.591(50)
92	−0.494(3)	1.982(50)	1.760(50)	4.260(50)	0.941(50)
94	−0.823(3)	4.077(50)	3.640(50)	8.496(50)	2.081(50)
96	−1.033(3)	6.248(50)	5.609(50)	12.756(50)	3.493(50)

C. Infrared isotope shifts in SnH

Simon *et al.* measured the low-lying rovibrational spectra (vibrational-rotational transitions within the $X^2\Pi_{1/2}$ electronic ground state) of the stable isotopomers of SnH using infrared laser spectroscopy [58]. Figure 9 shows a plot of the mass-modified isotope shifts in the $P(2.5)_{1\leftarrow 0}$ rovibrational transition against the mass-modified changes in mean-squared nuclear charge radii of Sn from the analysis of the Barrett radii and the ratios of the radial moments obtained from nonoptical experiments [59]. This approach is fully equivalent to the King-plot analysis utilizing atomic isotope shifts, since the atomic isotope shifts are linearly related to the changes in mean-squared nuclear charge radii. Plotting the mass-modified molecular isotope shifts against the mass-modified changes in radii allows us to also test the validity of Eq. (16) using the values of $\delta\langle r^2\rangle^{A,A'}$ taken from direct measurements of $\langle r^2\rangle$ from nonoptical methods. The

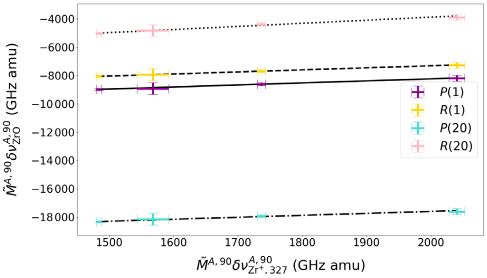

FIG. 7. King plots for the $P(1)$, $R(1)$, $P(20)$, and $R(20)$ lines of the $C^1\Sigma^+ - X^1\Sigma^+$ transition in ZrO [56] and the 327-nm transition in Zr$^+$ [57]. All error bars arise from the 1σ uncertainties of the isotope shifts (Table IV) and the uncertainties of the mass measurements taken from the 2020 Atomic Mass Evaluation [52].

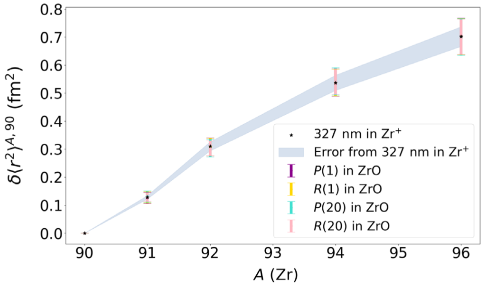

FIG. 8. Comparison of the changes in the mean-squared nuclear charge radii $\delta\langle r^2\rangle^{A,90}_{\mathrm{Zr}}$ of the stable Zr isotopes extracted using the 327-nm transition in Zr$^+$ and from four rotational lines in ZrO. The uncertainties (also given in Table VI) stem from the experimental uncertainties in the isotope shifts (Table IV) and the molecular isotope shift factors extracted from the King plot (Table V) using Eq. (2). The reference errors (gray band) correspond to the uncertainty in the radii extracted from the 327-nm transition in Zr$^+$.

tin chain provides a good test case for this alternative approach to the King-plot analysis, as it contains the highest number of stable isotopes across the periodic table, with a mass difference of more than 10 amu between the heaviest and lightest stable isotopes.

The transition frequencies along with the isotope shifts and the extracted changes in the mean-squared charge radii are listed in Table VII. A precision in the order of 38 MHz was reported in Ref. [58], without giving an exact value. Therefore, a conservative uncertainty of 50 MHz is used for the molecular frequency measurements in the present analysis, leading to a slightly greater uncertainty in the isotope-shift values.

TABLE V. Molecular isotope-shift factors Ψ (in GHz fm^{-2}) and Ξ (in GHz amu) for the four rotational transitions in ZrO analyzed with the King-plot method against the 327-nm isotope shifts in Zr$^+$.

	Ψ	Ξ
$P(1)$	−3.0(7)	−12 000(800)
$R(1)$	−3.0(7)	−11 000(800)
$P(20)$	−2.9(7)	−21 200(800)
$R(20)$	−4.6(8)	−9600(800)

TABLE VI. Changes in the mean-squared nuclear charge radii of $^{90\text{–}92,94,96}$Zr extracted with laser spectroscopy using the 327-nm transition in Zr$^+$ [57] and four rotational lines in ZrO [56].

A	$\delta\langle r^2\rangle^{A,90}_{327}$	$\delta\langle r^2\rangle^{A,90}_{P(1)}$	$\delta\langle r^2\rangle^{A,90}_{R(1)}$	$\delta\langle r^2\rangle^{A,90}_{P(20)}$	$\delta\langle r^2\rangle^{A,90}_{R(20)}$
90	0(0)	0(0)	0(0)	0(0)	0(0)
91	0.128(6)	0.126(20)	0.129(20)	0.131(21)	0.129(15)
92	0.310(16)	0.308(32)	0.308(31)	0.304(31)	0.304(27)
94	0.537(27)	0.537(48)	0.538(48)	0.541(49)	0.542(46)
96	0.702(35)	0.703(65)	0.703(65)	0.701(65)	0.701(62)

If Eq. (16) holds for the rovibrational transition under consideration, a linear fit can be applied to the plot in Fig. 9 whose slope corresponds to the field-shift factor Ψ and the y intercept to the mass-shift factor Ξ:

$$\Psi_{P(2.5)} = +0.4(1.6),$$
$$\Xi_{P(2.5)} = +23470(1410).$$

TABLE VII. Transition frequencies (in cm^{-1}) for the $P(2.5)_{1\leftarrow 0}$ rovibrational transition in the $X^2\Pi_{1/2}$ electronic ground state of SnH, and the corresponding isotope shifts (in GHz) with respect to ^{122}SnH. The model-independent Barrett radii ($R^{\mu}_{k\alpha}$, in fm) and the ratios of the second radial moment (V_2) from Ref. [59] used to calculate the literature values of the changes in mean-squared charge radii of Sn ($\delta\langle r^2\rangle^{A,122}$ in fm^2) are given for completeness. The extracted changes in mean-squared charge radii of Sn from the isotope shifts in the $X^2\Pi_{1/2}$ $P(2.5)_{1\leftarrow 0}$ transition in SnH ($\delta\langle r^2\rangle^{A,122}_{P(2.5)}$ in fm^2) are also given.

A	$P(2.5)_{1\leftarrow 0}$	$\delta\nu^{A,122}_{P(2.5)}$	$R^{\mu}_{k\alpha}$	V_2	$\delta\langle r^2\rangle^{A,122}$	$\delta\langle r^2\rangle^{A,122}_{P(2.5)}$
112	1629.2956	+16.941(71)	5.8770(15)	1.279 19	−0.655(15)	−0.658(216)
114	1629.1749	+13.323(71)	5.8979(15)	1.279 31	−0.509(15)	−0.502(207)
116	1629.0581	+9.821(71)	5.9188(15)	1.279 71	−0.371(15)	−0.374(194)
117	1629.0007	+8.100(71)	5.9250(14)	1.279 81	−0.330(15)	−0.341(223)
118	1628.9455	+6.446(71)	5.9386(15)	1.279 92	−0.235(15)	−0.223(211)
119	1628.8898	+4.776(71)	5.9423(14)	1.279 99	−0.210(15)	−0.206(205)
120	1628.8364	+3.175(71)	5.9566(16)	1.280 07	−0.109(16)	−0.096(209)
122	1628.7305	0(0)	5.9723(15)	1.280 22	0(0)	0(0)
124	1628.6282	−3.067(71)	5.9857(15)	1.280 37	+0.093(16)	+0.109(186)

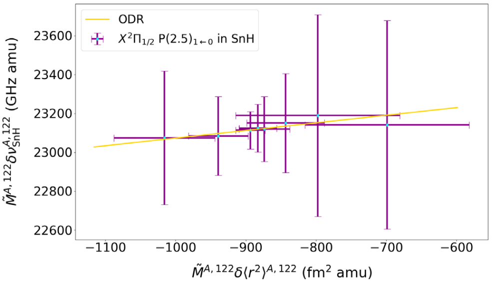

FIG. 9. Mass-modified isotope shifts in the $P(2.5)_{1\leftarrow0}$ rovibrational transition in SnH against the mass-modified changes in mean-squared nuclear charge radii of Sn. All error bars arise from the 1σ uncertainties of the literature isotope shifts (Table VII) and the uncertainties of the mass measurements taken from the 2020 Atomic Mass Evaluation [52].

The field-shift factor $\Psi_{P(2.5)}$ is consistent with 0, which implies that the experimental precision is not sufficient to unambiguously resolve the small field shift in the rovibrational transition. A small field shift is indeed expected for such a transition, as it does not involve a direct change of electronic state; the electronic overlap with the nucleus can change between the upper and lower rovibrational states only as a result of a coupling between the molecular rotation and the average electrostatic potential experienced by the electron.

As seen in Table VII, the nominal values of $\delta\langle r^2\rangle_{\mathrm{Sn}}^{A,A'}$ extracted from the molecular isotope shifts are in agreement with the values from nonoptical experiments, falling within the error of the nonoptical values for all isotopes. However, the values extracted from the molecular measurements are accompanied by large uncertainties, which originate from the small field shift of the transition and its large fractional uncertainty.

IV. DISCUSSION AND OUTLOOK

As it can be seen from the results of Sec. III, the changes in the mean-squared nuclear charge radii of Yb extracted using the T_0 fitted parameter and the ${}^{O}P$-branch features in YbF are remarkably consistent with those extracted from the high-resolution spectroscopy of Yb$^+$. Similarly, the analysis of isotope shifts in ZrO and Zr$^+$ leads to consistent values for the changes in mean-squared charge radii between the zirconium ionic and the molecular systems.

In the case of SnH, while the nominal values of $\delta\langle r^2\rangle_{\mathrm{Sn}}^{A,A'}$ extracted from the infrared isotope shifts are in general agreement with the literature values from nonoptical experiments, the uncertainties in the charge radii demonstrate that the field shift in the considered transition is consistent with 0. Possibly, had the experimental fractional uncertainty in the molecular measurements been smaller, the small but possibly nonzero field shift could have been resolved for the rovibrational transition. However, narrow-linewidth laser systems operating in the infrared regime are not widely available as of yet. Therefore, the present case might be generally representative of rovibrational transitions and their sensitivity to the field shift using state-of-the-art equipment. This result can guide experimentalists in selecting transitions to study nuclear-size effects in diatomic molecules. Additionally, as further discussed in Sec. IV B, the observation that the field shift in the vibrational transition is consistent with zero provides information on the change in the electronic wave function and its coupling to the nuclear motion.

Overall, the results of Sec. III indicate that the laser spectroscopy of diatomic molecules can be used to accurately extract the changes in mean-squared nuclear charge radii consistent with the results from atomic (ionic) spectroscopy, as demonstrated with optical isotopes shift in YbF and ZrO. The analysis of the isotope shifts in the T_0 parameter in YbF, which includes values for isotopomers with odd-A isotopes of Yb, also confirms that nuclear-structure effects, such as the appearance of odd-even staggering, can be captured by molecular measurements (Fig. 5).

Furthermore, the results of the analysis of both P and R rotational lines with low and higher J values alike in ZrO indicate that the molecular King-plot approach might also be a tool for molecular-structure studies. According to Eq. (16), the molecular isotope-shift factors Ψ and Ξ are linked to the fundamental molecular parameters f_{kl}^{Λ} and δ_{kl}^{Λ} that, analogous to the atomic case, provide information about the overlap of the valence electrons with the nuclear volume and the breakdown of the Born-Oppenheimer approximation, respectively.

Additionally, as the values of $\delta\langle r^2\rangle_{\mathrm{Yb}}^{A,172}$ extracted from the $A^2\Pi_{1/2}$ $(\nu = 0)$ T_0 parameter in YbF are consistent with those from the 369.4-nm in Yb$^+$, it is seen that the isotope shifts in the term energy T_0 of a vibronic state can also be used in a King-plot analysis with accuracy. Experimental term-energy measurements in diatomic molecules are also possible with low-resolution laser spectroscopy (laser linewidth of a few GHz), as already demonstrated in the case of RaF [29,60]. While the mass shift was not considered in the analysis of isotope shifts in Ref. [29] [due to the large mass of the species, which significantly dampens the presence of the mass shift, as seen in Eq. (2)], the results of Sec. III indicate that a complete consideration of the mass shift could be included using the King-plot method.

The potential impact of the results of the present work can be discussed in relation to nuclear-structure studies with laser spectroscopy at RIB facilities and molecular-physics research.

A. Importance for nuclear physics

To trace how nuclear structure evolves across long isotopic and isotonic chains, RIB facilities have been developed, where nuclei with extreme proton-to-neutron ratios are produced for experimental study. ISOL is a RIB production method that provides since many decades high-quality radioactive beams for precision nuclear-structure studies and as probes for materials science, biochemical, and atomic research [61,62]. With the thick-target ISOL technique, short-lived nuclides are produced by impinging highly energetic beams of protons onto a thick target material, typically composed of UC_x, LaC_x, UO_2, or ZrO_2, although other materials have also been successfully used. By heating the target material to a high temperature (approximately 2000 °C), the produced nuclei diffuse to the surface of the target as they form, and then effuse within a vapor into an ion-source region. Following ionization, the beam is mass purified using magnetic dipolar mass separators, before being delivered to an experimental station. Overall, radioactive beams with half-lives down to a few milliseconds can be studied experimentally at RIB facilities.

Because of its versatility, laser spectroscopy—collinear [63] and in source [64–66]—has been used to study the evolution of ground-state properties across the chart of the nuclides, from helium ($Z = 2$) isotopes up to the superheavies ($Z \geq 100$) [2]. However, the area of the nuclide chart that has been studied with laser spectroscopy features several noticeable gaps, including the light and reactive isotopic chains from boron to fluorine and from silicon to chlorine ($Z < 20$), the majority of refractory isotopic chains belonging to the transition metals, and most nuclides in the actinide region [2]. The reason for these gaps is the reactive and/or refractory nature of the atoms: In the course of their diffusion and effusion from the ISOL target, reactive atoms form molecules with high efficiency, while refractive atoms stick to the target matrix. As a result, the delivered radioactive beams are of prohibitively limited intensity, far below the minimum requirements of state-of-the-art laser-spectroscopy experiments (approximately 0.1–100 atoms per second, depending on the technique).

A potential pathway toward the study of such nuclei with laser spectroscopy is to deliver them in the form of a molecular beam. Molecular extraction at ISOL facilities has already demonstrated improvements in the delivery of certain reactive [67] and refractory [68] species. By exposing the ISOL target to a gas of choice during nuclide production, such as a fluorination or sulfurization agent, the species of interest can form molecules that are significantly more volatile than their atomic constituents.

The results of the present work demonstrate that the isotope shifts in radioactive molecules could be used to accurately extract values for $\delta\langle r^2\rangle^{A,A'}$. Importantly, as most refractory isotopic chains contain three or more stable isotopes, existing studies of isotope shifts (and isotope-shift factors) based on atomic laser spectroscopy and nonoptical methods already exist. Therefore, the developed King-plot analysis for molecular measurements in the current work demonstrates that mean-squared charge radii of short-lived isotopes can be extracted from molecular isotope-shift measurements without the need for detailed molecular field- and mass-shift calculations. The analysis of ZrO/Zr^+ in Sec. III B is one such example; while in-target simulations show that a long range of radioactive Zr isotopes can be produced within a thick ISOL target, atomic Zr is refractory and therefore, it cannot be extracted efficiently from a thick target. However, thin-ISOL approaches such as the one used in Ref. [57] allow for the efficient extraction of atomic Zr, but the isotopic range producible with this technique is significantly more limited than for thick-ISOL techniques. Therefore, studying nuclear-size effects in (volatile) molecular beams of Zr may allow for the study of short-lived Zr isotopes that are otherwise inaccessible with atomic spectroscopy. As Eq. (16) does not introduce limitations in terms of the nonsubstituted atom in the diatomic molecule, such a study can be done on fluorides, oxides, nitrides, etc., depending on the species that can be extracted most efficiently in each case. While this approach could be beneficial for nuclear-structure studies of the Zr chain, it is not the only case that would benefit from the approach; numerous reactive and refractory species have been successfully produced in molecular form, often with a considerable enhancement in beam purity or extraction efficiency [26,27,69].

While in the absence of a framework like the King-plot analysis, the need for detailed molecular-structure calculations prior to each experimental study would decelerate experimental progress, the ability to calculate these factors for diatomic molecules using quantum-chemistry methods is also important. As seen in Eq. (16), the molecular isotope-shift factors Ψ and Ξ are linked to the molecular parameters $f_{kl}^{\Lambda,A}$ and $\delta_{kl}^{\Lambda,A}$ which could be calculated using *ab initio* methods. In certain cases, such calculations can be more accurate in the diatomic molecule than in the constituent atomic systems, thus leading to more isotopic chains accessible by laser spectroscopy. The reason is that the laser-spectroscopic study of nuclei whose atomic structure contains more than two valence electrons, such as many lanthanide and actinide species, is often challenging. The valence electronic space of such atoms complicates the accurate calculation of the isotope-shift factors [46], which, in certain cases, can be very challenging even with state-of-the-art computational tools. Typically, such systems are studied as atomic ions, where the reduction in the valence electronic space allows for more accurate calculations. However, this strategy can lead to unfavorable transitions outside the optical range, or require high charge numbers that are beyond the technical capabilities of most RIB facilities. By placing the atom in a chemical bond, the number of valence quasiparticles included in the calculation can, strictly speaking, be reduced. As a result, the diatomic molecule can be within reach of computational packages such as implementations of the accurate and precise Fock-space relativistic coupled cluster, which are currently limited to two valence quasiparticles [70], and the extension of which to more valence quasiparticles is nontrivial. On the contrary, the constituent atom having three or more valence electrons would be incompatible with the same packages. For instance, accurate relativistic coupled-cluster calculations of HfF^+ [71] and ThO [72] have been successfully performed at the singles-doubles-triples and perturbatively quadruples level, while the Hf and Th atoms have four valence electrons and would therefore present a serious challenge for calculations at the same level of accuracy (multiple charge states of the Hf were recently calculated [73] only at the singles and doubles level, and the agreement with experiment was significantly worse than what is achievable with the approach in Refs. [71,72] as shown in the case of ThO). By utilizing a King-plot analysis that involves atomic and molecular isotope shifts, the atomic isotope-shift factors can be extracted from the molecular ones. The radioactive nuclei can then be studied within whichever system, atomic or molecular, leads to more favorable experimental parameters, such as efficiency and technical readiness.

Overall, Eq. (16) allows for relating the isotope-shift factors of atoms and molecules, and the link between the factors Ψ and Ξ and fundamental molecular parameters also allows for calculating the molecular isotope-shift factors with quantum chemistry. Consequently, the experimental progress in the laser spectroscopy of radioactive molecules can utilize decades of advances in atomic laser spectroscopy for cases where that is possible, as well as enable the study of systems that are currently inaccessible in atomic form due to technical or computational difficulties. Therefore, accelerated progress in the study of the charge radii of short-lived nuclei using laser spectroscopy could be achieved through the study of radioactive molecules. As *ab initio* nuclear theory is progressing rapidly, expanding the experimental capabilities to more weakly bound isotopes and new isotopic chains is becoming progressively more important. In certain cases, joint experimental-theoretical studies of the nuclear charge radius of isotopes and chains that are currently experimentally inaccessible would provide a pathway to currently insufficiently studied physics, such as the role of many-body nuclear forces, continuum effects, nucleon clustering, and nucleon superfluidity, as aforementioned.

B. Molecular-structure information

A close observation of the extracted isotope-shift factors for YbF, ZrO, and SnH in Sec. III shows that a systematic study of Ψ and Ξ in a diatomic molecule could provide information about the electronic wave function and its coupling to the nuclear motion.

As seen from the isotope-shift factors of the rotational lines in ZrO (Table V), while Ψ and Ξ are very similar for the lines $P(1)$ and $R(1)$, the mass-shift factor Ξ scales very strongly with J for the P branch, while for the R branch, both Ψ and Ξ scale strongly with J. Such patterns could be potentially used to benchmark theoretical calculations of the influence of the rotational quantum number J on the electronic overlap with the nucleus. Additionally, understanding the different behavior of the P and R lines would lead to molecular-structure information that is not easily accessible through other experimental observables. For instance, P and R lines with a common rotational substate [such as $P(1)$ and $R(1)$] could be used to extract the nuclear-electronic overlap and electron correlation energy in a single electronic state through the combination difference [41], rather than a property that depends on the difference between two electronic states, such as the atomic case of F.

In analogy with the atomic mass shift, the evolution of the molecular mass-shift factor Ξ could provide information on the difference in electronic correlation energy between molecular states. In the molecular case, however, the normal mass shift, whose formulation is well understood in atoms as the component of the mass shift that does not depend on electron correlations, might possess a different formulation with additional dependence on the vibrational and rotational degrees of freedom. For instance, in the case of YbF, the factors for the two P-branch features exhibit an interesting effect: The mass-shift factor Ξ changes sign as J increases, going from $+1720(240)$ for $J = 3$ to $-4900(600)$ for $J = 9$. While such a change might indicate that the coupling between molecular rotation and electronic energy leads to a drastic change in the electronic correlation energy for different rotational states, this interpretation is contradicted by the significantly weaker dependence of Ψ on J, and further unsupported by the very simple electronic structure of the free radical YbF. A possible explanation for the change of sign in Ξ with increasing J is that the molecular normal mass shift in fact also contains a strong dependence on the rotational quantum number J. Systematic studies with the molecular King-plot method could thus potentially be used to study both the electronic correlation energy in molecules, even resolving its dependence on the vibrational and rotational degrees of freedom, and the contributions to the isotope shift that do not stem from electron correlations.

In the case of SnH, interestingly both the absolute and the relative magnitudes of the infrared isotope shifts (Table VII) are significantly greater than those typically encountered in atomic Sn (see, for example, Ref. [74]). Since the field shift contributes only slightly, if at all (the contribution certainly is smaller than the resolution achieved in this analysis), isotope shifts of such a magnitude for this transition might indicate that a molecular effect akin to the specific mass shift in atoms has a significantly larger magnitude in some diatomic molecules compared to their constituent atoms. As the specific mass shift originates from the change in the electron correlation energy as a result of the change in nuclear mass, molecular systems might be more sensitive probes for the study of such effects than their atomic constituents.

Additionally, although the field shift in the studied vibrational transition in SnH is consistent with zero, resolving a nonzero field shift in broadband vibrational transitions would also probe the electronic wave function, as the electrons spend less time on average within the nuclear volume(s) for a higher molecular vibrational energy. By tracing the evolution of the field-shift factor across transitions between states with high vibrational quantum numbers as well as overtone transitions ($|\delta\nu| > 1$), the nuclear-electronic temporal overlap can also be studied.

Understanding how the isotope-shift factors scale with the rotational (and vibrational, although not explicitly demonstrated in this work) quantum numbers is also of importance for mass-independent, multi-isotopomer studies for astrophysics. The detection of signatures of pure-rotational transitions in diatomic molecules has been recognized as a more powerful pathway to identify the isotopic composition of astrophysical environments compared to x-ray and γ-ray spectroscopy [75]. However, for isotopomers containing short-lived radioactive atoms, the laboratory measurement of the rotational transition energies can be difficult, as it requires the development of equipment in specialized facilities that is not yet in place. Therefore, a mass-independent, multi-isotopomer analysis of the stable isotopomers of the molecules can be employed to allow for the transition frequencies in the radioactive isotopomers to be extrapolated from those in the stable ones (for example, see Ref. [76]). In such an analysis, the field- and mass-related parameters f_{kl} and δ_{kl} introduced in the Dunham expansion [Eq. (9)] are assumed to be independent of ν and J for a given electronic state; that is, all vibrational and rotational transitions within a given electronic state are characterized by the same set of f_{kl} and δ_{kl}. The results of this work, however, demonstrate that this assumption is not fully realistic, since the field- and mass-shift factors Ψ and Ξ, which are linked to f_{kl} and δ_{kl} as per Eq. (16), can be strongly dependent on ν and J. While extending the molecular King-plot analysis to pure-rotational transitions in diatomic molecules is beyond the scope of this work, further developments in this direction could therefore benefit the multi-isotopomer analysis for nuclear astrophysics.

To the knowledge of the authors, such molecular-structure information is not easily accessible by other techniques. The molecular King-plot analysis, as demonstrated in this work, opens a path for the study of new observables in molecular physics with laser spectroscopy. Importantly, laser-spectroscopic experiments on molecules have also been successful, as in the case of RaF [28,29], with ultra-high-sensitivity experiments, such as the collinear resonance ionization spectroscopy beamline, which is optimized to study species that remain bound for down to 5 ms [77] and rare species with production rates as low as a few tens per second [78]. Therefore, field- and mass-shift studies can also be performed in weakly bound diatomic molecules, molecules containing short-lived radioactive nuclides, or molecular beams of low purity, making the approach versatile.

V. CONCLUSIONS

In the present work, an isotope-shift expression for diatomic molecules that is linear with respect to the change in the nuclear charge radii $\delta\langle r^2\rangle^{A',A''}$ is used in a King-plot analysis in combination with isotope-shift measurements in ionic atoms. Such an approach can be used to extract $\delta\langle r^2\rangle^{A',A''}$ from molecular isotope shifts using known isotope shifts and isotope-shift factors in atomic transitions, or to study aspects of the molecular wave function.

To demonstrate the validity of the expression, a King-plot analysis of isotope shifts in the electronic spectra of $^{170-174,176}$YbF [48] is performed in combination with isotope-shift measurements in the 369.4-nm transition in Yb$^+$ [49]. The isotope shifts in both the fitted $A^2\Pi_{1/2}$ $(\nu = 0)$ T_0 parameters of $^{170-174,176}$YbF as well as the $^{O}P_{12}(3)$ $(F' = 2,\ F'' = 2)$ and $^{O}P_{12}(9)$ $(F' = 8,\ F'' = 9)$ branch features of the $A^2\Pi_{1/2}$ $(\nu = 0) \leftarrow X^2\Sigma^+$ $(\nu = 0)$ transition of the isotopomers containing the even-A Yb isotopes are analyzed.

The King-plot analysis is used to compare the values of $\delta\langle r^2\rangle^{A',A''}$ extracted from the spectroscopy of YbF with those extracted using Yb$^+$. The agreement between the molecular- and atomic-extracted values is excellent, demonstrating that a King-plot analysis of optical molecular isotope shifts can be used with accuracy. The agreement in $\delta\langle r^2\rangle^{A',A''}$ extracted both from the term energy as well as two P-branch features indicates that both low- and high-resolution laser spectroscopy of molecules could be used for measurements of $\delta\langle r^2\rangle^{A',A''}$.

Similarly, the analysis of optical isotope shifts in P- and R-branch rotational lines in the $C^1\Sigma^+ - X^1\Sigma^+$ transition in ZrO with isotope shifts in the 327-nm transition in Zr$^+$ also yields consistent values of $\delta\langle r^2\rangle^{A',A''}$. Additionally, the difference in the isotope-shift factors between the P- and R-branch transitions for $J = 1$ and $J = 20$ reveals a quantum-number dependence on the change in the field and mass shift across rotational transitions. As a result, the King-plot method could be used to gain insights into molecular structure through a detailed study of the evolution of the isotope-shift factors as a function of the molecular quantum numbers.

Lastly, isotope-shift measurements of the $P(2.5)_{1\leftarrow 0}$ rovibrational transition in the electronic ground state $X^2\Pi_{1/2}$ for the stable isotopomers of SnH [58] using infrared spectroscopy are analyzed in combination with values for the changes in mean-squared nuclear charge radii from nonoptical techniques [59]. The extracted field shift for this vibrational transition is consistent with zero, indicating that the transition is not sensitive to the nuclear volume within the achieved resolution. While this transition would therefore not be useful for the measurement of nuclear charge radii, this observation provides information on the change in the electronic wave function in a transition that does not involve a change in electronic state. To the knowledge of the authors, such information is not experimentally accessible via other methods.

The results of the current work can lead to experimental progress in nuclear-structure research by contributing to the study of nuclei with refractory and reactive atoms at thick-ISOL facilities, which are important for the study of unique nuclear phenomena and their role in the nuclear charge radius, while the systematic analysis of isotope-shift factors across many transitions in a molecule could be used to extract molecular-structure information that is not accessible by other methods.

ACKNOWLEDGMENTS

M. A.-K. and G. N. acknowledge financial support from FWO, as well as from the Excellence of Science program (Grant No. 40007501), and the KU Leuven Project No. C14/22/104. S. G. W. is supported by U.S. DOE Grant No. DE-SC0021176. A. A. B. gratefully acknowledges financial support from the Deutsche Forschungsgemeinschaft (DFG, German Research Foundation) Project No. 328,961,117 SFB 1319 ELCH. The authors would like to thank R. Berger (University of Marburg), T. Steimle (Arizona State University), R. F. Garcia Ruiz (Massachusetts Institute of Technology), E. Tiemann (Leibniz Universität Hannover), and Lukáš Pašteka (Comenius University) for useful discussions and Sonja Kujanpää (Jyväskylä University) for Fig. 1.

[1] W. H. King, *Isotope Shifts in Atomic Spectra* (Springer Science & Business Media, New York, 2013).

[2] P. Campbell, I. D. Moore, and M. R. Pearson, *Laser Spectroscopy for Nuclear Structure Physics*, Prog. Part. Nucl. Phys. **86**, 127 (2016).

[3] P.-G. Reinhard, W. Nazarewicz, and R. F. Garcia Ruiz, *Beyond the Charge Radius: The Information Content of the Fourth Radial Moment*, Phys. Rev. C **101**, 021301(R) (2020).

[4] P.-G. Reinhard and W. Nazarewicz, *Nuclear Charge Densities in Spherical and Deformed Nuclei: Toward Precise Calculations of Charge Radii*, Phys. Rev. C **103**, 054310 (2021).

[5] A. Koszorús *et al.*, *Charge Radii of Exotic Potassium Isotopes Challenge Nuclear Theory and the Magic Character of* $N = 32$, Nat. Phys. **17**, 439 (2021).

[6] L. J. Vormawah, M. Vilén, R. Beerwerth, P. Campbell, B. Cheal, A. Dicker, T. Eronen, S. Fritzsche, S. Geldhof, A. Jokinen, S. Kelly, I. D. Moore, M. Reponen, S. Rinta-Antila, S. O. Stock, and A. Voss, *Isotope Shifts from Collinear Laser Spectroscopy of Doubly Charged Yttrium Isotopes*, Phys. Rev. A **97**, 042504 (2018).

[7] K. Blaum, J. Dilling, and W. Nörtershäuser, *Precision Atomic Physics Techniques for Nuclear Physics with Radioactive Beams*, Phys. Scr. **T152**, 014017 (2013).

[8] R. F. Garcia Ruiz *et al.*, *Unexpectedly Large Charge Radii of Neutron-Rich Calcium Isotopes*, Nat. Phys. **12**, 594 (2016).

[9] R. P. de Groote *et al.*, *Measurement and Microscopic Description of Odd-Even Staggering of Charge Radii of Exotic Copper Isotopes*, Nat. Phys. **16**, 620 (2020).

[10] M. Kortelainen, Z. Sun, G. Hagen, W. Nazarewicz, T. Papenbrock, and P.-G. Reinhard, *Universal Trend of Charge Radii of Even-Even Ca-Zn Nuclei*, Phys. Rev. C **105**, L021303 (2022).

[11] H.-W. Hammer, S. König, and U. van Kolck, *Nuclear Effective Field Theory: Status and Perspectives*, Rev. Mod. Phys. **92**, 025004 (2020).

[12] B. R. Barrett, P. Navrátil, and J. P. Vary, *Ab Initio No Core Shell Model*, Prog. Part. Nucl. Phys. **69**, 131 (2013).

[13] G. Hagen, T. Papenbrock, M. Hjorth-Jensen, and D. J. Dean, *Coupled-Cluster Computations of Atomic Nuclei*, Rep. Prog. Phys. **77**, 096302 (2014).

[14] P. Navrátil, S. Quaglioni, G. Hupin, C. Romero-Redondo, and A. Calci, *Unified Ab Initio Approaches to Nuclear Structure and Reactions*, Phys. Scr. **91**, 053002 (2016).

[15] H. Hergert, S. K. Bogner, T. D. Morris, A. Schwenk, and K. Tsukiyama, *The In-Medium Similarity Renormalization Group: A Novel Ab Initio Method for Nuclei*, Phys. Rep. **621**, 165 (2016).

[16] V. Somà, C. Barbieri, T. Duguet, and P. Navrátil, *Moving away from Singly-Magic Nuclei with Gorkov Green's Function Theory*, Eur. Phys. J. A **57**, 135 (2021).

[17] A. J. Miller, K. Minamisono, A. Klose, D. Garand, C. Kujawa, J. D. Lantis, Y. Liu, B. Maaß, P. F. Mantica, W. Nazarewicz, W. Nörtershäuser, S. V. Pineda, P.-G. Reinhard, D. M. Rossi, F. Sommer, C. Sumithrarachchi, A. Teigelhöfer, and J. Watkins, *Proton Superfluidity and Charge Radii in Proton-Rich Calcium Isotopes*, Nat. Phys. **15**, 432 (2019).

[18] M. Chernykh, H. Feldmeier, T. Neff, P. von Neumann-Cosel, and A. Richter, *Structure of the Hoyle State in* ^{12}C, Phys. Rev. Lett. **98**, 032501 (2007).

[19] Y. Kanada-En'yo, Proton Radii of Be, B, and C Isotopes, Phys. Rev. C **91**, 014315 (2015).

[20] T. Duguet, V. Somà, S. Lecluse, C. Barbieri, and P. Navrátil, *Ab Initio Calculation of the Potential Bubble Nucleus* ^{34}Si, Phys. Rev. C **95**, 034319 (2017).

[21] G. Hagen, M. Hjorth-Jensen, G. R. Jansen, R. Machleidt, and T. Papenbrock, *Continuum Effects and Three-Nucleon Forces in Neutron-Rich Oxygen Isotopes*, Phys. Rev. Lett. **108**, 242501 (2012).

[22] J. Carlson, S. Gandolfi, F. Pederiva, S. C. Pieper, R. Schiavilla, K. E. Schmidt, and R. B. Wiringa, *Quantum Monte Carlo Methods for Nuclear Physics*, Rev. Mod. Phys. **87**, 1067 (2015).

[23] A. Ekström, G. R. Jansen, K. A. Wendt, G. Hagen, T. Papenbrock, B. D. Carlsson, C. Forssén, M. Hjorth-Jensen, P. Navrátil, and W. Nazarewicz, *Accurate Nuclear Radii and Binding Energies from a Chiral Interaction*, Phys. Rev. C **91**, 051301(R) (2015).

[24] S. J. Novario, G. Hagen, G. R. Jansen, and T. Papenbrock, *Charge Radii of Exotic Neon and Magnesium Isotopes*, Phys. Rev. C **102**, 051303 (2020).

[25] B. Hu, W. Jiang, T. Miyagi, Z. Sun, A. Ekström, C. Forssén, G. Hagen, J. D. Holt, T. Papenbrock, S. R. Stroberg, and I. Vernon, *Ab Initio Predictions Link the Neutron Skin of* ^{208}Pb *to Nuclear Forces*, Nat. Phys. **18**, 1196 (2022).

[26] U. Köster, O. Arndt, E. Bouquerel, V. N. Fedoseyev, H. Frånberg, A. Joinet, C. Jost, I. S. K. Kerkines, and R. Kirchner, *Progress in ISOL Targetion Source Systems*, Nucl. Instrum. Methods Phys. Res., Sect. B **266**, 4229 (2008).

[27] J. Ballof, *Radioactive Molecular Beams at CERN-ISOLDE*, Ph.D. thesis, Johannes Gutenberg University of Mainz, 2021.

[28] R. F. Garcia Ruiz *et al.*, *Spectroscopy of Short-Lived Radioactive Molecules*, Nature (London) **581**, 396 (2020).

[29] S. M. Udrescu *et al.*, *Isotope Shifts of Radium Monofluoride Molecules*, Phys. Rev. Lett. **127**, 033001 (2021).

[30] M. Athanasakis *et al.*, *Radioactive Molecules at ISOLDE*, CERN Technical Report No. CERN-INTC-2021-017, 2021.

[31] W. Demtröder, *Laser Spectroscopy* (Springer, New York, 1982), Vol. 2.

[32] S. Truppe, S. Marx, S. Kray, M. Doppelbauer, S. Hofsäss, H. C. Schewe, N. Walter, J. Pérez-Ríos, B. G. Sartakov, and G. Meijer, *Spectroscopic Characterization of Aluminum Monofluoride with Relevance to Laser Cooling and Trapping*, Phys. Rev. A **100**, 052513 (2019).

[33] N. H. Pilgram, A. Jadbabaie, Y. Zeng, N. R. Hutzler, and T. C. Steimle, *Fine and Hyperfine Interactions in* ^{171}YbOH *and* ^{173}YbOH, J. Chem. Phys. **154**, 244309 (2021).

[34] A. H. M. Ross, R. S. Eng, and H. Kildal, *Heterodyne Measurements of* ^{12}C^{8}O, ^{13}C^{16}O, *and* ^{13}C^{18}O *Laser Frequencies; Mass Dependence of Dunham Coefficients*, Opt. Commun. **12**, 433 (1974).

[35] J. K. G. Watson, *The Isotope Dependence of Diatomic Dunham Coefficients*, J. Mol. Spectrosc. **80**, 411 (1980).

[36] H. Knöckel and E. Tiemann, *Isotopic Field Shift in the Transition* $A0^{++}-X^1\Sigma^+$ *of* PbS, Chem. Phys. **68**, 13 (1982).

[37] H. Knöckel and E. Tiemann, *Isotope shift of the transition* $A0^{++}-X^1\Sigma^+$ *of* PbO, Chem. Phys. Lett. **104**, 83 (1984).

[38] H. Knöckel, T. Kröckertskothen, and E. Tiemann, *Molecular-Beam-Laser Studies of the States* $X^1\Sigma+$ *and* $A0^+$ *of* PbS, Chem. Phys. **93**, 349 (1985).

[39] J. L. Dunham, *The Energy Levels of a Rotating Vibrator*, Phys. Rev. **41**, 721 (1932).

[40] Not to be confused with the spherical tensors that are typically represented by the same symbol.

[41] G. Herzberg, *Molecular Spectra and Molecular Structure* (D. Van Nostrand, Princeton, 1945).

[42] S. Knecht and T. Saue, *Nuclear Size Effects in Rotational Spectra: A Tale with a Twist*, Chem. Phys. **401**, 103 (2012).

[43] A. Almoukhalalati, A. Shee, and T. Saue, *Nuclear Size Effects in Vibrational Spectra*, Phys. Chem. Chem. Phys. **18**, 15406 (2016).

[44] J. Schlembach and E. Tiemann, *Isotopic Field Shift of the Rotational Energy of the* Pb-*Chalcogenides and* Tl-*Halides*, Chem. Phys. **68**, 21 (1982).

[45] R. J. Le Roy, *Improved Parameterization for Combined Isotopomer Analysis of Diatomic Spectra and Its Application to HF and DF*, J. Mol. Spectrosc. **194**, 189 (1999).

[46] B. Cheal, T. E. Cocolios, and S. Fritzsche, *Laser Spectroscopy of Radioactive Isotopes: Role and Limitations of Accurate Isotope-Shift Calculations*, Phys. Rev. A **86**, 042501 (2012).

[47] B. Ohayon, R. F. Garcia Ruiz, Z. H. Sun, G. Hagen, T. Papenbrock, and B. K. Sahoo, *Nuclear Charge Radii of* Na *Isotopes: Interplay of Atomic and Nuclear Theory*, Phys. Rev. C **105**, L031305 (2022).

[48] T. C. Steimle, T. Ma, and C. Linton, *The Hyperfine Interaction in the* $A^2\Pi_{1/2}$ *and* $X^2\Sigma^+$ *States of Ytterbium Monofluoride*, J. Chem. Phys. **127**, 234316 (2007).

[49] A.-M. Mårtensson-Pendrill, D. S. Gough, and P. Hannaford, *Isotope Shifts and Hyperfine Structure in the 369.4-nm* $6s$-$6p_{1/2}$ *Resonance Line of Singly Ionized Ytterbium*, Phys. Rev. A **49**, 3351 (1994).

[50] B. E. Sauer, J. Wang, and E. A. Hinds, *Laser-rf Double Resonance Spectroscopy of* ^{174}YbF *in the* $X^2\Sigma^+$ *State: Spin-Rotation, Hyperfine Interactions, and the Electric Dipole Moment*, J. Chem. Phys. **105**, 7412 (1996).

[51] T. C. Steimle, T. Ma, and C. Linton, *The Hyperfine Interaction in the* $A^2\Pi_{1/2}$ *and* $X^2\Sigma^+$ *States of Ytterbium Monofluoride*, J. Chem. Phys. **127**, 234316 (2007); **128**, 209903(E) (2008).

[52] M. Wang, W. J. Huang, F. G. Kondev, G. Audi, and S. Naimi, *The AME 2020 Atomic Mass Evaluation (II). Tables, Graphs and References**, Chin. Phys. C **45**, 030003 (2021).

[53] The mean-squared nuclear charge radii in Ref. [49] are given with respect to ^{176}Yb. There is a disagreement between the values of the mean-squared charge radii in Ref. [49] and Refs. [54,55]. An explanation for the discrepancy can be found in Ref. [49]. The disagreement between the results of the two works falls beyond the scope of the present work, as the linearity of the molecular isotope shift would be valid for any choice of isotope-shift factors for Yb$^+$.

[54] D. L. Clark, M. E. Cage, D. A. Lewis, and G. W. Greenlees, *Optical Isotopic Shifts and Hyperfine Splittings for* Yb, Phys. Rev. A **20**, 239 (1979).

[55] I. Angeli and K. P. Marinova, *Table of Experimental Nuclear Ground State Charge Radii: An Update*, At. Data Nucl. Data Tables **99**, 69 (2013).

[56] B. Simard, S. A. Mitchell, M. R. Humphries, and P. A. Hackett, *High-Resolution Spectroscopy and Photophysics of Refractory Molecules at Low Temperature: The* $C^1\Sigma^+-X^1\Sigma^+$ *system of* ZrO, J. Mol. Spectrosc. **129**, 186 (1988).

[57] P. Campbell, H. L. Thayer, J. Billowes, P. Dendooven, K. T. Flanagan, D. H. Forest, J. A. R. Griffith, J. Huikari, A. Jokinen, R. Moore, A. Nieminen, G. Tungate, S. Zemlyanoi, and J. Äystö, *Laser Spectroscopy of Cooled Zirconium Fission Fragments*, Phys. Rev. Lett. **89**, 082501 (2002).

[58] U. Simon, M. Petri, W. Zimmermann, and W. Urban, *Infrared Diode-Laser Spectroscopy of the Ground State of* SnH *(*$X^2\Pi_{1/2}$*)*, Mol. Phys. **71**, 1163 (1990).

[59] G. Fricke and K. Heilig, *Nuclear Charge Radii, 50-Sn Tin: Datasheet from Landolt-Börnstein—Group I Elementary Particles, Nuclei and Atoms, Vol. 20, Nuclear Charge Radii*, 10.1007/10856314_52.

[60] In such cases, the uncertainty in the extracted $\delta\langle r^2\rangle^{A',A''}$ will probably be greater than the error bars for T_0 in Sec. III, as the T_0 values used in the present analysis are extracted from a statistical fit involving high-resolution optical measurements.

[61] Y. Blumenfeld, T. Nilsson, and P. Van Duppen, *Facilities and Methods for Radioactive Ion Beam Production*, Phys. Scr. **T152**, 014023 (2013).

[62] M. J. G. Borge and B. Jonson, *ISOLDE Past, Present and Future*, J. Phys. G **44**, 044011 (2017).

[63] R. Neugart, J. Billowes, M. L. Bissell, K. Blaum, B. Cheal, K. T. Flanagan, G. Neyens, W. Nörtershäuser, and D. T. Yordanov, *Collinear Laser Spectroscopy at ISOLDE: New Methods and Highlights*, J. Phys. G **44**, 064002 (2017).

[64] B. A. Marsh *et al.*, *New Developments of the In-Source Spectroscopy Method at RILIS/ISOLDE*, Nucl. Instrum. Methods Phys. Res., Sect. B **317**, 550 (2013).

[65] R. Heinke, T. Kron, S. Raeder, T. Reich, P. Schönberg, M. Trümper, C. Weichhold, and K. Wendt, *High-Resolution In-Source Laser Spectroscopy in Perpendicular Geometry*, Hyperfine Interact. **238**, 6 (2017).

[66] I. Pohjalainen, I. D. Moore, T. Kron, S. Raeder, V. Sonnenschein, H. Tomita, N. Trautmann, A. Voss, and K. Wendt, *In-Gas-Cell Laser Ionization Studies of Plutonium Isotopes at IGISOL*, Nucl. Instrum. Methods Phys. Res., Sect. B **376**, 233 (2016).

[67] J. Ballof, C. Seiffert, B. Crepieux, C. E. Düllmann, M. Delonca, M. Gai, A. Gottberg, T. Kröll, R. Lica, M. Madurga Flores, Y. Martinez Palenzuela, T. M. Mendonca, M. Owen, J. P. Ramos, S. Rothe, T. Stora, O. Tengblad, and F. Wienholtz, *Radioactive Boron Beams Produced by Isotope Online Mass Separation at CERN-ISOLDE*, Eur. Phys. J. A **55**, 65 (2019).

[68] U. Köster, P. Carbonez, A. Dorsival, J. Dvorak, R. Eichler, S. Fernandes, H. Frånberg, J. Neuhausen, Z. Novackova, R. Wilfinger, and A. Yakushev, *(Im-) Possible ISOL Beams*, Eur. Phys. J. Special Topics **150**, 285 (2007).

[69] M. Au and J. Ballof, *Molecular Sidebands for Radioactive Ion Beam Extraction*, 10.5281/zenodo.6884293 (2022).

[70] A. V. Oleynichenko, A. Zaitsevskii, L. V. Skripnikov, and E. Eliav, *Relativistic Fock Space Coupled Cluster Method for Many-Electron Systems: Non-Perturbative Account for Connected Triple Excitations*, Symmetry **12**, 1101 (2020).

[71] L. V. Skripnikov, *Communication: Theoretical Study of* HfF^+ *Cation to Search for the T,P-Odd Interactions*, J. Chem. Phys. **147**, 021101 (2017).

[72] L. V. Skripnikov, *Combined 4-Component and Relativistic Pseudopotential Study of* ThO *for the Electron Electric Dipole Moment Search*, J. Chem. Phys. **145**, 214301 (2016).

[73] S. O. Allehabi, V. A. Dzuba, and V. V. Flambaum, *Theoretical Study of the Electronic Structure of Hafnium (*Hf, $Z = 72$*) and Rutherfordium (*Rf, $Z = 104$*) Atoms and Their Ions: Energy Levels and Hyperfine-Structure Constants*, Phys. Rev. A **104**, 052811 (2021).

[74] C. Gorges *et al.*, *Laser Spectroscopy of Neutron-Rich Tin Isotopes: A Discontinuity in Charge Radii across the* $N = 82$ *Shell Closure*, Phys. Rev. Lett. **122**, 192502 (2019).

[75] B. A. McGuire, *2021 Census of Interstellar, Circumstellar, Extragalactic, Protoplanetary Disk, and Exoplanetary Molecules*, Astrophys. J. Suppl. Ser. **259**, 30 (2022).

[76] A. A. Breier, B. Waßmuth, G. W. Fuchs, J. Gauss, and T. F. Giesen, *Mass-Independent Analysis of the Stable Isotopologues of Gas-Phase Titanium Monoxide* TiO, J. Mol. Spectrosc. **355**, 46 (2019).

[77] G. J. Farooq-Smith *et al.*, *Laser and Decay Spectroscopy of the Short-Lived Isotope* ^{214}Fr *in the Vicinity of the* $N = 126$ *Shell Closure*, Phys. Rev. C **94**, 054305 (2016).

[78] R. P. de Groote *et al.*, *Dipole and Quadrupole Moments of* $^{73\text{–}78}$Cu *as a Test of the Robustness of the* $Z = 28$ *Shell Closure near* ^{78}Ni, Phys. Rev. C **96**, 041302(R) (2017).

Chapter 4

Spectroscopy of excited states in RaF

For more than a decade, radium monofluoride (RaF) has been under theoretical study as a promising probe system to perform precision tests of the SM by searching for nuclear, hadronic, and leptonic symmetry-violating moments [119, 120].

As in general with polar molecules, the internal electric field in RaF (in the order of a few GV/cm) is orders of magnitude stronger than what can be currently applied in the laboratory. Therefore, in the presence of such an intense electric field, the theorized electric dipole moment of the electron (eEDM) will give rise to a precession of the electronic spin about the direction of the electric field at a frequency proportional to the product of the EDM and the effective electric field. The internal effective electric field E_{eff} acting on the electron can thus be understood as a measure of the molecule's sensitivity to the presence of the eEDM. Due to its sizeable E_{eff} [119, 120, 121, 122], RaF is a promising candidate for experimental searches of the eEDM.

In a similar manner, RaF is under consideration as a promising candidate for the first measurement of the symmetry-violating nuclear Schiff and magnetic quadrupole moments across the chart of the nuclides. This promise arises simultaneously from a predicted enhancement in the magnitude of such symmetry-violating moments in the non-spin-zero radium nuclei, and from the high sensitivity of the electronic structure of RaF to the presence of these moments [120, 119, 121, 122, 123].

The former benefit stems from the size and shape of the radium nuclei. In the approximate, semi-analytical expression for the magnitude of the Schiff moment [20, 124], as an example, the moment scales both with the nuclear quadrupole deformation β_2 and the square of the nuclear octupole deformation β_3^2 (see Section 2.1). Simultaneously, a strong dependence on the size of the system (scaling as $ZA^{2/3}$) and the energy splitting of opposite-parity states with the same angular momentum ($\Delta E_{\pm}$) means that heavy and deformed nuclei with opposite-parity rotational doublet states and non-zero nuclear spin, such as ^{225}Ra ($I^{\pi} = 1/2^{+}$, $\Delta E_{\pm} =$ 55.16 keV) [20], are expected to have significantly enhanced symmetry-violating nuclear moments.

The main benefit of RaF compared to other systems, however, is its laser-coolable structure [2]. The experimental precision of spectroscopic experiments is proportional to the coherence time of the measurement cycle, and the number of molecules that can be simultaneously probed in each measurement cycle. Therefore, the ability to achieve three-dimensional laser cooling in a neutral ensemble (where the molecular number density is not limited by space-charge effects, as with HfF^{+} ions [70]) cooled to $\sim \mu$K temperatures offers a great potential for maximizing the experimental precision.

As explained in Chapter 1, achieving the unprecedented precision that is necessary for searches of new physics requires joint and simultaneous experimental and theoretical efforts along multiple directions. While experimental methods with high sensitivity to the symmetry-violating observables are a necessity, making progress in the development of precision molecular theory is equally pivotal. And to achieve the latter, concentrated experimental efforts are also necessary, in the form of preparatory spectroscopic studies of the molecules of interest that can benchmark the predictions of precision molecular theory.

Interpreting experimental measurements to extract values of symmetry-violating nuclear moments requires input from both nuclear and molecular theory. Therefore, the ability to identify a statistically significant discrepancy between the measured magnitudes and the SM predictions is strongly dependent on the precision of nuclear and molecular calculations alike. For the latter, highly accurate and precise calculations of the sensitivity of the probe system to the presence of the respective nuclear moment are necessary. Therefore, to test the limits of the SM through the experimental searches for nuclear Schiff, anapole, and MQM moments, among others, making progress in maximizing the accuracy and precision of quantum chemistry is a prerequisite.

The importance of improving the quality of theory for searches of new physics cannot be overstated, as evidenced by the 1997 atomic parity violation (APV) experiment for the measurement of the anapole moment in ^{133}Cs [125] and the recent search for a nonlinearity in the King plot of Yb [83].

While the two experiments differ in the physics they probe, they are similar in their effort to measure an observable and search for a discrepancy between the measured magnitude and the SM prediction. In the case of the APV experiment in Cs [125], Wood *et al.* performed a successful measurement of a shift in atomic energy levels under a reverting external field, thus attributed to arise from a parity-violating interaction. The statistically significant shift in the energy of electronic states in ^{133}Cs, however, has not yet translated into a value of the weak nuclear charge Q_W – as originally intended – that is precise enough to meaningfully challenge the SM prediction.

The primary reason is the limited precision of state-of-the-art quantum chemistry, even though it has surpassed the 99% level. Despite the relative simplicity of the cesium atom, improving the precision of the calculations needed to extract a value for the weak nuclear charge that challenges the SM remains an active topic of research [126, 127, 128, 129, 130, 131], with many different atomic observables being used to evaluate the performance of theory.

The case of the recent search for a King-plot nonlinearity in Yb by Hur *et al.* [83] differs from that of APV in Cs, but faces similar limitations. To the second order of the radial moment $\langle r^n \rangle$ expansion, the relationship between the isotope shifts in an electronic transition and the mean-squared nuclear charge radii of the isotopic chain is linear (see Chapter 2).

Deviations from linearity observed with high-precision spectroscopy were recently proposed as a potential pathway to investigate the existence of a boson that does not arise in the SM, and which mediates a new force (sometimes referred to as the "fifth force") between neutrons and electrons. Notably, higher-order symmetry-conserving nuclear effects can also lead to nonlinear contributions to the King plot, thus complicating a possible measurement that proves the existence of such a boson.

Thus, following the first experiment to detect nonlinear contributions to the King plot in Yb^+ [84], Hur *et al.* recently reported evidence of a nonlinear King-plot contribution in Yb^+ and Yb at the 240σ level [83]. In contrast to APV experiments, the King plot experiment is independent of the atomic structure, and thus the need for developing high-precision atomic calculations is evaded. Hur *et al.* could still not conclude on the existence of a new force, however, because of the limitations in nuclear theory. As nuclear theory still cannot predict the SM contributions to the nonlinearity with sufficient accuracy and precision, no conclusions can so far be made on the BSM contributions.

To prevent similar situations of a non-null but inconclusive measurement in the case of RaF, the preparatory spectroscopy that is necessary for designing a future high-precision experimental search should also be used to challenge the predictions of quantum chemistry. Through the systematic comparison between experimental measurements and the predictions of state-of-the-art molecular theory, a deep understanding of the electronic structure of the molecule can be obtained while simultaneously guiding the developments of molecular theory towards greater precision and accuracy.

This chapter presents the analysis and results of a laser-spectroscopic study of excited electronic states in RaF. The work presented in this chapter appears in

- M. Athanasakis-Kaklamanakis, S. G. Wilkins, L. V. Skripnikov, *et al.*, *Pinning down electron correlations in RaF via spectroscopy of excited states*, Under review (2023)

which is included in Section 4.4.

4.1 Experiment

The experimental campaign during which the herein presented data set was gathered was one of the most technically complex CRIS experiments performed, and was planned to simultaneously serve multiple scientific goals. A high-resolution laser system (injection-seeded pulsed Ti:Sa seeded by a continuous-wave Sirah Matisse Ti:Sa) was prepared to perform rotationally and hyperfine-resolved spectroscopy in ^{225,226}RaF, while two pulsed dye lasers (Sirah Cobra and Spectra Physics PDL), two grating Ti:Sa lasers, a frequency-doubled etalon-based Ti:Sa laser, and a second-harmonic (532 nm) Nd:YAG laser were prepared to perform spectroscopy on excited electronic states. Lastly, a grating Ti:Sa laser and two pulsed dye lasers were further used to measure the ionization potential of RaF, which is beyond the scope of this thesis.

Six different laser ionization schemes were prepared to performed the spectroscopy of the excited electronic states. The schemes are shown in Fig. 4.1. All excited states were measured using broadband lasers exciting transitions starting from either the ground state $X\ ^2\Sigma_{1/2}$ $(v = 0, 1)$ or the first excited state $A\ ^2\Pi_{1/2}$ $(v = 0, 1)$. The properties of these states are known to high precision from the high-resolution laser spectroscopy of the $A\ ^2\Pi_{1/2} \leftarrow X\ ^2\Sigma_{1/2}$ transition [2]. Therefore, in each broadband spectrum used to discover new excited electronic states, only the properties of the upper electronic state (hitherto unknown) were varied during the fit (referred to as *floating*).

The properties of the excited electronic states were extracted from the broadband spectra, and are reported in this thesis. In the next section, details on the analysis of the spectra to extract the spectroscopic information of the excited states are given, followed by a summary of the results. An article comparing the excitation energies of the newly discovered states with the predictions of Fock-space relativistic coupled-cluster calculations was written based on the results, which is included at the end of the next section.

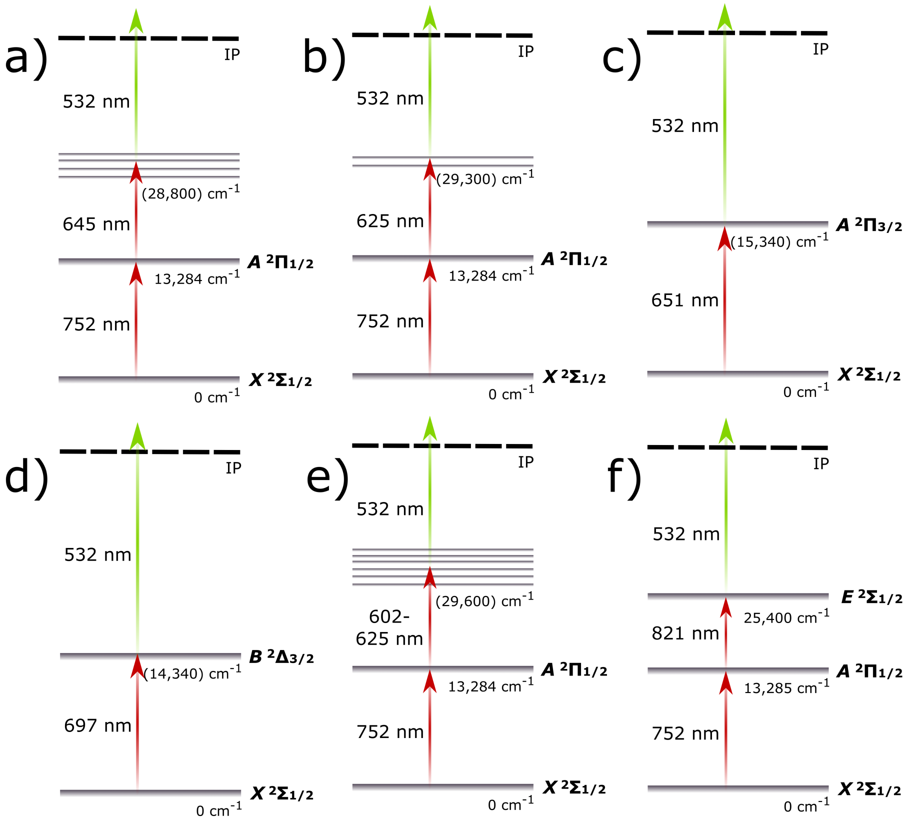

Figure 4.1: Laser schemes used to search for all excited electronic and vibrational states in RaF presented in this chapter.

4.2 Properties of excited electronic states

Due to the linewidth of the scanning lasers, varying between 1 and 10 GHz, the rotational structure of the electronic states could not be resolved, except for some cases where a partial resolution was achieved. As a result, the broadband spectra were analyzed using the contour-fitting routine[1] of the PGOPHER package [132].

---

[1] `http://pgopher.chm.bris.ac.uk/Help/contourfitting.htm`

Contrary to line-fitting routines applied to high-resolution spectra, contour fitting does not attempt to reproduce the frequencies of individual spectral lines, such as rotational lines. For broadband spectra, where individual rotational lines are only poorly distinguished if at all, such routines are not applicable due to the overlapping peaks. Instead, contour fitting attempts to match the shape of the envelope of the overlapping rotational peaks of a simulation to that of the measured structure. As a result, while the molecular parameters that correspond to small corrections to the molecular Hamiltonian cannot be extracted with sufficient precision, the term energy and the rotational constant B of the band can be generally extracted in a satisfactory manner.

4.2.1 Spectrum binning

The data acquisition system at CRIS gathers data from the different hardware components asynchronously. That is, each device records its current value with a certain repetition rate that is independent from that of other devices.

To be able to combine the values of all devices into one data set in a consistent manner, each device also records the timestamp (relative to the beginning of the UNIX epoch) at which each data line is registered. Afterwards, all files from the different devices are combined into one data set according to the respective timestamps (with nanosecond resolution) in a time-sorted manner. Details on the merging of the different files are given in the thesis of Ruben P. de Groote, KU Leuven [133].

In CRIS experiments, the spectra are obtained by scanning the wavelength of the spectroscopy laser while keeping the wavelength of the other lasers in the multi-step scheme fixed. The scanning speed is adapted to the experimental conditions of each study (laser linewidth, desired resolution, ion production rate, and more). In the search for excited electronic states in RaF, where a frequency range of a few thousand cm^{-1} had to be scanned, the scan speed was typically chosen around 1 cm^{-1} per minute. To obtain a histogram of the recorded wavelengths and count rates, the wavelength measurements of the scanning laser have to be digitized into bins. In narrowband spectra aiming to measure the hyperfine structure of short-lived atoms, the choice of bin size is critical, and thus an extensive investigation of the impact of bin size onto the extracted hyperfine constants is needed. In the case of broadband molecular spectra presented here, a bin size of 3 GHz, which is comparable to the laser linewidths, is significantly smaller than the total size of all measured structures and thus does not introduce aberrations in the binned histogram, while it accelerates the fitting procedures. A bin size of 3 GHz was thus used to produce all binned spectra for contour fitting, which was found to be smaller than the uncertainty in the fitted excitation energy in all spectra.

The Python scripts used to import, Doppler-shift, apply a time-of-flight gate to keep only ion counts within the time window of the bunch arriving at CRIS, and bin the data for this thesis can be found in the appendix (Section A).

4.2.2 Molecular Hamiltonian

To perform the contour fit using PGOPHER, different molecular parameters can be floated, that is, allowed to be varied in the error-minimization procedure. Choosing the appropriate molecular parameters to be floated is important: enough parameters should be selected such that the agreement with experiment is satisfactory, but if too many parameters are simultaneously floated, a successful fit can be found that includes unphysical best-fit values for the parameters. Additionally, for the given resolution of the broadband RaF spectra, certain molecular parameters that define slight corrections to the energies of the rotational lines cannot be resolved, and should thus be excluded.

The parameter selection was made based on the Hamiltonian for molecules corresponding to Hund's cases (a) and (b). The $^2\Pi$ and $^2\Delta$ states in RaF behave similarly to the coupling description of Hund's case (a), where the projections of the electronic angular momentum (Λ) about the internuclear axis and the spin angular momentum[2] (Σ) are good quantum numbers. For such states, the origin T_0, the rotational constant B, the centrifugal distortion of the rotational constant D, and the Λ-doubling

---

[2] Not to be confused with Σ states, in which case the Greek letter simply denotes $\Lambda = 0$ where Λ is the orbital angular momentum of the electron about the internuclear axis.

constant p were floated. The spin-orbit coupling constant A could not be resolved as its effect was indistinguishable from that of T_0 for the given resolution, and was thus not floated.

The ${}^2\Sigma_{1/2}$ states behave according to the description of Hund's case (b). In that case, and since for ${}^2\Sigma_{1/2}$ states we have $\Lambda = 0$, the spin-orbit coupling vanishes and instead the spin-rotation coupling is strong. Therefore, for ${}^2\Sigma_{1/2}$ states, the spin-rotation coupling constant γ was floated, while the Λ-doubling constant p was kept to 0, as it applies only to states with $\Lambda > 0$. So, for the ${}^2\Sigma_{1/2}$ states, T_0, B, D, and γ were floated.

4.2.3 Temperature distribution

As contour fitting finds the best-fit molecular parameters by matching the overall shapes of the simulation and the measurement, it is a useful tool to extract the temperature distribution(s) of the studied ensemble. That is because the shape of a measured molecular band corresponds to the relative intensities of the underlying unresolved rotational lines, which is the main probe to extract the temperature distribution of the ensemble [134].

All obtained spectra were measured starting from either the electronic ground state $X\ {}^2\Sigma_{1/2}$ or the first excited state $A\ {}^2\Pi_{1/2}$. For the transitions from the ground state, the spectroscopy was performed on the molecular beam with the population distribution that is directly delivered by the ISOLDE cooler-buncher. On the contrary, for the transitions starting from the $A\ {}^2\Pi_{1/2}$ state, the spectroscopy step is preceded by another resonant transition, for example the $v' = 0 \leftarrow v'' = 0$ vibrational band of the $A\ {}^2\Pi_{1/2} \leftarrow X\ {}^2\Sigma_{1/2}$ electronic transition, centered around the Q branch. Therefore, for the high-lying states presented in this chapter, which were measured starting from the $A\ {}^2\Pi_{1/2}$ state, all molecules probed by the spectroscopy (scanning) laser were initially found at a single vibrational state and had low J values.

Although the ISOLDE cooler-buncher nominally cools the beam at room temperature with a uniform distribution [114], the measured spectra for the transitions from the ground state revealed that the delivered beam was significantly non-uniform, requiring the consideration of multiple temperature subgroups within the ensemble to achieve good agreement with the experiment. The non-uniform temperature distribution was included in the PGOPHER contour fitting in this doctoral work using the Custom Population Function[3] option.

The internal temperature of a molecular ensemble manifests in the relative population of rotational states within each electronic-vibrational band. Therefore, the temperature distribution can be modelled as a distribution function of molecules across states with different J values. In the present analysis, each temperature subgroup was modelled as a symmetric Gaussian distribution centered around a J value (J_c):

$$g_J = e^{-b(J-J_c)^2} \tag{4.1}$$

where b is a factor describing the width of the distribution. The value of J_c defines the nominal temperature assigned to the distribution, as J_c can be linked to the rotational temperature of the ensemble as:

$$J_c = \sqrt{\frac{kT}{2hcB}} - \frac{1}{2} \tag{4.2}$$

where h is Planck's constant, c is the speed of light, B is the rotational constant of the electronic-vibrational state, k is the Boltzmann constant, and T is the ensemble temperature. The $\frac{1}{2}$ term is present in the cases of strong spin-rotation coupling, such as states corresponding to Hund's case (b).

Therefore, Eq. 4.1 can be expressed as:

$$g_J = e^{-b(J-\sqrt{\frac{kT}{2hcB}}+\frac{1}{2})^2} \tag{4.3}$$

For a non-uniform ensemble, that is, an ensemble that contains more than 1 temperature groups, the intensity of each temperature group must be normalized with respect to the total number of molecules in the ensemble. The normalization condition can be expressed as the sum of

---

[3] `http://pgopher.chm.bris.ac.uk/Help/custompopulationfunction.htm`

all intensities across all temperature groups g_J^i equaling N_{mol}:

$$\sum_{i=1}^{i_{\max}} \sum_{J=1}^{J_{\max}} g_J^i = N_{\mathrm{mol}} \tag{4.4}$$

where the sum across J is not expressed as an integral because g_J is a discrete function.

This condition gives rise to a normalization factor A^i for each g_J^i population distribution, equal to

$$A^i = \frac{\sum_{J=1}^{J_{\max}} g_J^i}{\sum_{i=1}^{i_{\max}} \sum_{J=1}^{J_{\max}} g_J^i} = \frac{\sum_{J=1}^{J_{\max}} g_J^i}{N_{\mathrm{mol}}} \tag{4.5}$$

Therefore, the normalized distribution function g_J^* can be written as:

$$g_J^* = A^i e^{-b^i (J - \sqrt{\frac{kT}{2hcB}} + \frac{1}{2})^2} \tag{4.6}$$

Broadband molecular spectroscopy allows us to extract the number $i_{\max}$ of distinct rotational distribution functions (that is, ensemble temperature groups) in the molecular beam, the average temperature of each group T^i, and the relative fraction of each group A^i.

The choice of Gaussian temperature profiles is not typical, as Boltzmann profiles would be a more natural choice for the rotational-state distribution of buffer-gas-cooled diatomic molecules. The choice for Gaussian over Boltzmann profiles is supported by the observed behavior of second-step scans, as shown in Fig. 4.2. While in such spectra the beam has been resonantly excited by a preceding excitation step, fitting the experimental spectrum requires the use of a Gaussian rotational-state distribution over a Boltzmann one (see Fig. 4.2). When fitting the experimental spectra of first-step scans, a lower reduced chi-squared was also obtained when using Gaussian over Boltzmann profiles.

It is unclear what physical mechanism promotes a Gaussian-type distribution following buffer-gas cooling in the RFQcb over a Boltzmann distribution, and further systematic tests are needed at ISOLDE to understand these mechanisms. The current analysis is the first of such kind at ISOLDE, and it is by no means complete or its results are

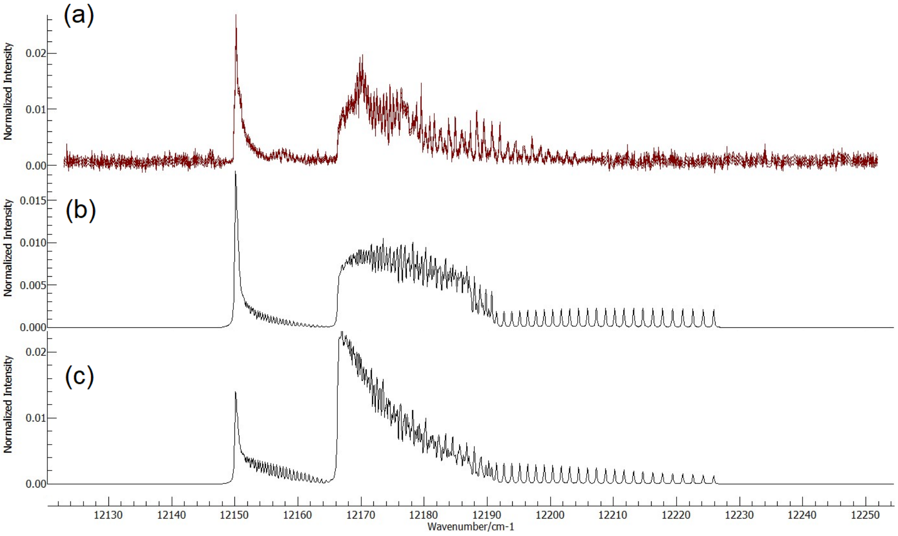

Figure 4.2: Comparison of Gaussian and Boltzmann profiles for the rotational-state distribution in RaF, using a second-step scan as an example ($E\ ^2\Sigma_{1/2} \leftarrow A\ ^2\Pi_{1/2}$). **(a)** Experimental spectrum. **(b)** Best-fit simulation using a uniform Gaussian rotational-state distribution at room temperature ($J_c = 22.5$). **(c)** Simulation using the best-fit molecular parameters from (b), but substituting the Gaussian room-temperature distribution for a uniform Boltzmann distribution at 300 K.

absolute. Further systematic work is necessary in order to shed light on the realistic distribution of rotational states in molecules cooled at the ISCOOL RFQcb.

4.2.4 Uncertainty estimation

The results of the contour fitting routine of PGOPHER automatically return the reduced chi $\sqrt{\chi_r^2}$ of the fit, the standard deviation in each fitted parameter σ, and the correlation matrix for the fitted parameters C. To account for the dispersion in the data set, the standard deviation of each fitted parameter was scaled by the reduced chi χ_r of the fit to arrive at the uncertainties reported here.

Due to the way that the contour-fitting algorithm of PGOPHER works, the user guide [132] warns that the fitting routine cannot shift the position of a simulated peak by more than the user-set linewidth [132]. As a consequence of this algorithmic limitation, the contour-fitting routine is prone to converging to local (and not global) minima in error minimization.

To provide at least a basic account of the propensity of the fitting algorithm to converge to local minima, a systematic uncertainty has to be set. In the present case, the Voigt linewidth for each spectrum was chosen as a systematic uncertainty for the corresponding excitation energy. The Voigt linewidth for each spectrum was chosen manually to best match the observed structure and varied between 0.26 and 0.51 cm^{-1}.

Systematic uncertainties stemming from the wavelength meter, Stark shifts due to the high-power 3-step laser scheme, and an imperfect calibration of the voltage meter contribute to a total of less than ± 0.02 cm^{-1}, as outlined in the high-resolution study of ^{226}RaF [2], and are included in the total systematic uncertainty.

4.2.5 Results and discussion

The fitted molecular parameters of the excited states in RaF are given in Table 4.1 and the experimental and fitted spectra are shown in Appendix B. While the transition energies between the upper and lower states in each broadband spectrum could be reliably extracted from the contour fits, the fitted values of B, γ, p, and D are strongly dependent on the initial parameters used in the simulated spectrum. Consequently, rigorous conclusions on the structure of RaF should be drawn only with respect to the excitation energies of the measured states. For the states where no value is given for D, a value that is not consistent with 0 could not be determined from the fit.

As seen on Table 4.1, the majority of the newly discovered states could be firmly assigned, thanks to highly precise and accurate predictions of *ab initio* molecular theory. The unassigned states likely correspond to higher vibrational substates of not yet discovered electronic states. Assigning these states requires more precise knowledge of their molecular parameters, since γ, p, and D are expected to vary only slightly between vibrational substates of the same electronic state. Therefore, such conclusions on vibrational assignments are not widely feasible in the present study.

Some states assigned as higher vibrational states of an electronic state were measured while scanning the second step in a three-step scheme, while the first step was exciting molecules to the $v = 1$ vibrational state of $A\ ^2\Pi_{1/2}$, which enabled observing $v' = 0, 1, 2 \leftarrow v'' = 1$ transitions. The $G\ ^2\Pi_{1/2}$ $v = 2$ vibrational state was extracted from the $v' = 2 \leftarrow v'' = 0$ transition from the $A\ ^2\Pi_{1/2}$ state.

The spectra from the $A\ ^2\Pi_{1/2}$ (0) state to the $G\ ^2\Pi_{1/2}$ (0) and $E\ ^2\Sigma_{1/2}$ (0) states were resolved well enough to permit a direct line fitting of the R-branch peaks, and the results were consistent with those from contour fitting.

The fitted spectra can be found in Appendix B. A detailed explanation on the decision-making behind the assignment of each state can be found in the Supplemental Information of Article 2, and thus it is repeated here.

In addition to the new states presented in this thesis, Table 4.1 includes information on vibrational substates of the $X\ ^2\Sigma_{1/2}$ and $A\ ^2\Pi_{1/2}$ electronic states that can be extracted from the previously reported results in Refs. [5, 2]. The excitation energies for the $v > 0$ substates are extracted from the difference in reported transition wavenumbers between diagonal and non-diagonal transitions. For instance, the excitation energy of the $X\ ^2\Sigma_{1/2}$ (1) state is extracted by the difference of the $0 \leftarrow 0$ and $0 \leftarrow 1$ transitions between the two electronic states.

Notably, a similar approach was used for the re-assigned excitation energy of the $C\ ^2\Sigma_{1/2}$ (0) state. While new spectra were obtained in this experiment for both the $0 \leftarrow 0$ and $0 \leftarrow 1$ transitions from the ground state, the non-uniform temperature distribution of the molecular ensemble delivered by the ISCOOL RFQcb severely complicated the fitting of these spectra for the assignment of the $C\ ^2\Sigma_{1/2}$ (0) state. Specifically, the fitted γ parameter for the $C\ ^2\Sigma_{1/2}$ (0) state is unphysically high, more than two orders of magnitude higher than expected. Therefore, the new assignment is performed using the reported transition energies from

Ref. [5] by re-interpreting the $C\ ^2\Sigma_{1/2} \leftarrow X\ ^2\Sigma_{1/2}$ (0←0) transition as (0←1) instead, and thus adding the excitation energy of the $X\ ^2\Sigma_{1/2}$ (1) state to it to yield the excitation energy of $C\ ^2\Sigma_{1/2}$ (0).

	E (cm^{-1})	B (cm^{-1})	γ (cm^{-1})	p (cm^{-1})	D (cm^{-1})
$X\ ^2\Sigma_{1/2}$* (0)	0	0.191985(5)[15]	0.00585(3)[7]		1.40(5)[10]e-7
$X\ ^2\Sigma_{1/2}$* (1)	438.4(11)	0.19092(4)[6]	0.00581(5)[15]		1.2(3)[4]e-7
$X\ ^2\Sigma_{1/2}$* (2)	873.8(16)				
$A\ ^2\Pi_{1/2}$* (0)	13,284.427(1)[22]	0.191015(5)[15]		-0.41071(3)[7]	1.40(5)[10]e-7
$A\ ^2\Pi_{1/2}$* (1)	13,716.9(5)	0.18997(4)[6]		-0.40978(10)[20]	1.5(3)[4]e-7
$A\ ^2\Pi_{1/2}$* (2)	14,145.8(12)				
$B\ ^2\Delta_{3/2}$ (0)	14,332.82(13)[51]	0.19231(9)			1.07(2)e-6
($B\ ^2\Delta_{5/2}$)** (0)	15,142.7(5)				
$A\ ^2\Pi_{3/2}$ (0)	15,334.52(23)[35]	0.19251(9)			1.49(7)e-9
$C\ ^2\Sigma_{1/2}$** (0)	16,613.6(12)				
$E\ ^2\Sigma_{1/2}$ (0)	25,451.11(11)[26]	0.19974(14)	0.0691(11)		5(5)e-8
$E\ ^2\Sigma_{1/2}$ (1)	25,929.13(12)[26]	0.19937(19)	0.0763(11)		1.5(7)e-8
$G\ ^2\Pi_{1/2}$ (0)	28,774.16(51)[35]	0.20038(110)		-0.3599(209)	
$G\ ^2\Pi_{1/2}$ (1)	29,270.32(32)[35]	0.19713(59)		-0.3676(151)	
$G\ ^2\Pi_{1/2}$ (2)	29,754.48(72)[35]	0.19806(185)		-0.3380(185)	
$G\ ^2\Pi_{3/2}$ (0)	29,225.57(28)[51]	0.20228(68)			8.8(41)e-7
$G\ ^2\Pi_{3/2}$ (1)	29,717.15(24)[51]	0.20178(43)			9.4(22)e-7
($H\ ^2\Sigma_{1/2}$) (0)	29,665.52(11)[51]	0.21076(35)	0.0608(22)		
($I\ ^2\Delta_{3/2}$) (0)	29,693.15(24)[51]	0.20442(94)		-1.2(3)e-4	6.5(7)e-6
$I\ ^2\Delta_{5/2}$ (0)	29,801.59(7)[35]	0.20263(12)			8.95(7)e-8
? ($^2\Sigma_{1/2}$) (?)	29,268.38(86)[26]	0.21619(524)			4(7)e-6
? ($^2\Pi_{1/2}$) (?)	29,649.53(7)[35]	0.20147(9)			

* Molecular constants taken from Ref. [2]. Excitation energies extracted from values in Ref. [5].
** Taken from Ref. [5]. Reassigned in this work, based on more accurate calculations and new measurements (see Article 2 in Section 4.4).

Table 4.1: Molecular parameters of excited states in RaF measured with broadband laser spectroscopy. The deduced vibrational quantum number v of the excited state is given in parenthesis in the first column. Some states could not be firmly assigned, and thus their term label is preceded by '?'. Statistical uncertainties are given in round brackets and represent 1 reduced-chi-scaled standard deviation. Systematic uncertainties are in given in square brackets.

The comparison between the experimentally measured excitation energies and the quantum-chemistry predictions that guided the assignment of states in Table 4.1 is the topic of Article 1, and thus will not be further discussed in this chapter. However, it is worthwhile to highlight the accuracy of the predicted excitation energies that guided our assignment.

The comparison between experiment and theory is shown in Table 4.2, which appears as Table 1 in Article 1. Evidently, the level of agreement between experiment and theory is exceptionally high, reaching the part-per-ten-thousand level for the ($H\ ^2\Sigma_{1/2}$) state, which is unprecedented for *ab initio* calculations of relativistic molecules. Therefore, adopting the present assignment is justified.

In addition to presenting for the first time several newly discovered high-lying states, the present work also corrects the previous assignment of low-lying states in RaF. The changes in the low-lying assignment compared to that shown in Ref. [5] is shown in Table 4.3. For the $C\ ^2\Sigma_{1/2}$ state, the previous assignment was based on a transition from the ground state that was measured at 16,175.2(5) cm^{-1}, that was interpreted as $C\ ^2\Sigma_{1/2} \leftarrow X\ ^2\Sigma_{1/2}$ ($v' = 0 \leftarrow v'' = 0$). In the 2021 experiment, a transition at ~16,610 cm^{-1} from the $X\ ^2\Sigma_{1/2}$ $v = 0$ state was measured, whose spectrum had the same profile and twice the intensity of the spectrum that was previously assigned to the $C\ ^2\Sigma_{1/2} \leftarrow X\ ^2\Sigma_{1/2}$ ($v' = 0 \leftarrow v'' = 0$) transition. The higher intensity and similar spectral profile indicate that the new measurement in fact corresponds to the $v' = 0 \leftarrow v'' = 0$ transition, while the previously measured transition corresponds to the $v' = 0 \leftarrow v'' = 1$ line instead. Therefore, it is now determined that the $C\ ^2\Sigma_{1/2} \leftarrow X\ ^2\Sigma_{1/2}$ ($v' = 0 \leftarrow v'' = 0$) transition corresponds to the newly measured resonance at 16,613.6(12) cm^{-1}.

Moreover, a new transition was found at 14,332.82 cm^{-1} from $X\ ^2\Sigma_{1/2}$ $v' = 0$. The energy of the upper state is in good agreement with the prediction for the $B\ ^2\Delta_{3/2}$ state, while the previous assignment for $B\ ^2\Delta_{3/2}$ at 15,142.7(5) cm^{-1} agrees well with the prediction for the $B\ ^2\Delta_{5/2}$ state instead. As a result, here we adopt a new assignment for the $B\ ^2\Delta_{3/2}$ state at 14,332.82(13)[51] cm^{-1} according to the new measurement, and we tentatively assign the $B\ ^2\Delta_{5/2}$ at 15,142.7(5) cm^{-1}. The assignment is tentative because the $B\ ^2\Delta_{5/2} \leftarrow X\ ^2\Sigma_{1/2}$ is strongly forbidden, and it is unclear what the expected spectral intensity of such a forbidden transition can be at the CRIS experiment.

Temperature distribution from the RFQcb

The spectral properties of the $A\ ^2\Pi_{1/2}$ (not included in Table 4.1, as the values from Ref. [2] are quoted in the table instead), $A\ ^2\Pi_{3/2}$, $B\ ^2\Delta_{3/2}$, and $C\ ^2\Sigma_{1/2}$ states were extracted from spectra where the lower molecular state was the $X\ ^2\Sigma_{1/2}$ ground state. As a result, the measured spectra hold information about the temperature uniformity of the molecular beam delivered to the CRIS experiment by the ISCOOL RFQcb that cools and bunches the continuous ion stream.

The information on the temperature distribution of the beam can be modeled through a summation of Gaussian rotational-state population groups, as explained in Section 4.2.3. The fitted temperature-distribution parameters for the scans giving rise to the low-lying states in this thesis are shown in Table 4.4.

The distribution of the RaF beam into multiple different temperature groups is visualized in Figs. 4.4-4.7. Evidently, a drastic change in the performance of the ISCOOL RFQcb at cooling the molecular beam to room temperature ($\sim$300 K) occurred at some point between scans 3818 and 4243. While multiple ensembles with different average temperatures comprised the delivered molecular beam before scan 4243, the average temperature for scans 3804 and 3808-3813 remained consistently between room temperature and 400 K, while for scans 4243-4244 the average temperature was above 800 K.

The change in the cooling performance of the RFQcb likely stems from a re-tuning of the trap electrodes in an attempt to improve the shape of the time-of-flight (tof) profile of the beam.

In Fig. 4.3, the tof profile of the resonantly ionized RaF molecules arriving at the CRIS ion detector is shown for two scans: scan 3745, where the beam appears to be uniformly in a single temperature group at 380 K, and scan 4243 where the beam contained five distinct temperature groups with an average temperature of 820 K. The ideal shape of the tof profile for CRIS experiments is a Gaussian curve with a FWHM of 2 μs or less, such that the spatial spread of the ion bunch is smaller than the interaction region of the CRIS beamline. In scan 3745 (left of Fig. 4.3), the tof profile does not resemble a Gaussian distribution and has a very wide structure, resulting in only a fraction of the beam fitting into the CRIS interaction region.

Consequently, the voltage of the trapping electrodes in the ISCOOL RFQcb was re-tuned in the course of the experiment, in order to provide a narrower structure with a Gaussian profile. A typical example of the resulting tof profile can be seen on the right of Fig. 4.3, where only a minor fraction of the tof profile is abruptly cut due to not fitting in the interaction region. As seen in Table 4.4, however, the better tof profile was accompanied by significantly worse cooling performance for the RFQcb. **Therefore, the profile of the observed tof structure does not reflect a successfully thermalized ensemble, despite its appearance as a Gaussian-like profile.** Broadband molecular spectroscopy with the CRIS experiment can therefore also function as a powerful diagnostic tool for the performance of the ISCOOL RFQcb at ISOLDE.

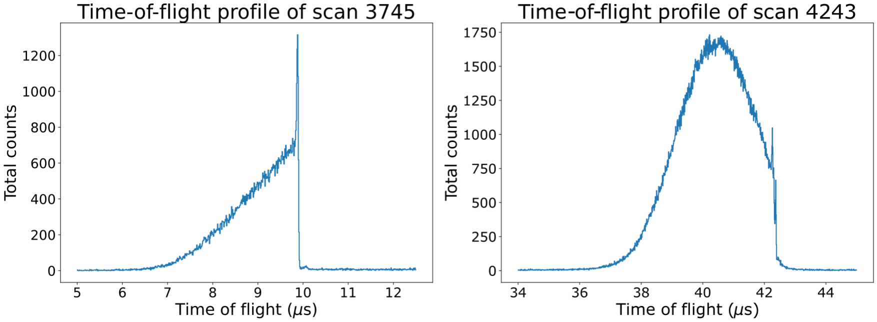

Figure 4.3: Time-of-flight profiles of resonantly ionized RaF at CRIS.

It is important to note that even when the weighted-average temperature of the beam is close to room temperature, the presence of multiple temperature groups significantly complicates the fitting procedure of the broadband spectrum, such as in the case of scans 3808-3813, where a spectrum of the $A\ ^2\Pi_{3/2} \leftarrow X\ ^2\Sigma_{1/2}$ transition was obtained.

Fig. 4.8 shows the fit of the measured spectrum used to extract the molecular parameters of the $A\ ^2\Pi_{3/2}$ state using multiple temperature groups, as well as simulations of the spectrum using the fitted molecular parameters but assuming a uniform temperature distribution at 300 K and 329 K. Evidently, no significant difference can be discerned between the spectrum of a beam at 300 K and that at 329 K (Fig. 4.8b). However, when the weighted-average temperature of the beam is at 329 K but the molecules are in a non-uniform distribution of temperature

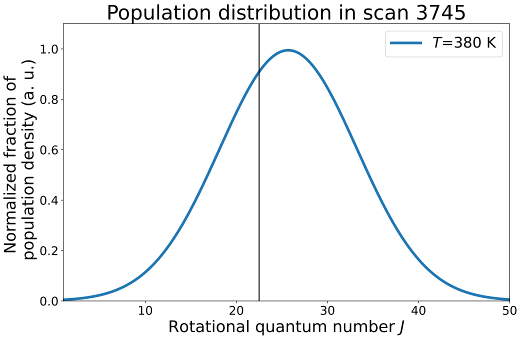

Figure 4.4: Visual representation of rotational population distributions (temperature groups) for scan 3745. The vertical line denotes the value of J that corresponds to room temperature.

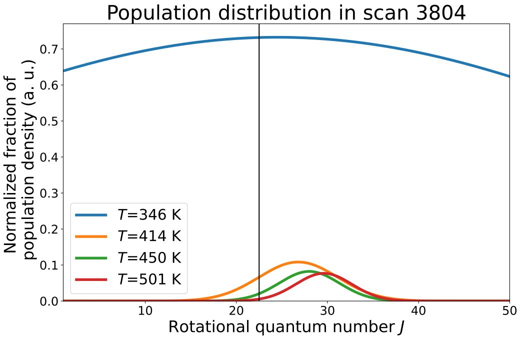

Figure 4.5: Visual representation of rotational population distributions (temperature groups) for scan 3804. The vertical line denotes the value of J that corresponds to room temperature.

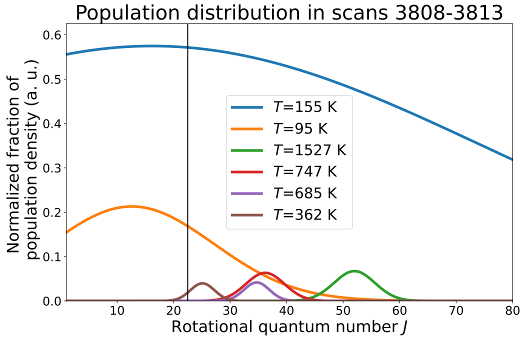

Figure 4.6: Visual representation of rotational population distributions (temperature groups) for scans 3808-3813. The vertical line denotes the value of J that corresponds to room temperature.

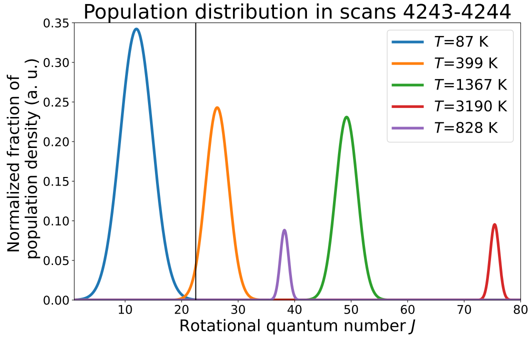

Figure 4.7: Visual representation of rotational population distributions (temperature groups) for scans 4243-4244. The vertical line denotes the value of J that corresponds to room temperature.

sub-groups (Fig. 4.8a), the observed spectrum changes drastically, including an apparent shift in the center of the structure. Fitting such deformed and shifted structure is challenging and introduces statistical and systematic errors. Therefore, it is crucial that cooler-bunchers involved in the spectroscopy of radioactive molecules, such as the ISCOOL RFQcb for CRIS experiments, are well-tuned to produce narrow and thermalized bunches of Gaussian profiles with the beam occupying uniform distributions centered at room-temperature.

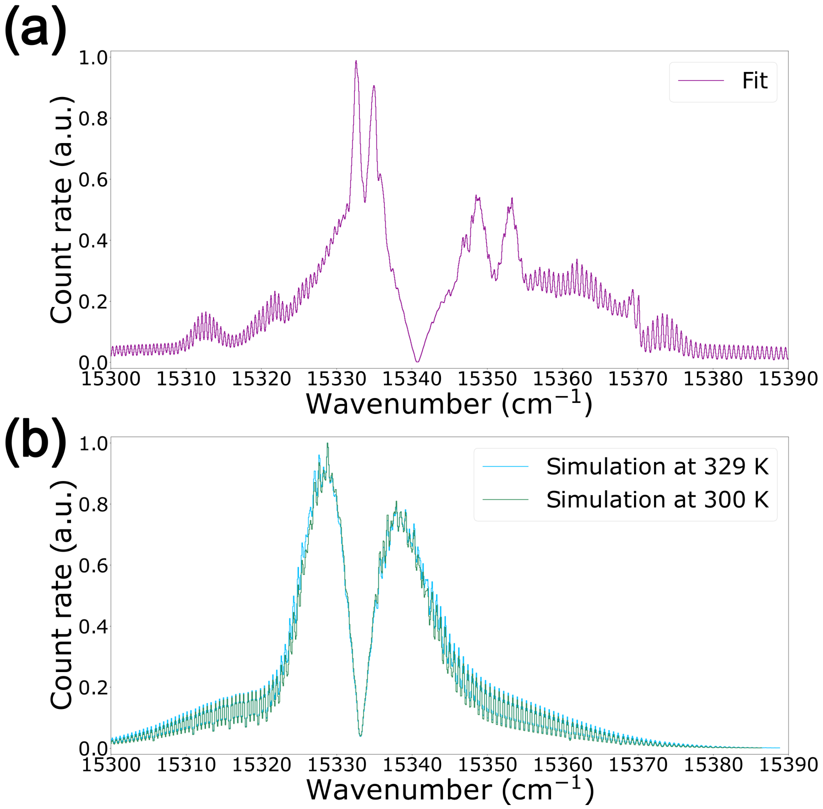

Figure 4.8: **(a)** Simulations of the measured $A\ ^2\Pi_{3/2} \leftarrow X\ ^2\Sigma_{1/2}$ spectrum using the best-fit molecular parameters, containing a non-uniform temperature distribution in the beam. **(b)** Simulations of the $A\ ^2\Pi_{3/2} \leftarrow X\ ^2\Sigma_{1/2}$ spectrum using the fitted parameters but assuming a uniform temperature distribution centered at 300 K and 329 K.

Considerations for the A $^2\Pi_{1/2}$ state

Owing to the nature of the three-step laser schemes used in this study, the $A\ ^2\Pi_{1/2} \leftarrow X\ ^2\Sigma_{1/2}$ transition is the only one that was measured with a laser step that was not immediately followed by non-resonant ionization. Instead, following the scanning step of the $A\ ^2\Pi_{1/2} \leftarrow X\ ^2\Sigma_{1/2}$ transition, a second resonant transition exciting to the $G\ ^2\Pi_{1/2}$ (0) state was used, finally followed by a non-resonant step at 532 nm.

Contrary to non-resonant laser ionization, every resonant optical transition is associated with a range of J values that it excites and allows for subsequent excitation. This characteristic J selectivity emerges due to the dipole-allowed rules for rotational transitions, and the width of the J-selective range of the resonant step is defined by the linewidth of the laser employed. A laser with a linewidth of many inverse centimeters could likely excite molecules found in the whole range of J values. However, the lasers available at CRIS at the time of this study had linewidths of 10 GHz or less.

As a result of this double J selectivity (a separate J range allowed by each of the two laser steps), special care needs to be taken when fitting and interpreting spectra obtained with three-step schemes. As an extreme case, a situation can be considered where the first laser step is at a frequency that excites molecules (from a uniform distribution) in rotational states with J in the range 10 to 20, while the following laser step is kept at a frequency that corresponds to transitions from rotational states with J in the range 30 to 40.

In that case, no molecule that is successfully excited by the first laser step will also be excited by the second step, and vice versa. Consequently, no resonantly ionized molecules will be counted on the ion detector, despite both laser steps being on resonance with *some* rotational lines between the lower and upper electronic states.

When one of the two laser steps is scanned, the obtained spectrum will have a distorted shape: the parts of the P, Q, and R branches whose J numbers are within the allowed range of the following laser step will be much stronger in intensity than all other parts of the spectral range.

To obtain accurate results when fitting such spectra, the effect of double J

selectivity has to be accounted for. During contour fitting with PGOPHER, this effect can be included in two ways.

Firstly, a J range that the upper electronic state is allowed to take can be explicitly defined, directly simulating the effect of double J selectivity.

Secondly, as this effect is akin to the beam being found in a non-uniform rotational-state distribution, where molecules are initially found predominantly in the J range that the non-scanning laser excites, it can theoretically be accounted for by introducing distinct temperature groups in the contour fitting.

To compare the accuracy of the two approaches, the broadband spectrum of the $A\ ^2\Pi_{1/2} \leftarrow X\ ^2\Sigma_{1/2}$ transition was fitted using both ways. This transition is suitable for such tests, as it has been measured with narrowband spectroscopy as well [2], obtaining results that are fully independent from the temperature uniformity of the molecular beam.

The results of the two approaches attempting to account for the double J selectivity of the three-step laser scheme are shown in Fig. 4.9, where they are compared with the molecular parameters extracted from narrowband spectroscopy [2].

The results for the restricted J range (blue points in Fig. 4.9) were obtained by assuming a uniform molecular beam at room temperature, but allowing the molecules to only obtain J values between 9 and 30. This range was determined by the wavelength that the second step was fixed at during the scan of the first step, which was compared with the best-fit simulation of the corresponding second excited state. From the simulated structure of the $G\ ^2\Pi_{1/2} \leftarrow A\ ^2\Pi_{1/2}$ transition, it was determined that the second step was inducing J-selectivity for the J = 9-30 range.

The results for the full J range (red points in Fig. 4.9) were obtained by allowing the molecules to obtain all J values, but simulating the molecular beam in terms of Gaussian temperature distribution groups. Two Gaussian distributions were floated, yielding the results shown for scan 3745 in Table 4.4, where the fraction of one distribution was consistent with zero. Evidently, the results obtained with an unrestricted J range are in better agreement with narrowband spectroscopy.

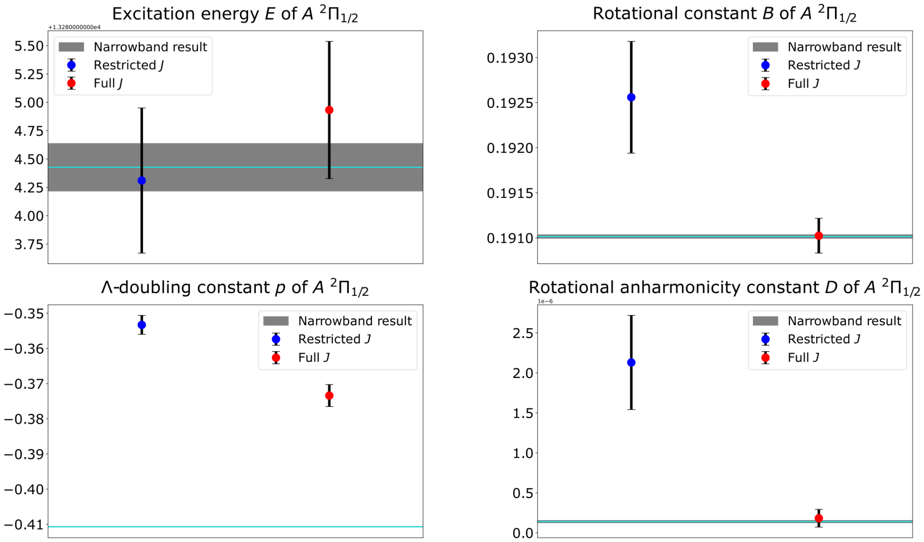

Figure 4.9: Comparison of fitted molecular parameters of the $A\ ^2\Pi_{1/2}$ state from broadband and narrowband [2] spectroscopy. The effect of the three-step laser scheme on the broadband results was simulated using (a) a restricted J range that the $A\ ^2\Pi_{1/2}$ could have and (b) no restriction on the J range but a simulated non-uniform temperature distribution.

A complementary analysis of this data set can be found in the Master's thesis of C. M. Fajardo Zambrano [135].

4.3 Lifetime of the $A\ ^2\Pi_{1/2}$ state

The lifetime of the upper electronic state ($A\ ^2\Pi_{1/2}$) in the proposed $A\ ^2\Pi_{1/2} \leftarrow X\ ^2\Sigma_{1/2}$ laser-cooling transition in RaF is of high importance, as it quantifies the total time required for the laser-cooled ensemble to reach the Doppler temperature limit. When the transition is used for one- or two-dimensional laser slowing, the lifetime of the upper state determines the distance required to bring a molecular beam to rest [14].

In this thesis, information on the lifetime of the $A\ ^2\Pi_{1/2}$ state was acquired using a three-step scheme by measuring the resonant ion count rate as a function of the delay of the second and third laser pulses (ionizing steps) with respect to the first laser pulse (excitation step), which was driving the $A\ ^2\Pi_{1/2} \leftarrow X\ ^2\Sigma_{1/2}$ transition.

The measurements were performed with the three-step laser scheme that was also used for the isotope-shift measurements (Chapter 5), shown in Fig. 4.1a. The three laser pulses were initially overlapped in time according to their rising edge, determining the 0-ns delay point in the measurement. The pulse length of the first laser is approximately 50 ns, while that of the second and third lasers is approximately 20 ns.

The laser timing was controlled using different channels of a low-jitter ($\sim$200 ps) 9520 Quantum Composer. The timing of the third laser step was referenced with respect to that of the second step. Therefore, by changing the delay of the second step with respect to the first, the pulses of the second and third steps remained overlapped in time throughout the measurement.

For each chosen delay value, the ion counts were recorded for a total of 60 seconds. The count rate for each delay value was determined by fitting the 60-s count rate window with a constant function, retrieving the best fit and standard deviation for the constant value. The resulting curve of ion rate against delay is shown in Fig. 4.10. It must be noted at this point that the x-axis values in Fig. 4.10 should be considered with a large systematic offset, since the the 0-ns delay point was determined imprecisely. The relative difference in delay between the data points, however, is precise, as it was determined using the Quantum Composer, which has 0.2-ns resolution.

As the laser steps are kept on resonance, if the delay of the ionizing steps is increased with respect to the excitation step, the average number of molecules available for ionization from the $A\ ^2\Pi_{1/2}$ state without de-exciting to the ground state decreases due to spontaneous radiative decay. By fitting a decay function to the curve of ion count rate against relative delay, we can thus extract the radiative lifetime of the $A\ ^2\Pi_{1/2}$ state.

Typically, the pulsed time structure of the lasers needs to be taken into account in the fit, so that population gain is also modeled during the

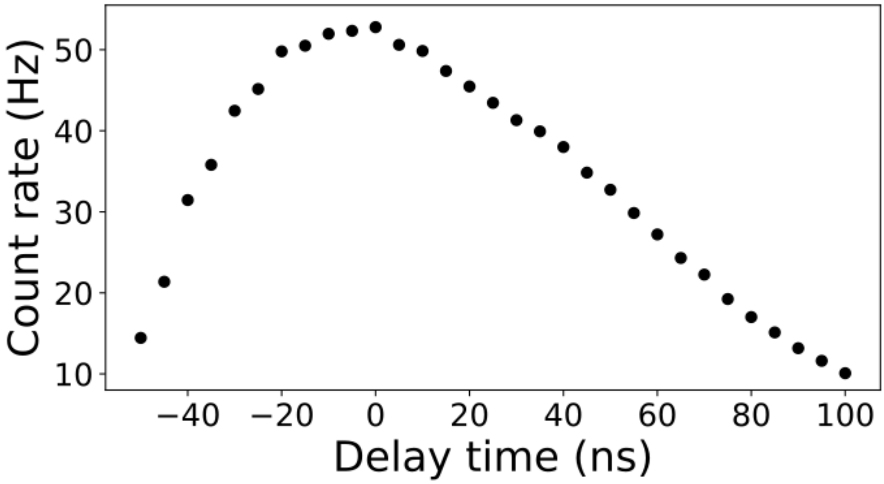

Figure 4.10: Ion count rate as a function of the time delay between the ionization and excitation steps in RaF. The point of 0-ns delay was determined by overlapping in time the rising edge of all laser pulses.

excitation pulse, as the excitation laser continuously drives molecules to the excited state. Once the excitation pulse ends, the population gain in the excited state stops while the population loss continues. Here, we can consider only data points that were recorded when the ionizing steps interacted with the molecules after the excitation pulse had fully ended, eliminating the need for a more complex function that includes population gain.

In this case, the selection of data points for analysis can be performed without precise knowledge of the excitation pulse length. When only population loss is considered, the ion count rate N as a function of the delay t between ionizing and excitation steps follows the exponential decay law

$$N(t) = N_0 e^{-t/\tau} \tag{4.7}$$

where N_0 is the ion count rate at the end of the excitation pulse and τ is the radiative lifetime of the $A\ ^2\Pi_{1/2}$ state. When the natural logarithm is taken on both sides of Eq. 4.7, a function that is linear with respect

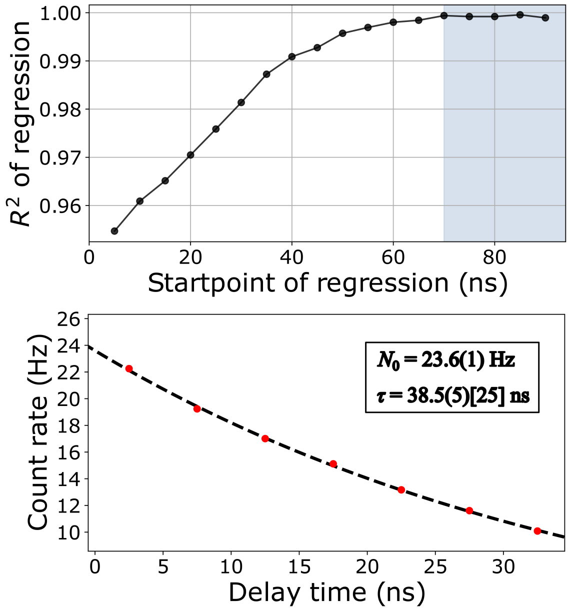

Figure 4.11: Top: R^2 of linear regression of increasingly larger subsets of the natural logarithm of the data set shown in Fig. 4.10. The x-axis here denotes the start point of the subset in question. Bottom: Fitted decay law (eq. 4.7) on the data points identified by the grey band in the top figure and putting time zero at the start of that section.

to the relative laser delay t is obtained

$$\ln N(t) = \ln N_0 - \frac{1}{\tau} t \tag{4.8}$$

Before the excitation pulse has fully ended, the continuous pumping into the $A\ ^2\Pi_{1/2}$ state results in a function $N(t)$ of a different form than Eq. 4.7, whose natural logarithm is in turn non-linear with t. Consequently, we can identify the point when the ionizing lasers interact with the molecules immediately after the excitation pulse has ended by finding the point where a linear regression with the natural logarithm of the data produces a maximal R^2.

The analysis for this part of the investigation was done by taking increasingly bigger slices of the data set and performing a linear regression on their natural logarithm, beginning with the last data points in Fig. 4.10. It is expected that the final data points in the lifetime curve (Fig. 4.10) take place in the regime where the excitation pulse has already ended, and therefore their natural logarithm follows the linear trend of Eq. 4.8. By gradually including earlier data points in the data subset and performing a linear regression, it is expected that the resulting R^2 will begin decreasing at the point when the ionizing steps begin overlapping with the excitation step, leading to a non-linear expression with a sub-optimal R^2.

The results of this analysis are shown at the top of Fig. 4.11. The x-axis denotes the data point of Fig. 4.10 where the subset used in the linear regression started. Evidently, the data points from Fig. 4.10 that have a delay from 70 ns to 100 ns follow a fully linear trend when expressed in their natural logarithm. Including data points at 65 ns and earlier leads to a gradually decreasing R^2, indicating that the excitation and ionizing lasers are at least partially overlapping at those points, and so these points are not included in the decay curve fit.

Consequently, only the data points from Fig. 4.10 with a delay of 70 ns up to 100 ns are included in the lifetime fit, and the delay axis is offset such that the data point that was prior assigned at 70 ns becomes the 2.5-ns point, and the prior point at 100 ns point is now at 32.5 ns. The additional offset of 2.5-ns accounts for the limited step size in the delay of the measurements and the consideration that the start of the linear regime at the top of Fig. 4.11 might lie between 65 and 70 ns, rather than exactly at 70 ns.

Fitting a curve of the form of Eq. 4.7 gives $N_0 = 23.6(1)$ Hz and $\tau = 38.5(5)[25]$ ns. A systematic uncertainty of 2.5 ns has been added, which corresponds to half the delay step size of the measurements.

The lifetime of the $A\ ^2\Pi_{1/2}$ state is in agreement with the previous estimate of an upper bound of 50 ns [5] and confirms the fast photon scattering of the transition.

4.4 Article 2: Pinning down electron correlations in RaF via spectroscopy of excited states

Pinning down electron correlations in RaF via spectroscopy of excited states

M. Athanasakis-Kaklamanakis[1,2,*] S. G. Wilkins[3,4,†] L. V. Skripnikov[5,‡] Á. Koszorús[1,2] A. A. Breier[6] M. Au[7,8] I. Belošević[9] R. Berger[10] M. L. Bissell[11] A. Borschevsky[12] A. Brinson[3] K. Chrysalidis[7] T. E. Cocolios[2] R. P. de Groote[2] A. Dorne[2] C. M. Fajardo-Zambrano[2] R. W. Field[13] K. T. Flanagan[11,14] S. Franchoo[15,16] R. F. Garcia Ruiz[3,4] K. Gaul[10] S. Geldhof[2] T. F. Giesen[6] D. Hanstorp[17] R. Heinke[7] T. A. Isaev[5] A. A. Kyuberis[12] S. Kujanpää[18] L. Lalanne[2,1] G. Neyens[2,§] M. Nichols[17] L. F. Pašteka[12,19] H. A. Perrett[11] J. R. Reilly[11] S. Rothe[7] S.-M. Udrescu[3] B. van den Borne[2] Q. Wang[20] J. Wessolek[11,7] X. F. Yang[21] C. Zülch[10] and the ISOLDE Collaboration

[1] *Experimental Physics Department, CERN, CH-1211 Geneva 23, Switzerland*
[2] *KU Leuven, Instituut voor Kern- en Stralingsfysica, B-3001 Leuven, Belgium*
[3] *Department of Physics, Massachusetts Institute of Technology, Cambridge, MA 02139, USA*
[4] *Laboratory for Nuclear Science, Massachusetts Institute of Technology, Cambridge, MA 02139, USA*
[5] *Affiliated with an institute covered by a cooperation agreement with CERN.*
[6] *Laboratory for Astrophysics, Institute of Physics, University of Kassel, Kassel 34132, Germany*
[7] *Systems Department, CERN, CH-1211 Geneva 23, Switzerland*
[8] *Department of Chemistry, Johannes Gutenberg-Universität Mainz, 55099 Mainz, Germany*
[9] *TRIUMF, Vancouver BC V6T 2A3, Canada*
[10] *Fachbereich Chemie, Philipps-Universität Marburg, Marburg 35032, Germany*
[11] *Department of Physics and Astronomy, The University of Manchester, Manchester M13 9PL, United Kingdom*
[12] *Van Swinderen Institute of Particle Physics and Gravity,*
University of Groningen, Groningen 9712 CP, Netherlands
[13] *Department of Chemistry, Massachusetts Institute of Technology, Cambridge, MA 02139, USA*
[14] *Photon Science Institute, The University of Manchester, Manchester M13 9PY, United Kingdom*
[15] *Laboratoire Irène Joliot-Curie, Orsay F-91405, France*
[16] *University Paris-Saclay, Orsay F-91405, France*
[17] *Department of Physics, University of Gothenburg, Gothenburg SE-41296, Sweden*
[18] *Department of Physics, University of Jyväskylä, Jyväskylä FI-40014, Finland*
[19] *Department of Physical and Theoretical Chemistry,*
Faculty of Natural Sciences, Comenius University, Bratislava, Slovakia
[20] *School of Nuclear Science and Technology, Lanzhou University, Lanzhou 730000, China*
[21] *School of Physics and State Key Laboratory of Nuclear Physics and Technology, Peking University, Beijing 100971, China*

(Dated: August 16, 2023)

We report the spectroscopy of 11 electronic states in the radioactive molecule radium monofluoride (RaF). The observed excitation energies are compared with state-of-the-art relativistic Fock-space coupled cluster (FS-RCC) calculations, which achieve an agreement of $\geq 99.71\%$ (within $\sim$8 meV) for all states. High-order electron correlation and quantum electrodynamics corrections are found to be important at all energies. Establishing the accuracy of calculations is an important step towards high-precision studies of these molecules, which are proposed for sensitive searches of physics beyond the Standard Model.

The Standard Model (SM) of particle physics fails to explain several fundamental observations, such as the matter-antimatter asymmetry and the strong charge-parity problem [1]. To reconcile the discrepancies, several theories extending beyond the Standard Model (BSM) have been proposed. To understand the limitations of the SM and to assess the validity of candidate BSM theories, precision tests of the SM and searches for new physics using atomic and molecular spectroscopy are being pursued [1] among other approaches. Such experiments typically aim to measure deviations from the SM for nuclear and hadronic symmetry-violating properties, such as the nuclear Schiff moment [2], or to detect properties that do not arise in the SM or are predicted to be significantly below the current experimental sensitivity, such as the electric dipole moment of the electron (eEDM) [3–5].

Due to the degree of precision (down to 10^{-35} e cm [6]) required by experiments aiming to perform such measurements, ongoing and future searches are focused on systems with maximum sensitivity to the presence of the various moments. Polar molecules containing a heavy and a light nucleus can have close-lying opposite-parity states and strong internal fields, thus leading to an enhanced sensitivity to the presence of symmetry-violating moments, 10^3-10^5 times larger as compared to atoms [1, 7]. HfF$^+$ [3] and ThO [4] are such examples, which were used to set the most stringent upper bounds to the eEDM to date at $|d_e| < 4.1 \times 10^{-30}$ e cm, while YbF [8], ThF$^+$ [9], BaF [10], and YbOH [11] are also being investigated, among others. Because the uncertainty in such spectroscopic searches scales with the inverse of the coherence time τ of probing each individual molecule as $\sigma \propto \frac{1}{\tau}$, radium monofluoride (RaF) is a promising system to explore the limits of the SM, as RaF is amenable to direct laser cooling [12, 13]. Additionally, its ground state is highly sensitive to the eEDM [14–17] as well as to nuclear spin-dependent parity- or time-reversal violation (NSD-PV) [12, 18–20], depending on the chosen isotope of the octupole-deformed radium nucleus [21].

Extracting values of the symmetry-violating moments from experimental searches requires the calculation of molecular constants that quantify the sensitivity of the molecule to the moment of interest. Both in atoms and molecules [1, 22], the theoretical precision and accuracy of the calculated molecular parameters will dictate the limit to which the symmetry-violating moment can be determined. As these sensitivity parameters are not experimentally measurable, benchmarking and improving the accuracy and precision of *ab initio* molecular theory across other observables, which can be measured in the laboratory, is a critical and necessary step towards precision tests of the SM. Therefore, joint experimental and theoretical efforts should be devoted to evaluating the accuracy and precision of state-of-the-art *ab initio* methods for many different properties of the structure of RaF.

The experimental study of RaF is complicated by the radioactive decay of the radium nuclei, which all have half-lives from nanoseconds to at most a few days, except for ^{226}Ra and ^{228}Ra (years). These two long-lived isotopes have zero nuclear spin and are therefore not suited for the study of symmetry-violating nuclear moments. Radioactive ion beam (RIB) facilities are favorable not only for the preparatory spectroscopic studies needed to understand the electronic structure of the different isotopologues of RaF, but also for future precision experiments. The first spectroscopic studies on RaF molecules were performed at the ISOLDE radioactive beam facility at CERN [23]. This resulted in initial insight into the low-energy electronic-vibrational structure of RaF [24], the observation of a strong isotope shift across several short-lived isotopologues [25], and a realistic laser-cooling scheme [13].

The initial experiment and the interpretation of the data were driven by prior quantum chemistry calculations of the electronic structure of RaF [14, 26]. Subsequent theoretical studies including a higher-level treatment of electron correlations and quantum electrodynamics (QED) effects [27] suggest a re-evaluation of some of the previous assignments [24]. Furthermore, the prediction of excited-state energies and transitions with a precision of a few tens of cm^{-1} (few meV) [27, 28] call for experimental verification of the accuracy of the computational techniques.

This work reports on the experimental study of RaF by observing 11 excited electronic states up to 30,000 cm^{-1} above the ground state. The measured excitation energies are compared to state-of-the-art relativistic Fock-space coupled cluster calculations, in which corrections from QED and high-order electron correlation effects are applied to high-lying electronic states for the first time.

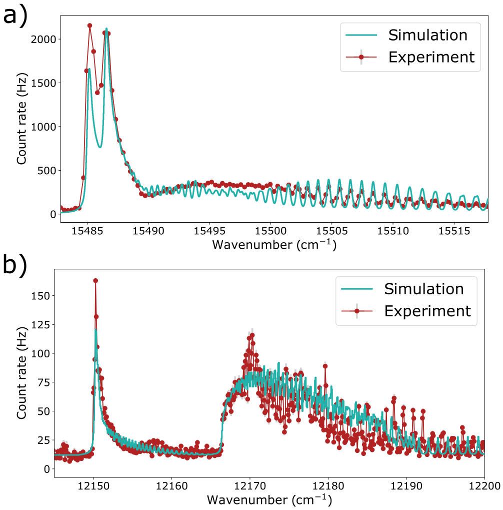

FIG. 1. Example spectra. **(a)** $G\ ^2\Pi_{1/2} \leftarrow A\ ^2\Pi_{1/2}$ ($v' = 0 \leftarrow v'' = 0$). **(b)** $E\ ^2\Sigma_{1/2} \leftarrow A\ ^2\Pi_{1/2}$ ($v' = 0 \leftarrow v'' = 0$). The simulated spectra were constructed using the best-fit molecular parameters determined using contour fitting with PGOPHER [29]. The x-axis corresponds to the wavenumber of the scanning laser.

The experimental setup is described in detail in Ref. [24] and the Supplemental Material of this Letter. Laser spectroscopy of ^{226}RaF was performed using the Collinear Resonance Ionization Spectroscopy (CRIS) experiment at CERN-ISOLDE. The delivered bunched beam of RaF$^+$ was initially neutralized via collisions with sodium vapor in a charge-exchange cell and then resonantly ionized with a series of collinear pulsed laser beams that were synchronized with the molecular bunches. For each scheme, the molecules underwent either one or two resonant excitations starting from the electronic ground state using tunable titanium-sapphire (Ti:Sa) or pulsed dye lasers (PDLs). A high-power 532-nm Nd:YAG laser was used to ionize the molecules that had been resonantly excited. The molecular excitation energies were measured by scanning the frequency of the tunable laser used for a resonant transition while monitoring the ion count rate. Example spectra are shown in Fig. 1.

The level search was facilitated by preparing multiple laser-ionization schemes based on two PDLs with nominal linewidths ν of 0.8 and 9 GHz and two grating-based broadband pulsed Ti:Sa lasers (ν = 3 GHz). A total wavenumber range of 3,935 cm^{-1} was scanned in a period of a few days. The search for excited states of the ^{226}RaF molecule was guided by theoretical predictions from relativistic Fock-space coupled cluster calculations with single- and double-excitation amplitudes (FS-RCCSD), using doubly augmented Dyall CV4Z basis sets [30, 31] and correlating 27 electrons (27e-augCV4Z) within the Dirac-Coulomb Hamiltonian. Such calculations can be completed within a few days using the DIRAC code [32, 33] and are therefore very well suited to guide the experimental efforts. Although such calculations have a limited accuracy for higher-lying states (within hundreds of cm^{-1}) it is sufficient to direct the experimental search to the correct energy range, leading to the experimental discovery of 6 new excited states (blue lines in Fig. 2).

Further information about the laser systems, measurement procedure, and data analysis can be found in the Supplemental Material.

In Fig. 2, the experimentally measured excitation energies are compared with the predictions from several *ab initio* calculations at different levels of sophistication. FS-RCCSD calculations were performed at an extended level of correlation treatment, using enhanced basis sets, and an improved electronic Hamiltonian compared to the 27e-augCV4Z calculations that guided the experiment. The excellent agreement between the observed level energies and the most advanced calculations allowed for electronic-state assignments.

To improve the treatment of electron correlations, the correlation space was expanded to include 69 electrons (triangles in Fig. 2). Including the remaining 28 electrons that correspond to the $1s$–$3d$ shells of Ra, thus correlating all 97 RaF electrons, only modified the level energies by up to 2 cm^{-1} (see Table 3 in Supplemental Material), which is significantly smaller than the overall theoretical uncertainty.

To improve the basis-set quality, calculations were performed with the extended (ext) AE3Z [34, 35] (crosses in Fig. 2) and AE4Z [28, 35] (squares in Fig. 2) basis sets, which include a greater number of functions for a more accurate description of the electronic states. A further correction for the incompleteness of the basis sets (CBS correction) was implemented based on the scalar-relativistic treatment of valence and outer-core electrons [36–38] using the CFOUR code [39] (see Supplemental Material for more details).

Finally, the accuracy of the electronic Hamiltonian was improved by taking into account the Gaunt inter-electron interaction [40] and QED effects [41], with the latter made possible recently for molecular 4-component calculations [28]. Additionally, higher-order electron correlation effects encoded in the triple-excitation amplitudes (T) were included via the FS-RCCSDT approach using the EXP-T code [42, 43]. The challenging calculation of the T contribution to the excitation energies was feasible thanks to the use of compact relativistic basis sets [34, 44, 45], developed for use with the 2-component generalized relativistic effective-core potential (GRECP) as the Hamiltonian [36–38]. The triple-excitation amplitudes were calculated for the 27 outermost electrons (correction denoted as 27e-T), including down to the $5d$ Ra electrons.

The CBS, Gaunt, QED, and 27e-T corrections are included in the diamond markers displayed in Fig. 2 and compared to the experimental excitation energies in Table I.

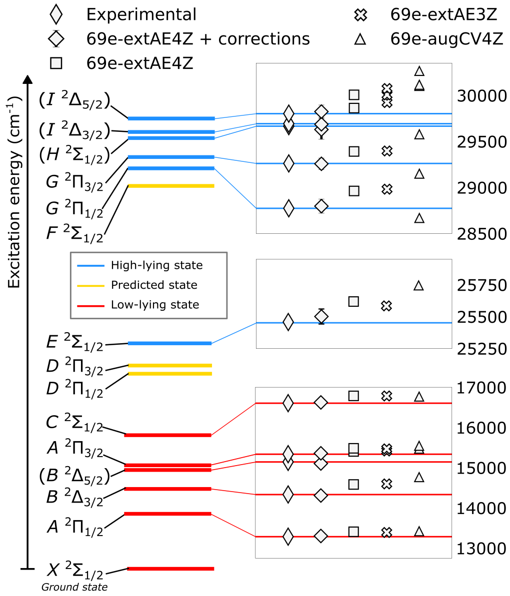

FIG. 2. **Left:** Calculated level diagram of RaF up to 30,000 cm^{-1}. The levels in red and blue have been observed experimentally, while the levels in yellow could not be searched for within the available time. The term symbols have been assigned according to the 69e-extAE4Z + corrections calculations (see text for details). **Right:** Comparison of experimental excitation energies with respect to the ground state (in cm^{-1}) and FS-RCCSD calculations at different levels of *ab initio* sophistication. Uncertainties are included only for the most precise calculations (diamonds) and in most cases are smaller than the data marker.

An overall agreement of at least 99.71% is achieved for all level energies, which allowed assigning the term characters of several states and the revision of earlier tentative assignments. A transition observed at 16,175.2(5) cm^{-1} in Ref. [24] was previously assigned as $C\ ^2\Sigma_{1/2} \leftarrow X\ ^2\Sigma_{1/2}$ ($v' = 0 \leftarrow v'' = 0$). The theoretical precision achieved in the present study together with the new measurements indicate that this transition does not correspond to the lowest electronic excitation energy of the upper state, but rather corresponds to the

($v' = 0 \leftarrow v'' = 1$) vibrational transition, as suggested in Ref. [27]. Instead, a new transition observed in this work very close to the predicted value of 16,615 cm^{-1} is identified as the $v' = 0 \leftarrow v'' = 0$ vibronic transition to the $C\ ^2\Sigma_{1/2}$ state (see Supplemental Material for details of the reassigned energy). Additionally, a transition observed at 15,142.7(5) cm^{-1} in Ref. [24] was previously tentatively assigned as ($B\ ^2\Delta_{3/2}$) $\leftarrow$ $X\ ^2\Sigma_{1/2}$ ($v' = 0 \leftarrow v'' = 0$). The close agreement of this transition energy with the calculated value of 15,099 cm^{-1} (Table I) leads to the tentative reassignment of this transition as ($B\ ^2\Delta_{5/2}$)$\leftarrow$ $X\ ^2\Sigma_{1/2}$ ($v' = 0 \leftarrow v'' = 0$). Finally, a new transition observed at 14,332.82(13)[51] cm^{-1} is closer to the theoretical prediction for the excitation energy of the $B\ ^2\Delta_{3/2}$ state, and is in agreement with the predictions in Ref. [27]. Thus, the assignment of the $B\ ^2\Delta_{3/2}$ state at 14,332.82(13)[51] cm^{-1} is adopted. The term assignments for the higher-lying states (blue lines in Fig. 2), observed in this work for the first time, are driven by the highly accurate *ab initio* calculations and elaborated upon in the Supplemental Material.

Fig. 3a and 3b present a detailed comparison of the impact of each of the corrections discussed above. In particular, the impact of treating triple-excitation amplitudes at high electronic excitation energies is clearly visible in Fig. 3b. The 27e-T correction has the most prominent effect in improving the agreement with experiment among all listed corrections and for all considered high-lying states. This correction is much larger in high-lying states (Fig. 3b) than in the low-lying ones (Fig. 3a), demonstrating the need for spectroscopic studies of electronic states far above the ground state to understand the role of correlations in the electronic structure. Fig. 3a also demonstrates the importance of choosing an appropriate basis set for calculations of excited electronic states even energetically close to the ground state, as the difference between 69e-extAE4Z and 69e-CV4Z is considerable for all states.

Finally, in Fig. 3c the impact of including QED corrections and an iterative treatment of triple-excitation amplitudes is presented. Such a study was previously performed for the low-lying states using single-reference relativistic coupled cluster theory with single, double, triple, and perturbative quadruple excitation amplitudes [46], and by including QED effects [27, 28]. The contribution of QED effects was found to be especially important for the low-lying states up to 17,000 cm^{-1} above the ground state, having a greater effect on improving the agreement with the experimental excitation energies than the iterative treatment of triple-excitation amplitudes in the FS-RCC models.

Fig. 3c confirms that the impact of QED effects is indeed significant at low energies, but it decreases in importance as the average distance of the valence electrons from the heavy Ra nucleus increases for greater excitation energies. On the other hand, the higher-order electron correlation effects captured by the iterative treatment of triple-excitation amplitudes are of increasing importance for higher-energy states, but remain non-negligible energetically close to the ground state. This is explained by the participation of non-valence outer-core electrons in the higher-energy excitations. Specifically for the excitation energies of the high-lying states, it is found that the contribution of $5d$ electrons plays a particularly important role (see Table III in Supplemental Material).

TABLE I. Comparison of experimental and theoretical electronic excitation energies (T_0, in units of cm^{-1}) in RaF. The theoretical values correspond to the 69e-extAE4Z calculations with 27e-T, CBS, Gaunt, and QED corrections (diamonds in Fig. 2). The normalized theoretical agreement (%) is reported as $1 - \frac{|E_{\mathrm{th}} - E_{\mathrm{exp}}|}{E_{\mathrm{exp}}}$. The states in parentheses are tentatively assigned. Statistical and systematic errors are given in round and square brackets.

State	Experimental	69e-extAE4Z+corr.	Agreement
$X\ ^2\Sigma_{1/2}$	0	0	
$A\ ^2\Pi_{1/2}$	13,284.427(1)[20]*	13,299(36)	**99.89**
$B\ ^2\Delta_{3/2}$	14,332.82(13)[51]**	14,300(61)	**99.77**
($B\ ^2\Delta_{5/2}$)	15,142.7(5)$^\$$	15,099(70)	**99.71**
$A\ ^2\Pi_{3/2}$	15,334.52(23)[35]	15,355(35)	**99.87**
$C\ ^2\Sigma_{1/2}$	16,613.6(12)$^\#$	16,615(69)	**99.99**
$E\ ^2\Sigma_{1/2}$	25,451.11(11)[26]	25,520(84)	**99.73**
$G\ ^2\Pi_{1/2}$	28,774.16(51)[35]	28,824(111)	**99.83**
$G\ ^2\Pi_{3/2}$	29,225.57(28)[51]	29,284(90)	**99.80**
($H\ ^2\Sigma_{1/2}$)	29,665.52(11)[51]	29,663(156)	**99.99**
($I\ ^2\Delta_{3/2}$)	29,693.15(24)[51]	29,715(102)	**99.92**
($I\ ^2\Delta_{5/2}$)	29,801.59(7)[35]	29,852(106)	**99.83**

* Value from Ref. [13].

** Previously tentatively assigned at 15,142.7(5) cm^{-1} [24].

$^\$$ Value from Ref. [24]. Previously tentatively assigned as $B\ ^2\Delta_{3/2}$ ($v = 0$).

$^\#$ Extracted using values reported in Ref. [24] following reassignment in this work. The previous assignment at 16,175.2(5) cm^{-1} [24] was deduced from a measured transition that is now reassigned as $C\ ^2\Sigma_{1/2} \leftarrow X\ ^2\Sigma_{1/2}$ ($v' = 0 \leftarrow v'' = 1$) instead of $v' = 0 \leftarrow v'' = 0$.

A highly accurate and precise treatment of electron correlation in RaF can be critical for the efforts to calculate the sensitivity of molecular electronic states to nuclear, hadronic, and leptonic symmetry-violating moments. All previous theoretical studies of the sensitivity to different symmetry-violating moments in RaF [14–17, 47–49] have reported results either using CCSD theory (with triple-excitation amplitudes included only via approximations in some works), or using the Zeroth-Order Regular Approximation based on a mean-field approach and density functional theory, which do not fully capture correlations. An investigation of the effect of high-order correlation effects on these constants is thus also needed. Moreover, the current results highlight the accuracy of the FS-RCC method, which is applicable also to molecules whose states have a multi-reference charac-

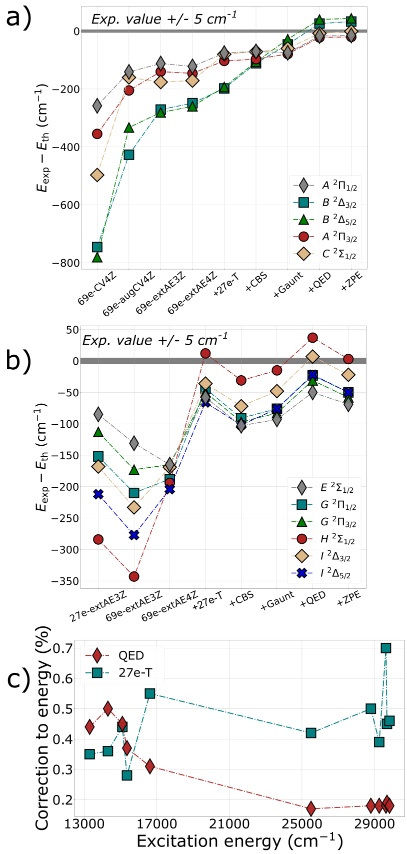

FIG. 3. Evolution of the predicted excitation energies as a function of increasing theoretical sophistication for (**a**) the five lowest-lying states and (**b**) the six high-lying states. The unambiguous identification of high-lying states through their angular momentum projections is not possible with the CV4Z basis sets and thus they are not included in (b). The '+ZPE' label corresponds to the zero-point vibrational energy correction. (**c**) Evolution of the QED and 27e-T corrections to the excitation energies calculated at the 69e-extAE4Z level.

ter, where single-reference CCSD(T) theory is not applicable.

In conclusion, Fig. 2 and Table I show that the 69e-extAE4Z calculations with 27e-T, CBS, Gaunt, and QED corrections reproduce the experimentally measured energies up to 30,000 cm^{-1} with an agreement of 99.71% or higher, which surpasses that of all previous relativistic FS-RCCSD calculations for RaF (Ref. [50] and references therein). The achieved agreement justifies the assigned angular momenta and term characters for the observed levels. Three additional states are predicted to exist (yellow lines in Fig. 2 with details in the Supplemental Material), which could not yet be identified within the available experimental time. The present study, both experimental and theoretical, paves the way for future high-resolution studies of these states and tests the predictive power of the calculations, whose reliability is a prerequisite for future precision studies and BSM probes.

SUPPLEMENTAL INFORMATION

The binned spectra that were analyzed will be available in the form of PGOPHER overlay files after publication at the reserved doi: 10.5281/zenodo.8196151. The raw data and analysis code can be provided upon request to the authors. Further information on the experimental and theoretical methods are provided in the Supplemental Material.

ACKNOWLEDGMENTS

We thank the ISOLDE collaboration and the ISOLDE technical teams for their support.

Financial support from FWO, as well as from the Excellence of Science (EOS) programme (No. 40007501) and the KU Leuven project C14/22/104, is acknowledged. The STFC consolidated grants ST/V001116/1 and ST/P004423/1 and the FNPMLS ERC grant agreement 648381 are acknowledged. SGW, RFGR, and SMU acknowledge funding by the Office of Nuclear Physics, U.S. Department of Energy Grants DE-SC0021176 and DE-SC002117. AAB, TFG, RB, and KG acknowledge funding from the Deutsche Forschungsgemeinschaft (DFG) – Projektnummer 328961117 – SFB 1319 ELCH. We thank the Center for Information Technology at the University of Groningen for their support and for providing access to the Peregrine high performance computing cluster. MAu, MN, and JW acknowledge funding from the EU's H2020-MSCA-ITN Grant No. 861198 'LISA'. DH acknowledges financial support from the Swedish Research Council (2020-03505).

DECLARATIONS

The authors declare no conflict of interest.

---

[*] m.athkak@cern.ch
[†] wilkinss@mit.edu
[‡] skripnikov_lv@pnpi.nrcki.ru

§ gerda.neyens@kuleuven.be

[1] M. S. Safronova, D. Budker, D. DeMille, D. F. J. Kimball, A. Derevianko, and C. W. Clark, Search for new physics with atoms and molecules, Reviews of Modern Physics **90**, 10.1103/RevModPhys.90.025008 (2018).

[2] V. V. Flambaum and J. S. Ginges, Nuclear Schiff moment and time-invariance violation in atoms, Physical Review A **65**, 9 (2002).

[3] T. S. Roussy, L. Caldwell, T. Wright, W. B. Cairncross, Y. Shagam, K. B. Ng, N. Schlossberger, S. Y. Park, A. Wang, J. Ye, and E. A. Cornell, An improved bound on the electron's electric dipole moment, Science **381**, 46 (2023).

[4] V. Andreev, D. G. Ang, D. DeMille, J. M. Doyle, G. Gabrielse, J. Haefner, N. R. Hutzler, Z. Lasner, C. Meisenhelder, B. R. O'Leary, C. D. Panda, A. D. West, E. P. West, and X. Wu, Improved limit on the electric dipole moment of the electron, Nature **562**, 355 (2018).

[5] C. Cesarotti, Q. Lu, Y. Nakai, A. Parikh, and M. Reece, Interpreting the electron EDM constraint, Journal of High Energy Physics **2019**, 10.1007/JHEP05(2019)059 (2019).

[6] Y. Ema, T. Gao, and M. Pospelov, Standard model prediction for paramagnetic electric dipole moments, Phys. Rev. Lett. **129**, 231801 (2022).

[7] V. V. Flambaum and V. A. Dzuba, Electric dipole moments of atoms and molecules produced by enhanced nuclear Schiff moments, Physical Review A **101**, 042504 (2020).

[8] J. Lim, J. R. Almond, M. A. Trigatzis, J. A. Devlin, N. J. Fitch, B. E. Sauer, M. R. Tarbutt, and E. A. Hinds, Laser Cooled YbF Molecules for Measuring the Electron's Electric Dipole Moment, Physical Review Letters **120**, 123201 (2018).

[9] D. N. Gresh, K. C. Cossel, Y. Zhou, J. Ye, and E. A. Cornell, Broadband velocity modulation spectroscopy of ThF+ for use in a measurement of the electron electric dipole moment, Journal of Molecular Spectroscopy **319**, 1 (2016).

[10] P. Aggarwal, H. L. Bethlem, A. Borschevsky, M. Denis, K. Esajas, P. A. B. Haase, Y. Hao, S. Hoekstra, K. Jungmann, T. B. Meijknecht, M. C. Mooij, R. G. E. Timmermans, W. Ubachs, L. Willmann, A. Zapara, and The NL-eEDM Collaboration, Measuring the electric dipole moment of the electron in BaF, The European Physical Journal D **72**, 197 (2018).

[11] B. L. Augenbraun, Z. D. Lasner, A. Frenett, H. Sawaoka, C. Miller, T. C. Steimle, and J. M. Doyle, Laser-cooled polyatomic molecules for improved electron electric dipole moment searches, New Journal of Physics **22**, 10.1088/1367-2630/ab687b (2020).

[12] T. A. Isaev, S. Hoekstra, and R. Berger, Laser-cooled RaF as a promising candidate to measure molecular parity violation, Physical Review A - Atomic, Molecular, and Optical Physics **82**, 1 (2010).

[13] S. M. Udrescu, S. G. Wilkins, A. A. Breier, R. F. Garcia Ruiz, M. Athanasakis-Kaklamanakis, M. Au, R. Berger, I. Belosevic, M. L. Bissell, K. Chrysalidis, T. E. Cocolios, R. P. de Groote, A. Dorne, K. T. Flanagan, S. Franchoo, K. Gaul, S. Geldhof, T. F. Giesen, D. Hanstorp, R. Heinke, A. Koszorús, S. Kujanpää, L. Lalanne, G. Neyens, M. Nichols, H. A. Perrett, J. R. Reilly, S. Rothe, B. van den Borne, Q. Wang, J. Wessolek, X. F. Yang, and K. Zülch, Precision spectroscopy and laser cooling scheme of a radium-containing molecule, Under review (2023).

[14] T. A. Isaev and R. Berger, Lasercooled radium monofluoride: A molecular all-in-one probe for new physics, arXiv **1302.5682**, 10.48550/ARXIV.1302.5682 (2013).

[15] A. D. Kudashov, A. N. Petrov, L. V. Skripnikov, N. S. Mosyagin, T. A. Isaev, R. Berger, and A. V. Titov, Ab initio study of radium monofluoride (RaF) as a candidate to search for parity- and time-and-parity-violation effects, Physical Review A - Atomic, Molecular, and Optical Physics **90**, 1 (2014).

[16] S. Sasmal, H. Pathak, M. K. Nayak, N. Vaval, and S. Pal, Relativistic coupled-cluster study of RaF as a candidate for the parity- and time-reversal-violating interaction, Physical Review A **93**, 62506 (2016).

[17] C. Zhang, X. Zheng, and L. Cheng, Calculations of time-reversal-symmetry-violation sensitivity parameters based on analytic relativistic coupled-cluster gradient theory, Phys. Rev. A **104**, 012814 (2021).

[18] N. Auerbach, V. V. Flambaum, and V. Spevak, Collective T- and P-odd electromagnetic moments in nuclei with octupole deformations, Physical Review Letters **76**, 4316 (1996).

[19] V. Spevak, N. Auerbach, and V. V. Flambaum, Enhanced T-odd, P-odd electromagnetic moments in reflection asymmetric nuclei, Physical Review C - Nuclear Physics **56**, 1357 (1997).

[20] A. N. Petrov and L. V. Skripnikov, Energy levels of radium monofluoride RaF in external electric and magnetic fields to search for P- and T,P-violation effects, Phys. Rev. A **102**, 62801 (2020).

[21] P. A. Butler, L. P. Gaffney, P. Spagnoletti, K. Abrahams, M. Bowry, J. Cederkäll, G. de Angelis, H. De Witte, P. E. Garrett, A. Goldkuhle, C. Henrich, A. Illana, K. Johnston, D. T. Joss, J. M. Keatings, N. A. Kelly, M. Komorowska, J. Konki, T. Kröll, M. Lozano, B. S. Nara Singh, D. O'Donnell, J. Ojala, R. D. Page, L. G. Pedersen, C. Raison, P. Reiter, J. A. Rodriguez, D. Rosiak, S. Rothe, M. Scheck, M. Seidlitz, T. M. Shneidman, B. Siebeck, J. Sinclair, J. F. Smith, M. Stryjczyk, P. Van Duppen, S. Vinals, V. Virtanen, N. Warr, K. Wrzosek-Lipska, and M. Zielińska, Evolution of Octupole Deformation in Radium Nuclei from Coulomb Excitation of Radioactive 222Ra and 228Ra Beams, Physical Review Letters **124**, 42503 (2020).

[22] J. S. Ginges and V. V. Flambaum, Violations of fundamental symmetries in atoms and tests of unification theories of elementary particles, Physics Reports **397**, 63 (2004).

[23] R. Catherall, W. Andreazza, M. Breitenfeldt, A. Dorsival, G. J. Focker, T. P. Gharsa, G. T J, J.-L. Grenard, F. Locci, P. Martins, S. Marzari, J. Schipper, A. Shornikov, and T. Stora, The ISOLDE facility, Journal of Physics G: Nuclear and Particle Physics **44**, 094002 (2017).

[24] R. F. Garcia Ruiz, R. Berger, J. Billowes, C. L. Binnersley, M. L. Bissell, A. A. Breier, A. J. Brinson, K. Crysalidis, T. E. Cocolios, B. S. Cooper, K. T. Flanagan, T. F. Giesen, R. P. de Groote, S. Franchoo, F. P. Gustafsson, T. A. Isaev, A. Koszorus, G. Neyens, H. A. Perrett, C. M. Ricketts, S. Rothe, L. Schweikhard, A. R. Vernon, K. D. A. Wendt, F. Weinholtz, S. G. Wilkins, and X. F. Yang, Spectroscopy of short-lived radioactive molecules,

Nature **581**, 396 (2020).

[25] S. M. Udrescu, A. J. Brinson, R. F. Garcia Ruiz, K. Gaul, R. Berger, J. Billowes, C. L. Binnersley, M. L. Bissell, A. A. Breier, K. Chrysalidis, T. E. Cocolios, B. S. Cooper, K. T. Flanagan, T. F. Giesen, R. P. de Groote, S. Franchoo, F. P. Gustafsson, T. A. Isaev, A. Koszorus, G. Neyens, H. A. Perrett, C. M. Ricketts, S. Rothe, A. R. Vernon, K. D. A. Wendt, F. Wienholtz, S. G. Wilkins, and X. F. Yang, Isotope Shifts of Radium Monofluoride Molecules, Physical Review Letters **127**, 033001 (2021).

[26] T. A. Isaev, S. Hoekstra, L. Willmann, and R. Berger, Ion neutralisation mass-spectrometry route to radium monofluoride (RaF), arXiv **1310.1511**, 10.48550/ARXIV.1310.1511 (2013).

[27] A. Zaitsevskii, L. V. Skripnikov, N. S. Mosyagin, T. Isaev, R. Berger, A. A. Breier, and T. F. Giesen, Accurate ab initio calculations of RaF electronic structure appeal to more laser-spectroscopical measurements, The Journal of Chemical Physics **156**, 44306 (2022).

[28] L. V. Skripnikov, Approaching meV level for transition energies in the radium monofluoride molecule RaF and radium cation Ra+ by including quantum-electrodynamics effects, The Journal of Chemical Physics **154**, 201101 (2021).

[29] C. M. Western, PGOPHER: A program for simulating rotational, vibrational and electronic spectra, Journal of Quantitative Spectroscopy and Radiative Transfer **186**, 221 (2017).

[30] K. G. Dyall, Relativistic double-zeta, triple-zeta, and quadruple-zeta basis sets for the 4s, 5s, 6s, and 7s elements, The Journal of Physical Chemistry A **113**, 12638 (2009).

[31] K. G. Dyall, Core correlating basis functions for elements 31–118, Theor. Chem. Acc. **131**, 1217 (2012).

[32] DIRAC, a relativistic ab initio electronic structure program, Release DIRAC19 (2019), written by A. S. P. Gomes, T. Saue, L. Visscher, H. J. Aa. Jensen, and R. Bast, with contributions from I. A. Aucar, V. Bakken, K. G. Dyall, S. Dubillard, U. Ekström, E. Eliav, T. Enevoldsen, E. Faßhauer, T. Fleig, O. Fossgaard, L. Halbert, E. D. Hedegård, B. Heimlich–Paris, T. Helgaker, J. Henriksson, M. Iliaš, Ch. R. Jacob, S. Knecht, S. Komorovský, O. Kullie, J. K. Lærdahl, C. V. Larsen, Y. S. Lee, H. S. Nataraj, M. K. Nayak, P. Norman, G. Olejniczak, J. Olsen, J. M. H. Olsen, Y. C. Park, J. K. Pedersen, M. Pernpointner, R. di Remigio, K. Ruud, P. Sałek, B. Schimmelpfennig, B. Senjean, A. Shee, J. Sikkema, A. J. Thorvaldsen, J. Thyssen, J. van Stralen, M. L. Vidal, S. Villaume, O. Visser, T. Winther, and S. Yamamoto (available at http://dx.doi.org/10.5281/zenodo.3572669, see also http://www.diracprogram.org).

[33] T. Saue, R. Bast, A. S. P. Gomes, H. J. A. Jensen, L. Visscher, I. A. Aucar, R. Di Remigio, K. G. Dyall, E. Eliav, E. Fasshauer, T. Fleig, L. Halbert, E. D. Hedegård, B. Helmich-Paris, M. Iliaš, C. R. Jacob, S. Knecht, J. K. Laerdahl, M. L. Vidal, M. K. Nayak, M. Olejniczak, J. M. H. Olsen, M. Pernpointner, B. Senjean, A. Shee, A. Sunaga, and J. N. P. van Stralen, The DIRAC code for relativistic molecular calculations, J. Chem. Phys. **152**, 204104 (2020).

[34] L. V. Skripnikov, Nuclear magnetization distribution effect in molecules: Ra^+ and raf hyperfine structure, The Journal of Chemical Physics **153**, 114114 (2020).

[35] K. G. Dyall, Relativistic double-zeta, triple-zeta, and quadruple-zeta basis sets for the light elements H–Ar, Theor. Chem. Acc. **135**, 128 (2016).

[36] A. V. Titov and N. S. Mosyagin, Generalized relativistic effective core potential: Theoretical grounds, International Journal of Quantum Chemistry **71**, 359 (1999).

[37] N. S. Mosyagin, A. V. Zaitsevskii, and A. V. Titov, Shape-consistent relativistic effective potentials of small atomic cores, international review of atomic and molecular physics, Review of Atomic and Molecular Physics **1**, 63 (2010).

[38] N. S. Mosyagin, A. V. Zaitsevskii, L. V. Skripnikov, and A. V. Titov, Generalized relativistic effective core potentials for actinides, International Journal of Quantum Chemistry **116**, 301 (2016).

[39] J. F. Stanton, J. Gauss, M. E. Harding, P. G. Szalay, *et al.*, “CFOUR” (2011), CFOUR: a program package for performing high-level quantum chemical calculations on atoms and molecules, http://www.cfour.de .

[40] J. Sikkema, L. Visscher, T. Saue, and M. Iliaš, The molecular mean-field approach for correlated relativistic calculations, The Journal of Chemical Physics **131**, 124116 (2009).

[41] V. M. Shabaev, I. I. Tupitsyn, and V. A. Yerokhin, Model operator approach to the lamb shift calculations in relativistic many-electron atoms, Physical Review A **88**, 012513 (2013).

[42] A. V. Oleynichenko, A. Zaitsevskii, L. V. Skripnikov, and E. Eliav, Relativistic Fock Space Coupled Cluster Method for Many-Electron Systems: Non-Perturbative Account for Connected Triple Excitations, Symmetry **12**, 10.3390/sym12071101 (2020).

[43] A. V. Oleynichenko, A. Zaitsevskii, and E. Eliav, Towards high performance relativistic electronic structure modelling: The EXP-T program package, in *Supercomputing*, Commun. Comput. Inf. Sci., Vol. 1331, edited by V. Voevodin and S. Sobolev (Springer International Publishing, Cham, 2020) pp. 375–386.

[44] L. V. Skripnikov, N. S. Mosyagin, and A. V. Titov, Relativistic coupled-cluster calculations of spectroscopic and chemical properties for element 120, Chemical Physics Letters **555**, 79 (2013).

[45] L. V. Skripnikov, Combined 4-component and relativistic pseudopotential study of ThO for the electron electric dipole moment search, The Journal of Chemical Physics **145**, 214301 (2016).

[46] M. Kállay and J. Gauss, Approximate treatment of higher excitations in coupled-cluster theory, The Journal of Chemical Physics **123**, 214105 (2005).

[47] K. Gaul and R. Berger, Zeroth order regular approximation approach to electric dipole moment interactions of the electron, The Journal of Chemical Physics **147**, 14109 (2017).

[48] K. Gaul, S. Marquardt, T. Isaev, and R. Berger, Systematic study of relativistic and chemical enhancements of P,T-odd effects in polar diatomic radicals, Phys. Rev. A **99**, 32509 (2019).

[49] K. Gaul and R. Berger, Toolbox approach for quasi-relativistic calculation of molecular properties for precision tests of fundamental physics, The Journal of Chemical Physics **152**, 044101 (2020).

[50] Y. Osika and M. Shundalau, Fock-space relativistic coupled cluster study on the RaF molecule promising for the laser cooling, Spectrochimica Acta Part A: Molecular and

Biomolecular Spectroscopy **264**, 120274 (2022).

Supplemental Material: Pinning down electron correlations in RaF via spectroscopy of excited states

M. Athanasakis-Kaklamanakis,[1, 2, *] S. G. Wilkins,[3, 4, †] L. V. Skripnikov,[5, ‡] Á. Koszorús,[1, 2] A. A. Breier,[6] M. Au,[7, 8] I. Belošević,[9] R. Berger,[10] M. L. Bissell,[11] A. Borschevsky,[12] A. Brinson,[3] K. Chrysalidis,[7] T. E. Cocolios,[2] R. P. de Groote,[2] A. Dorne,[2] C. M. Fajardo-Zambrano,[2] R. W. Field,[13] K. T. Flanagan,[11, 14] S. Franchoo,[15, 16] R. F. Garcia Ruiz,[3, 4] K. Gaul,[10] S. Geldhof,[2] T. F. Giesen,[6] D. Hanstorp,[17] R. Heinke,[7] T. A. Isaev,[5] A. A. Kyuberis,[12] S. Kujanpää,[18] L. Lalanne,[2, 1] G. Neyens,[2, §] M. Nichols,[17] L. F. Pašteka,[12, 19] H. A. Perrett,[11] J. R. Reilly,[11] S. Rothe,[7] S.-M. Udrescu,[3] B. van den Borne,[2] Q. Wang,[20] J. Wessolek,[11, 7] X. F. Yang,[21] C. Zülch,[10] and the ISOLDE Collaboration

[1] *Experimental Physics Department, CERN, CH-1211 Geneva 23, Switzerland*
[2] *KU Leuven, Instituut voor Kern- en Stralingsfysica, B-3001 Leuven, Belgium*
[3] *Department of Physics, Massachusetts Institute of Technology, Cambridge, MA 02139, USA*
[4] *Laboratory for Nuclear Science, Massachusetts Institute of Technology, Cambridge, MA 02139, USA*
[5] *Affiliated with an institute covered by a cooperation agreement with CERN.*
[6] *Laboratory for Astrophysics, Institute of Physics, University of Kassel, Kassel 34132, Germany*
[7] *Systems Department, CERN, CH-1211 Geneva 23, Switzerland*
[8] *Department of Chemistry, Johannes Gutenberg-Universität Mainz, 55099 Mainz, Germany*
[9] *TRIUMF, Vancouver BC V6T 2A3, Canada*
[10] *Fachbereich Chemie, Philipps-Universität Marburg, Marburg 35032, Germany*
[11] *Department of Physics and Astronomy, The University of Manchester, Manchester M13 9PL, United Kingdom*
[12] *Van Swinderen Institute of Particle Physics and Gravity,*
University of Groningen, Groningen 9712 CP, Netherlands
[13] *Department of Chemistry, Massachusetts Institute of Technology, Cambridge, MA 02139, USA*
[14] *Photon Science Institute, The University of Manchester, Manchester M13 9PY, United Kingdom*
[15] *Laboratoire Irène Joliot-Curie, Orsay F-91405, France*
[16] *University Paris-Saclay, Orsay F-91405, France*
[17] *Department of Physics, University of Gothenburg, Gothenburg SE-41296, Sweden*
[18] *Department of Physics, University of Jyväskylä, Jyväskylä FI-40014, Finland*
[19] *Department of Physical and Theoretical Chemistry,*
Faculty of Natural Sciences, Comenius University, Bratislava, Slovakia
[20] *School of Nuclear Science and Technology, Lanzhou University, Lanzhou 730000, China*
[21] *School of Physics and State Key Laboratory of Nuclear Physics and Technology, Peking University, Beijing 100971, China*

(Dated: August 16, 2023)

EXTENDED METHODS

Production

Accelerated beams of ^{226}RaF$^+$ were produced at the CERN-ISOLDE radioactive ion beam facility [1]. Prior to the experiment, short- and long-lived radioactive isotopes, among which ^{226}Ra nuclei ($t_{1/2}$ = 1600 years), were produced by impinging 1.4-GeV protons onto a room-temperature uranium carbide target. During the experiment, the irradiated target was heated up to 2000 °C to extract the produced radionuclides from within the solid matrix. By exposing the target to a constant flow of CF$_4$, the radium atoms formed ^{226}Ra^{19}F molecules that were ionized using a rhenium surface ion source. The ^{226}RaF$^+$ ions were then accelerated to 40 keV and mass-separated from other radiogenic species using two dipolar magnetic separators. The continuous, isotopically pure beam of ^{226}RaF$^+$ was then accumulated in a radiofrequency quadrupolar cooler-buncher (RFQcb), which released the ^{226}RaF$^+$ beam in bunches with a 5-μs temporal spread once every 20 ms. The internal temperature of the beam was cooled from ∼2000 °C to near room temperature after being trapped in the RFQcb in the presence of a helium buffer gas. A typical ^{226}RaF$^+$ beam intensity of 1.2×10^6 ions per second was then sent into the CRIS beam line.

Laser setup

Multiple laser schemes were used for the spectroscopy of the excited states in RaF. The spectrum of the previously reported $A\ ^2\Pi_{1/2}$ state was measured using a grating-based titanium:sapphire (Ti:Sa) laser scanned around 752 nm (in the molecular rest frame), corresponding to the transition from the ground state. The transition from the electronic ground state to this level was then used as the first step in three-step schemes to search for the higher-lying levels (at excitation energies higher than $C\ ^2\Sigma_{1/2}$), using either its $v' = 0 \leftarrow v'' = 0$ or $v' = 1 \leftarrow v'' = 1$ vibrational transitions. In all schemes, the ionization was induced by a non-resonant excitation driven by a 532-nm Nd:YAG laser. The excitation energies of the states $B\ ^2\Delta_{3/2}$, $A\ ^2\Pi_{3/2}$, and $C\ ^2\Sigma_{1/2}$ were re-measured with two-step schemes by scanning a pulsed dye laser around 697 nm (Pyridine 1) for the $B\ ^2\Delta_{3/2}$ state, and around 651 nm and 601 nm (DCM) for the $A\ ^2\Pi_{3/2}$ and $C\ ^2\Sigma_{1/2}$ states, followed by the 532-nm non-resonant step. The new excitation energies assigned to the low-lying states are compared to our previous assignment [2] in Table I.

The remaining states were measured using three-step laser schemes. To search for the transition to the $E\ ^2\Sigma_{1/2}$ state, the second laser step was scanned around 821 nm with a second grating-based Ti:Sa laser. For the transitions to the $G\ ^2\Pi_{1/2}$, $G\ ^2\Pi_{3/2}$, $H\ ^2\Sigma_{1/2}$, $I\ ^2\Delta_{3/2}$, and $I\ ^2\Delta_{5/2}$ states, the second laser-excitation step was scanned around 644 nm, 625 nm, 610 nm, 609 nm, and 605 nm, respectively, using a pulsed dye laser (DCM).

All lasers used in this work were pulsed. The Ti:Sa lasers were pumped by a 532-nm Nd:YAG laser operating at 1 kHz, while the pulsed dye lasers were pumped by 532-nm Nd:YAG lasers operating at 50 Hz. The non-resonant 532-nm Nd:YAG laser was operating at 50 Hz, as well. The relative timing between the laser steps was controlled by triggering the Q-switches of the pulsed lasers using a multi-channel, ultra-low-jitter clock (Quantum Composer 9528). As the excited-state lifetimes were not known for the newly discovered electronic states, all three steps were temporally overlapped. The wavelengths of the pulsed dye lasers (Spectra Physics PDL and Sirah Cobra) were measured using a HighFinesse WS6-600 wavemeter and the wavelengths of the Ti:Sa lasers were measured using a HighFinesse WSU-2 wavemeter. The WSU-2 wavemeter was continuously calibrated by monitoring at the same time the wavelength of a diode laser locked to a hyperfine peak in rubidium (Toptica DL PRO 780).

Data analysis

The measured wavenumbers in the acquired spectra were firstly Doppler-shifted to the molecular rest frame wavenumber $\tilde{\nu}$ according to the expression $\tilde{\nu} = \frac{1-\beta}{\sqrt{1-\beta^2}}\tilde{\nu}_0$, where $\beta = v/c$ with c the speed of light, and $\tilde{\nu}_0$ the wavenumber in the lab frame. The velocity of the beam was determined from their kinetic energy, which was defined by the platform voltage of the radiofrequency cooler-buncher that drifted over time between 39,905 and 39,910 kV. Fluctuations and drifts of the platform voltage were monitored by continuous measurements (1 measurement per second) of the real voltage using a calibrated potential divider (PTB PT60-2) and a digital multimeter (Agilent 34401A). The voltage measurements (precision of 10 mV at 40 kV) were then used to accurately determine the velocity of the ^{226}RaF beam for each wavenumber measurement. Following Doppler-shifting, the spectra were binned with a bin size of 3 GHz.

The binned spectra were analyzed using the contour-fitting routine of the PGOPHER package [3]. The state origin T_0, rotational constant B, centrifugal distortion constant D, spin-rotation coupling constant γ (only for Σ states), and Λ-doubling constant p (only for Π and Δ states) were varied during the fitting routine to reach agreement between simulation and experiment. Interpretation of the fitted values of B, D, γ, and p will be presented in a future publication. The fitted rotational constants B increase for higher excitation energies, which is consistent with the calculated equilibrium bond length (r_e in Table V) that decreases for higher excitation energies.

All measured spectra involved electronic transitions starting from either the $X\ ^2\Sigma_{1/2}$ or the $A\ ^2\Pi_{1/2}$ states. The molecular parameters of these two states are known from the high-resolution laser spectroscopy of the $A\ ^2\Pi_{1/2} \leftarrow X\ ^2\Sigma_{1/2}$ transition in ^{226}RaF [4]. As a result, in the present study only the properties of the upper electronic state in each spectrum were varied during each fit.

The agreement between simulated and measured spectra for the transitions starting from the electronic ground state $X\ ^2\Sigma_{1/2}$ was significantly improved if the Boltzmann population distribution of the molecular beam was substituted for the sum of Gaussian population distributions centered around different values of J. The emergence of distinct temperature groups in the ground-state population of the molecular beam is attributed to spatial aberrations in the electric potential and buffer-gas density of the RFQcb during this particular experiment, leading to the non-uniform cooling of the molecular beam.

The statistical uncertainty in the excitation energies was extracted by the standard deviation of the fitted parameter given by the contour-fitting routine of PGOPHER. The uncertainty in the raw data was the error in the count rate (y-axis) in the spectra, which was determined as the square root of the number of data points in each bin. The standard deviations of the fitted excitation energies were scaled by the square root of the reduced chi-squared of the fit $\sqrt{\chi^2_r}$.

A systematic uncertainty is considered for all excitation energies, which corresponds to the Voigt-peak linewidth set in PGOPHER to best match the observed linewidths for each spectrum, and aims to account for the propensity of the contour-fitting routine to converge to local minima, as it cannot move a simulated line by more than the set linewidth [3]. An additional component of 0.02 cm^{-1} is added to account for the combined sources of systematic error stemming from the experimental equipment (see Ref. [4]).

The best-fit values and uncertainties of the excitation energies were also obtained independently using a chi-squared minimization code written in Python and the correlated errors were determined by inspecting the corner plots of the fitted parameters. The results of the independent fitting were consistent with the results from the PGOPHER analysis, and thus the latter are used here.

The resolution of the spectra of transitions to the $G\ ^2\Pi_{1/2}$ and $E\ ^2\Sigma_{1/2}$ states was high enough to enable an analysis using the line-fitting routine of PGOPHER, which was found to yield results in agreement with contour-fitting of the same spectra. Only contour-fitting results are included in this work for the sake of consistency.

State assignment

$A\ ^2\Pi_{3/2}$

The spectrum of the transition from the electronic ground state to $A\ ^2\Pi_{3/2}$ was measured in the region where it had been previously measured in Ref. [2]. The spectrum was obtained using a laser with a linewidth of $\nu \sim 0.8$ GHz, as compared to the linewidth of $\nu \sim 10$ GHz used in Ref. [2]. Therefore, the newly acquired spectrum was fitted to re-assign the excitation energy of the state.

Due to unexpected complications in the cooling performance of the ISCOOL RFQcb, a non-uniform temperature profile complicated the fitting of the spectrum. In addition to the molecular parameters of the $A\ ^2\Pi_{3/2}$ state, the parameters for 6 Gaussian temperature profiles were also included in the contour fitting. Each Gaussian profile had the form $e^{-b(J-J_c)^2}$, where the parameter b defined the fraction of the total molecular beam found in this temperature profile, and J_c defined the rotational quantum number around which the profile is centered. J_c thus defined the average temperature of the Gaussian profile. Thus, as per the fitted parameters, 48% of the molecules were found at 155 K, 26% at 95 K, 8% at 747 K, 5% at 685 K, 5% at 362 K, and 8% at 1527 K, yielding a weighted average of the ensemble temperature of 329 K.

$B\ ^2\Delta_{3/2}$

The spectrum of the $B\ ^2\Delta_{3/2} \leftarrow X\ ^2\Sigma_{1/2}$ transition suffered from a non-uniform temperature composition as in the case of $A\ ^2\Pi_{3/2}$. The composition of the molecular beam in terms of Gaussian profiles differed from the spectrum to the $A\ ^2\Pi_{3/2}$ state, which is consistent with an observed time dependence for the performance of the RFQcb. The best contour fit was found when using 5 Gaussian profiles. As per the fitted parameters, 34% of the beam was found at 87 K, 24% at 399 K, 23% at 1367 K, 10% at 3199 K, and 9% at 828 K, yielding a weighted average of the ensemble temperature of 820 K. This is much higher than room temperature and the average temperature in the case of $A\ ^2\Pi_{3/2}$, consistent with an intervention in the RFQcb that took place in the course of the experiment aiming to improve the uniformity of the time-of-flight profile of the ion beam. The cooling performance of the RFQcb and the resulting time-of-flight are strongly coupled.

$B\ ^2\Delta_{5/2}$

The previously measured [2] spectrum that was tentatively assigned as a transition to $B\ ^2\Delta_{3/2}$ is now tentatively reassigned as a transition to $B\ ^2\Delta_{5/2}$. This assigned excitation energy is in agreement with the theoretical prediction. The transition $B\ ^2\Delta_{5/2} \leftarrow X\ ^2\Sigma_{1/2}$ is expected to be weak but allowed by the L-uncoupling interaction of the $B\ ^2\Delta_{5/2}$ state with $A\ ^2\Pi_{3/2}$, or less likely through the electric quadrupole matrix element. Therefore, in the absence of additional information that can be used to unambiguously identify the upper state, this assignment remains tentative.

$C\ ^2\Sigma_{1/2}$

The new assignment for the energy of the $C\ ^2\Sigma_{1/2}$ state follows from the observation of a transition in close agreement with the prediction at 16,615 cm^{-1}, starting from the electronic ground state. This transition lies outside the range that was scanned in Ref. [2] and was thus not observed previously. The spectral profile of this transition is very similar to that of the transition at 16,175.2 cm^{-1} that was previously assigned as $C\ ^2\Sigma_{1/2} \leftarrow X\ ^2\Sigma_{1/2}$ ($v' = 0 \leftarrow v'' = 0$), but its intensity is twice that of the transition at 16,175.2 cm^{-1}. As a result, it is concluded that it is the newly discovered transition that in fact corresponds to $C\ ^2\Sigma_{1/2} \leftarrow X\ ^2\Sigma_{1/2}$ ($v' = 0 \leftarrow v'' = 0$).

The temperature non-uniformity due to the RFQcb led to a very complicated and noisy spectrum in this case, and the fit was not deemed as reliable as that of the spectra reported in Ref. [2]. Therefore, the new assignment for the $C\ ^2\Sigma_{1/2}$ ($v = 0$) state was determined using the values reported in Ref. [2]. The excitation energy of the $X\ ^2\Sigma_{1/2}$ $v = 1$ was determined to be $E_X(1) = 438.4(11)$ cm^{-1} by taking the difference in energy between the $A\ ^2\Pi_{1/2} \leftarrow X\ ^2\Sigma_{1/2}$ ($v' = 0 \leftarrow v'' = 1$) and ($v' = 0 \leftarrow v'' = 0$) transitions. The excitation energy $E_X(1)$ was then added to the previous assignment of 16,175.2(5) cm^{-1}, to yield 16,613.6(12) cm^{-1}.

$E\ ^2\Sigma_{1/2}$

The energy of the $E\ ^2\Sigma_{1/2}$ state was assigned based on a transition starting from $A\ ^2\Pi_{1/2}$ ($v = 0$).

Only two transitions were discovered in a range of 1,500 cm^{-1} around the predicted excitation energy of the $E\ ^2\Sigma_{1/2}$ state. The spectra of both transitions have very similar shapes and are separated by approximately 480 cm^{-1}, which matches the calculated vibrational spacing of the state (Table V). Since the transition starts from $v = 0$ of the lower state, the two measured spectra were interpreted as belonging to transitions to $v = 0$ and $v = 1$ of the $E\ ^2\Sigma_{1/2}$ state, which is the only state predicted to lie within a few thousand cm^{-1} of the measured structures.

$G\ ^2\Pi_{1/2}$

The energy of the $G\ ^2\Pi_{1/2}$ state was assigned based on a transition starting from $A\ ^2\Pi_{1/2}$ $(v = 0)$.

A spectrum that starts from the same lower state as the one assigned as $G\ ^2\Pi_{1/2} \leftarrow A\ ^2\Pi_{1/2}$ $(v' = 0 \leftarrow v'' = 0)$ and has a very similar spectral profile was measured at approximately 980 cm^{-1} higher in energy (corresponding to approximately two times the calculated vibrational spacing for this state, Table V), which was interpreted as a transition to $G\ ^2\Pi_{1/2}$ $(v = 2)$. Additionally, in a transition starting from the $A\ ^2\Pi_{1/2}$ $(v = 1)$ state, a spectrum was observed at an excitation energy half-way between those of the $v = 0$ and $v = 2$ states, with a very similar spectral profile. Therefore, this third spectrum was interpreted as belonging to a transition to $G\ ^2\Pi_{1/2}$ $(v = 1)$. The intensity of the $v' = 0 \leftarrow v'' = 0$ transition was the highest, followed by that of $v' = 1 \leftarrow v'' = 1$ and then by that of the $v' = 2 \leftarrow v'' = 0$. The only other predicted state in the vicinity of $G\ ^2\Pi_{1/2}$ is $G\ ^2\Pi_{3/2}$. The transition strength of $G\ ^2\Pi_{1/2} \leftarrow A\ ^2\Pi_{1/2}$ $(v' = 0 \leftarrow v'' = 0)$ was the largest among all transitions measured from $A\ ^2\Pi_{1/2}$, which is highly improbable for the nominally forbidden transition $G\ ^2\Pi_{3/2} \leftarrow A\ ^2\Pi_{1/2}$. Therefore, the observed spectrum was assigned as $G\ ^2\Pi_{1/2} \leftarrow A\ ^2\Pi_{1/2}$ $(v' = 0 \leftarrow v'' = 0)$.

$G\ ^2\Pi_{3/2}$

The energy of the $G\ ^2\Pi_{3/2}$ state was assigned based on a transition starting from $A\ ^2\Pi_{1/2}$ $(v = 0)$.

Within a range of 400 cm^{-1} around the prediction for the transition energy to the $G\ ^2\Pi_{3/2}$ state, spectra of two transitions were found, and the excitation energy of both would be in agreement with the prediction. However, for only one of the two transitions, a second spectrum also starting from $A\ ^2\Pi_{1/2}$ $(v = 0)$ was measured at approximately 492 cm^{-1} higher in wavenumber that has a very similar spectral profile. This distance corresponds to the calculated vibrational spacing for the $G\ ^2\Pi_{3/2}$ state (Table V), and so these two spectra that had the same spectral profile were interpreted as transitions to $v = 0$ and $v = 1$ of $G\ ^2\Pi_{3/2}$.

$H\ ^2\Sigma_{1/2}$, $I\ ^2\Delta_{3/2}$, *and* $I\ ^2\Delta_{5/2}$

The energies of these three states were assigned based on transitions starting from $A\ ^2\Pi_{1/2}$ $(v = 0)$.

In the vicinity of the transitions assigned to these three states, multiple transitions were observed. Two of those transitions were identified as the $v' = 1 \leftarrow v'' = 0$ and $v' = 2 \leftarrow v'' = 0$ transitions to the $G\ ^2\Pi_{3/2}$ and $G\ ^2\Pi_{1/2}$ states, respectively.

At approximately 16,175 cm^{-1}, the transition $C\ ^2\Sigma_{1/2} \leftarrow X\ ^2\Sigma_{1/2}$ $(v' = 0 \leftarrow v'' = 1)$ was identified, while at approximately 16,610 cm^{-1}, the transition $C\ ^2\Sigma_{1/2} \leftarrow X\ ^2\Sigma_{1/2}$ $(v' = 0 \leftarrow v'' = 0)$ was identified. These two transitions did not arise from the combined effect of all three lasers in the excitation scheme, but only from the scanning laser and the non-resonant ionization step. Therefore, they were identified as transitions from the electronic ground state, rather than from $A\ ^2\Pi_{1/2}$ $(v = 0)$.

Two bands were assigned as transitions to $H\ ^2\Sigma_{1/2}$ $(v = 0)$ and $I\ ^2\Delta_{3/2}$ $(v = 0)$ based on the computational predictions. As the predicted energies of the two states are within uncertainties of each other, their assignment is tentative.

The spectrum that was assigned as belonging to the transition to $I\ ^2\Delta_{5/2}$ was identified due to its significantly lower intensity compared to all other spectra, which is consistent with the weak nature of the $I\ ^2\Delta_{5/2} \leftarrow A\ ^2\Pi_{1/2}$ $(v' = 0 \leftarrow v'' = 0)$ transition. As the transition is dipole-forbidden, the assignment is tentative.

One more, very weak spectral feature was identified at an excitation energy of approximately 29,650 cm^{-1}, whose spectral profile suggests the form of a $\Sigma \leftarrow \Pi$ spectrum. Neither a firm nor a tentative assignment was possible at the present time. Based on the calculated T_0 and ω_e for the $F\ ^2\Sigma_{1/2}$ state, this spectrum could correspond to the transition $F\ ^2\Sigma_{1/2} \leftarrow A\ ^2\Pi_{1/2}$ $(v' = 3 \leftarrow v'' = 0)$, whose strength is consistent with expected very low intensity of the observed structure. However, as no experimental information on the $F\ ^2\Sigma_{1/2}$ state has been obtained so far, a definite assignment cannot be made.

Calculations

For the 69-electron FS-RCCSD calculations, the ext-AE4Z basis set was used, which corresponds to the extended uncontracted Dyall's all-electron AE4Z basis set for Ra [5] from Ref. [6] and the uncontracted Dyall's AAEQZ basis set [7] for F. Explicitly, this basis set includes $[42s\,38p\,27d\,27f\,13g\,3h\,2i]$ Gaussian-type functions for Ra. In these FS-RCCSD calculations, the energy cutoff for virtual orbitals was set equal to 300 Hartree. For the 69-electron FS-RCCSD calculations using a doubly augmented Dyall's CV4Z basis set [5, 8], the energy cutoff for virtual orbitals was set to 100 Hartree.

The electronic ground state of the RaF$^+$ cation ($R_e = 2.165$ Å) was chosen as a Fermi-vacuum in the Fock-space (FS) calculation. Target states in the neutral RaF are considered as belonging to the one-particle sector of the FS. In the calculation, the Dirac–Coulomb Hamiltonian was used to solve the self-consistent (Dirac-Hartree-Fock) problem and then converted to the two-component all-electron Hamiltonian by means of the X2C technique within the molecular mean-field approximation [9]. In addition to the 69e-FS-RCCSD-extAE4Z calculations, further calculations with different numbers of correlated electrons and utilizing different basis sets were performed. These included 27- and 69-electron calculations in the standard (unmodified) uncontracted Dyall's CV4Z basis set and 17-, 27-, 35-, 69-, and 97-electron calculations in the extended AE3Z basis set [5, 7, 8] (see Tables III and IV). The latter extAE3Z basis set has been developed in Ref. [10] and includes $[38s\,33p\,24d\,14f\,7g\,3h\,2i]$ Gaussian-type functions for Ra and corresponds to the uncontracted AE3Z [7] basis set on F.

To take into account contributions of an extended number of basis functions with high angular momentum ($L \geq 4$) beyond those contained in extAE4Z, the scalar-relativistic variant of the valence part of the generalized relativistic effective core potential approach [11–13] was used, as well as the 37e-EOMEA-CCSD approach (which is equivalent to FS-RCCSD in the considered case) to treat electron correlations using the CFOUR code [14]. In this way, it was possible to extend the basis set towards higher harmonics in Ra up to $15g\,15h\,15i$ (with an additional increase of numbers of $s\,p\,d$ functions), which is intractable in practice within the Dirac-Coulomb Hamiltonian using available resources. Following Ref. [6], the extrapolated contribution of higher harmonics to the basis-set correction was also included. In the extrapolation scheme, the contribution of basis functions with an angular momentum L (for $L > 6$) is determined using the formula $A/L^5 + B/L^6$, where the coefficients A and B were derived from the directly calculated contributions of h- (L=5) and i- (L=6) harmonics. Thus, we calculated the sum of contributions for $L > 6$. This scheme has been optimized and tested in Ref. [6] for Ra$^+$ and RaF excitation energies, and has also been successfully applied to calculated excitation energies in Ba$^+$ and BaF [15]. The contribution of the increased basis set described above is termed "+CBS" in the main text.

Correlation effects beyond the FS-RCCSD model have been calculated as the difference in transition energies calculated within the relativistic FS-RCCSDT and FS-RCCSD approaches using specially constructed compact natural contracted basis sets [10, 16, 17], correlating 27 RaF electrons and employing two-component (valence) GRECP Hamiltonian.

The compact basis is constructed in such a way as to describe the 7S, 6D, 7P, 8S, 7D, 5F and 8P states of the Ra$^+$ cation, which are relevant for the considered electronic states of RaF. For these states in Ra$^+$, scalar-relativistic 37e-CCSD(T) calculations were performed in an extended basis set, yielding correlated one-particle density matrices. The matrices were averaged and diagonalized to obtain natural atomic orbitals; in addition, functions necessary to describe spin-orbit effects were also included. Orbitals with maximal eigenvalues (occupation numbers) were used for the compact basis set in the RaF calculations. In principle, such a procedure could also be used within the Dirac-Coulomb Hamiltonian. However, at present one cannot use contracted Gaussian basis sets for heavy elements such as Ra in available implementations of the Dirac-Coulomb Hamiltonian. Another obstacle to the direct use of the Dirac-Coulomb Hamiltonian for the compact basis-set construction is the presence of serious practical limitations in the size of the original basis set that is used to construct correlated density matrices.

Lastly, the contributions of QED [6, 18] as well as Gaunt inter-electron effects [9] were calculated at the FS-RCCSD level.

In the large-scale calculations described above, we calculated differences between total energies of the excited electronic states and the ground state at the internuclear distance $R = 4.23$ Bohr, which is close to the equilibrium internuclear distance of the electronic ground state of RaF. However, to account for the difference in total energies at the equilibrium distance of each state, it was necessary to determine the equilibrium internuclear distances for each electronic state (Table V). The obtained "non-verticality" contributions were added to the vertical "bulk" 69-electron FS-RCCSD excitation energies obtained in the large-scale calculations. To calculate these contributions, potential energy curves for all considered electronic states were calculated.

Similarly to Ref. [19], the potential energy curve for the electronic ground state was calculated within the two-component (valence) GRECP approach using the single-reference coupled cluster with single, double and perturbative triple cluster amplitudes CCSD(T) method. To obtain potential energy curves for excited electronic states as a function of the internuclear distance R, the excitation energy calculated at the FS-RCCSD level for a given value of R was added to the energy of the electronic ground state for the same value of R. In these calculations, 37 electrons were included in the correlation treatment. For Ra, we used the $[25s\,17p\,12d\,9f\,4g\,2h]$ basis set optimized for the GRECP calculations, while for F the uncontracted Dyall's AAEQZ basis set [7] was employed.

To characterize molecular terms in the ΛS scheme, the mean values of the electron orbital angular momentum projection operator on the molecular axis were calculated at the FS-RCCSD level (within the finite-field approach) and rounded up to an integer using the code developed in Ref. [17].

In the uncertainty estimations, it is considered that the basis set correction (CBS) has an uncertainty of 50%. The calculations did not take into account the retardation part of the Breit interaction. According to the data for the Ra$^+$ ion [6, 20], the contribution of the retardation part of the Breit interaction to the transition energies in Ra$^+$ is within 20% of the Gaunt interaction effect. Thus, the uncertainty due to the excluded retardation part of the Breit interaction is estimated as 20% of the Gaunt-effect contribution. The accuracy of the model QED operator approach is high [18, 21]. Therefore, the uncertainty of the QED correction is suggested to be in the order of 20%. The uncertainty of the high-order correlation effects (beyond the FS-RCCSDT model) can be estimated by comparing the FS-RCCSDT result with the single-reference coupled cluster with single, double, triple and perturbative quadruple cluster amplitudes, CCSDT(Q) [22, 23]. According to our calculations performed for states of RaF with near single-reference character, the correlation corrections to FS-RCCSD calculated with the FS-RCCSDT and CCSDT(Q) methods agree within 60%. To be more conservative, in the uncertainty estimation it is suggested that the higher-order correlation contribution is valid within 75%. The final uncertainty estimation of the theoretical electronic excitation energies was conservatively calculated as the square root of the sum of squares of the uncertainties described above for each state.

FS-RCCSD calculations were performed using the DIRAC [24, 25] code. FS-RCCSDT calculations were performed using the using EXP-T code [26, 27]. Single reference relativistic coupled cluster calculations were performed with the MRCC [22, 23] code. All scalar relativistic correlation calculations were performed using the CFOUR [14] code. Matrix elements of the QED model Hamiltonian were calculated within the code developed in Ref. [6].

---

[*] m.athkak@cern.ch

[†] wilkinss@mit.edu

[‡] skripnikov_lv@pnpi.nrcki.ru

[§] gerda.neyens@kuleuven.be

[1] R. Catherall, W. Andreazza, M. Breitenfeldt, A. Dorsival, G. J. Focker, T. P. Gharsa, G. T J, J.-L. Grenard, F. Locci, P. Martins, S. Marzari, J. Schipper, A. Shornikov, and T. Stora, The ISOLDE facility, Journal of Physics G: Nuclear and Particle Physics **44**, 094002 (2017).

[2] R. F. Garcia Ruiz, R. Berger, J. Billowes, C. L. Binnersley, M. L. Bissell, A. A. Breier, A. J. Brinson, K. Crysalidis, T. E. Cocolios, B. S. Cooper, K. T. Flanagan, T. F. Giesen, R. P. de Groote, S. Franchoo, F. P. Gustafsson, T. A. Isaev, A. Koszorus, G. Neyens, H. A. Perrett, C. M. Ricketts, S. Rothe, L. Schweikhard, A. R. Vernon, K. D. A. Wendt, F. Weinholtz, S. G. Wilkins, and X. F. Yang, Spectroscopy of short-lived radioactive molecules, Nature **581**, 396 (2020).

[3] C. M. Western, PGOPHER: A program for simulating rotational, vibrational and electronic spectra, Journal of Quantitative Spectroscopy and Radiative Transfer **186**, 221 (2017).

[4] S. M. Udrescu, S. G. Wilkins, A. A. Breier, R. F. Garcia Ruiz, M. Athanasakis-Kaklamanakis, M. Au, R. Berger, I. Belosevic, M. L. Bissell, K. Chrysalidis, T. E. Cocolios, R. P. de Groote, A. Dorne, K. T. Flanagan, S. Franchoo, K. Gaul, S. Geldhof, T. F. Giesen, D. Hanstorp, R. Heinke, A. Koszorús, S. Kujanpää, L. Lalanne, G. Neyens, M. Nichols, H. A. Perrett, J. R. Reilly, S. Rothe, B. van den Borne, Q. Wang, J. Wessolek, X. F. Yang, and K. Zülch, Precision spectroscopy and laser cooling scheme of a radium-containing molecule, Under review (2023).

[5] K. G. Dyall, Core correlating basis functions for elements 31–118, Theor. Chem. Acc. **131**, 1217 (2012).

[6] L. V. Skripnikov, Approaching meV level for transition energies in the radium monofluoride molecule RaF and radium cation Ra+ by including quantum-electrodynamics effects, The Journal of Chemical Physics **154**, 201101 (2021).

[7] K. G. Dyall, Relativistic double-zeta, triple-zeta, and quadruple-zeta basis sets for the light elements H–Ar, Theor. Chem. Acc. **135**, 128 (2016).

[8] K. G. Dyall, Relativistic double-zeta, triple-zeta, and quadruple-zeta basis sets for the 4s, 5s, 6s, and 7s elements, The Journal of Physical Chemistry A **113**, 12638 (2009).

[9] J. Sikkema, L. Visscher, T. Saue, and M. Iliaš, The molecular mean-field approach for correlated relativistic calculations, The Journal of Chemical Physics **131**, 124116 (2009).

[10] L. V. Skripnikov, Nuclear magnetization distribution effect in molecules: Ra$^+$ and raf hyperfine structure, The Journal of Chemical Physics **153**, 114114 (2020).

[11] A. V. Titov and N. S. Mosyagin, Generalized relativistic effective core potential: Theoretical grounds, International Journal of Quantum Chemistry **71**, 359 (1999).

[12] N. S. Mosyagin, A. V. Zaitsevskii, and A. V. Titov, Shape-consistent relativistic effective potentials of small atomic cores, international review of atomic and molecular physics, Review of Atomic and Molecular Physics **1**, 63 (2010).

[13] N. S. Mosyagin, A. V. Zaitsevskii, L. V. Skripnikov, and A. V. Titov, Generalized relativistic effective core potentials for actinides, International Journal of Quantum Chemistry **116**, 301 (2016).

[14] J. F. Stanton, J. Gauss, M. E. Harding, P. G. Szalay, *et al.*, “CFOUR” (2011), CFOUR: a program package for performing high-level quantum chemical calculations on atoms and molecules, http://www.cfour.de .

[15] L. V. Skripnikov, D. V. Chubukov, and V. M. Shakhova, The role of qed effects in transition energies of heavy-atom alkaline earth monofluoride molecules: A theoret-

ical study of ba+, baf, raf, and e120f, J. Chem. Phys. **155**, 144103 (2021).

[16] L. V. Skripnikov, N. S. Mosyagin, and A. V. Titov, Relativistic coupled-cluster calculations of spectroscopic and chemical properties for element 120, Chemical Physics Letters **555**, 79 (2013).

[17] L. V. Skripnikov, Combined 4-component and relativistic pseudopotential study of ThO for the electron electric dipole moment search, The Journal of Chemical Physics **145**, 214301 (2016).

[18] V. M. Shabaev, I. I. Tupitsyn, and V. A. Yerokhin, Model operator approach to the lamb shift calculations in relativistic many-electron atoms, Physical Review A **88**, 012513 (2013).

[19] A. Zaitsevskii, L. V. Skripnikov, N. S. Mosyagin, T. Isaev, R. Berger, A. A. Breier, and T. F. Giesen, Accurate ab initio calculations of RaF electronic structure appeal to more laser-spectroscopical measurements, The Journal of Chemical Physics **156**, 44306 (2022).

[20] E. Eliav, U. Kaldor, and Y. Ishikawa, Transition energies of barium and radium by the relativistic coupled-cluster method, Phys. Rev. A **53**, 3050 (1996).

[21] M. Y. Kaygorodov, Y. S. Kozhedub, I. I. Tupitsyn, A. V. Malyshev, D. A. Glazov, G. Plunien, and V. M. Shabaev, Relativistic calculations of the ground and inner-l-shell excited energy levels of berylliumlike ions, Phys. Rev. A **99**, 032505 (2019).

[22] M. Kállay and J. Gauss, Approximate treatment of higher excitations in coupled-cluster theory, The Journal of Chemical Physics **123**, 214105 (2005).

[23] "MRCC", m. Kállay, P. R. Nagy, D. Mester, Z. Rolik, G. Samu, J. Csontos, J. Csóka, P. B. Szabó, L. Gyevi-Nagy, B. Hégely, I. Ladjánszki, L. Szegedy, B. Ladóczki, K. Petrov, M. Farkas, P. D. Mezei, and á. Ganyecz: The MRCC program system: Accurate quantum chemistry from water to proteins, J. Chem. Phys. 152, 074107 (2020)." "MRCC, a quantum chemical program suite written by M. Kállay, P. R. Nagy, D. Mester, Z. Rolik, G. Samu, J. Csontos, J. Csóka, P. B. Szabó, L. Gyevi-Nagy, B. Hégely, I. Ladjánszki, L. Szegedy, B. Ladóczki, K. Petrov, M. Farkas, P. D. Mezei, and á. Ganyecz. See www.mrcc.hu.

[24] DIRAC, a relativistic ab initio electronic structure program, Release DIRAC19 (2019), written by A. S. P. Gomes, T. Saue, L. Visscher, H. J. Aa. Jensen, and R. Bast, with contributions from I. A. Aucar, V. Bakken, K. G. Dyall, S. Dubillard, U. Ekström, E. Eliav, T. Enevoldsen, E. Faßhauer, T. Fleig, O. Fossgaard, L. Halbert, E. D. Hedegård, B. Heimlich–Paris, T. Helgaker, J. Henriksson, M. Iliaš, Ch. R. Jacob, S. Knecht, S. Komorovský, O. Kullie, J. K. Lærdahl, C. V. Larsen, Y. S. Lee, H. S. Nataraj, M. K. Nayak, P. Norman, G. Olejniczak, J. Olsen, J. M. H. Olsen, Y. C. Park, J. K. Pedersen, M. Pernpointner, R. di Remigio, K. Ruud, P. Sałek, B. Schimmelpfennig, B. Senjean, A. Shee, J. Sikkema, A. J. Thorvaldsen, J. Thyssen, J. van Stralen, M. L. Vidal, S. Villaume, O. Visser, T. Winther, and S. Yamamoto (available at http://dx.doi.org/10.5281/zenodo.3572669, see also http://www.diracprogram.org).

[25] T. Saue, R. Bast, A. S. P. Gomes, H. J. A. Jensen, L. Visscher, I. A. Aucar, R. Di Remigio, K. G. Dyall, E. Eliav, E. Fasshauer, T. Fleig, L. Halbert, E. D. Hedegård, B. Helmich-Paris, M. Iliaš, C. R. Jacob, S. Knecht, J. K. Laerdahl, M. L. Vidal, M. K. Nayak, M. Olejniczak, J. M. H. Olsen, M. Pernpointner, B. Senjean, A. Shee, A. Sunaga, and J. N. P. van Stralen, The DIRAC code for relativistic molecular calculations, J. Chem. Phys. **152**, 204104 (2020).

[26] A. V. Oleynichenko, A. Zaitsevskii, L. V. Skripnikov, and E. Eliav, Relativistic Fock Space Coupled Cluster Method for Many-Electron Systems: Non-Perturbative Account for Connected Triple Excitations, Symmetry **12**, 10.3390/sym12071101 (2020).

[27] A. V. Oleynichenko, A. Zaitsevskii, and E. Eliav, Towards high performance relativistic electronic structure modelling: The EXP-T program package, in *Supercomputing*, Commun. Comput. Inf. Sci., Vol. 1331, edited by V. Voevodin and S. Sobolev (Springer International Publishing, Cham, 2020) pp. 375–386.

TABLE I. Comparison of electronic excitation wavenumbers (T_0, in cm^{-1}) assigned to low-lying states in RaF between Ref. [2] and the present work. All assignments refer to the $v = 0$ vibrational state of each electronic state.

	Garcia et al. 2020	This work	Theory
$B\ ^2\Delta_{3/2}$	15,142.7(5)*	14,332.82(13)[51]	14,300(61)
$(B\ ^2\Delta_{5/2})$	—	15,142.7(5)**	15,099(70)
$A\ ^2\Pi_{3/2}$	15,344.6(50)	15,334.52(23)[35]	15,355(35)
$C\ ^2\Sigma_{1/2}$	16,175.2(5)$^{\$}$	16,613.6(12)	16,615(69)

* Tentatively assigned in Ref. [2].

** With the discovery of a state at 14,332.82(13)[51] cm^{-1}, the previously measured transition is tentatively re-interpreted in this work as $B\ ^2\Delta_{5/2} \leftarrow X\ ^2\Sigma_{1/2}$ ($v' = 0 \leftarrow v'' = 0$), bringing the tentative assignment of both levels in excellent agreement with our more accurate theoretical predictions.

$^{\$}$ Following the new measurements, this transition is re-interpreted as $C\ ^2\Sigma_{1/2} \leftarrow X\ ^2\Sigma_{1/2}$ ($v' = 0 \leftarrow v'' = 1$). Using the values reported in Ref. [2], we place the $v' = 0 \leftarrow v'' = 0$ transition at 16,613.6(12) cm^{-1}, in agreement with the theoretical prediction.

TABLE II. Theoretical adiabatic electronic excitation energies (T_e, in cm^{-1}) calculated at the 69e-FS-RCCSD-extAE4Z level including higher-order corrections. Each column presents cumulative results, adding a contribution to the values in the column to its left. In the final column, the zero-point vibrational energy is added to T_e to arrive at T_0 that is compared with experiment.

State	69e-extAE4Z	+27e-CCSDT	+CBS	+Gaunt	+QED	T_0
X $^2\Sigma_{1/2}$	0	0	0	0	0	0
A $^2\Pi_{1/2}$	13,406	13,360	13,354	13,359	13,301	13,299
B $^2\Delta_{3/2}$	14,582	14,531	14,444	14,379	14,307	14,300
B $^2\Delta_{5/2}$	15,403	15,336	15,249	15,171	15,103	15,099
A $^2\Pi_{3/2}$	15,481	15,438	15,432	15,414	15,357	15,355
C $^2\Sigma_{1/2}$	16,785	16,694	16,685	16,674	16,622	16,615
D $^2\Pi_{1/2}$	22,724	22,504	22,442	22,388	22,323	22,320
D $^2\Pi_{3/2}$	23,074	22,852	22,790	22,734	22,671	22,673
E $^2\Sigma_{1/2}$	25,616	25,509	25,554	25,544	25,501	25,520
F $^2\Sigma_{1/2}$	28,410	28,067	28,080	28,050	27,995	28,019
G $^2\Pi_{1/2}$	28,962	28,818	28,865	28,850	28,797	28,824
G $^2\Pi_{3/2}$	29,391	29,276	29,323	29,309	29,257	29,284
H $^2\Sigma_{1/2}$	29,860	29,654	29,697	29,681	29,629	29,663
I $^2\Delta_{3/2}$	29,862	29,729	29,765	29,741	29,686	29,715
I $^2\Delta_{5/2}$	30,006	29,868	29,904	29,878	29,824	29,852

TABLE III. Theoretical results (in cm^{-1}) calculated at the FS-RCCSD-extAE3Z level for different numbers of correlated electrons. Unless specified in parenthesis, the shell contributions refer to electron shells belonging to the Ra atom.

State	97e	69e	35e	27e	17e	Shell contributions			
						$1s, ..., 3d$ (97e-69e)	$1s$(F) $4s4p4d4f$ (69e-35e)	$5s5p$ (35e-27e)	$5d$ (27e-17e)
X $^2\Sigma_{1/2}$	0	0	0	0	0	0	0	0	0
A $^2\Pi_{1/2}$	13,396	13,396	13,356	13,346	13,061	0	40	10	284
B $^2\Delta_{3/2}$	14,604	14,604	14,528	14,491	14,133	0	76	37	358
B $^2\Delta_{5/2}$	15,424	15,423	15,356	15,318	14,920	0	67	38	397
A $^2\Pi_{3/2}$	15,476	15,475	15,423	15,400	15,084	2	51	24	316
C $^2\Sigma_{1/2}$	16,792	16,790	16,745	16,727	16,446	2	45	18	280
D $^2\Pi_{1/2}$	22,899	22,899	22,837	22,814	22,443	1	62	23	371
D $^2\Pi_{3/2}$	23,238	23,237	23,177	23,154	22,769	1	60	23	385
E $^2\Sigma_{1/2}$	25,582	25,582	25,542	25,536	25,208	0	40	7	328
F $^2\Sigma_{1/2}$	28,457	28,457	28,400	28,389	27,995	0	57	11	394
G $^2\Pi_{1/2}$	28,985	28,985	28,936	28,926	28,542	0	49	9	384
G $^2\Pi_{3/2}$	29,400	29,400	29,351	29,339	28,955	1	49	11	384
H $^2\Sigma_{1/2}$	30,009	30,009	29,960	29,950	29,565	0	49	10	385
I $^2\Delta_{3/2}$	29,926	29,926	29,873	29,861	29,457	0	53	13	404
I $^2\Delta_{5/2}$	30,078	30,078	30,026	30,013	29,605	0	52	13	408

TABLE IV. Theoretical electronic excitation energies (in cm^{-1}) calculated with FS-RCCSD using the CV4Z and augmented CV4Z basis sets, for 27- and 69-electron correlation spaces. The results obtained with the non-augmented CV4Z basis set could not conclusively identify the energy of the three highest-lying states in this study.

State	27e-CV4Z	69e-CV4Z	69e-augCV4Z
X $^2\Sigma_{1/2}$	0	0	0
A $^2\Pi_{1/2}$	13,517	13,542	13,425
B $^2\Delta_{3/2}$	15,009	15,079	14,770
B $^2\Delta_{5/2}$	15,856	15,924	15,478
A $^2\Pi_{3/2}$	15,648	15,690	15,549
C $^2\Sigma_{1/2}$	17,079	17,112	16,773
D $^2\Pi_{1/2}$	23,491	23,537	22,762
D $^2\Pi_{3/2}$	23,819	23,864	23,105
E $^2\Sigma_{1/2}$	26,052	26,069	25,739
F $^2\Sigma_{1/2}$	29,149	29,185	28,671
G $^2\Pi_{1/2}$	30,779	30,804	29,152
G $^2\Pi_{3/2}$	31,362	31,390	29,580
H $^2\Sigma_{1/2}$	—	—	30,105
I $^2\Delta_{3/2}$	—	—	30,118
I $^2\Delta_{5/2}$	—	—	30,268

TABLE V. Calculated equilibrium bond length and harmonic vibrational spacing for the states under 30,000 cm^{-1} from the ground state.

State	r_e (Å)	ω_e (cm^{-1})
X $^2\Sigma_{1/2}$	2.24	440
A $^2\Pi_{1/2}$	2.24	435
B $^2\Delta_{3/2}$	2.25	426
B $^2\Delta_{5/2}$	2.25	430
A $^2\Pi_{3/2}$	2.24	437
C $^2\Sigma_{1/2}$	2.26	427
D $^2\Pi_{1/2}$	2.24	434
D $^2\Pi_{3/2}$	2.23	444
E $^2\Sigma_{1/2}$	2.19	481
F $^2\Sigma_{1/2}$	2.17	488
G $^2\Pi_{1/2}$	2.18	495
G $^2\Pi_{3/2}$	2.18	496
H $^2\Sigma_{1/2}$	2.18	510
I $^2\Delta_{3/2}$	2.18	497
I $^2\Delta_{5/2}$	2.18	497

Table 4.2: Comparison of experimental and theoretical electronic excitation energies (T_0, in units of cm^{-1}) in RaF. The theoretical values correspond to the 69e-extAE4Z calculations with 27e-T, CBS, Gaunt, and QED corrections (see Article 2 for details). The normalized theoretical agreement (%) is reported as $1 - \frac{|E_{\text{th}} - E_{\text{exp}}|}{E_{\text{exp}}}$. The states in parentheses are tentatively assigned. Statistical and systematic errors are given in round and square brackets.

State	Experimental	69e-extAE4Z+corr.	Agreement
$X\ ^2\Sigma_{1/2}$	0	0	
$A\ ^2\Pi_{1/2}$	13,284.427(1)[20]*	13,299(36)	**99.89**
$B\ ^2\Delta_{3/2}$	14,332.82(13)[51]**	14,300(61)	**99.77**
$(B\ ^2\Delta_{5/2})$	15,142.7(5)$^{\$}$	15,099(70)	**99.71**
$A\ ^2\Pi_{3/2}$	15,334.52(23)[35]	15,355(35)	**99.87**
$C\ ^2\Sigma_{1/2}$	16,613.6(12)$^{\#}$	16,615(69)	**99.99**
$E\ ^2\Sigma_{1/2}$	25,451.11(11)[26]	25,520(84)	**99.73**
$G\ ^2\Pi_{1/2}$	28,774.16(51)[35]	28,824(111)	**99.83**
$G\ ^2\Pi_{3/2}$	29,225.57(28)[51]	29,284(90)	**99.80**
$(H\ ^2\Sigma_{1/2})$	29,665.52(11)[51]	29,663(156)	**99.99**
$(I\ ^2\Delta_{3/2})$	29,693.15(24)[51]	29,715(102)	**99.92**
$I\ ^2\Delta_{5/2}$	29,801.59(7)[35]	29,852(106)	**99.83**

* Value from Ref. [2].

** Previously tentatively assigned at 15,142.7(5) cm^{-1} [5].

$^{\$}$ Value from Ref. [5]. Energy previously tentatively assigned as $B\ ^2\Delta_{3/2}$ ($v = 0$).

\# Extracted from values reported in Ref. [5]. The previous assignment at 16,175.2(5) cm^{-1} [5] was deduced from a measured transition that is now reassigned as $C\ ^2\Sigma_{1/2} \leftarrow X\ ^2\Sigma_{1/2}$ ($v' = 0 \leftarrow v'' = 1$) instead of $v' = 0 \leftarrow v'' = 0$.

Table 4.3: Comparison of electronic excitation energies (in cm^{-1}) assigned to low-lying states in RaF between Ref. [5] and this thesis. All assignments refer to the $v = 0$ vibrational state of each electronic state.

	Garcia et al. 2020	This work	Theory
$B\ ^2\Delta_{3/2}$	15,142.7(5)*	14,332.82(13)[51]	14,300(61)
$B\ ^2\Delta_{5/2}$	—	15,142.7(5)**	15,099(70)
$A\ ^2\Pi_{3/2}$	15,344.6(50)	15,334.52(23)[35]	15,355(35)
$C\ ^2\Sigma_{1/2}$	16,175.2(5)$^{\$}$	16,613.6(12)	16,615(69)

* Tentatively assigned in Ref. [5].

** With the discovery of a state at 14,332.82(13)[51] cm^{-1}, the previously measured transition is tentatively re-interpreted in this work as $B\ ^2\Delta_{5/2} \leftarrow X\ ^2\Sigma_{1/2}$ ($v' = 0 \leftarrow v'' = 0$), bringing the tentative assignment of both levels in excellent agreement with our more accurate theoretical predictions.

$^{\$}$ Following the new measurements, this transition is re-interpreted as $C\ ^2\Sigma_{1/2} \leftarrow X\ ^2\Sigma_{1/2}$ ($v' = 0 \leftarrow v'' = 1$). Using the values reported in Ref. [5], we place the $v' = 0 \leftarrow v'' = 0$ transition at 16,613.6(12) cm^{-1}, in agreement with the theoretical prediction.

Table 4.4: Information on the temperature distribution of the ensembles composing the RaF beam delivered by the ISCOOL RFQcb to the CRIS experiment.

	A^i (%)	b^i	J_c^i	T^i (K)
Scan 3745	100	0.0937763	25.7	380
	10^{-20}	47906.256	29.9	512
Weighted average				**380**
Scan 3804	73.4	0.0002473	24.5	346
	10.8	0.0265240	26.8	414
	8.2	0.0460373	28.0	450
	7.6	0.0526319	29.6	501
Weighted average				**374**
Scans 3808-3813	49.3	0.0001451	16.2	155
	25.6	0.0023817	12.6	95
	7.9	0.0382976	52.0	1527
	7.5	0.0431695	36.2	747
	5.0	0.0993234	34.7	685
	4.7	0.1097810	25.1	362
Weighted average				**329**
Scans 4243-4244	34.2	0.0609924	12.0	87
	24.3	0.1209796	26.3	399
	23.1	0.1338509	49.2	1367
	9.5	0.7835511	75.4	3190
	8.8	0.9164272	38.2	828
Weighted average				**820**

Chapter 5

Measurements in short-lived RaF isotopomers

5.1 Motivation for isotope-shift measurements in RaF

The experimental campaign that gave rise to the results presented in Chapter 4 also included broadband measurements of the $v' = 0 \leftarrow v'' = 0$ vibrational transition of $A\ ^2\Pi_{1/2} \leftarrow X\ ^2\Sigma_{1/2}$ for the longest range of molecular isotopomers to date (spanning 20 atomic mass units).

The general motivation of performing measurements across many isotopomers of RaF is to extract the isotope shifts in the $A\ ^2\Pi_{1/2} \leftarrow X\ ^2\Sigma_{1/2}$ ($v' = 0 \leftarrow v'' = 0$) transition. Measurements of isotope shifts have been a staple of atomic laser spectroscopy for nuclear-structure research for many decades [8, 7], as the isotope shifts are sensitive to the changes in mean-squared nuclear charge radii $\delta\langle r^2\rangle$ of short-lived radioactive nuclei. The evolution of $\delta\langle r^2\rangle$ in the radium chain has been extensively studied, with measurements spanning from ^{208}Ra up to ^{233}Ra [3, 136, 137, 138]. For isotope shifts in diatomic molecules, a brief summary of the key literature can be found in Chapter 3.

Isotope-shift measurements across a long chain of RaF isotopomers are of interest for both nuclear and molecular structure. Firstly, as a probe for nuclear-structure research, performing measurements in RaF as opposed to atomic (or ionic) Ra can potentially bypass the overwhelming isobaric contamination of surface-ionized francium that limits the range of radium isotopes that can be measured with existing laser-spectroscopic techniques at RIB facilities [137]. As FrF is bound by a single, purely ionic chemical bond, FrF^+ is not a stably bound species and cannot be extracted from the high-temperature environment of ISOL targets. Therefore, by extracting RaF and mass-separating it from the contamination using a dipolar magnetic separator, the otherwise overwhelming contamination of Fr^+ with mass A is fully filtered out of the RaF^+ beam, whose mass is $A + 19$ atomic mass units due to the presence of $^{19}\mathrm{F}$.

Secondly, isotope-shift measurements allow for the extraction of the molecular isotope-shift factors; namely, the molecular field-shift factor Ψ and mass-shift factor Ξ. Like in the atomic case, the field-shift factor quantifies the spatial overlap of the electronic wavefunction with the nuclear volume, while the molecular mass-shift factor is not yet fully understood but is related to the total electron correlation energy and the breakdown of the Born-Oppenheimer approximation (Chapter 3).

For molecules of interest for precision tests of the SM, calculations of molecular sensitivity factors to symmetry-violating moments often quantify the theoretical error by also calculating the electromagnetic fields in the molecule and comparing them with experimental values for the magnetic dipole hyperfine constants (for example, see Refs. [119, 139, 140] for RaF, HfF^+, and ThO). The reasoning for such comparisons is that the symmetry-violating nuclear moments also emerge from the multipole expansion of the nuclear potential, similar to the symmetry-preserving magnetic dipole and electric quadrupole moments. Therefore, the calculated sensitivities to the symmetry-violating moments can be best benchmarked through the accuracy of the factors for the symmetry-preserving (and experimentally studied) ones. For the eEDM, which is not a nuclear property, the molecular sensitivity is quantified by the internal effective electric field E_{eff} in the molecule, which can be semi-empirically linked to the magnetic dipole matrix elements, as well [141].

However, the molecular sensitivity to symmetry-preserving and symmetry-violating nuclear moments does not necessarily emerge from identical interactions. For instance, contrary to the nuclear magnetic dipole moment, which manifests in the molecular hyperfine structure through both a long-distance interaction that does not require spatial electron-nucleus overlap and a Fermi-contact interaction that does [142], the nuclear EDM is fully shielded by the potential of the electron cloud, leading to no net long-distance interaction with the electrons (this is the result of the Schiff theorem [72]). Instead, it is only the contact interaction of nucleus-penetrating relativistic valence electrons, which interact with a P, T-violating intranuclear electric field (emerging from the nuclear EDM), that gives rise to an overall P, T-violating shift in the electronic energy of a polarized molecule [72, 9].

Due to the critical role of the electron-nucleus spatial overlap, benchmarks of molecular sensitivity calculations for P, T-violating nuclear moments based on the field-shift factor would be highly beneficial. Nevertheless, so far no such benchmarks have taken place for molecules of interest for precision tests of the SM.

A central reason for this is that measurements of molecular isotope shifts are scarce, since no element heavier than Pb has three or more sufficiently long-lived isotopes, and thus the isotope-shift measurements must be performed at RIB facilities. So far, no isotope-shift measurements have been performed for heavy polar molecules promising for searches of the nuclear Schiff moment, with the exception of recent measurements in RaF [4].

The previous work in RaF by Udrescu *et al.* [4] presented isotope shifts for the 0←0, 1←1, 2←2, and 3←3 vibrational transitions of $A\ ^2\Pi_{1/2} \leftarrow X\ ^2\Sigma_{1/2}$ across the 5 longest-lived RaF isotopomers, $^{223-226,228}$RaF. In this thesis, measurements of the 0←0 vibrational transition in $A\ ^2\Pi_{1/2} \leftarrow X\ ^2\Sigma_{1/2}$ are reported for $^{210,212-214,224-227,230}$RaF. The purpose of these measurements was to constrain the statistical error of the field-shift factor in RaF at an improved level compared to the study by Udrescu *et al.*

In the following sections, firstly we extract the molecular field-shift factors in RaF using the approach outlined in Chapter 3, starting from the measured isotope shifts reported in Ref. [4]. This impacts the uncertainties of the field-shift factors in comparison to the results of Ref. [4]. Secondly, the newly obtained measurements are presented and analyzed. It is shown that due to lineshape distortions caused by the use of a three-step laser scheme, the new results are not fit for constraining the field-shift factor, but they provide important insights into the systematic effects of molecular spectroscopy with CRIS and they demonstrate that the technique is capable of studying isotopomers with low production rates.

5.2 Independent analysis of published results

The isotope shifts for different vibrational transitions of $A\ ^2\Pi_{1/2} \leftarrow X\ ^2\Sigma_{1/2}$ that were published by Udrescu *et al.* are shown in Table 5.1 in the original units (cm^{-1}) and in Table 5.2 in units of GHz, which are more common in isotope-shift studies.

Table 5.1: Isotope shifts (in cm^{-1}) for different diagonal vibrational transitions of the $A\ ^2\Pi_{1/2} \leftarrow X\ ^2\Sigma_{1/2}$ electronic transition in RaF, with respect to the transition energies in ^{226}RaF. The table appears as Table 1 in Ref. [4].

	$\delta\nu^{A,226}_{0\leftarrow0}$	$\delta\nu^{A,226}_{1\leftarrow1}$	$\delta\nu^{A,226}_{2\leftarrow2}$	$\delta\nu^{A,226}_{3\leftarrow3}$
^{223}RaF	0.269(9)	0.278(14)	0.274(30)	0.298(63)
^{224}RaF	0.176(13)	0.177(28)	0.178(31)	0.064(80)
^{225}RaF	0.117(46)	0.100(74)	0.121(75)	0.001(31)
^{226}RaF	0	0	0	0
^{228}RaF	-0.184(17)	-0.179(26)	-0.251(60)	-0.374(123)

Table 5.2: Isotope shifts appearing in Table 5.1 in units of GHz.

	$\delta\nu^{A,226}_{0\leftarrow0}$	$\delta\nu^{A,226}_{1\leftarrow1}$	$\delta\nu^{A,226}_{2\leftarrow2}$	$\delta\nu^{A,226}_{3\leftarrow3}$
^{223}RaF	8.1(3)	8.3(4)	8.2(9)	8.9(19)
^{224}RaF	5.3(4)	5.3(8)	5.3(9)	1.9(24)
^{225}RaF	3.5(14)	3.0(22)	3.6(22)	0.0(9)
^{226}RaF	0	0	0	0
^{228}RaF	-5.5(5)	-5.4(8)	-7.5(18)	-11.2(37)

The analysis that the authors followed uses values for the changes of the mean-squared nuclear charge radii $\delta\langle r^2\rangle^{A,226}$ that are extracted from isotope shifts for the 468-nm 7s $^2\mathrm{S}_{1/2}$ →7p $^2\mathrm{P}_{1/2}$ transition in $^{223-226,228}\mathrm{Ra}^+$, as reported in Ref. [138] and summarized by Wansbeek *et al.* [3]. Using these values of $\delta\langle r^2\rangle^{A,226}$ and ignoring the mass-shift contribution (following the assessment by Wansbeek *et al.*, informed by their calculations of the mass-shift factor and justified as due to the large mass of the system), the authors thus extracted experimental values for the molecular field-shift factors F^{ii}_{RaF} through the general first-order isotope-shift equation:

$$\delta\nu^{A,226}_{i\leftarrow i} = F^{ii}_{\mathrm{RaF}}\delta\langle r^2\rangle^{A,226} + K^{ii}_{\mathrm{RaF}}\frac{M^A - M^{226}}{M^A M^{226}} \tag{5.1}$$

By assuming that $\frac{M^A-M^{226}}{M^A M^{226}} = 0$ for all masses M^A, thus ignoring the mass-shift factor K^{ii}_{RaF}, the equation can be simplified to:

$$\delta\nu^{A,226}_{i\leftarrow i} = F^{ii}_{\mathrm{RaF}}\delta\langle r^2\rangle^{A,226} \tag{5.2}$$

As per Eqns. 5.2-5.1, a separate linear fit for each value of i from 0 to 3 (denoting the 4 vibrational transitions tabulated in Tables 5.1-5.2) yields F^{ii}_{RaF} as the slope of the respective fit.

In Ref. [3], Wansbeek *et al.* carried out detailed quantum-chemistry calculations of the field- and mass-shift factors for the 468-nm 7s $^2\mathrm{S}_{1/2}$ → 7p $^2\mathrm{P}_{1/2}$ transition in Ra^+, taking into account higher-order contributions to the atomic structure due to nuclear deformation. Following a holistic review of the results of Dirac-Fock and coupled-cluster calculations using a spherical and a deformed Fermi models for the nuclear distribution, Wansbeek *et al.* deduced a computational uncertainty of 5% in their calculated field-shift factor F_{468} for Ra^+ and recommended revised values of $\delta\langle r^2\rangle^{A,226}$ in Table 6 of Ref. [3].

While Udrescu *et al.* made reference to the extended calculations by Wansbeek *et al.*, they did not make use of the values for $\delta\langle r^2\rangle^{A,226}$ or the isotope shifts B^i that Wansbeek *et al.* recommended in their RaF analysis. Specifically, they calculated the F_{468} factor for the same transition in Ra^+ using relativistic Fock-space coupled-cluster theory at the singles and doubles level correlating 27 electrons [FSCCSD(27e)] and a Gaussian nuclear model. As their value for F_{468} deviated by 3% from that of Wansbeek *et al.*, it was expressed that a 3% uncertainty should be considered due to the use of the simplistic Gaussian nuclear model instead of the more detailed deformed Fermi model. Such a 3% error contribution was thus considered for their calculations of F^{ii}_{RaF} using FSCCSD(27e).

This deduced uncertainty, however, is incorrect, as the value by Wansbeek *et al.* has a 5% uncertainty. Adding the 3% deviation and the 5% uncertainty in quadrature, assuming they are uncorrelated, leads to a 6% overall error contribution for the calculations by Udrescu *et al.*

Despite the authors acknowledging that their calculation of F_{468} for Ra^+ is less detailed than that by Wansbeek *et al.*, the values of $\delta\langle r^2\rangle^{A,226}$ used in their analysis of the isotope shifts in RaF were extracted using the measured 468-nm isotope shifts in Ra^+ [138] and their newly calculated value for F_{468}, which is expressed in text as $F_{468} = -1.283(3)$ cm^{-1} fm^{-2}. While the relative error of 0.2% in their expressed F_{468} is probably a typographic error, the decision to not use the values recommended by the in-depth review of Wansbeek *et al.* was not justified in the text.

Moreover, the experimentally deduced field-shift factors in RaF F^{ii}_{RaF} that are reported in Table 2 of Ref. [4] by Udrescu *et al.* are given with relative errors of 2.8%, 4.5%, 8.6%, and 19.3% for $i = 0, 1, 2, 3$, respectively. These results call for revision, as it appears that the value for F^{00}_{RaF} is more precise than the value for F_{468} that is used as a precursor in extracting F^{ii}_{RaF}, whether a 6% or a 3% error is considered for F_{468}.

Therefore, an independent re-analysis of the results for F^{ii}_{RaF} is needed to extract the errors for F^{ii}_{RaF} in a more robust way, using the measured isotope shifts in RaF reported in Ref. [4] and following the approach of Article 1.

In the present analysis, the molecular field-shift factors are extracted from a King plot using the isotope shifts B^i (note the unconventional notation by Wansbeek *et al.*) and F_{468} directly, rather than through $\delta\langle r^2\rangle$ (used in Ref. [4]). By ignoring the mass shift, Wansbeek *et al.* extracted $\delta\langle r^2\rangle^{A,214}$ from the following expression, which appears as

Eqn. 4 in Ref. [3] (with slightly different subscripts and superscripts):

$$\delta\langle r^2\rangle^{A,214} = \frac{1}{F_{468}} B^{A,214} \tag{5.3}$$

where the superscripts are modified here to highlight that their results were retrieved with ^{214}Ra as the reference. Therefore, the $B^{A,214}$ values reported by Wansbeek *et al.* are simply the isotope shifts for the 468-nm transition, albeit with an unconventional notation. We can use $B^{A,214}$ and F_{468} in a King-plot analysis with the molecular isotope shifts to extract the F^{ii}_{RaF} factors.

Wansbeek *et al.* tabulated the values of isotope shifts B in Table 6 of Ref. [3], but they are referenced with respect to the value for ^{214}Ra. To convert $B^{A,214}$ to $B^{A,226}$, the value of $B^{226,214}$ was subtracted from all other values as $B^{A,226} = B^{A,214} - B^{226,214}$. The resulting $B^{A,226}$ values are given in Table 5.3 of this chapter.

For F_{468}, we can obtain the value from an orthogonal distance regression (ODR) (shown in Fig. 5.1) using the $B^{A,226}$ and $\delta\langle r^2\rangle$ data reported by Wansbeek *et al.*, as per Eqn 5.3, yielding $F_{468} = -39.0(19)$ GHz fm^{-2}. The uncertainty is set at 5% of the nominal value, as specified by Wansbeek *et al.* The value of $F_{468} = -39.0(19)$ GHz fm^{-2} that we find by performing ODR with $B^{A,226}$ and $\delta\langle r^2\rangle$ is different from the value of $F_{468} = -39.8$ GHz fm^{-2} that Wansbeek *et al.* mention in their text. It is unclear why the value they report differs from the ODR result of the isotope shifts and radii they also report. Possibly, it can be attributed to a typographic error, or the value they mention does not consider all the nuclear-shape corrections they derived. In this chapter, the ODR value of $F_{468} = -39.8$ GHz fm^{-2} is used.

With the knowledge of $B^{A,226}$ and F_{468}, the values for F^{ii}_{RaF} were extracted from the following simplified King-plot relation

$$\delta\nu^{A,226}_{i\leftarrow i} = \frac{F^{ii}_{\mathrm{RaF}}}{F_{468}} B^{A,226} \tag{5.4}$$

for the 4 diagonal vibrational transitions ($i = 0, 1, 2, 3$).

An ODR routine was performed for each vibrational line. The resulting best-fit slopes were:

$$\frac{F^{00}_{\mathrm{RaF}}}{F_{468}} = 0.661(15)$$

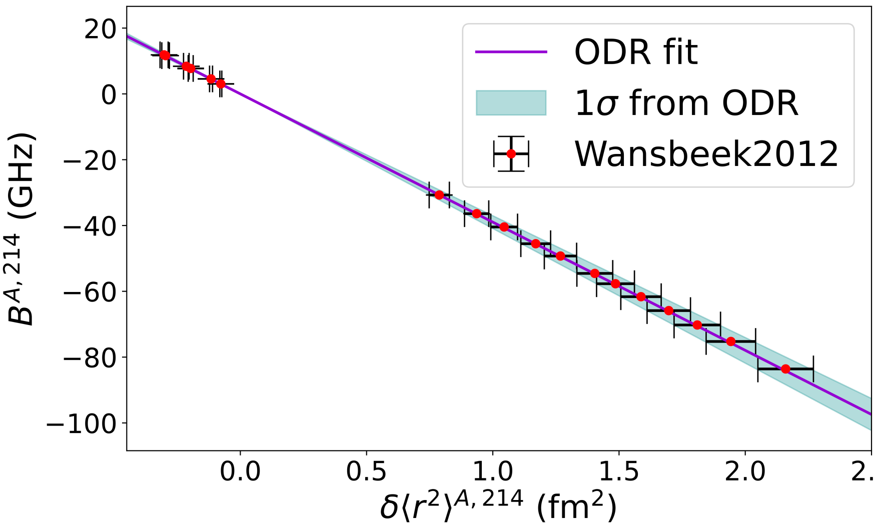

Figure 5.1: Result of orthogonal distance regression (ODR) between $\delta\langle r^2\rangle^{A,214}$ and $B^{A,214}$ from Ref. [3].

$$\frac{F^{11}_{\mathrm{RaF}}}{F_{468}} = 0.676(12)$$

$$\frac{F^{22}_{\mathrm{RaF}}}{F_{468}} = 0.680(50)$$

$$\frac{F^{33}_{\mathrm{RaF}}}{F_{468}} = 0.560(210)$$

Therefore, when multiplied by the previously extracted $F_{468} = -39.0(19)$ GHz fm^{-2}, the following values were obtained for F^{ii}_{RaF}:

$$F^{00}_{\mathrm{RaF}} = -25.8(14)[3] \text{ GHz fm}^{-2}$$

$$F^{11}_{\mathrm{RaF}} = -26.3(14)[3] \text{ GHz fm}^{-2}$$

$$F^{22}_{\mathrm{RaF}} = -26.6(22)[3] \text{ GHz fm}^{-2}$$

$$F^{33}_{\mathrm{RaF}} = -21.9(84)[2] \text{ GHz fm}^{-2}$$

The errors in brackets stem from the ODR and those in square brackets are systematic and correspond to 1% of the nominal value to account for neglecting the mass shift in the King plot. These results are compared to those by Udrescu *et al.* in Fig. 5.6, where all results are shown in units of $\mathrm{cm}^{-1}\ \mathrm{fm}^{-2}$, following the convention in Ref. [4]. The results are also compared in Table 5.4.

As expected, only minimal differences are seen in the nominal values of the field-shift factors, stemming from the slight difference in the value of F_{468} that is used in each analysis. However, the 1σ error of F^{00}_{RaF} is found in the current analysis to be more than a factor-2 greater compared to the value of Udrescu *et al.*, while the errors for the other factors are also larger. Evidently, all relative errors in the re-analyzed F^{ii}_{RaF} factors are slightly larger than 5%, as expected. In Fig. 5.7, the values for $\delta\langle r^2\rangle^{A,226}$ extracted from the isotope shifts in the 0←0 line using the re-analyzed field-shift factor are shown and compared for the F^{00}_{RaF} value of each analysis.

Table 5.3: Summary of isotope shifts B used in the current analysis. The values of $B^{A,214}$ are taken from Table 6 of Ref. [3] where they appear as B^i.

A_{Ra}	$B^{A,214}$ (MHz)	$B^{A,226}$ (GHz)
223	-45533(23)	12.159(37)
224	-49274(24)	8.418(38)
225	-54560(27)	3.132(40)
226	-57692(29)	0(0)
228	-65864(34)	-8.172(45)

5.3 Analysis of new measurements

To extend the range of isotope shifts measured in Ref. [4], new measurements of the $A\ ^2\Pi_{1/2} \leftarrow X\ ^2\Sigma_{1/2}$ (0←0) transition were performed in the short-lived $^{210,212-214,223,224,226,227,230}$Ra that contain radium nuclei with half-lives down to 2.44 s for ^{214}RaF, which marks

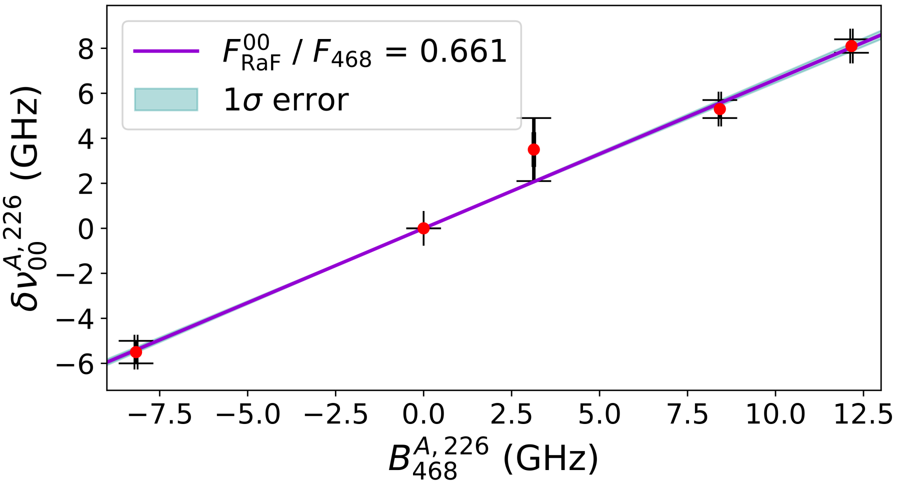

Figure 5.2: King plot used to extract F^{00}_{RaF}.

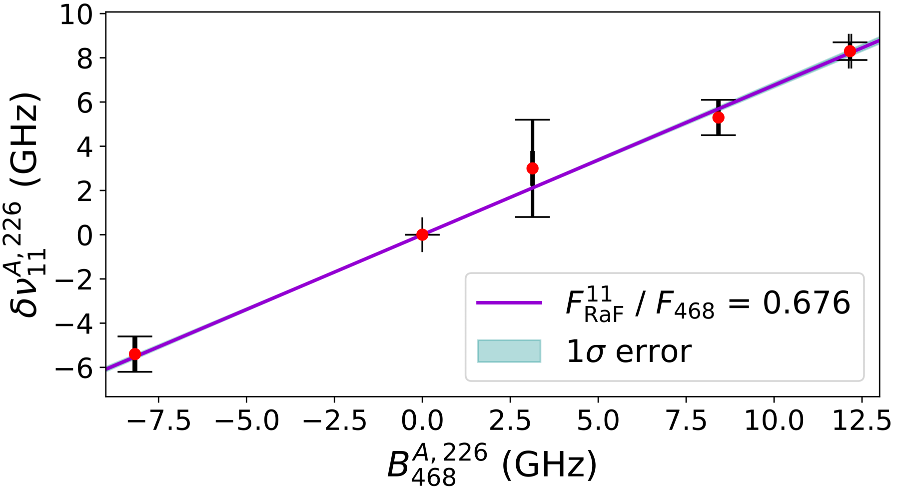

Figure 5.3: King plot used to extract F^{11}_{RaF}.

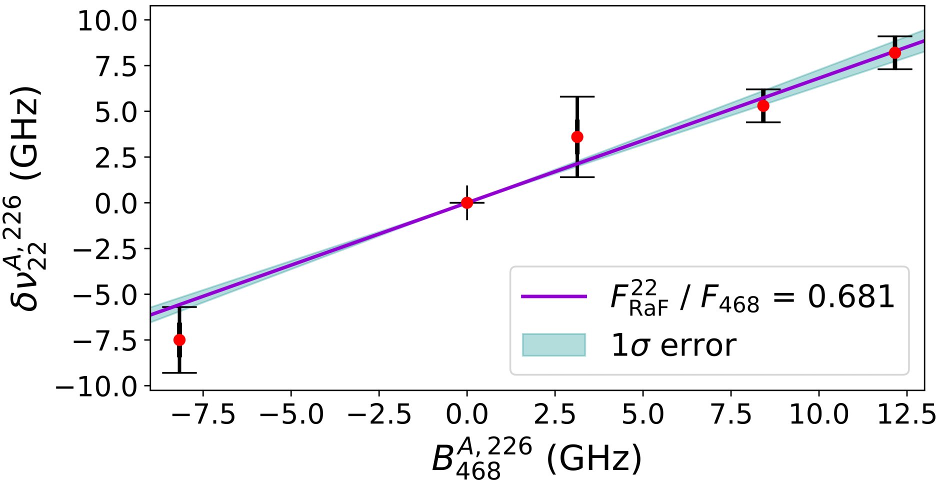

Figure 5.4: King plot used to extract F_{RaF}^{22}.

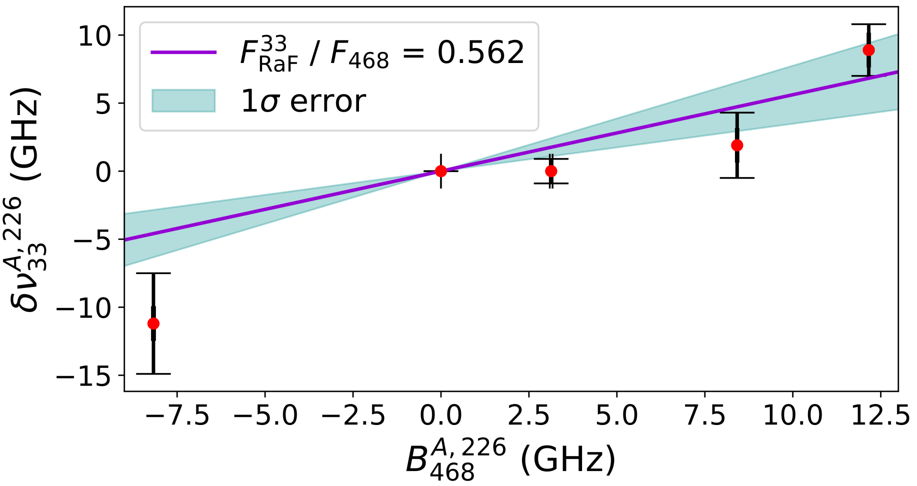

Figure 5.5: King plot used to extract F_{RaF}^{33}.

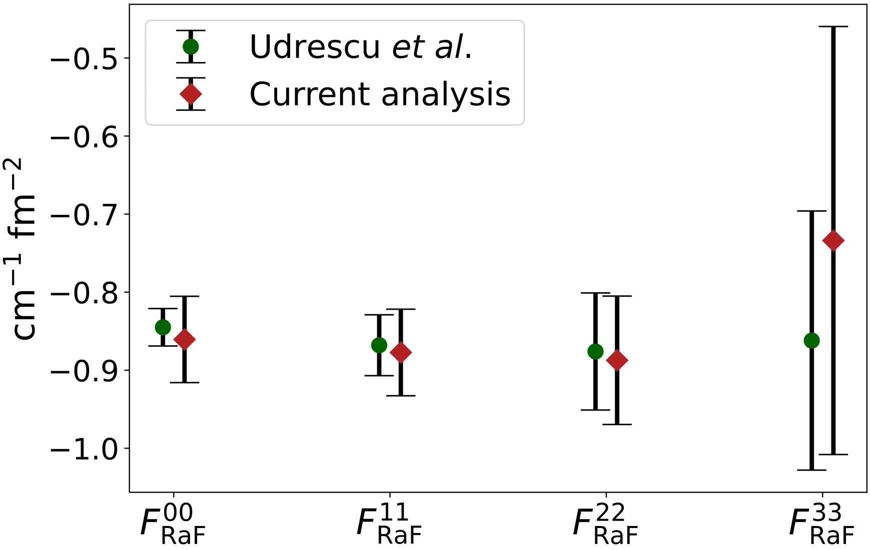

Figure 5.6: Comparison of extracted F^{ii}_{RaF} between Udrescu *et al.* [4] and the current re-analysis.

Table 5.4: Comparison of F^{ii}_{RaF} (in units of cm^{-1} fm^{-2}) between Ref. [4] and the independent analysis in this chapter.

	Udrescu *et al.*	Current re-analysis
F^{00}_{RaF}	-0.845(24)	-0.861(55)
F^{11}_{RaF}	-0.868(39)	-0.877(55)
F^{22}_{RaF}	-0.876(75)	-0.887(82)
F^{33}_{RaF}	-0.862(166)	-0.734(274)

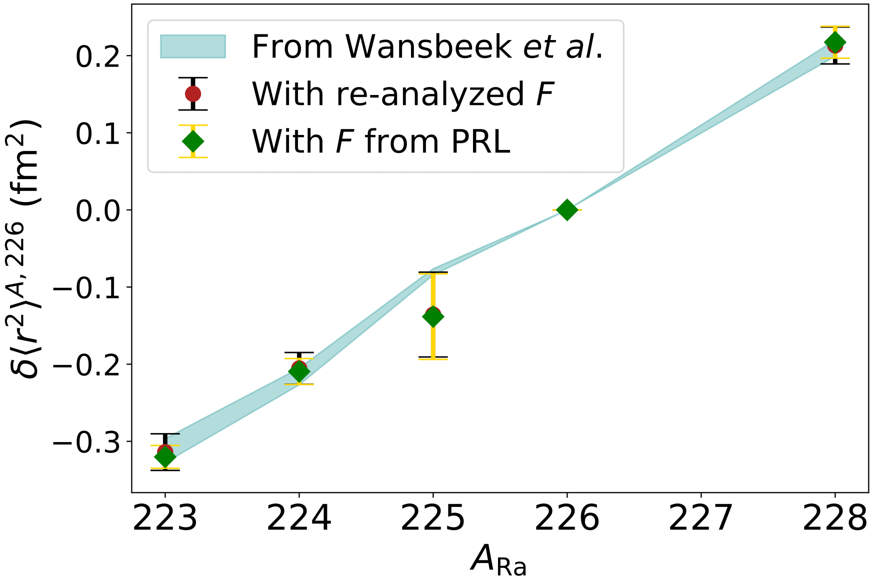

Figure 5.7: Comparison of changes in mean-squared charge radii extracted from the $\delta\nu^{A,226}_{0\leftarrow0}$ isotope shifts using the re-analyzed F^{00}_{RaF} and the value presented in Ref. [4].

this as the study of the shortest-lived radioactive molecule to date to the knowledge of the author.

The goal of the experiment was to attempt accessing isotopomers that contain Ra isotopes beyond the range accessible by atomic spectroscopy at ISOLDE. However, when studying very neutron-deficient RaF, the combined mass of the neutron-deficient Ra and ^{19}F approaches that of neutron-rich atomic francium, which is very intensely produced at ISOL facilities. Consequently, the attempt to measure $^{207-209}$RaF with the CRIS experiment was hindered by the overwhelming presence of $^{226-228}$Fr. Consequently, only down to ^{210}RaF could be studied with broadband laser spectroscopy.

Due to the lower production rates of the short-lived isotopes compared to the long-lived $^{223-226,228}$RaF, leading to a reduced signal-to-noise ratio, the two-step laser scheme used in Ref. [4] (Fig. 5.8a) could not be employed, as the use of 355-nm non-resonant ionization leads to a high spectroscopic background. The spectra were thus measured using the most efficient three-step laser scheme found in the experiment described in Chapter 4, where the $A\ ^2\Pi_{1/2} \leftarrow X\ ^2\Sigma_{1/2}$ (0←0) transition acted as the first step while the second resonant step was kept fixed. The use of two resonant transitions enabled the use of 532-nm non-resonant ionization, leading to lower background. The laser scheme used is shown in Fig. 5.8b. As seen in Fig. 5.9a, the two-step scheme with 355 nm leads to ×2 higher signal but ×10 higher background compared to the employed three-step scheme.

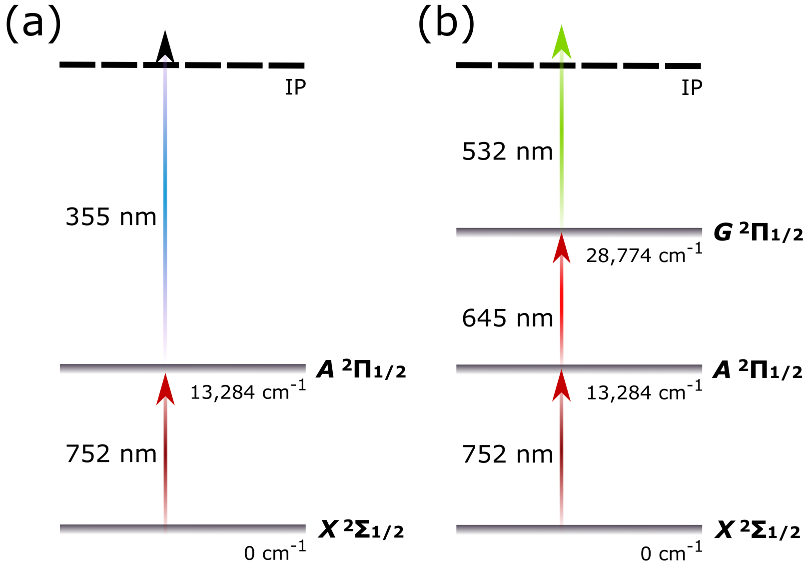

Figure 5.8: **(a)** Laser scheme used for the measurements in long-lived RaF in Ref. [4]. **(b)** Laser scheme used for the short-lived isotopomers in this thesis.

All spectra were binned using a 3-GHz bin size, identical to the analysis in Chapter 4. For the isotopomers where more than 1 scan was obtained, all scans for the same isotopomer were combined into one spectrum. The spectra were then analyzed with the contour-fitting routine of PGOPHER [132] to extract the excitation energy of the $A\ ^2\Pi_{1/2}\ v = 0$ state and trace its shift as a function of radium mass number.

The molecular parameters of the $X\ ^2\Sigma_{1/2}$ and the $A\ ^2\Pi_{1/2}$ states are known with good precision from the analysis of narrowband spectroscopy in ^{226}RaF [2]. The initially set parameters for all PGOPHER contour fits were scaled from the molecular parameters of ^{226}RaF reported in Ref. [2]. The parameter scaling from ^{226}Ra^{19}F to any other isotopomer ^{A}Ra^{19}F follows the simple relation that also holds for Dunham parameters [101, 87]:

$$Y^{A,19} = \frac{\mu^{226,19}}{\mu^{A,19}} Y^{226,19} \tag{5.5}$$

where $Y^{A,19}$ is a molecular parameter of ^{A}Ra^{19}F and $\mu^{A,19}$ is the reduced molecular mass $\mu = \frac{M_A^{\mathrm{Ra}} M_{19}^{\mathrm{F}}}{M_A^{\mathrm{Ra}} + M_{19}^{\mathrm{F}}}$ with M_A^{Ra} and M_{19}^{F} being the masses of ^{A}Ra and ^{19}F, respectively, taken from the 2020 Atomic Mass Evaluation.

During the fitting process, the γ and D parameters of the $X\ ^2\Sigma_{1/2}$ state and the p and D parameters of the $A\ ^2\Pi_{1/2}$ state were fixed to the mass-scaled values while fitting the upper and lower rotational constants B_Σ and B_Π and the excitation energy E of the $A\ ^2\Pi_{1/2}$ state.

The effect of double J selectivity caused by the two resonant transitions in the three-step scheme induces a shift in the center of gravity of the measured spectrum, which appears as an effective isotope shift. This is visualized in Fig. 5.9b. As a result, the isotope shifts cannot be analyzed by fitting a skewed Voigt profile on the measured structure, as previously done for the two-step spectra presented in Ref. [4]. In Chapter 4, the effect of double J selectivity was treated at a satisfactory level by fitting the spectrum with a non-uniform temperature distribution. The same approach was followed in this analysis too, with 3 separate temperature groups being considered for each spectrum.

Beyond an effective isotope shift, the effect of double J selectivity due to the three-step scheme induces general lineshape distortions, which depend on the mismatch between the two J-selective regions of the resonant steps. As seen in Fig. 5.10, the shape of the structure differs drastically for each scan, as the isotope shift in the second step was not taken into account between isotopomers, and thus the overlap between the J-selective ranges of the first and second steps evolves. These distortions increase the difficulty of accurately fitting these spectra.

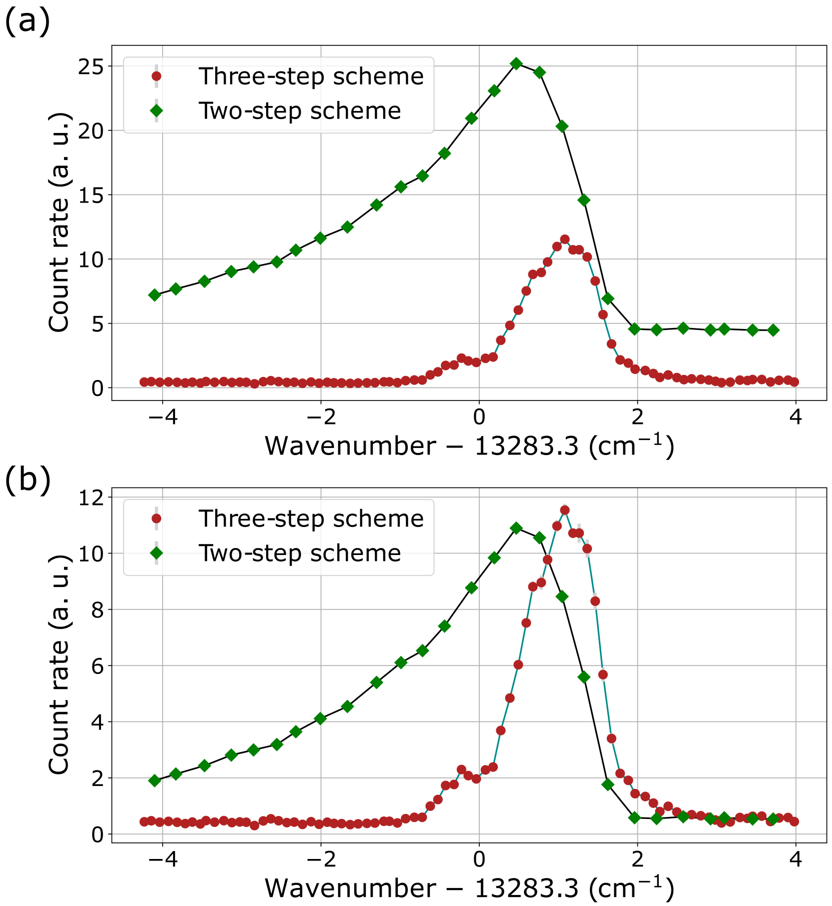

Figure 5.9: Comparison of spectra of the $A\ ^2\Pi_{1/2} \leftarrow X\ ^2\Sigma_{1/2}$ $(0 \leftarrow 0)$ transition obtained with a two-step (Fig. 5.8a) and a three-step (Fig. 5.8b) laser scheme. **(a)** Spectra shown at the scale and magnitude they were obtained. **(b)** The spectrum obtained with the two-step scheme is scaled down to the height and background of the one obtained with the three-step scheme.

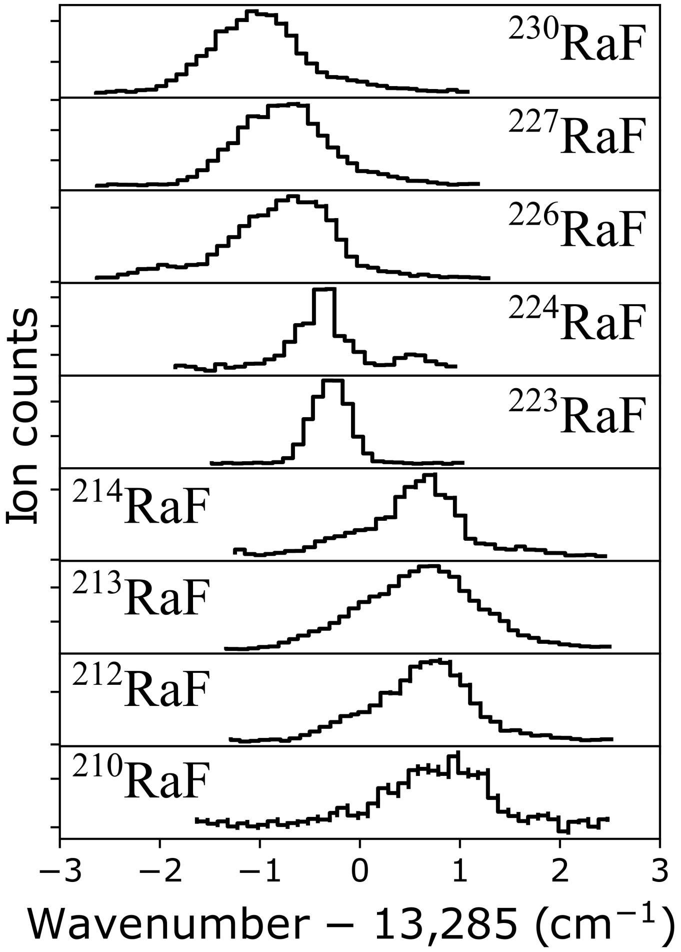

Figure 5.10: Measured broadband spectra for the $A\ ^2\Pi_{1/2} \leftarrow X\ ^2\Sigma_{1/2}$ $(0 \leftarrow 0)$ transition in RaF isotopomers. An offset of $-13,285$ cm^{-1} is applied to the x-axis.

5.3.1 Results

The fitted results are given in Table 5.5. Using the re-analyzed value for F^{00}_{RaF} from the previous section, the isotope shifts from Table 5.5 were used to extract changes in the mean-squared nuclear charge radii for the radium isotopes, which are visually compared to the values from Wansbeek *et al.* [3] in Fig. 5.11.

Evidently, the measured isotope shifts are not at all consistent with the trend that should be expected based on the changes in charge radii measured with atomic spectroscopy, which is in stark contrast with the measurements in the long-lived isotopomers that agree with the literature trend. (Fig. 5.7).

Table 5.5: Excitation energies E (in cm^{-1}) and isotope shifts $\delta\nu^{A,226}$ (in GHz) for the $A\ ^2\Pi_{1/2}$ $v = 0$ band in newly measured isotopomers. The reduced chi (χ_r) of the contour fit for each isotopomer is also included, as well as the fitted rotational constants (in cm^{-1}) for the lower ($X\ ^2\Sigma_{1/2}$) and upper ($A\ ^2\Pi_{1/2}$) states. Errors in parentheses are statistical and have been scaled by χ_r. Systematic errors of 0.52 cm^{-1} are considered for the excitation energies as in Chapter 4 but not denoted.

	χ_r	E	$\delta\nu^{A,226}$	B_Σ	B_Π
^{210}RaF	1.7	13286.32(5)	41.6(16)	0.193901(38)	0.193000(80)
^{212}RaF	2.1	13286.40(6)	44.1(18)	0.193301(40)	0.191691(76)
^{213}RaF	4.2	13286.60(7)	50.2(21)	0.193193(16)	0.191623(55)
^{214}RaF	4.1	13285.81(8)	26.4(23)	0.193095(80)	0.192061(353)
^{226}RaF	2.8	13284.93(8)	0(0)	–	–
^{227}RaF	2.6	13284.87(5)	-1.7(16)	0.195297(77)	0.193537(190)
^{230}RaF	2.9	13284.46(7)	-14.1(20)	0.194024(75)	0.192311(212)

The inconsistent results for the excitation energies can be attributed to the erratic lineshapes in the new measurements due to the three-step scheme (see Fig. 5.10). This is exemplified in Fig. 5.12. The same spectrum has a drastically different shape when the second step is kept fixed at different wavelengths. As a result, without precise knowledge of the structure of the second step, which can be obtained only through narrowband laser spectroscopy, the J-selective range of the second step cannot be constrained well enough to accurately extract the excitation energy of the $A\ ^2\Pi_{1/2}$ state, as the range of J values that the second step promotes to the last excitation step are not known with high accuracy.

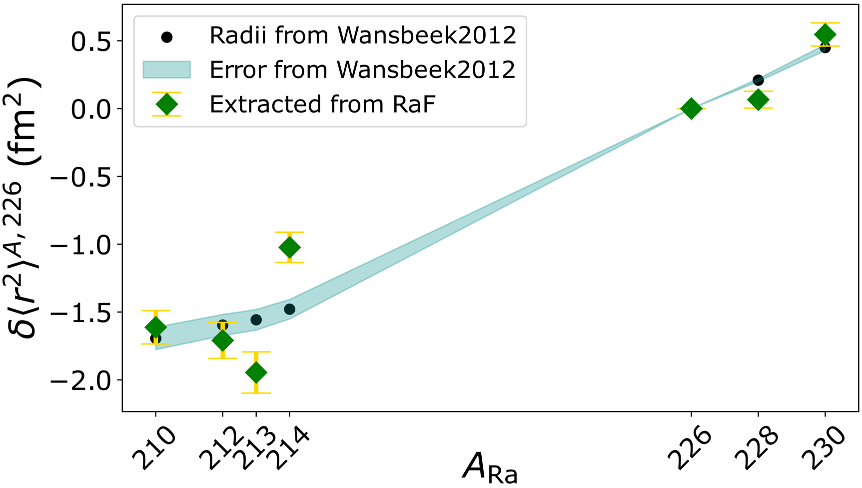

Figure 5.11: Comparison of mean-squared nuclear charge radii $\langle r^2\rangle^{A,226}$ for radium isotopes, extracted from the new measurements of isotope shifts in short-lived RaF isotopomers and the results of atomic spectroscopy given in Ref. [3].

5.3.2 Considerations for a future re-measurement

Laser scheme selection

The results of this section highlight the need for a re-measurement of the presented data in the short-lived isotopomers of RaF. As demonstrated by Ref. [4], the use of a two-step scheme does not cause the problems that hinder the accurate analysis of the new isotope-shift measurements, and should thus be preferred for such future measurements.

However, as shown in Fig. 5.9a, the two-step scheme results in a ×5 worse signal-to-noise ratio, which can be prohibitive in the study of weakly produced isotopomers. Additionally, for neutron-deficient isotopomers, the presence of neutron-rich atomic Fr has to be considered, whose low IP leads to a strong contribution to the non-resonant background with 355 nm.

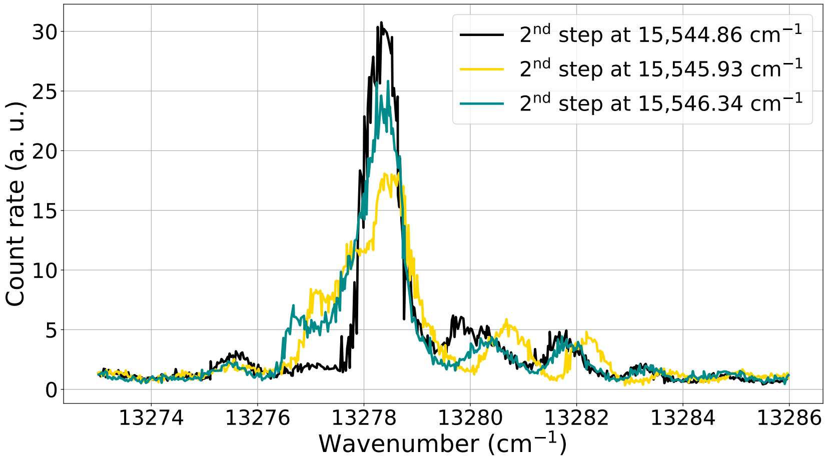

Figure 5.12: Changes in the spectrum of the $A\ ^2\Pi_{1/2} \leftarrow X\ ^2\Sigma_{1/2}$ $(1 \leftarrow 1)$ transition for different wavelengths of the second resonant transition in the three-step scheme.

Moreover, contrary to the atomic picture, the large amount of possible rovibrational states that a molecule can populate even at room temperature leads to a significantly reduced spectroscopic efficiency than what is typically achieved for atoms at CRIS, even when using a broadband laser. As a result, isobaric contamination is especially problematic in the case of molecular spectroscopy. The reduced efficiency is also the reason that new measurements for neutron-rich radium beyond ^{230}Ra were not attempted with RaF, even in the absence of isobaric Fr, as the production yields were too low for the achieved efficiency. Therefore, the choice of a suitable scheme for isotope shifts in RaF has to be made with care.

Consequently, in terms of a two-step scheme, the one used in the past (Fig. 5.9a) is unsuitable due to the use of 355-nm non-resonant ionization, especially in the presence of Fr contamination. When looking at the measured and predicted level scheme of RaF in Fig. 2 of Article 2 (Section 4.4), there are only two electronic states ($D\ ^2\Pi_{1/2,3/2}$) that could combine strong dipole-allowed transitions from the ground state and subsequent non-resonant ionization at 532 nm, but these states have not been experimentally confirmed yet.

From the higher-lying states, the $G\ ^2\Pi_{1/2,3/2}$ doublet could potentially have strong transitions from the ground state and would be ionizable with 532 nm, but the transitions from the ground state (at $\sim$350 nm) are not easily excitable with the harmonics of titanium:sapphire lasers. As a result, while broadband spectroscopy with a frequency-doubled pulsed dye laser could be performed (using Pyridine 1 or 2), the possibility of performing narrowband spectroscopy of the same transition in the future at CRIS is challenging, requiring the cumbersome use of a pulsed dye amplifier. Prior to designing a future re-measurement of isotope shifts far from ^{226}RaF with optimal conditions, the excitation energy and transition strength from the ground state to the $D\ ^2\Pi_{1/2,3/2}$ doublet must thus be experimentally confirmed.

Feasibility of rovibrational cooling

For a universal improvement of spectroscopic efficiency across all transitions and in all molecular species, the molecules delivered from ISOLDE need to be rovibrationally cooled to below room temperature. That is because even at room temperature, molecular ensembles are distributed across hundreds and up to thousands of rovibrational states. Moreover, the analysis in Chapter 4 showed that in many cases, large fractions of the molecular beam from ISOLDE have temperatures significantly higher than room temperature, with even less favorable population distributions. As a result, only a tiny fraction of the total molecular beam can be probed at any given time, given the limited linewidth of the scanning lasers.

As part of the doctoral work covered in this thesis, a publication that discusses the feasibility of rovibrational cooling in the case of RaF$^+$ was co-authored [143] (see Article 4 in Appendix C). As discussed in this publication, to compress the rovibrational distribution of molecules delivered to CRIS, two approaches that can work on a wide range of molecular species could be explored: optical pumping and cryogenic buffer-gas cooling. Sympathetic cooling of the molecular ions prior to charge exchange, which could be a natural option, is highly effective for translational cooling but not for rovibrational cooling, as the Coulomb repulsion hinders the collisions that induce the relaxation.

In the optical-pumping approach, femtosecond lasers (whose linewidths are Fourier-limited and thus span across nanometers) are used to continuously drive all rovibrational transitions between two electronic states simultaneously, thanks to their wide spectral output. By shaping the spectral output of the femtosecond laser in a way that eliminates the wavelengths that correspond to transitions from the vibrational ground state of the lower state but still exciting transitions from all other vibrational substates, the $v = 0$ band of the lower electronic state acts as a dark state to which all the molecules are eventually pumped. This approach was firstly demonstrated with photo-associated Cs_2 dimers, initially implementing only vibrational cooling [144] and subsequently extending the technique to rotational states as well [145], being applicable to a very wide range of species [146]. Recently, the technique was extended to cool SiO^+ to any arbitrary rotational state of choice, not just the lowest one [147].

Due to the wide spectral output of femtosecond lasers, however, the spectral density of the delivered power is low, and as a result this approach is not highly efficient. For diagonal molecules like RaF, where de-excitations with $\Delta v \neq 0$ (for instance from the $v' = 1$ upper state to the $v'' = 0$ dark state) are weak, an even lower efficiency is expected. Therefore, this approach cannot be applied in-flight on neutralized species, since the high kinetic energy of the beam at RIB facilities limits the interaction time to the microsecond range.

Instead, the optical pumping approach would need to take place in the ISCOOL RFQcb, where molecular ions are trapped for several tens of milliseconds. As explored in Ref. [143], however, RaF^+ does not possess electronic transitions in the optical spectrum, and therefore this cooling approach is not applicable to the case of RaF.

Instead, the approach of cryogenic buffer-gas cooling would have to be pursued. Rovibrational cooling through relaxation induced by collisions with cryogenic helium or neon buffer gas is most frequently the first step in cooling a molecular ensemble for precision spectroscopy [148], with universal applicability including complex and weakly bound polyatomic species.

Buffer-gas cooling also requires millisecond-scale interaction times, and so it is not applicable in-flight either. Its implementation thus requires the development of a cryogenic buncher at CRIS, which is a costly and complicated investment, but may be envisioned in the future.

Chapter 6

First laser spectroscopy of AcF

6.1 Motivation

Like RaF, actinium monofluoride (AcF) is a heavy polar molecule of high interest for precision tests of the SM. The nuclei of the Ac ($Z = 89$) isotopic chain are non-spherical, with static octupole deformation predicted [17] in the vicinity of the longest-lived isotope ^{227}Ac ($T_{1/2} = 21.8$ y). The spacing between the ground state and the opposite-parity rotational doublet pairs is only $\sim$27 and $\sim$40 keV for the longest-lived isotopes ^{225,227}Ac, respectively. As a result, several studies have indicated that the symmetry-violating moments in the actinium nuclei are among the largest throughout the nuclear chart [149, 150, 20, 124, 21].

By placing the actinium nuclei within a polar diamagnetic molecule with actinium-centered valence electrons, the large P, T-violating nuclear moments can be combined with an electronic structure that is highly sensitive to their presence. A high-precision experiment based on such a molecule would thus be a promising candidate for the first successful measurement of a nuclear Schiff or magnetic quadrupole moment across the nuclear chart, which would in turn shed light on so far unknown P, T-violating nuclear interactions.

In Ref. [151], Skripnikov *et al.* performed *ab initio* calculations of the sensitivity of the ground state of different diatomic molecules to the

Schiff moment of the actinium nucleus. All three studied actinium compounds (AcF, AcN, and AcO^+) were found to be sensitive to the Schiff moment and, combined with the predicted magnitudes of the moment for ^{225,227}Ac [149], the sensitivity is expected to result in a measurable signal above the precision limit reached by an experimental search in TlF a few decades ago (see Ref. [152] and Table 3 of Ref. [151]).

While Skripnikov *et al.* found AcF to have a lower sensitivity to the Schiff moment compared to AcN and AcO^+, the volatility of a fluoride compound as compared to the typical refractory nature of metal oxides and nitrides can be expected to lead to more intensely produced beams for precision experiments, thus compensating for the slightly lower molecular sensitivity in the overall achievable experimental precision, making AcF a candidate molecule of high interest.

Notably, Skripnikov *et al.* highlighted the important role of electron correlations in the electronic structure of AcF. Despite AcF possessing only one more valence electron than RaF, the great agreement between *ab initio* theory and experiment that was achieved for the electronic structure of RaF (see Article 2) is unlikely in the case of AcF, due to the enhanced electron correlations. To test the limits of *ab initio* quantum chemistry and by extension the validity of the Schiff-moment sensitivity calculations of Ref. [151] in the case of AcF, experimental measurements of the electronic excitation energies and chemical properties, such as the IP, are necessary.

Additionally, laser spectroscopy of AcF has important nuclear and medical physics motivation. The core of such interest is in the expected high-temperature volatility of the compound, which would lead to an easier and more intense production compared to the refractory Ac atom at thick-ISOL RIB facilities like ISOLDE. Volatilization of refractory atoms by fluorination for the improved production of radioactive beams has been extensively studied at ISOLDE, enhancing the extraction of many refractory atoms [153, 31, 154, 33, 155]. Confirming a similar result in the case of actinium would provide access to more Ac isotopes for nuclear-structure studies, as well as open a pathway for intense, isotopically pure beams of the medical radioisotope ^{225}Ac [156]. The nuclear and medical motivation for the study of AcF is elaborated in Ref. [157].

With such multidisciplinary motivation and following a successful proposal for radioactive beam time at ISOLDE [157], during my doctoral studies I coordinated the first laser spectroscopy on AcF using the CRIS experiment at ISOLDE in 2022. The experiment and the results are described in the following sections.

6.2 Experiment

Beams of $^{227}\mathrm{AcF}^{+}$ were produced at the ISOLDE facility by irradiating a room-temperature UC_x target with 1.4-GeV protons, producing $^{227}\mathrm{Ac}$ nuclides by fragmentation of the $^{238}\mathrm{U}$ target nuclei, and at a later time heating the target up to 1600 °C in the presence of CF_4 gas, as per the production method described by Au *et al.* in Ref. [155]. $^{227}\mathrm{AcF}$ was produced by the reaction of $^{227}\mathrm{Ac}$ with the CF_4 gas, and $^{227}\mathrm{AcF}^{+}$ cations were created in the ISOLDE versatile arc-discharge ion source [158], modified by the addition of the CF_4 leak [155].

To purify the $^{227}\mathrm{AcF}^{+}$ ($t_{1/2} = 21.8$ years) beam from all other radioactive ions produced by the VADIS, the ion beam was mass-filtered by the dipolar magnetic ISOLDE High-Resolution Separator. Prior production tests led by M. Au (Johannes Gutenberg University Mainz) demonstrated that the ion beam at this stage is composed of only $^{227}\mathrm{AcF}^{+}$, as the $^{227}\mathrm{RaF}^{+}$ isobaric contamination has decayed due to the shorter half-life of $^{227}\mathrm{Ra}$ ($t_{1/2} = 42.2$ minutes) and the asynchronous proton irradiation and beam extraction.

The continuous beam of mass-separated $^{227}\mathrm{AcF}^{+}$ cations was then cooled by colliding with a room-temperature helium buffer gas and bunched in the ISCOOL RFQcb [114]. Ion bunches of $\sim$5-μs temporal spread were delivered to the CRIS experiment once every 20 ms with a typical beam intensity of 1.2×10^6 ions per second.

No experimental spectroscopic information about AcF was available in the literature prior to the experiment, with theoretical calculations also being scarce and incomplete. The CRIS setup is well-suited to search for new electronic states in neutral atoms and molecules thanks to the broadband, continuously scannable pulsed lasers and the low background inherent to resonance ionization spectroscopy. Contrary to laser-induced fluorescence spectroscopy, however, knowledge of the ionization potential of the atom or molecule is crucial for CRIS experiments.

In the absence of any prior measurements of resonant transition frequencies, the first search for electronic transitions needs to be performed using a two-step laser scheme, where the frequency of the first laser is scanned while the second laser non-resonantly ionizes all molecules driven to an excited electronic state by the first laser. Therefore, if no prior experimental measurements are available, computational predictions of the ionization potential (IP), excited electronic states within at least 355 nm from the IP (corresponding to the lowest-wavelength non-resonant laser available at CRIS), and transition dipole moments (TDMs) from the ground state need to be produced.

Ab initio calculations of the electronic structure of AcF were thus produced independently by two theory groups (group of Anastasia Borschevsky at the University of Groningen, Netherlands and group of Leonid Skripnikov at the Petersburg Nuclear Physics Institute, Russia) for the needs of the CRIS experiment. Both groups performed Fock-space relativistic coupled-cluster calculations with single- and double-cluster amplitudes, including higher-order corrections at different levels.

Because electron correlations play a significant role in the structure of AcF, it is expected that incorporating computationally costly higher-order corrections in the electronic treatment, such as a fully iterative treatment of triple-cluster amplitudes and a perturbative treatment of quadruple-cluster amplitudes, will have significant influence on the predicted structure. However, combined with the size of the system and thus the need for a fully relativistic treatment of a compound with two valence electrons, the implementation of such corrections was not possible for the prediction of all properties prior to the experiment.

The IP of AcF, which is the more tractable of the calculated properties, was thus predicted by the two groups to be $48,600 \pm 250$ cm^{-1} and $48,848 \pm 123$ cm^{-1}, which also determined that sodium vapor should be used for charge exchange over potassium, as its IP is closer to the calculated value for AcF. In terms of the electronic map, which is the most daunting task, the two sets of calculations showed significant disagreement, with one set predicting 15 electronic states under 30,000 cm^{-1} and the other set predicting 34 states. In RaF, by comparison, less than half of the number of states is expected, with only 14 electronic states under 30,000 cm^{-1} (see Article 2).

The third harmonic of the Nd:YAG laser was used as a non-resonant step corresponding to ∼355 nm, or $28,195.5$ cm^{-1}. For a predicted IP of 48,848(123) cm^{-1}, a two-step laser scheme with one resonant transition thus needs to excite the AcF molecules from the ground state to a state above $48,848 - 28,195.5 = 20,652.5$ cm^{-1}. Based on the calculated TDMs for states above this excitation energy, the strongest transitions from the ground state were expected for an excited state with $\Omega = 1$ at $26,198$ cm^{-1}, and the second strongest transition to another state with $\Omega = 1$ at 24,084 cm^{-1}.

The first spectroscopy of RaF [5] was performed with the fundamental harmonic of the scanning Ti:Sa laser and 355-nm non-resonant ionization. In AcF, however, the second harmonic of the Ti:Sa laser is required. The SHG of the Ti:Sa laser was done by single-pass frequency-doubling with a beta barium borate (BBO) crystal cut at 30.4 degrees, which is optimal for frequency-summing of two photons at ∼770 nm. A continuously tunable grating-based nanosecond Ti:Sa laser with a fundamental-harmonic linewidth of ∼3 GHz was used.

As the fundamental wavelength of the laser is tuned, a combination of two effects in SHG lead to significant experimental complications. Firstly, the optimal incidence angle of the laser beam and the surface of the BBO crystal changes, resulting in a rapidly decreasing power for the frequency-doubled beam. Secondly, as the incidence angle becomes suboptimal, the frequency-doubled light exits the BBO crystal at an increasing angle with respect to the incidence axis. When these effects are left uncontrolled, the effective scanning range of the first step is dramatically reduced down to only a few cm^{-1}, as the frequency-doubled light quickly loses all of its power and its alignment with the neutral molecules in the beamline's interaction region. To eliminate these effects and extend the scanning range of the laser scheme, a position-stabilization device (PSD) and a motorized crystal-angle control (MCAC) system were installed.

For position stabilization, a commercial active laser beam stabilization setup by MRC Systems was installed. The PSD by MRC systems controlled the vertical and horizontal degrees of freedom of the first mirror after the SHG crystal of the scanning Ti:Sa laser such that a reflection spot of the laser light was maintained at the center of a target segmented photodiode. The reflection spot was created using a BSF10-A beam sampler by Thorlabs placed along the laser path such that the distance from the sampler to the segmented photodiode was approximately the same as the distance from the sampler to the CRIS interaction region. This way, stabilizing the reflection spot at the center of the PSD segmented photodiode ensured that the laser path was also stabilized through the interaction region.

For crystal-angle stabilization, an MCAC system was made in-house for the purposes of this run. The BBO crystal was mounted onto a K5X1 5-axis kinematic mount by Thorlabs and the vertical control pin was replaced for a PIA13 motorized piezo inertia actuator by Thorlabs. Using a BSF10-A beam sampler, a small pick-off reflection was created from the frequency-doubled laser beam after the BBO crystal, which was sent onto a photodiode detector that was placed behind an iris diaphragm. The laser power onto the detector was continuously monitored using a Thorlabs PM100USB power meter. Using a proportional-integral-differential (PID) feedback loop program written in Python, the BBO crystal angle was being dynamically adjusted so as to maintain a constant power level on the photodiode.

The combined use of the PSD and MCAC systems enabled a continuously scannable range of $\sim$500 cm^{-1} in the second harmonic of Ti:Sa without a significant power drop or spatial misalignment.

To search for higher-lying states and to attempt a measurement of the IP by locating the photoionization threshold, two more Ti:Sa lasers and two pulsed-dye lasers were used. The complete laser setup is shown in Fig. 6.1. The numbered optical components labeled as $F\#$ are flip mirrors that can alter the beam paths to overlap different lasers and to interchange between different schemes.

As higher-lying state searches require three-step schemes, they rely on the successful discovery of an electronic transition with the two-step laser scheme. Two possible three-step searches were prepared prior to the experiment on the assumption that an electronic transition would be successfully discovered in the vicinity of 26,000 cm^{-1}.

For the three-step searches, the first step was delivered by a frequency-doubled etalon-based broadband Ti:Sa laser ($\sim$3 GHz fundamental linewidth), intending to drive the strongest transition expected to be discovered around 26,000 cm^{-1} by the two-step scheme. The second (scanning) step was delivered by a pulsed-dye laser (PDL) with DCM or Pyridine 1 dye. The non-resonant ionization step was delivered by the first (1064 nm) or second harmonic (532 nm) of the Nd:YAG laser that was supplying the 355-nm non-resonant light in the two-step scheme. For the IP search, the second harmonic of the grating-based Ti:Sa was used as the scanning second step to locate the onset of photoionization. The laser schemes used for the spectroscopy of AcF are shown in Fig. 6.2 and a summary of the scan ranges in Fig. 6.3.

A narrowband pulsed Ti:Sa cavity seeded by a continuous wave Sirah Matisse Ti:Sa laser was also prepared for high-resolution spectroscopy of successfully identified transitions.

6.3 Results

All experimental parameters were optimized by firstly performing spectroscopy of the $A\ {}^2\Pi_{1/2} \leftarrow X\ {}^2\Sigma_{1/2}$ transition in ^{226}RaF using a two-step scheme with a 355-nm non-resonant step. Once resonance was achieved and the molecules-laser positions and timings were optimized, the magnetic dipole separator was switched to $A = 227 + 19$ and a search for transitions in AcF began using the two-step scheme.

Upon illuminating the neutralized AcF beam with the two-step scheme (Fig. 6.2a) to search for a resonant electronic transition, an unexpectedly high non-resonant spectroscopic background was observed. The background arose due to molecules being ionized by the 355-nm non-resonant laser without a resonant excitation driven by the first step. The non-resonant background was only slightly reduced when 532-nm non-resonant light was used, but it was drastically reduced when 1064-nm light was used. A comparison of the non-resonant background for

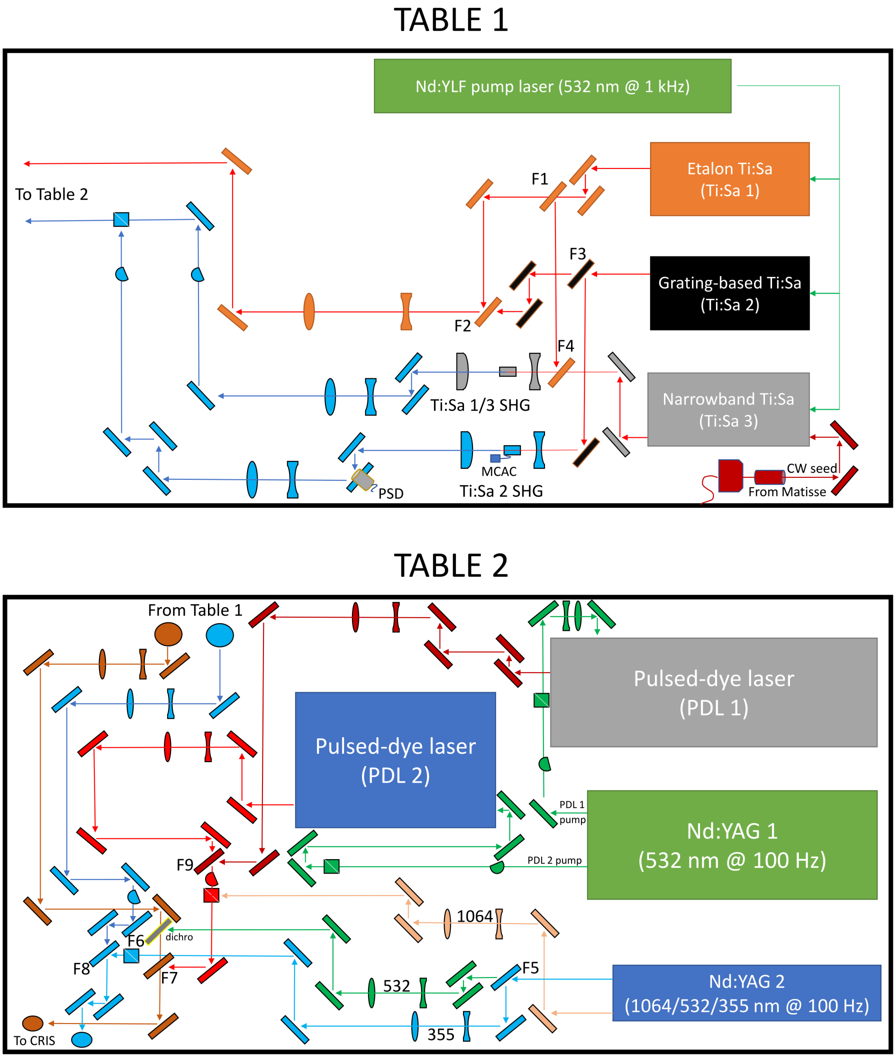

Figure 6.1: Layout of optical tables set up for the spectroscopy of AcF. The optical components labeled as *F#* are flip mirrors used to interchange between laser schemes, while PSD and MCAC are the position-stabilization device and the motorized crystal-angle control setup, respectively. Table 1 is situated approximately 20 meters from the CRIS beamline, while Table 2 is placed next to the beamline.

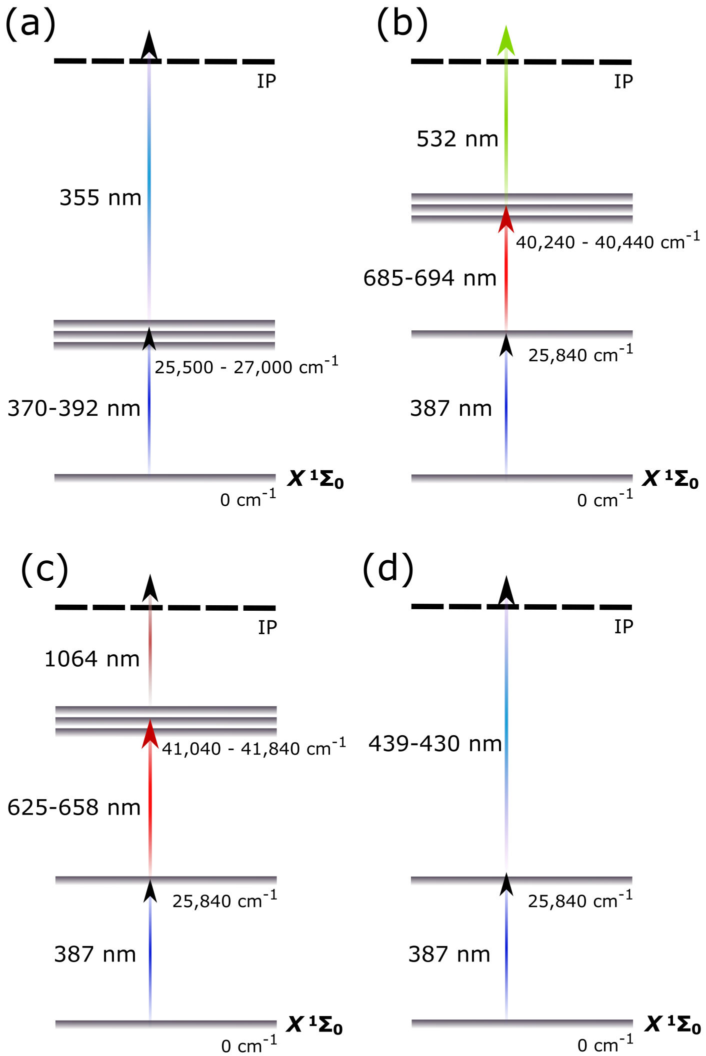

Figure 6.2: Laser schemes used for the excited-state searches in AcF. **(a)** Two-step scheme used to search for the first electronic transition. **(b)** Three-step scheme for a second-step scan with Pyridine 1 dye. **(c)** Three-step scheme for a second-step scan with DCM dye. **(d)** Two-step scheme for the search of the IP by scanning across the photoionization threshold.

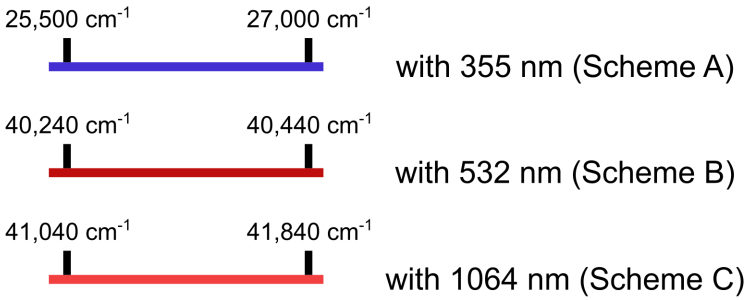

Figure 6.3: Summary of scan ranges in AcF.

different wavelength of the non-resonant light in AcF and RaF (measured in this experimental campaign) can be seen in Fig. 6.4. The non-resonant background is higher in AcF than in RaF, despite the latter having a lower IP by ~8,000 cm^{-1}.

As the beam composition had been extensively studied under identical conditions in the past and it was known to consist of only ^{227}AcF, and the background abruptly dropped when 1064-nm light was used, it is deduced that the background is caused due to a fraction of the molecules populating a metastable state after charge exchange. The background reduction with 1064 nm indicates that the metastable state lies more than 9,399 cm^{-1} below the IP, while the high background with 355 and 532 nm indicate that the state lies within 18,797 cm^{-1} from the IP. Using a predicted IP of 48,848(123) cm^{-1}, these observations place the excitation energy of the metastable state with respect to the ground state in the range 30,051-39,449 cm^{-1}. It is likely that more than 1 metastable states are populated in charge exchange, for instance the components of one or more Δ triplets.

6.3.1 $(8)\Pi_1 \leftarrow X\ {}^1\Sigma_0$

The non-resonant background significantly complicates the state search, effectively placing only very strong transitions within reach of discovery. The two-step scheme was thus used to search in the range 25,500-

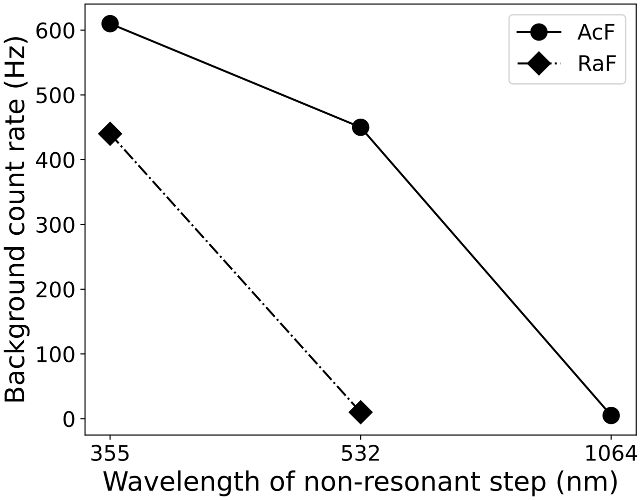

Figure 6.4: Comparison of spectroscopic background for non-resonant light of different wavelength in AcF and RaF. The pulse energy for each wavelength was comparable in the two cases. For 355 nm, typical pulse energy was 40 mJ, while for 532 nm it was 15 mJ.

27,000 cm^{-1} for the strongest dipole-allowed transition from the ground state, which the computational predictions prior to the experiment placed around ~26,000 cm^{-1}. An electronic transition was successfully discovered and the measured spectrum is shown in Fig. 6.5.

Despite the richness of the electronic map of AcF indicated by the predictions and by more elaborate calculations produced recently [6], no other transition from the ground state was observed within the 1,500-cm^{-1} scanning range of the two-step scheme (Fig. 6.2a). Most likely, the resonant ion signal produced from weaker transitions was not measurable due to the high non-resonant background. Since the energy of the strongest transition from the ground state was predicted at 26,166 cm^{-1} [6], within less than 350 cm^{-1} of the measured transition in Fig. 6.5, it is adopted in this thesis that the discovered transition corresponds to $(8)\Pi_1 \leftarrow X\ ^1\Sigma_0$ identified by Skripnikov *et al.* as the strongest transition from the ground state [6].

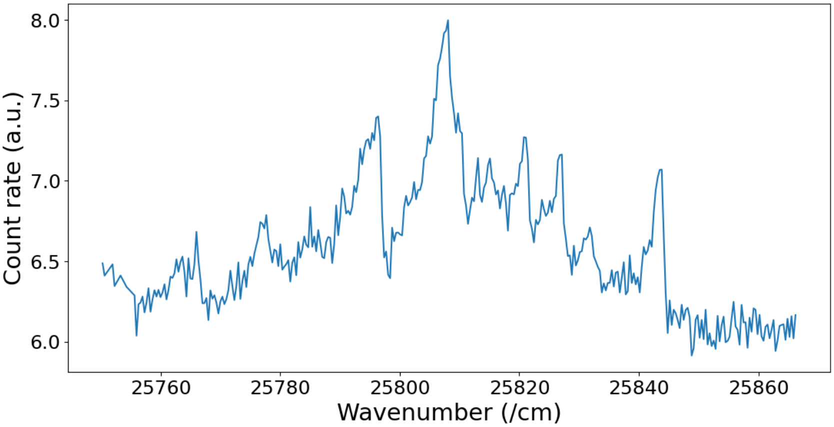

Figure 6.5: Spectrum of an electronic transition in AcF measured with CRIS. The units in the y-axis correspond to counts per bunch.

Skripnikov *et al.* calculated the lifetime of the $(8)\Pi_1$ state to be 6.65 ns [6], which corresponds to approximately 1/10 of the pulse length of the laser driving the excitation in this experiment. As a result, even though lifetime measurements were obtained akin to the case of RaF (Section 4.3), they cannot be analyzed without an elaborate optical-pumping model as in the case of RaF. In the absence of measured Einstein coefficients for the transitions from the lower and upper states to other states in AcF, such an elaborate analysis cannot be completed. Regardless, the observed trend of the raw ion counts as a function of the delay of the ionization laser step following the excitation laser (Fig. 6.6) evidently plateaus before 30 ns, placing a conservative experimental upper bound to this value.

The measured spectrum for the $(8)\Pi_1 \leftarrow X\ ^1\Sigma_0$ transition was analyzed with the contour-fitting routine of PGOPHER, following the same method as for the excited states in RaF (Section 4.2.5). All peaks were fitted simultaneously. In the absence of any information for either the upper or the lower state from high-resolution spectroscopy, as with RaF, the contour-fitting analysis was performed by deriving values for the rotational constant B_v and its anharmonicity constant D_v for the lower

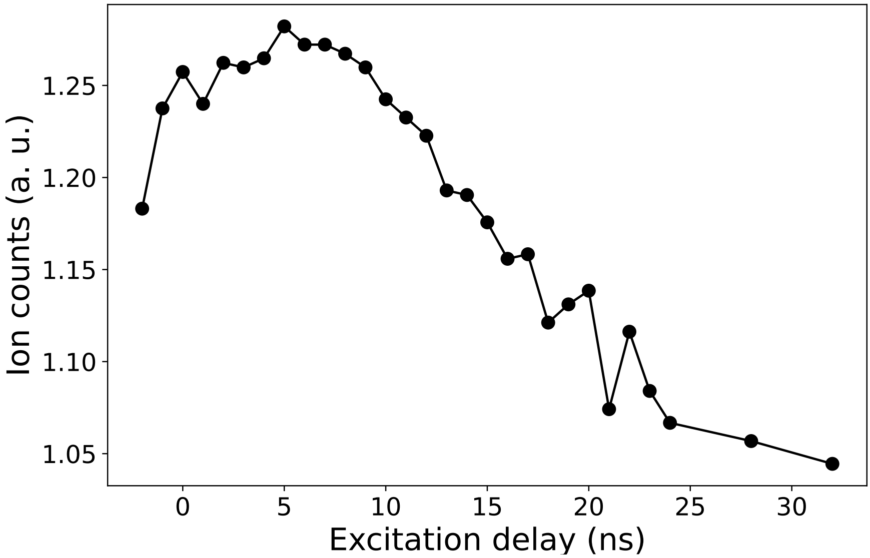

Figure 6.6: Ion counts as a function of the delay between the laser driving the $(8)\Pi_1 \leftarrow X\ ^1\Sigma_0$ transition in AcF and the subsequent non-resonant ionization step in the two-step scheme (Fig. 6.2a).

and the upper states using the calculated harmonic frequencies and equilibrium bond lengths from Skripnikov *et al.* [6]. Specifically, the values for B_v and D_v for $v', v'' =$ 0-6 are shown in Table 6.4. No values were used for the γ and p spectroscopic constants. As the $(8)\Pi_1$ state has a strong multi-reference character [6] and its calculation is less accurate, the rotational constants of the upper states were fitted as well, along with the excitation energies.

In the absence of evidence for an atypical vibrational progression (for instance, as a result of an avoided-crossings situation), the excitation energy of the $(8)\Pi_1$ state was determined as the transition energy of the rightmost peak in Fig. 6.7, as the peak is presumed to correspond to the $(8)\Pi_1 \leftarrow X\ ^1\Sigma_0$ $(0 \leftarrow 0)$ transition. The excitation energy of the $(8)\Pi_1$ state is thus reported at 25,844.09(14)[52] cm^{-1}. The spectrum and best-fit simulation for the $(8)\Pi_1 \leftarrow X\ ^1\Sigma_0$ $(0 \leftarrow 0)$ transition are shown

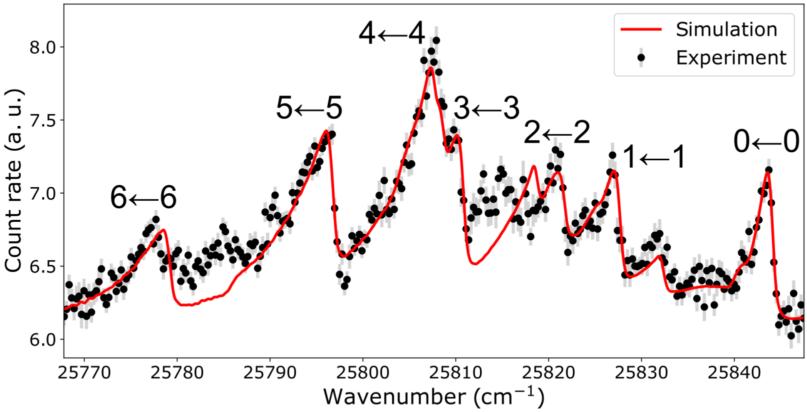

Figure 6.7: Annotated spectrum and simulation for the $(8)\Pi_1 \leftarrow X\ ^1\Sigma_0$ vibrational transitions in AcF, showing all fitted vibrational bands according to the assignment in Table 6.5.

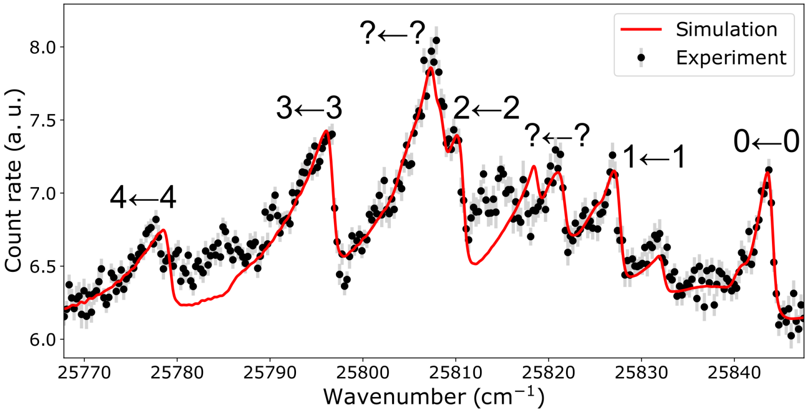

Figure 6.8: Annotated spectrum and simulation for the $(8)\Pi_1 \leftarrow X\ ^1\Sigma_0$ vibrational transitions in AcF, showing all fitted vibrational bands according to the alternative assignment listed in Table 6.6.

in Fig. 6.9. Further investigations, including high-resolution spectroscopy, are needed to confirm that this band indeed corresponds to the $0 \leftarrow 0$ transition.

In total, 7 bands are identified in Fig. 6.5, presumed to correspond to diagonal vibrational transitions. The transition energies of the vibrational bands are listed in Table 6.5, along with the fitted values for the rotational constants of the upper vibrational states. The reduced χ^2 of the fit was 4.16. As in the case of RaF, a systematic uncertainty of 0.5 cm^{-1} is considered to provide a conservative account of the propensity of contour fitting to converge at local minima based on the assumed Voigt linewidth, and 0.02 cm^{-1} is considered for the remaining sources of absolute energy shifts.

It can be seen in Table 6.5 that the spacing between the transition energies is not constant and fluctuates strongly. This is an indication that vibrational bands belonging to different electronic transitions might be intertwined in the measured structure.

An alternative assignment of the measured bands is listed in Table 6.6 and shown in Fig. 6.8. The diagonal vibrational transitions in $(8)\Pi_1 \leftarrow X\ {}^1\Sigma_0$ are spaced more equally, and transitions from vibrational states up to $v'' = 4$ are part of this assignment, as in the case of RaF [5]. However, the two vibrational bands at 25,821.70 and 25,808.66 cm^{-1} cannot be explained with this assignment, and could possibly not belong to $(8)\Pi_1 \leftarrow X\ {}^1\Sigma_0$ at all. This observation is further supported by the trend in rotational constant B of the upper states. The two bands might thus correspond to non-diagonal vibrational transitions $(v'' - v' \neq 0)$ of a different electronic transition. Overall, the assignment in Table 6.6 thus seems more likely.

6.3.2 High-lying states

Following the discovery of the $(8)\Pi_1 \leftarrow X\ {}^1\Sigma_0$ transition with the two-step scheme, higher-lying states were searched for using the three-step schemes in Fig. 6.2b and 6.2c. Due to the marginal reduction in the background when using 532-nm instead of 355-nm light for the non-resonant step, no transitions were discovered with Scheme B (Fig. 6.2b).

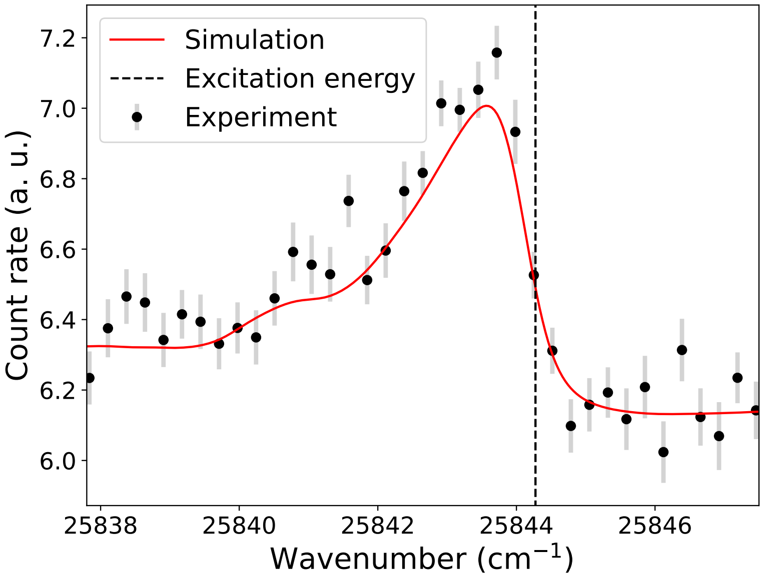

Figure 6.9: Spectrum and simulation for the $(8)\Pi_1 \leftarrow X\ ^1\Sigma_0$ $(0 \leftarrow 0)$ transition in AcF. The fitted excitation energy of the $(8)\Pi_1$ state is 25,844.09(14)[52] cm^{-1} and it is denoted by a dashed vertical line.

Using Scheme B, the structure shown in Fig. 6.7 was not observed when the first step was scanned. This is evidence that the structure in Fig. 6.7 does not correspond to a transition from the suspected metastable state but indeed from the ground state, as the total photon energy delivered by the first and non-resonant steps should have successfully ionized the molecules if the transition was starting from the metastable state.

The background reduction thanks to the use of 1064-nm light in Scheme C (Fig. 6.2c) was drastic enough to enable a more extensive search for states with excitation energies between 41,040 and 41,840 cm^{-1}. No transitions strong enough to lead to a large signal-to-noise ratio were discovered. A weak second-step transition was discovered, shown in Fig. 6.10. Despite the very low signal-to-noise ratio of the measured spectrum, the peak persisted across multiple scans, and a clear effect

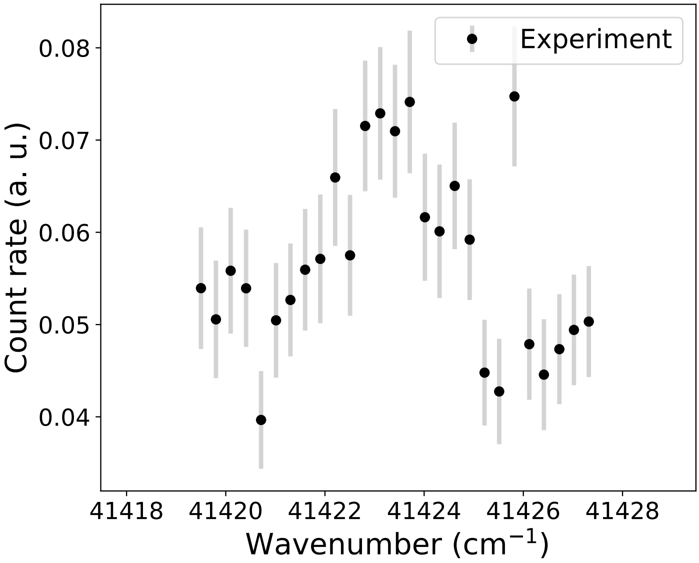

Figure 6.10: Suspected peak in second-step scan using the three-step Scheme C (Fig. 6.2c). The x-axis gives the sum of the wavenumbers of the first and second steps. The center of the peak is at 41,423 cm^{-1}.

on the ion count rate was observed when each of the three laser steps were blocked from illuminating the molecules. Therefore, it is concluded that the peak shown in Fig. 6.10 corresponds to a component centered at 41,423 cm^{-1} of a resonant transition from $(8)\Pi_1$ to an unknown higher-lying state.

6.3.3 Ionization potential

An attempt was made to measure the IP of AcF by observing the threshold of photoionization as a function of total photon energy delivered to the molecules. For this measurement, Scheme D (Fig. 6.2d) was used. The first step was excited by the second harmonic of the etalon-based Ti:Sa, and the second step by the second harmonic of the grating-based Ti:Sa (Fig. 6.1). The wavelength of the second step was set to different values

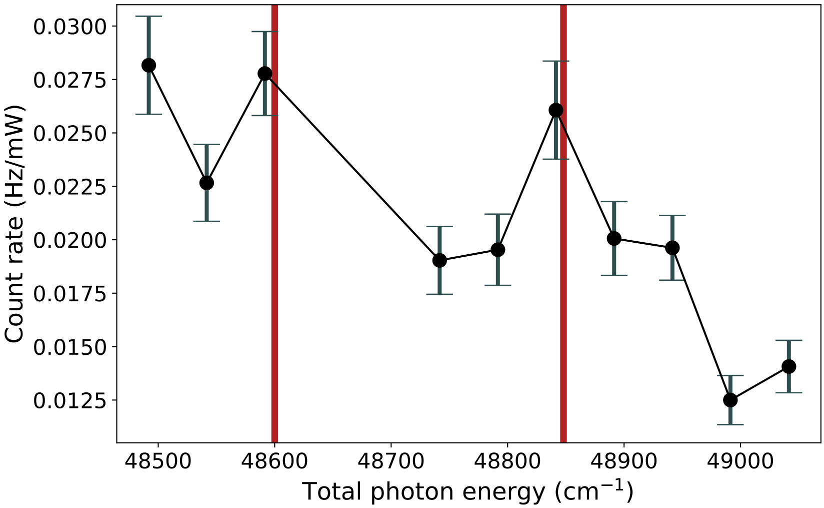

Figure 6.11: Attempted IP measurement in AcF. The vertical red lines denote the IP predictions that were calculated prior to the experiment.

such that the total photon energy delivered to the molecules was in the vicinity of the predicted values for the IP.

For each photon-energy data point, the ion count rate was measured for 1000 s. The count rate over time was then fitted with a constant value, yielding a mean value and its uncertainty. The results were then divided by the power of the second step at each set wavelength to yield a curve of power-normalized ion count rate as a function of total photon energy. The curve is shown in Fig. 6.11.

Evidently, the results are not conclusive, as a consequence of the large non-resonant background due to the suspected presence of a metastable state.

6.4 Next steps

Section 6.3 reports the first ever spectroscopic results in AcF. Although the unexpectedly high non-resonant background complicated the search for excited states, a strong transition from the ground state was successfully measured and assigned as $(8)\Pi_1 \leftarrow X\ ^1\Sigma_0$ following the predictions and assignment of Skripnikov *et al.* [6].

The high strength of the measured transition is confirmed by its radiative lifetime, which was measured to have an upper bound of 30 ns. This transition is suitable for fluorescence-based state detection in experimental schemes for the measurement of symmetry-violating nuclear moments [159]. As the sensitivity to the nuclear Schiff moment lies in the $^1\Sigma_0$ ground state, efficient state detection based on laser-induced fluorescence is optimal when the strongest transition from the ground state is used. The transition presented here, which appears to be the strongest transition from the ground state and also lies in a region of the electromagnetic spectrum where photo-multiplier tubes have high quantum efficiency, is thus an ideal choice for this purpose.

To further assist the experimental design of a search for the nuclear Schiff moment of ^{225,227}Ac with AcF, the spectrum of the $(8)\Pi_1 \leftarrow X\ ^1\Sigma_0$ transition needs to be measured in high resolution, similar to the recent CRIS study of RaF [2]. To achieve a high resolution with a good signal-to-noise ratio in the spectroscopy of radioactive molecules, however, a scheme far more sensitive than Scheme A (Fig. 6.2a) needs to be devised.

The reason is the prohibitively high background created by the 355-nm step. The high-resolution study of RaF showed that, for typical beam intensities at CRIS, only about 100 molecules per second populate each rotational state. High-resolution spectroscopy of the $(8)\Pi_1 \leftarrow X\ ^1\Sigma_0$ transition is thus not possible with the >400-Hz non-resonant background due to 355- or 532-nm light (Fig. 6.4).

Instead, a three-step scheme using 1064-nm non-resonant light needs to be used along with an efficient second-step transition. In Ref. [6], a transition from $(8)\Pi_1$ to a state with $\Omega = 2$ at 40,302 cm^{-1} is identified, having a TDM at 1/3-1/4 of the TDM for $(8)\Pi_1 \leftarrow X\ ^1\Sigma_0$. Therefore, while the resonant count rate will be ×3-4 lower than in Scheme A for a three-step scheme using this transition, the 100-fold reduction in non-resonant background due to the 1064-nm step will enable spectroscopy in high resolution.

High-resolution spectroscopy of the $(8)\Pi_1 \leftarrow X\ ^1\Sigma_0$ transition is also of interest for nuclear-structure studies. The $^1\Sigma_0$ ground state of AcF has a simple, single-reference character, unlike the ground state of the Ac atom [6]. As a result, the electric field gradient can be calculated more precisely in AcF than in the Ac atom, and as a result the spectroscopic nuclear quadrupole moment of the Ac nucleus can be extracted with higher precision from the spectroscopy of AcF.

Additionally, the measurement of the IP needs to be repeated using an efficient three-step scheme. Due to the complexity of the molecule, high-precision calculations of the IP are significantly more tractable than for the excitation energies. Skripnikov *et al.* demonstrated that the correction of up to quadruple-cluster amplitudes remained significant for the calculation of the IP in AcF [6], which is a level of precision not currently possible to be reached for energy levels. It is therefore important to provide an experimental value for comparison, which would indicate whether quintuple-cluster amplitudes are also necessary.

Lastly, similar experiments to measure the electronic structure of the AcF^+ are also important for future plans to perform precision tests of the SM using AcF. AcF^+ is of interest for precision measurements directly in its electronic structure, as it is paramagnetic, and thus sensitive to the nuclear magnetic quadrupole moment, and expected to be laser-coolable as a cation. This means that a precision experiment in an ion trap can be devised, taking advantage of the long coherence time demonstrated in the eEDM search with HfF^+ [160], while further increasing the coherence time and quantum-state control with direct laser cooling. Alternatively, AcF^+ can be used as a precursor in a precision experiment based on AcF by taking advantage of its electronic structure and its electric charge for ensemble cooling and manipulation, before being neutralized in a temperature-preserving manner (for instance, possibly through charge exchange with Rydberg-state alkali atoms [161, 162, 163, 164] that have been cooled in a magneto-optical trap).

State No.	Ω	Energy (cm^{-1})	TDM $\|d\|$, a.u.
1	0+	0	
2	1	8271	0.033
3	2	8902	
4	3	9970	
5	0-	11150	
6	0+	11561	0.449
7	1	12227	0.564
8	2	13697	
9	2	14593	
10	1	16202	0.987
11	0-	16953	
12	1	17509	0.888
13	0+	18977	1.557
14	0-	20741	
15	0+	20768	0.564
16	1	21177	0.529
17	2	21821	
18	2	22134	
19	0+	23020	0.581
20	1	23530	0.016
21	3	24004	
22	1	24084	1.409
23	4	25203	
24	2	25789	
25	1	26198	2.016
26	0-	26299	
27	0+	26383	0.051
28	4	26613	
29	1	27732	0.052
30	3	27820	
31	0+	27905	0.719
32	2	27931	
33	3	29953	
34	2	30077	
35	0+	30082	1.313
36	1	30202	0.046
37	0-	30213	
38	1	30893	1.072

Table 6.1: First part of electronic state energies, relative transition dipole moments (TDM), and projections of total angular momentum Ω in AcF predicted by the Skripnikov group at the Petersburg Nuclear Physics Institute, Russia prior to the experimental run, to guide the state search.

State No.	Ω	Energy (cm^{-1})	TDM $\lvert d \rvert$, a.u.
39	2	31169	
40	1	31619	0.069
41	0-	32004	1.157
42	3	32522	
43	2	32756	
44	0-	33330	
45	1	33408	0.150
46	0-	33716	
47	1	33810	0.376
48	1	33991	0.476
49	4	34046	
50	0+	34130	0.055
51	0-	34586	
52	2	34866	
53	3	35106	
54	0+	35281	0.087
55	0+	35747	0.028
56	2	35836	
57	0-	36523	
58	1	36717	0.030
59	1	37166	0.663
60	3	37710	
61	0+	37715	0.130
62	2	37865	
63	1	38279	0.242
64	1	38768	0.106
65	0+	39265	0.589
66	0-	39271	
67	2	39350	
68	1	40489	0.002
69	2	40624	
70	0-	40691	

Table 6.2: Second part of electronic state energies, relative transition dipole moments (TDM), and projections of total angular momentum Ω in AcF predicted by the Skripnikov group at the Petersburg Nuclear Physics Institute, Russia prior to the experimental run, to guide the state search.

State No.	Ω	Energy (cm^{-1})	TDM $\|d\|$, a.u.
71	0+	40733	0.368
72	1	41025	0.070
73	2	41185	
74	3	41224	
75	1	41466	0.339
76	2	41825	
77	4	42044	
78	1	42117	0.042
79	2	42336	
80	2	42569	
81	1	42629	0.050
82	3	42804	
83	2	43462	
84	1	43802	0.396
85	3	43806	
86	0+	44018	0.339
87	3	44185	
88	2	44607	
89	0-	45697	
90	0+	46217	0.074
91	1	46463	0.048
92	3	47138	
93	0-	47213	
94	0+	47337	0.081
95	2	47377	
96	1	47623	0.002
97	2	48073	
98	4	48108	
99	0+	48483	0.165
100	1	48869	0.047
101	5	49262	
102	2	49325	
103	1	49469	0.003
104	0-	49836	
105	1	49958	0.035

Table 6.3: Third part of electronic state energies, relative transition dipole moments (TDM), and projections of total angular momentum Ω in AcF predicted by the Skripnikov group at the Petersburg Nuclear Physics Institute, Russia prior to the experimental run, to guide the state search.

Table 6.4: Summary of spectroscopic constants used in the contour-fitting analysis of the $(8)\Pi_1 \leftarrow X\ ^1\Sigma_0$ transition in AcF. The values for R_e and ω_e are taken from Skripnikov *et al.* [6]. The anharmonicity constant is taken to be $D_v = D_e$ for all v.

	$X\ ^1\Sigma_0$	$(8)\Pi_1$
R_e (m)	2.110×10^{-10}	2.127×10^{-10}
ω_e (cm^{-1})	541	549
B_e (cm^{-1})	0.21598	0.21254
D_e (cm^{-1})	6.4×10^{-7}	6.0×10^{-7}
α_e (cm^{-1})	-5.2×10^{-4}	-4.9×10^{-4}
B_0 (cm^{-1})	0.21572	0.21229
B_1 (cm^{-1})	0.21520	0.21180
B_2 (cm^{-1})	0.21469	0.21131
B_3 (cm^{-1})	0.21417	0.21081
B_4 (cm^{-1})	0.21365	0.21032
B_5 (cm^{-1})	0.21314	0.20983
B_6 (cm^{-1})	0.21262	0.20933

Table 6.5: Transition energies of measured vibrational bands in the $(8)\Pi_1 \leftarrow X\ ^1\Sigma_0$ electronic transition in AcF.

	δE (cm^{-1})	$B_{(8)\Pi}$ (cm^{-1})
$0 \leftarrow 0$	25,844.09(14)[52]	0.21453(29)
$1 \leftarrow 1$	25,827.68(24)[52]	0.21352(39)
$2 \leftarrow 2$	25,821.70(33)[52]	0.21290(31)
$3 \leftarrow 3$	25,810.81(20)[52]	0.21498(35)
$4 \leftarrow 4$	25,808.66(31)[52]	0.21366(23)
$5 \leftarrow 5$	25,796.79(18)[52]	0.21449(18)
$6 \leftarrow 6$	25,779.63(27)[52]	0.21436(70)

Table 6.6: Alternative assignment of the measured vibrational bands in Table 6.5.

	$\delta E_{(8)\Pi \leftarrow X\ \Sigma}$ (cm^{-1})	$B_{(8)\Pi}$ (cm^{-1})
$0 \leftarrow 0$	25,844.09(14)[52]	0.21453(29)
$1 \leftarrow 1$	25,827.68(24)[52]	0.21352(39)
$2 \leftarrow 2$	25,810.81(20)[52]	0.21498(35)
$3 \leftarrow 3$	25,796.79(18)[52]	0.21449(18)
$4 \leftarrow 4$	25,779.63(27)[52]	0.21436(70)
$? \leftarrow ?$	25,821.70(33)[52]	0.21290(31)
$? \leftarrow ?$	25,808.66(31)[52]	0.21366(23)

Chapter 7

Upgrades at CRIS for efficient molecular spectroscopy

The doctoral work presented in this thesis also included technical progress towards improving central aspects of the CRIS experiment: to reduce the measurement time per scan during CRIS campaigns and to enable spectroscopy of molecular beams from an offline ion source. Both areas of technical work qualify as universal upgrades at CRIS, as they benefit both atomic and molecular campaigns, but they are also of special importance for molecular spectroscopy.

Contrary to the simpler atomic picture, the hfs in molecular spectra manifests as splittings in rovibronic lines, and thus its measurement requires the simultaneous knowledge of the vibrational and rotational structures (see Chapter 2). Therefore, a precise extraction of molecular hfs factors requires measuring sufficient rovibronic lines to pin down all factors – vibrational, rotational, and hfs – in the molecular Hamiltonian.

To account for mass-dependent variations in the vibrational and rotational constants, many rovibronic transitions have to be measured in high resolution for each isotopomer separately[1]. Therefore, while the spectroscopy of atoms requires a single scan for a sufficiently constrained

---

[1] Using the Born-Oppenheimer approximation, the molecular factors of an isotopomer can be extracted from those of a reference isotopomer. The accuracy of

measurement of the hfs, more than 10 scans (each for a different rotational line) are typically required for a sufficiently constrained molecular case.

To accelerate the spectroscopy at CRIS such that molecular spectroscopy can be performed in a reasonable timescale, the technical work performed as part of this thesis was partly focused on implementing the technique of voltage scanning. Voltage scanning is routinely used at conventional CLS experiments but previous attempts at CRIS were unsuccessful. Using an improved electrode design and a dedicated control software, voltage scanning was successfully used in commissioning runs with stable and radioactive beams, demonstrating fully consistent atomic hfs constants with those obtained with laser scanning (see Article 3).

Regarding the availability of stable beams for offline spectroscopy, CRIS has made use of different offline ion source designs in the past. While the operation of plasma ion sources was prohibitively unstable, a laser-ablation ion source that is still in use today was successfully utilized to study the stable isotopes of In, Sn, Zn, Cu, and Ag. However, the laser-ablation ion source has also proven to be operationally unstable and it cannot produce intense room-temperature molecular beams.

The availability of stable molecular beams at CRIS would serve a dual purpose. On the one hand, preparatory studies on stable atomic or molecular beams are highly desirable in advance of experiments with radioactive beams. Such studies are used to assess the spectroscopic efficiency and sensitivity to nuclear observables for the electronic transitions planned for study. On the other hand, as shown in Chapter 3, currently unexplored nuclear effects in molecular spectra require extensive laser-spectroscopic campaigns for a full investigation. As many atoms contain 3 or more stable isotopes and each atom can form molecules with different ligands, progress in the intersection of nuclear and molecular physics based on such effects can still be made without radioactive beams. With the development of an offline molecular ion source at CRIS, these studies can complement the scientific activities of the experiment when radioactive beams are not available. Therefore, as the existing laser-ablation ion source is not well-suited to produce intense, room-

---

this procedure is not high for all cases, and should be avoided when measuring the hfs of isotopes without known moments.

temperature molecular beams, a new ion source was designed as part of this doctoral work to enable these features.

The technical work performed on implementing voltage scanning at CRIS and designing a new laser-ablation ion source is elaborated in the following subsections.

7.1 Voltage scanning

7.1.1 Motivation and limitations

In traditional laser-induced fluorescence CLS beamlines, voltage scanning is almost invariably used over laser scanning to bring the beam to resonance with the spectroscopy laser. The principle relies on the high kinetic energy (KE) of the beam. In a collinear geometry, the laser wavelength that the fast beam observes in its rest frame is Doppler-shifted by several cm^{-1}. As a result, spectroscopy can be performed either by changing the wavelength of the laser (laser scanning) or by tuning the KE of the beam using an electrode (voltage scanning) to bring the beam in resonance with the laser in its rest frame.

Voltage scanning offers multiple benefits compared to laser scanning for narrowband spectroscopy. The narrowband tunable laser systems used for high-resolution laser spectroscopy at CLS beamlines and CRIS rely on "locking" the laser cavity with piezocontrollers of different optical components. A locked cavity is stabilized to a specific mode of operation using fast feedback loops that adjust the position of mirrors and etalons based on the reading of a wavelength meter (wavemeter). As a result, due to the limited readout rate of the wavemeter, tuning the output wavelength of a locked laser has to be performed in the order of tens of milliseconds at best.

In the case of a pulsed narrowband laser, such as the injection-seeded Ti:Sa laser used at CRIS [115], two levels of cavity locking apply: firstly, a CW Ti:Sa laser is locked to produce the single-mode narrowband "seed" laser, and secondly, the pulsed Ti:Sa cavity is locked to optimize the transmission of photons at the seed wavelength around the optical cavity.

Therefore, tuning the output wavelength of the pulsed injection-seeded Ti:Sa laser is especially delicate: the wavelength of the seed has to be tuned slowly enough (less than 10 MHz per second) such that both the CW and the pulsed cavities remain locked.

Typically, laser scanning needs to be limited to rates significantly below $\sim$10 MHz per second. For intense beams of atoms or molecules, such as isotopes close to stability with production rates of $\geq 10^5$ ions/second, enough data to narrow down the statistical errors could be gathered with CRIS even with considerably faster scan rates. Therefore, CRIS experiments could be accelerated if the limitations of laser scanning were bypassed.

By performing spectroscopy with voltage scanning, the narrowband lasers can be kept at a single wavelength under locked conditions for the duration of the scan (or a large part of it), improving the stability of the apparatus. Additionally, the spectroscopy can be significantly accelerated for the majority of the beams of interest, as voltage slew rates in the volt-per-microsecond range are achievable (which would correspond to scan rates of GHz per second).

There is an additional benefit of voltage scanning that must not be overlooked. Although the tuning range of a laser's wavelength is necessarily continuous, since laser scanning is based on the mechanical motion of optical components, voltage scanning can neglect entire voltage (and so rest-frame frequency) ranges with no compromise in the stability of the system. This feature is especially helpful for species with wide hfs splittings or very well-known hfs constants. In such cases, the spectroscopy can be further accelerated by tuning the KE of the beam to correspond to rest-frame frequencies only for the regions where resonances are expected while completely skipping the unnecessary background.

Therefore, sustainably incorporating high-resolution molecular spectroscopy at CRIS as a routine scientific activity would significantly benefit from a robust implementation of voltage-scanning, such that the large frequency space that has to be scanned in high resolution for each isotopomer can be covered in realistic timescales. However, the successful utilization of voltage scanning is also faced with a challenge: changing the KE of an ion beam also results in a change of its focal length. This coupling can result in the ion beam being moved significantly out of focus or trajectory (if the ion beam is not centered on the axis of the tuning electrode), with the ions never reaching the final detector.

The CRIS beamline is more susceptible to the ion beam being defocused or steered out of path compared to conventional CLS beamlines due to its geometry. Due to the coupling of the tuning electrode and the beam's focal length and trajectory (as well as due to the need for strong optical transitions), conventional CLS beamlines have short interaction regions of a few tens of centimeters. At CRIS, the IR is 1.2-m long to permit the full atom bunch to interact with the laser pulses. Furthermore, the ion detector is placed after an electrostatic bend following the IR. As a result, beam steering at an angle of just a few degrees or changes in the focal length of a few centimeters can have a drastic effect on the beam transmission.

Previous attempts to implement voltage scanning at CRIS [165, 166] did not perform as intended because of these limitations. Due to aberrations in the electric field of the voltage-scanning electrode, the unwanted steering and focusing of the ion beam severely limited the tunable voltage range, and ultimately no CRIS spectrum could be measured using voltage scanning.

7.1.2 New implementation

To bypass this problem, a new implementation of voltage scanning at CRIS was attempted using an improved tuning electrode, designed by F. Wienholtz and W. Gins for the VITO experiment at ISOLDE [167]. The electrode is placed immediately before the CEC such that the KE of the atoms is tuned shortly before neutralization. To install the electrode and float it to the voltage of choice, the CEC support structure inside the vacuum chamber had to be modified.

Previously, the copper-based support structure of the CEC was in mechanical contact with the grounded vacuum chamber, permitting electrical conduction and grounding the structure. To be able to float the tuning electrode and the CEC to the voltage of choice, such electrical coupling had to be eliminated. This was achieved by installing 10-

mm-thick polyetheretherketone (PEEK) spacers under the legs of the CEC support structure, which were bolted onto the structure using 18-mm-long PEEK screws. PEEK was chosen as an electrically insulating material with ultra-low outgassing rates that does not obstruct the vacuum requirements of the region. Compared to nylon, PEEK also possesses a higher melting point, making it more favorable for a high-temperature environment such as the CEC.

As an additional modification, the components of the CEC cooling loop were also substituted to eliminate any direct electrical coupling with the grounded chamber through the bellows (see Fig. 7.1). During normal operation, the center of the CEC is heated to above 100 °C when using potassium vapor and 180 °C when using sodium vapor, but the ends of the cell must be kept at a lower temperature (close to the vapor's condensation point) such that the vapor does not spread to the full beamline. To this end, an active cooling loop is used. The previously used bellows for the coolant circulation were in mechanical contact with both the CEC support structure and the vacuum chamber, thus grounding the CEC and the tuning electrode. Consequently, they were substituted for an assembly of shorter bellows connected by electrically insulated CF16 adapters (not shown in Fig. 7.1). Additionally, a further modification was the choice of coolant. While a mixture of water and ethanol was very effective as a coolant in the past, the electrical conductivity of water prohibits its use during voltage scanning. Therefore, the electrically insulating perfluoropolyether coolant Galden HT200 was chosen.

7.1.3 Control and acquisition

Equipment

A custom power-supply assembly had to be used for supplying the voltage to the tuning electrode, as high slew rates and high setpoint precision are required to take full advantage of the power of voltage scanning.

The electronics assembly follows that of implementations at other CLS beamlines: a high-precision 16-bit digital-to-analog converter (DAC, National Instruments NI-USB-6211) is given a digital setpoint by the user PC and outputs a corresponding analog voltage in the range of -10 to

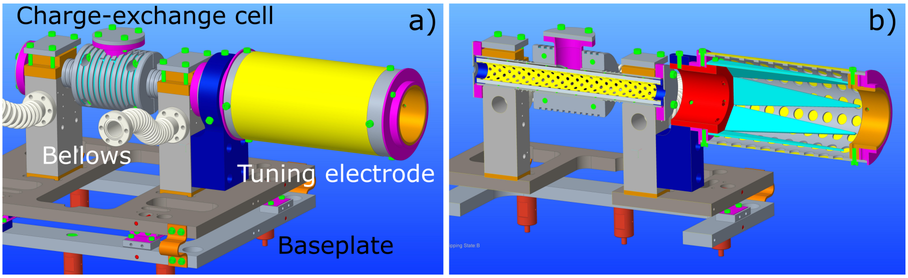

Figure 7.1: The charge-exchange cell (CEC) at CRIS attached to the electrode used for voltage scanning. **a)** Full view. The base plate is in electrical contact with the CEC and the electrode, thus all components are brought to voltage. The baseplate is supported by insulating PEEK spacers. **b)** Half-section view. The electrode is comprised of conjoint triangular electrodes (thus resembling a crown) that form a smoothly increasing potential at their center as the beam travels through it (right to left).

10 V. The set voltage is then supplied to a fast bipolar voltage amplifier (UltraVolt 1HVA24-BP1-F-SHV-5KV) with a maximum output voltage of 1 kV. The amplified output is connected in parallel to the tuning electrode and to a high-voltage potential divider (OhmLabs KV-30A) with a ratio 1,000:1. The real voltage supplied to the electrode is thus measured by a fast $7\frac{1}{2}$-digit multimeter (Keithley DMM7510) connected to the potential divider. The assembly is shown in Fig. 7.2.

In addition to the set voltage, the amplifier requires a precise 10.0 V reference voltage as well as two input voltages between 0.0 and 10.0 V that define the voltage and current output limits of the device. As the NI-USB-6211 DAC has only two analog output (AO) channels up to ±10 V, the precise reference voltage was supplied by the unused AO channel of the DAC. To specify the current and voltage output limits, however, no AO channels, which offer tunability, were available. Therefore, the limits were supplied as a constant +5 V signal from two digital-output (DO) channels. Although the voltage of the DO signal is not tunable, the specified limits were sufficient for normal operation without posing a risk to the operators.

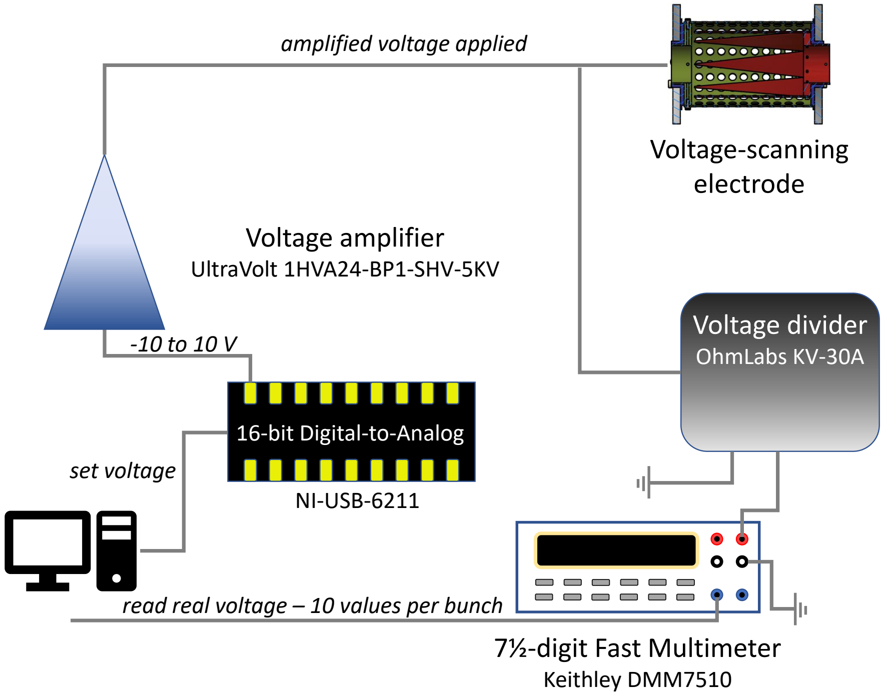

Figure 7.2: The DAQ electronics assembly for voltage scanning.

In other implementations of voltage scanning at CLS beamlines, the voltage supplied to the electrode is not monitored according to its real applied value, but rather according to a calibration curve of the correspondence between the set and applied voltages. This is done because the voltage setpoint given by the PC to the DAC can be registered at a very high rate (in the order of a few hundred microseconds per point) as it does not rely on a separate measurement device. However, this approach requires frequent calibration measurements between scans, and is also based on the assumption that the true correspondence between set and applied voltages does not diverge from the calibration curve in the course of a scan.

In the current implementation at CRIS, the need for calibration measurements is bypassed by using a fast-response digital multimeter to measure the real voltage applied to the electrode. The multimeter is read through the local area network and posted on an EPICS (Experimental Physics and Industrial Control System) process variable. A new real-voltage measurement can thus be read every 5 ms, corresponding to 2 voltage measurements between each atom bunch, which is a rate high enough for the purposes of the CRIS experiment that operates with a duty cycle of 100 Hz. Attempts to potentially increase the measurement frequency at CRIS in the future must remain mindful of the speed limitations of the voltmeter readout, however.

Triggering and synchronization

To ensure that all steps in the voltage-scanning sequence are applied for the same number of atom bunches, triggering a new voltage step needs to be synchronized with the bunch ejection from ISCOOL. To release the ion bunches from ISCOOL, CRIS triggers the fast voltage switch of the buncher's trapping electrode using an ultra-low jitter multi-channel function generator (Quantum Composer 9520). As a result, the trigger synchronization with the voltage-scanning setup is rather straightforward: a copy of the transistor-transistor-logic (TTL) signal that commands the bunch release from ISCOOL is supplied to a digital-input (DI) channel on the DAC. The NI-USB-6211 DAC can be programmed to keep track of how many triggers it has received in a DI channel using a loop counter, as well as initiate the AO channels in synchronization with the DI channels. The voltage step is thus changed in sync with the buncher by keeping track of the number of logical-true TTL signals since the last voltage change.

Furthermore, as CRIS specializes on atoms and molecules containing short-lived radioactive nuclei, the voltage-scanning setup has to be compatible with the study of species with very short half-lives; that is, species that decay shortly after a proton pulse bombards the ISOLDE target. In those cases, it is not sufficient to set a new step in the voltage-scanning sequence in sync with the buncher ejection, since not all bunches will contain the atoms of interest. Instead the voltage-scanning setup must operate in sync with the proton impact on the ISOLDE target. For this purpose, a TTL signal is supplied by the facility to the CRIS setup, which has a logical-true value when a proton pulse arrives at

ISOLDE and a logical-false at all other times. A copy of this signal is therefore supplied to a separate digital-input channel in the DAC, and so the synchronization channel can be switched at will between buncher ejection and proton impact.

Control software

The control software was constructed using Python and the PyQt5 package and its user interface is shown in Fig. 7.3. It is structured along three tabs. The "General" tab defines the start and end voltages for when a single voltage range is used, the total number of voltage steps and the voltage step-size, the triggers per step, and the sleep-time between steps taken when on internal trigger. It further allows choosing between trigger source (internal, buncher, or proton trigger), between scanning by step-size or by total number of steps, and between a single voltage range or a combination of multiple ranges ('Simple multi-range'). Lastly, it gives control over the amplifier (enabling or disabling), the choice to start or stop the scan, to restart the scan once the range is covered ('Loop scan'), or to freeze the scan at its current voltage.

The second tab, "Voltage ranges", allows defining a number of different ranges and enabling them using tick-boxes. When the "Simple multi-range" option is selected in the General tab, the enabled ranges are combined into one discontinuous scan.

The last tab, "Laser-Voltage Sequence", hosts a feature currently under development. By defining a maximum voltage limit and a rest-frame wavenumber range that has to be covered, the laser-voltage sequence feature aims to automatically generate a combination of voltage and laser steps to measure large wavenumber structures without a compromise in the beam trajectory. Voltage-scanning implementations in other CLS beamlines, where voltage and laser scanning are not combined, require applying very large voltages (up to ±10 kV) to cover large hfs structures. Such changes in the ion KE, however, inevitably result in significant changes to the ion trajectory and possibly to the laser-beam overlap. By defining a rest-frame wavenumber range instead of just a voltage range, the software can automatically calculate the different etalon positions for the spectroscopy laser such that it is moved to different wavelengths and kept static while the voltage is scanned across its maximum allowed range.

To finalize this feature, the etalon of the CW Matisse laser, which can be controlled through Python or LabView, needs to be connected to an EPICS process variable. A detailed troubleshooting and commissioning test is then required.

7.1.4 Commissioning tests

The voltage-scanning setup was tested with stable beams of ^{27}Al and ^{109}Ag from ISOLDE. The goals of the commissioning tests were a) to identify the valid voltage range where steering and focusing effects do not significantly alter the beam transport, and b) to compare the hfs constants extracted from laser and voltage scanning.

The test on ^{27}Al took place as part of ISOLDE experiment IS700[2]. The hfs of the $3s^2 3p\ ^2\mathrm{P}^\circ_{1/2} \rightarrow 3s^2 4s\ ^2\mathrm{S}_{1/2}$ transition in ^{27}Al is approximately 4-GHz wide, which, at a KE of ~40,000 V, corresponds to voltage-scanning range of approximately 200 V; within this voltage range, no beam-transport alterations were identified. A comparison of the ^{27}Al spectrum measured with laser and voltage scanning can be found in Ref. [168], which is added as Article 3 in this thesis.

The commissioning tests using ^{109}Ag were more extensive. Contrary to aluminium, the hfs of the $4d^{10} 5s\ ^2\mathrm{S}_{1/2} \rightarrow 4d^{10} 5p\ ^2\mathrm{P}^\circ_{3/2}$ transition in silver is rather wide, spanning more than 20 GHz for isotopes with $I > 0$. Therefore, the full structure cannot be scanned by voltage-tuning around a single laser wavelength. Instead, a combination of voltage and laser scanning is optimal.

The results of comparing the extracted hfs A constants for the upper and lower electronic states in ^{109}Ag are also given in Ref. [168]. Evidently, the results are fully consistent across the two approaches, with the voltage-scanning fit having a lower statistical error than the laser-scanning one.

As measuring the hfs of silver isotopes with voltage scanning also requires changing the laser wavelength to different setpoints (centered around

---

[2] IS700: `https://cds.cern.ch/record/2766524?ln=en`

a)

Simple multi-range ☐

Internal trigger

Scan by step size

Start voltage (V): -200

Stop voltage (V): 200

Step size (V): 1

Sleeptime between steps (ms): 150.0

Triggers per step: 2

Total scan steps: 100

20%

-118.2999 V

b)

☑ Range 1	-110	-50	☐ Range 6	0	0
☑ Range 2	50	230	☐ Range 7	0	0
☐ Range 3	0	0	☐ Range 8	0	0
☐ Range 4	0	0	☐ Range 9	0	0
☐ Range 5	0	0	☐ Range 10	0	0

30%

0.22999 V

c)

☐ Sequence 1		☐ Sequence 2		☐ Sequence 3		☐ Sequence 4	
☐ Laser setpoint 1	11001	☐ Laser setpoint 1	11002	☐ Laser setpoint 1	11003	☐ Laser setpoint 1	11004
☐ Voltage range 1	Range 1	☐ Voltage range 1	Range 1	☐ Voltage range 1	Range 1	☐ Voltage range 1	Range 1
☐ Laser setpoint 2	12001	☐ Laser setpoint 2	12002	☐ Laser setpoint 2	12003	☐ Laser setpoint 2	12004
☐ Voltage range 2	Range 1	☐ Voltage range 2	Range 1	☐ Voltage range 2	Range 1	☐ Voltage range 2	Range 1
☐ Laser setpoint 3	13001	☐ Laser setpoint 3	13002	☐ Laser setpoint 3	13003	☐ Laser setpoint 3	13004
☐ Voltage range 3	Range 1	☐ Voltage range 3	Range 1	☐ Voltage range 3	Range 1	☐ Voltage range 3	Range 1
☐ Laser setpoint 4	14001	☐ Laser setpoint 4	14002	☐ Laser setpoint 4	14003	☐ Laser setpoint 4	14004
☐ Voltage range 4	Range 1	☐ Voltage range 4	Range 1	☐ Voltage range 4	Range 1	☐ Voltage range 4	Range 1
☐ Laser setpoint 5	15001	☐ Laser setpoint 5	15002	☐ Laser setpoint 5	15003	☐ Laser setpoint 5	15004
☐ Voltage range 5	Range 1	☐ Voltage range 5	Range 1	☐ Voltage range 5	Range 1	☐ Voltage range 5	Range 1
☐ Laser setpoint 6	16002	☐ Laser setpoint 6	16002	☐ Laser setpoint 6	16003	☐ Laser setpoint 6	16004
☐ Voltage range 6	Range 1	☐ Voltage range 6	Range 1	☐ Voltage range 6	Range 1	☐ Voltage range 6	Range 1

30%

0.22918 V

Figure 7.3: Overview of the voltage-scanning control software. **a)** General tab. The real voltage applied to the electrode, measured by the fast voltmeter, is continuously shown at the bottom of the screen. A red light shows the status of the amplifier: bright red when the amplifier is active, dark when inactive. **b)** "Voltage ranges" tab. A combination of voltage ranges can be defined and combined into one large, discontinuous range. **c)** "Laser-Voltage Sequence": tab hosting a new feature that is currently underdevelopment.

the three structures seen in Fig. 1 in Article 3), the speedup that voltage scanning offers over laser scanning in the case of Ag serves as a general lower bound. Even in that case, the reduction in time per scan across different Ag isotopes was a factor of 3 or higher. Following the commissioning test in Ag, and due to the favorable system performance and the faster measurement rate of the approach, it was decided that voltage scanning was to be used for all hfs scans in the CRIS experiment of radioactive Ag isotopes (IS660[3]). Therefore, IS660 became the first experiment to utilize voltage scanning as the main approach to laser spectroscopy at the CRIS beamline.

With a reduction in time per scan of at least a factor of 3, voltage scanning can thus enable performing high-resolution laser spectroscopy of molecules at CRIS in a timescale at least three times shorter than the current capability. The speed-up factor is attributed more strongly to the high scan rates that are achievable with voltage scanning, rather than a specific feature of the hfs in Ag. Therefore, the speed-up factor can be expected to be transferrable to other species too, including molecules. For instance, voltage scanning was successfully also used in the IS714[4] experiment on Cr, with a similar speed-up.

7.1.5 Article 3: Voltage scanning and technical upgrades at the Collinear Resonance Ionization Spectroscopy experiment

---

[3] IS660: `http://cds.cern.ch/record/2717869?ln=en`

[4] IS714: `http://cds.cern.ch/record/2838648?ln=en`

Nuclear Instruments and Methods in Physics Research B 541 (2023) 86–89

Contents lists available at ScienceDirect

Nuclear Inst. and Methods in Physics Research, B

journal homepage: www.elsevier.com/locate/nimb

Voltage scanning and technical upgrades at the Collinear Resonance Ionization Spectroscopy experiment

Michail Athanasakis-Kaklamanakis [a,b,*,1], Jordan R. Reilly [c,**,1], Ágota Koszorús [a], Shane G. Wilkins [d,e], Louis Lalanne [b], Sarina Geldhof [b,2], Miranda Nichols [f], Quanjun Wang [g], Bram van den Borne [b], David Chorlton [c], Thomas E. Cocolios [b], Kieran T. Flanagan [c,h], Ronald F. Garcia Ruiz [d], Ruben de Groote [b], Dag Hanstorp [f], Gerda Neyens [b], Andrew J. Smith [c], Adam R. Vernon [d], Xiaofei F. Yang [i]

[a] *Experimental Physics Department, CERN, CH-1211 Geneva 23, Switzerland*
[b] *Instituut voor Kern- en Stralingsfysica, KU Leuven, B-3001 Leuven, Belgium*
[c] *School of Physics and Astronomy, The University of Manchester, Manchester M13 9PL, United Kingdom*
[d] *Department of Physics, Massachusetts Institute of Technology, Cambridge, MA, 02139, USA*
[e] *Laboratory for Nuclear Science, Massachusetts Institute of Technology, Cambridge, MA, 02139, USA*
[f] *Department of Physics, University of Gothenburg, SE 412 96 Gothenburg, Sweden*
[g] *School of Nuclear Science and Technology, Lanzhou University, Lanzhou 730000, China*
[h] *Photon Science Institute, The University of Manchester, Manchester M13 9PY, United Kingdom*
[i] *School of Physics and State Key Laboratory of Nuclear Physics and Technology, Peking University, Beijing 100971, China*

ARTICLE INFO

Keywords:
CRIS
Collinear resonance ionization spectroscopy
Laser spectroscopy
Voltage scanning
ISOLDE

ABSTRACT

To optimize the performance of the Collinear Resonance Ionization Spectroscopy (CRIS) experiment at CERN-ISOLDE, technical upgrades are continuously introduced, aiming to enhance its sensitivity, precision, stability, and efficiency. Recently, a voltage-scanning setup was developed and commissioned at CRIS, which improved the scanning speed by a factor of three as compared to the current laser-frequency scanning approach. This leads to faster measurements of the hyperfine structure for systems with high yields (more than a few thousand ions per second). Additionally, several beamline sections have been redesigned and manufactured, including a new field-ionization unit, an electrostatic bend with a larger deflection angle, and improved ion optics. The beamline upgrades are expected to yield an improvement of at least a factor of 5 in the signal-to-noise ratio by avoiding the use of high-power lasers (which yield non-resonantly produced ions) and providing time-of-flight separation between the resonant ions and the collisional background.

1. Introduction

Laser spectroscopy of radioactive atoms and ions has been a cornerstone of ground- and long-lived isomeric-state nuclear studies for several decades [1,2]. By measuring the hyperfine structure and isotope shifts of an electronic transition across multiple isotopes of the same element, the nuclear electromagnetic moments, nuclear spin, and changes in mean-squared nuclear charge radii can be measured. Systematic studies of these observables can then be used to study the strong nuclear interaction and the emergence of nuclear phenomena as a function of the nucleon numbers.

Traditionally, two approaches to laser spectroscopy have been most widely used on radioactive species: in-source resonance ionization spectroscopy (RIS) [3] and fluorescence-detection collinear laser spectroscopy (CLS) of fast beams [4]. As a merger of the two approaches, the collinear resonance ionization spectroscopy (CRIS) experiment at ISOLDE combines the high sensitivity of RIS with the high resolution of CLS. CRIS has thus successfully studied species with a production rate down to 20 nuclei per second [5], while also reaching a resolution of 20(1) MHz in the francium chain [6]. Recently, CRIS also ventured into the spectroscopy of radioactive molecules that are of interest for the study of fundamental symmetries [7,8]. Implementations of the CRIS

---

* Corresponding author at: Experimental Physics Department, CERN, CH-1211 Geneva 23, Switzerland.
** Corresponding author.
E-mail addresses: m.athkak@cern.ch (M. Athanasakis-Kaklamanakis), jordan.reilly@cern.ch (J.R. Reilly).

[1] These authors contributed equally to the work.

[2] Current address: GANIL, CEA/DRF-CNRS/IN2P3, B.P. 55027, 14076 Caen, France.

https://doi.org/10.1016/j.nimb.2023.04.054
Received 19 January 2023; Received in revised form 25 April 2023; Accepted 26 April 2023

technique are currently also under construction and commissioning at the IGISOL laboratory of the University of Jyväskylä, Finland and at the Facility for Rare Isotope Beams (FRIB), USA.

In this article, recent technical upgrades at the CRIS experiment are described. The commissioning of a voltage-scanning apparatus has demonstrated that narrowband spectroscopy at CRIS can be now performed 3–6 times faster, for cases that are not statistically limited by a low production yield (typically with yields above a few thousand ions per second). Moreover, upgrades on several sections of the CRIS beamline are expected to significantly improve the signal-to-noise ratio of the technique.

2. CRIS technique

In the CRIS technique, the fast, isobarically pure, cooled and bunched short-lived ions delivered by ISOLDE are firstly neutralized in a charge-exchange cell (CEC) filled with alkali vapour. The residual ions are deflected away from the beam, while the neutral atoms are transferred to the interaction region (IR). In the IR, the atoms are spatially and temporally overlapped with a series of laser pulses that step-wise resonantly excite an electron from the ground state (or a metastable state) to above the ionization potential. To avoid collisional ionization, the IR and the remaining part of the beamline are kept at a vacuum below 5×10^{-9} mbar. The ions are then deflected away from the residual neutral species (e.g. neutralized isobars) and onto a MagneToF single-ion detector, and the signal is then processed with a time digitizer with sub-ns resolution.

In a typical narrowband CRIS scheme [9], the atoms are excited from their initial hyperfine states by one or two consecutive resonant transitions. The spectroscopy transition is scanned in high resolution by changing the wavelength of a tunable narrowband laser. For transitions in the titanium sapphire (Ti:Sa) range, an injection-seeded cavity with a linewidth of ∼20 MHz is used [10], while a pulsed dye amplifier with a typical linewidth of ∼150 MHz is used for the dye ranges. For resonant transitions excited in lower resolution, a broadband Ti:Sa or dye laser with a linewidth of ∼3–10 GHz is used. A high-power Nd:YAG laser is used for non-resonant ionization [11].

3. Technical upgrade of the CRIS experiment

To optimize the performance of the CRIS experiment, technical upgrades to the beamline and laser systems are continuously developed, aiming to improve the spectroscopic background, efficiency, resolution, and precision of the technique. Previously, progress was reported on the development of a prototype field-ionization unit to reduce the background [11], the design of a radiofrequency cooler-buncher [12], and the installation of α- [13] and β-decay tagging [14,15] stations to filter out stable and long-lived contaminants from the radioactive species. Recently, the development focus at the CRIS experiment has been placed on the implementation of voltage scanning and the upgrade of the beamline sections beyond the IR (referred to herein as *the new end of the beamline*).

3.1. Voltage scanning

Instead of directly scanning the wavelength of the laser, CLS most often exploits the velocity of the fast beam and the Doppler effect to perform spectroscopy [4]. The fast beam can be brought in and out of resonance with a fixed-wavelength laser in its rest frame by introducing slight variations to the beam's kinetic energy. This approach is a staple in fluorescence-detection CLS and is often referred to as *voltage scanning*, since the kinetic energy is varied by applying varying voltages to a set of electrodes.

Voltage scanning offers significant benefits over laser scanning, and is thus strongly preferred in collinear experiments. By performing spectroscopy with voltage scanning, the narrowband laser system remains locked to a single wavelength and thus reaches greater stability over time, minimizing power fluctuations and leading to less noisy spectra. Additionally, the slew rate of the voltage-scanning electronics is typically considerably faster than the laser-scanning feedback loop based on the wavemeter reading, which measures the laser wavelength. As a result, for experiments on species with a sufficiently high production rate (in the order of $\sim 10^3$ ions per second), voltage scanning can significantly accelerate the experimental run-time. Additionally, voltage scanning allows for skipping unnecessary regions of background, which is more challenging with laser scanning due to the difficulty of stabilizing a narrowband laser cavity while scanning across discontinuous spectral ranges multiple times.

However, there is a caveat in voltage scanning; accelerating an ion beam also electrostatically focuses it, while decelerating de-focuses it. As a result, in CLS beamlines employing voltage scanning, the detection region has so far been placed as close as possible after the voltage-scanning electrode. The CRIS beamline, where the IR is 1.2 m long and the detector is after an electrostatic bend (see Fig. 2), is particularly sensitive to changes in the ion-beam focus. For CLS and CRIS experiments on neutral atoms, the voltage-scanning electrode must be placed before the CEC, further increasing the distance to the detector. Previous attempts to implement voltage scanning at CRIS [16,17] were thus unsuccessful as the ion transport through the beamline and onto the detector was significantly impacted by the changes in ion focus.

To bypass the past limitations related to ion transport, the new voltage-scanning setup at CRIS utilizes the electrode design reported by Gins et al. in Ref. [18]. The change in kinetic energy experienced by the ion beam while flying through the electrode is significantly smoother compared to the traditional design of resistively connected rings [19] that was also used in the past at CRIS. As a result, the aberrations in the beam collimation are presumed to be minimized, as shown below.

The voltage-scanning setup was commissioned on beams of ^{109,116}Ag and ^{27}Al, comparing the results of frequency- and voltage-scanning. As seen in Fig. 1, the results of the hyperfine-structure fits are consistent for both scanning approaches. As no compromise in the spectroscopic efficiency was observed, it is concluded that the ion transport due to the changes in beam focus is largely unaffected. A voltage range of 400 V was successfully tested with no efficiency loss during the commissioning tests, which corresponds to more than 4 GHz in frequency space in the case of silver.

Voltage scanning led to a 3–6 times reduced time per scan in the cases of silver and aluminium, depending on the isotope and its hyperfine structure. Overall, a potential time reduction per scan of up to 10 times is predicted from voltage scanning depending on the production yield, the wavelength range, the hyperfine structure, and the spectral resolution.

3.2. New end of the beamline

For the CRIS technique to continue to push its limits, a new design for the end of the beamline is under construction. The new design will replace the current beamline from the end of the laser-atom IR onwards, as shown in Fig. 2. The upgraded section consists of an energy-selective field ionization unit, a 34° bending chamber with collinear and anti-collinear laser access, a quadrupole triplet, deflection plates, a removable single-ion detector, and a decay spectroscopy station (DSS) that allows for β- and α-tagging. The DSS chamber will also be interchangeable with a neutral particle detector for experiments on the laser photodetachment of negative ions.

A new energy-selective field ionization unit offers the opportunity to substitute the conventional non-resonant laser ionization step into the continuum with the electrostatic ionization of Rydberg states, while separating the field-ionized species from collisionally ionized background. The design of the apparatus was firstly presented by Vernon et al. in Ref. [11]. As the atoms undergo field ionization, they are accelerated by hundreds of eV while the collisional ions remain at the

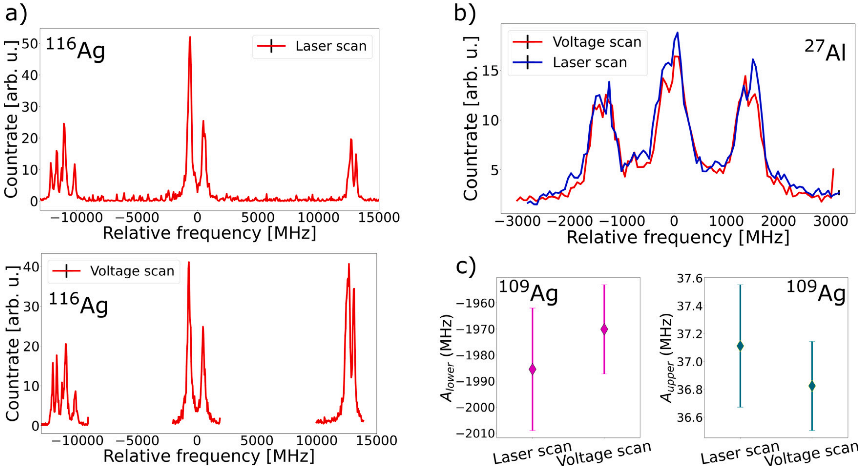

Fig. 1. Commissioning tests of voltage scanning at CRIS using beams of ^{116}Ag, ^{109}Ag, and ^{27}Al. **(a)** Comparison of laser and voltage scanning. Scanning of background regions can be skipped with the latter, which significantly reduces the measurement time. The change in relative peak strength is due to a change in the relative production of ^{116g,m}Ag during the experiment. **(b)** Visual comparison of spectra obtained with laser and voltage scanning, overlapped in the rest frame of the beam. **(c)** Comparison of the hyperfine *A* constants for the upper and lower electronic states in ^{109}Ag. The results from the hyperfine fit for the voltage scans are fully consistent with those from the laser scans.

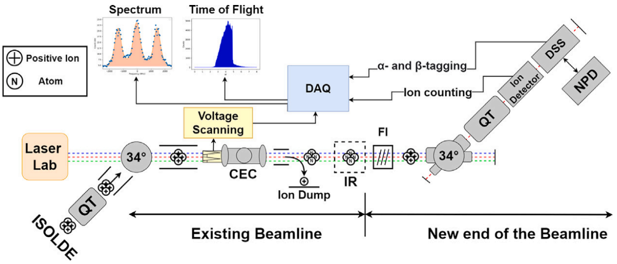

Fig. 2. Schematic diagram of the existing CRIS beamline coupled to the new end of the beamline. The new end connects to the existing beamline at the laser-atom interaction region (IR), after neutralization in the charge-exchange cell (CEC). The IR is followed by the energy-selective field ionization (FI) unit, the 34° bending chamber, a quadrupole triplet (QT), a MagneToF single-ion detector, and the interchangeable decay spectroscopy station (DSS) and neutral particle detector (NPD).

initial beam energy. This small increase enables their angular separation in the 34° bend. The resulting difference in the ion trajectories downstream allows for the collisional ions to be filtered with the use of mechanical slits or by adjusting the position of the single-ion detector to align with the ion beam trajectory. Field ionization also removes the requirement of a high-power ionization laser that significantly contributes to the spectroscopic background through the non-resonant ionization of isobaric contaminant species. These improvements are critical to reduce the background towards performing background-free spectroscopy on beams with isobaric contamination that is a million times more intense than the isotope of interest, which is vital for the study of radioactive isotopes with low production yields [20].

The angle of the new bending chamber is 70% larger than that of the existing bend. In addition to the improved angular separation of field-ionized and background ions, the increased bending angle allows for charge-state selection, such as between +1 and +2 ions. This is particularly advantageous for campaigns where ionic spectroscopy is preferred, such as Group II elements. Furthermore, the new bending chamber has been designed with two axes of laser access: one aligned with the laser-atom IR and one aligned with the chambers after the bend. The former is used for collinear (or anti-collinear) laser spectroscopy, whereas the latter can be used to perform photodetachment of negative ions in future campaigns.

Following the bending chamber, a quadrupole triplet and a set of deflector plates provide further control of the ion transport to the single-ion detector (MagneToF) and the DSS. The DSS will be equipped with α or β detectors and a fast tape station to allow for decay-assisted laser spectroscopy [13] and laser-assisted decay spectroscopy, separating the isotopes depending on their decay mechanisms and energy.

4. Summary and outlook

In conclusion, the CRIS experiment has been recently upgraded with the addition of a voltage-scanning apparatus to perform laser spectroscopy on short-lived species. Through voltage scanning, the time per scan of CRIS experiments can be potentially performed up to 10 times faster for isotopes produced with high yields (more than few thousand ions per second). Commissioning tests on ^{109,116}Ag and ^{27}Al have demonstrated that the hyperfine spectra measured with voltage and laser scanning are consistent. A voltage range of 400 V, which corresponds to a frequency range of ∼4 GHz in the case of silver, was confirmed to cause no significant changes in the beam transport that would compromise the accuracy or efficiency of the CRIS experiment.

Additionally, upgrades to several regions of the CRIS beamline have been designed and are currently under construction and testing. The new regions include a field-ionization unit, a sharper electrostatic bend, and improved ion optics after the bend towards a single-ion counter and a decay spectroscopy station. Incorporating a field-ionization unit and a sharper bend leading to the ion detector are predicted to improve the signal-to-noise ratio by a factor of 5 or more [11], with the possibility of background-free spectroscopy when combined with the decay station.

Declaration of competing interest

The authors of the manuscript titled Voltage scanning and technical upgrades at the Collinear Resonance Ionizaton Spectroscopy experiment would like to declare no conflict of interest in the manuscript submitted for publication as part of the proceedings series at EMIS2022 RAON.

Acknowledgements

This project has received funding from FWO, Belgium through IRI and regular projects, as well as from the Excellence of Science (EOS) programme (nr. 40007501), and the KU Leuven projects GOA15/010 and C14/22/104. The Department of Energy, Office of Science award DE-SC0021176 is also acknowledged.

References

[1] P. Campbell, I.D. Moore, M.R. Pearson, Laser spectroscopy for nuclear structure physics, Prog. Part. Nucl. Phys. 86 (2016) 127–180, http://dx.doi.org/10.1016/j.ppnp.2015.09.003, URL https://www.sciencedirect.com/science/article/pii/S0146641015000915.

[2] X. Yang, S. Wang, S. Wilkins, R.G. Ruiz, Laser spectroscopy for the study of exotic nuclei, Prog. Part. Nucl. Phys. 129 (2023) 104005, http://dx.doi.org/10.1016/j.ppnp.2022.104005, URL https://www.sciencedirect.com/science/article/pii/S0146641022000631.

[3] B.A. Marsh, B. Andel, A.N. Andreyev, S. Antalic, D. Atanasov, A.E. Barzakh, B. Bastin, C. Borgmann, L. Capponi, T.E. Cocolios, T. Day Goodacre, M. Dehairs, X. Derkx, H. De Witte, D.V. Fedorov, V.N. Fedosseev, G.J. Focker, D.A. Fink, K.T. Flanagan, S. Franchoo, L. Ghys, M. Huyse, N. Imai, Z. Kalaninova, U. Köster, S. Kreim, N. Kesteloot, Y. Kudryavtsev, J. Lane, N. Lecesne, V. Liberati, D. Lunney, K.M. Lynch, V. Manea, P.L. Molkanov, T. Nicol, D. Pauwels, L. Popescu, D. Radulov, E. Rapisarda, M. Rosenbusch, R.E. Rossel, S. Rothe, L. Schweikhard, M.D. Seliverstov, S. Sels, A.M. Sjödin, V. Truesdale, C. Van Beveren, P. Van Duppen, K. Wendt, F. Wienholtz, R.N. Wolf, S.G. Zemlyanoy, New developments of the in-source spectroscopy method at RILIS/ISOLDE, Nucl. Instrum. Methods Phys. Res. B 317 (2013) 550–556, http://dx.doi.org/10.1016/j.nimb.2013.07.070, URL https://www.sciencedirect.com/science/article/pii/S0168583X13008914.

[4] R. Neugart, J. Billowes, M.L. Bissell, K. Blaum, B. Cheal, K.T. Flanagan, G. Neyens, W. Nörtershäuser, D.T. Yordanov, Collinear laser spectroscopy at ISOLDE: new methods and highlights, J. Phys. G: Nucl. Part. Phys. 44 (6) (2017) 064002, http://dx.doi.org/10.1088/1361-6471/aa6642, URL https://iopscience.iop.org/article/10.1088/1361-6471/aa6642.

[5] R.P. de Groote, J. Billowes, C.L. Binnersley, M.L. Bissell, T.E. Cocolios, T. Day Goodacre, G.J. Farooq-Smith, D.V. Fedorov, K.T. Flanagan, S. Franchoo, R.F. Garcia Ruiz, W. Gins, J.D. Holt, Koszorús, K.M. Lynch, T. Miyagi, W. Nazarewicz, G. Neyens, P.G. Reinhard, S. Rothe, H.H. Stroke, A.R. Vernon, K.D. Wendt, S.G. Wilkins, Z.Y. Xu, X.F. Yang, Measurement and microscopic description of odd–even staggering of charge radii of exotic copper isotopes, Nat. Phys. 16 (6) (2020) 620–624, http://dx.doi.org/10.1038/s41567-020-0868-y.

[6] R.P. de Groote, I. Budinčević, J. Billowes, M. Bissell, T. Cocolios, G. Farooq-Smith, V. Fedosseev, K. Flanagan, S. Franchoo, R.F. Garcia Ruiz, H. Heylen, R. Li, K. Lynch, B. Marsh, G. Neyens, R. Rossel, S. Rothe, H. Stroke, K. Wendt, S. Wilkins, X. Yang, Use of a continuous wave laser and pockels cell for sensitive high-resolution collinear resonance ionization spectroscopy, Phys. Rev. Lett. 115 (13) (2015) 132501, http://dx.doi.org/10.1103/PhysRevLett.115.132501.

[7] R.F. Garcia Ruiz, R. Berger, J. Billowes, C.L. Binnersley, M.L. Bissell, A.A. Breier, A.J. Brinson, K. Crysalidis, T.E. Cocolios, B.S. Cooper, K.T. Flanagan, T.F. Giesen, R.P. de Groote, S. Franchoo, F.P. Gustafsson, T.A. Isaev, A. Koszorus, G. Neyens, H.A. Perrett, C.M. Ricketts, S. Rothe, L. Schweikhard, A.R. Vernon, K.D.A. Wendt, F. Weinholtz, S.G. Wilkins, X.F. Yang, Spectroscopy of short-lived radioactive molecules, Nature 581 (May) (2020) 396–400, http://dx.doi.org/10.1038/s41586-020-2299-4.

[8] S.M. Udrescu, A.J. Brinson, R.F. Garcia Ruiz, K. Gaul, R. Berger, J. Billowes, C.L. Binnersley, M.L. Bissell, A.A. Breier, K. Chrysalidis, T.E. Cocolios, B.S. Cooper, K.T. Flanagan, T.F. Giesen, R.P. de Groote, S. Franchoo, F.P. Gustafsson, T.A. Isaev, A. Koszorus, G. Neyens, H.A. Perrett, C.M. Ricketts, S. Rothe, A.R. Vernon, K.D.A. Wendt, F. Wienholtz, S.G. Wilkins, X.F. Yang, Isotope shifts of radium monofluoride molecules, Phys. Rev. Lett. 127 (3) (2021) 033001.

[9] A. Koszorús, J. Billowes, C.L. Binnersley, M.L. Bissell, T.E. Cocolios, B.S. Cooper, R.P. de Groote, G.J. Farooq-Smith, V.N. Fedosseev, K.T. Flanagan, S. Franchoo, R.F. Garcia Ruiz, W. Gins, K.M. Lynch, G. Neyens, F.P. Gustafsson, C. Ricketts, H.H. Stroke, A. Vernon, S.G. Wilkins, X.F. Yang, Resonance ionization schemes for high resolution and high efficiency studies of exotic nuclei at the CRIS experiment, Nucl. Instrum. Methods Phys. Res. B 463 (2020) 398–402, http://dx.doi.org/10.1016/j.nimb.2019.04.043, URL https://www.sciencedirect.com/science/article/pii/S0168583X19302277.

[10] V. Sonnenschein, I.D. Moore, S. Raeder, M. Reponen, H. Tomita, K. Wendt, Characterization of a pulsed injection-locked Ti:sapphire laser and its application to high resolution resonance ionization spectroscopy of copper, Laser Phys. 27 (8) (2017) 085701, http://dx.doi.org/10.1088/1555-6611/aa7834.

[11] A.R. Vernon, C.M. Ricketts, J. Billowes, T.E. Cocolios, B.S. Cooper, K.T. Flanagan, R.F. Garcia Ruiz, F.P. Gustafsson, G. Neyens, H.A. Perrett, B.K. Sahoo, Q. Wang, F.J. Waso, X.F. Yang, Laser spectroscopy of indium rydberg atom bunches by electric field ionization, Sci. Rep. 10 (1) (2020) 12306, http://dx.doi.org/10.1038/s41598-020-68218-5.

[12] C.M. Ricketts, B.S. Cooper, G. Edwards, H.A. Perrett, J. Billowes, C.L. Binnersley, T.E. Cocolios, K.T. Flanagan, R.F. Garcia Ruiz, R.P. de Groote, F.P. Gustafsson, A. Koszorús, G. Neyens, A.R. Vernon, X.F. Yang, A compact linear paul trap cooler buncher for CRIS, Nucl. Instrum. Methods Phys. Res. B 463 (2020) 375–377, http://dx.doi.org/10.1016/j.nimb.2019.04.054, URL https://www.sciencedirect.com/science/article/pii/S0168583X19302381.

[13] K.M. Lynch, J. Billowes, M.L. Bissell, I. Budincevic, T.E. Cocolios, R.P. De Groote, S. De Schepper, V.N. Fedosseev, K.T. Flanagan, S. Franchoo, R.F. Garcia Ruiz, H. Heylen, B.A. Marsh, G. Neyens, T.J. Procter, R.E. Rossel, S. Rothe, I. Strashnov, H.H. Stroke, K.D.A. Wendt, Decay-assisted laser spectroscopy of neutron-deficient francium, Phys. Rev. X 4 (1) (2014) 11055, http://dx.doi.org/10.1103/PhysRevX.4.011055.

[14] A. Koszorús, Collinear Resonance Ionization Spectroscopy of Potassium Isotopes: Crossing N=32 (Ph.D. thesis), KU Leuven, Leuven, 2019, pp. 1–210.

[15] A. Koszorús, X.F. Yang, W.G. Jiang, S.J. Novario, S.W. Bai, J. Billowes, C.L. Binnersley, M.L. Bissell, T.E. Cocolios, B.S. Cooper, R.P. de Groote, A. Ekström, K.T. Flanagan, C. Forssén, S. Franchoo, R.F.G. Ruiz, F.P. Gustafsson, G. Hagen, G.R. Jansen, A. Kanellakopoulos, M. Kortelainen, W. Nazarewicz, G. Neyens, T. Papenbrock, P.-G. Reinhard, C.M. Ricketts, B.K. Sahoo, A.R. Vernon, S.G. Wilkins, Charge radii of exotic potassium isotopes challenge nuclear theory and the magic character of N=32, Nat. Phys. (2021) http://dx.doi.org/10.1038/s41567-020-01136-5.

[16] K.T. Flanagan, Recent advances in laser spectroscopy at ISOLDE, Acta Phys. Polon. B 44 (3) (2013) 627–637, http://dx.doi.org/10.5506/APhysPolB.44.627.

[17] T.J. Procter, New Techniques of Laser Spectroscopy on Exotic Isotopes of Gallium and Francium (Ph.D. thesis), The University of Manchester, Manchester, 2013, pp. 1–149.

[18] W. Gins, R.D. Harding, M. Baranowski, M.L. Bissell, R.F. Garcia Ruiz, M. Kowalska, G. Neyens, S. Pallada, N. Severijns, P. Velten, F. Wienholtz, Z.Y. Xu, X.F. Yang, D. Zakoucky, A new beamline for laser spin-polarization at ISOLDE, Nucl. Instrum. Methods Phys. Res. A 925 (2019) 24–32, http://dx.doi.org/10.1016/j.nima.2019.01.082, URL https://www.sciencedirect.com/science/article/pii/S0168900219301536.

[19] K. Minamisono, P.F. Mantica, A. Klose, S. Vinnikova, A. Schneider, B. Johnson, B.R. Barquest, Commissioning of the collinear laser spectroscopy system in the BECOLA facility at NSCL, Nucl. Instrum. Methods Phys. Res. A 709 (2013) 85–94, http://dx.doi.org/10.1016/j.nima.2013.01.038, URL https://www.sciencedirect.com/science/article/pii/S0168900213001034.

[20] R.P. de Groote, J. Billowes, C.L. Binnersley, M.L. Bissell, T.E. Cocolios, T. Day Goodacre, G.J. Farooq-Smith, D.V. Fedorov, K.T. Flanagan, S. Franchoo, R.F. Garcia Ruiz, A. Koszorús, K.M. Lynch, G. Neyens, F. Nowacki, T. Otsuka, S. Rothe, H.H. Stroke, Y. Tsunoda, A.R. Vernon, K.D.A. Wendt, S.G. Wilkins, Z.Y. Xu, X.F. Yang, Dipole and quadrupole moments of $^{73-78}$Cu as a test of the robustness of the $Z = 28$ shell closure near ^{78}Ni, Phys. Rev. C 96 (4) (2017) 41302, http://dx.doi.org/10.1103/PhysRevC.96.041302.

7.2 New ion source for molecular and atomic beams

The offline[5] ion source is a core component of the CRIS setup, as it serves a dual purpose. On the one hand, offline spectroscopy of stable beams is often pursued for the preparation of experiments on radioactive isotopes [169]. On the other hand, the ability to perform spectroscopy on stable isotopes independently from the availability of ISOLDE also enables CRIS experiments of atomic- and molecular-physics importance [170, 171] that are independent from the activities on radioactive beams. Furthermore, the availability of stable beams is also vital for the commissioning of technical developments [172].

An ion source that is well-suited for offline laser spectroscopy at CRIS must satisfy a number of requirements. Firstly, the ionization method must be versatile and valid for a large number of atomic and molecular species; alternatively, the ion source must be compatible with different ionization methods. Secondly, for the establishment of molecular spectroscopy as a frequent scientific activity at CRIS, the offline ion source must be able to produce rotationally cool molecular ions at room temperature. Thirdly, the ion beam must have a narrow KE distribution, as a broad distribution leads to significant spectral broadening. Lastly, the ions must be accelerated to 10-30 keV to be delivered to the beamline without detriment to the beam emittance, ideally also in bunched form.

While designs of surface and plasma ion sources that are operationally reliable are readily available, such ion sources cannot simultaneously fulfill all of the aforementioned criteria. Surface ion sources are applicable only to a limited number of species that have an IP of 5 eV or less, while the fully versatile plasma ion sources also lead to the dissociation of most molecular species due to the high impact energy of the plasma. Laser ablation offers a promising alternative; reliable ionization is possible for virtually any atom and molecule [173], and its combination with gas cells is well-developed for the rotational cooling of molecules and reducing the KE distribution of atoms (for example, see Refs. [174] and [175]).

---

[5] *Offline* in the context of the CRIS experiment refers to equipment and activities related to the laser spectroscopy of beams not delivered by ISOLDE. As a result, a CRIS offline ion source refers to the equipment used for the independent delivery of non-radioactive ions to the CRIS experiment that is decoupled from ISOLDE.

7.2.1 Current ion source

A laser-ablation ion source has been operational at CRIS since 2017 (a schematic is shown in Ref. [170]). A 100-Hz second-harmonic Nd:YAG laser at 532 nm ablates a target that is oriented at approximately 45° between the ablation and the electrostatic-extraction axes. The ablation ions are extracted by a series of low-energy focusing electrodes that guide and collimate the beam. The ion acceleration is achieved with a voltage drop in the ion trajectory. The ablation region, where the ions are created, is floated to a high potential with respect to the lab ground. When the ablation ions that are produced within the floated source are then directed to a region that is electrically isolated from the source and whose potential is at lab ground, the previously slow ions are accelerated to a kinetic energy (in units of eV) equal to the potential difference between the two regions. A quadrupole steerer and an ion lens are then used on the fast beam for the injection into the CRIS beamline.

Despite its great success in the spectroscopy of In, Sn, and Zn, the existing ion source at CRIS faces several limitations. Firstly, the ablation and the extraction axes are perpendicular, which means that the ablation plume can never be aligned with the extraction field. As a result, only a tiny fraction of the ablation ions are successfully extracted from the source region. Secondly, the low-energy ion optics do not provide sufficient and decoupled steering and focusing. Lastly, the ablation region has not been designed to accommodate the presence of a buffer gas, which is necessary for ion thermalization and molecular formation. As a result, despite attempts, no resonance on a molecular species has ever been observed with the existing CRIS ion source. Additional limitations include the scarcity of beam diagnostics and the use of low-stability power supplies. Often, these limitations lead to fluctuations in the spatial distribution and the intensity of the beam that pose a big obstacle for laser spectroscopy.

A new offline ion source for CRIS was designed as part of the work presented in this thesis, marking progress in consolidating the CRIS efforts in molecular spectroscopy using radioactive and stable beams. The device was designed with the goal of addressing all the aforementioned specifications while placing a special emphasis on the reliable delivery of rotationally cooled molecular ions. By addressing the limitations of

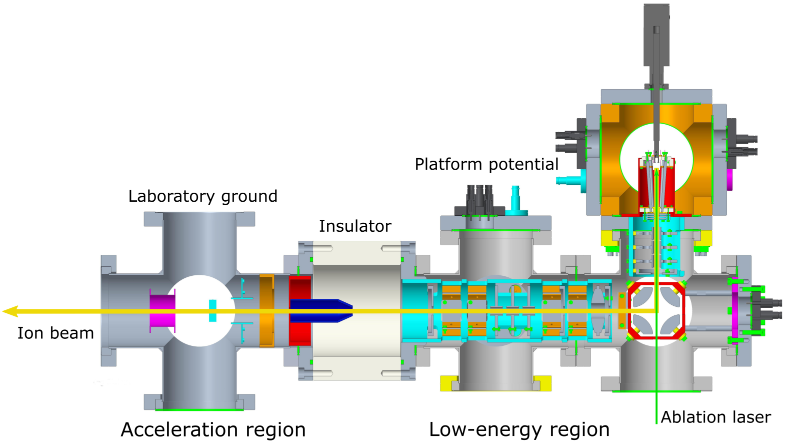

Figure 7.4: CAD schematic of the new CRIS ion source (front view).

the existing device, the new CRIS ion source has been designed to serve a universal upgrade to the CRIS experiment, improving the delivery of atomic and molecular beams alike.

7.2.2 New CRIS ion source

Front and side CAD schematics of the new ion source design are shown in Figs. 7.4 and 7.5. The laser ablation takes place within an octupole radiofrequency (RF) ion guide, such that the large radial distribution of the ions generated in the ablation plume is compressed directly after ionization. The ion guide is placed within a gas cell under constant gas flow. The gas is inserted behind the ablation target and exits the chamber through a 10-mm hole at the narrow end of the ion guide, thus guiding the ions along the electrostatic extraction field with high efficiency. Collisions with the gas thermalize the ions, narrowing down the KE distribution; by mixing the buffer gas with a chemical agent, the collisions also lead to molecular formation with a high efficiency.

After exiting the gas cell, the ions are focused by a triple einzel lens to the center of a quadrupole deflector. After the bend, the ions are compressed and refocused using a set of parallel-plate electrodes and a convex lens.

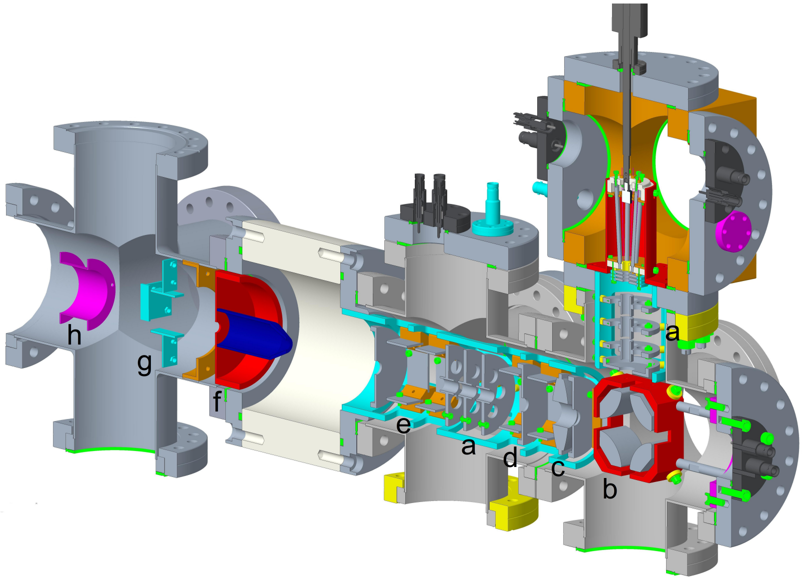

Figure 7.5: CAD schematic of the new CRIS ion source (side view). (a) Low-energy einzel lens for focusing the ion beam. (b) Quadrupole deflector. (c) Single low-energy focusing lens. (d) Collimator that can be monitored as a passive ion counter. (e) Up-down-left-right steerers. (f) Extractor of high-energy accelerated ions. (g) Up-down-left-right steerers of accelerated ions. (h) Single high-energy focusing lens.

With two sets of quadrupole steerers and another triple-lens assembly, they are guided to the voltage-drop region where they are accelerated. The post-acceleration region is kept as in the existing ion source.

A total of three ring electrodes are placed along the trajectory from the gas cell to the acceleration region, which serve as passive Faraday cups. That is, the ion current impinging on them can be constantly measured to provide information on the beam emittance without obstructing the beam traveling through them. The operational experience of past ion sources has deemed such diagnostics as highly desirable for the new design.

RF ion guide

The octupole ion guide is based on a design by Dr. Adam Vernon (Massachussetts Institute of Technology) and is shown in Fig. 7.6. Contrary to the typical geometry of a linear ion trap or ion guide, the inner radius of this device decreases along its length, giving it the form of a cone. The ratio between the radii of at the entrance and exit of the ion guide was chosen according to the optimal value obtained by ion trajectory simulations by Dr. Adam Vernon. Such calculations showed that the conical design can provide improved collimation and extraction efficiency compared to the straight geometry.

Between the eight poles carrying the RF potential, eight NIKROTHAL-80 wires with an electrical resistivity of 1.09 Ω mm^2/mm at 20 °C[6] are placed to provide the axial guiding DC potential. The wire ends at the top of the ion guide are connected to a high-voltage power supply, and thanks to their resistivity, a linearly decreasing axial potential is formed along the center of the ion guide, smoothly reaching a minimum at the ion guide exit.

The optimal frequency of the RF field was calculated to be 2 MHz, which will be produced by a Keysight 33511B arbitrary waveform generator. The radial-field optimization for the extraction of different masses through the ion guide will be performed by optimizing the amplitude of the RF field using a variable-gain amplifier, rather than the frequency.

To maximize the extraction efficiency of the ablation ions from the source region, the central axis of the ion guide is aligned with the path of the ablation laser. The ablation laser enters from underneath and ablates a target inside the ion guide, mounted onto a linear actuator (see Fig. 7.4). Thus, the axial DC field, the orientation of the ablation plume, and the direction of gas flow (as explained below) are all aligned for maximal efficiency.

---

[6] `https://www.kanthal.com/en/products/material-datasheets/wire/resistance-heating-wire-and-resistance-wire/nikrothal-80/`

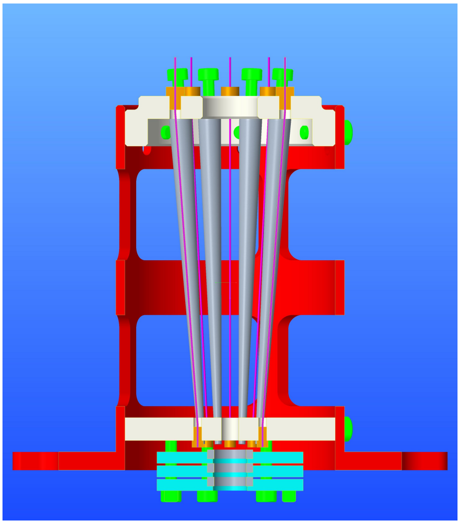

Figure 7.6: CAD schematic of the octupole ion guide in the new CRIS ion source. The resistive wires (magenta) provide the axial guiding DC potential, while the poles (grey) provide the containing radial field. The support structure (red) is further enclosed by aluminium walls (not shown).

Gas cell

The RF ion guide is placed in a gas cell filled with a helium buffer gas. The gas cell that houses the octupole is shown in Fig. 7.8. The gas is injected from a hole through the side wall, supplied from outside the vacuum chamber through a custom CF16 gas feedthrough. The gas is injected into the cell at a position that lies above the ablation target, while the only exit point from the cell coincides with the center of the ion guide. As a result, a smooth gas-pressure gradient that is overlapped with the extraction field guides the ions along the extraction axis starting from their production point.

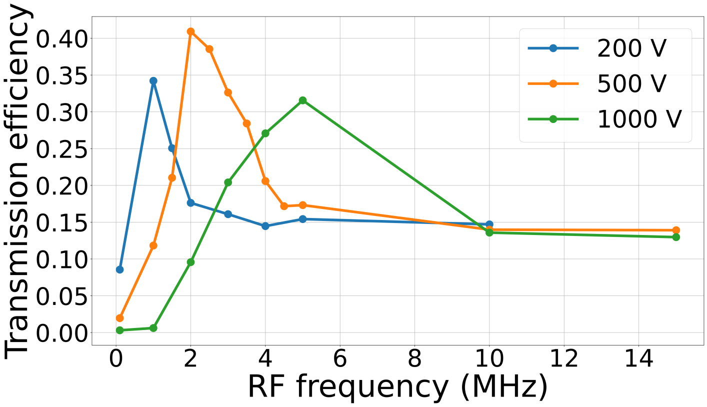

Figure 7.7: RF frequency curves for the octupole ion guide calculated using COMSOL. Three sets of calculations were performed for varying RF amplitudes. Tunability in the frequency range 1-5 MHz is thus desired.

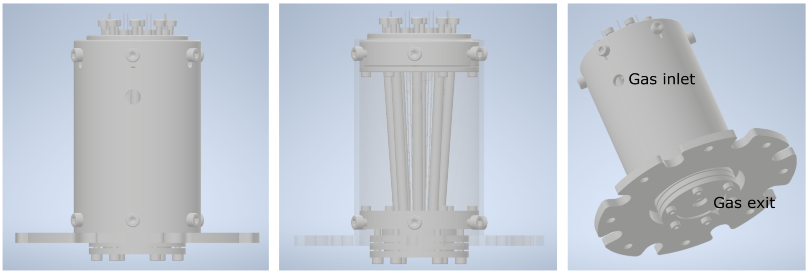

Figure 7.8: The gas cell used in the new ion source, which houses the octupole rf ion guide. The buffer gas is injected from the side wall above the ablation target and exits at the end of the ion guide.

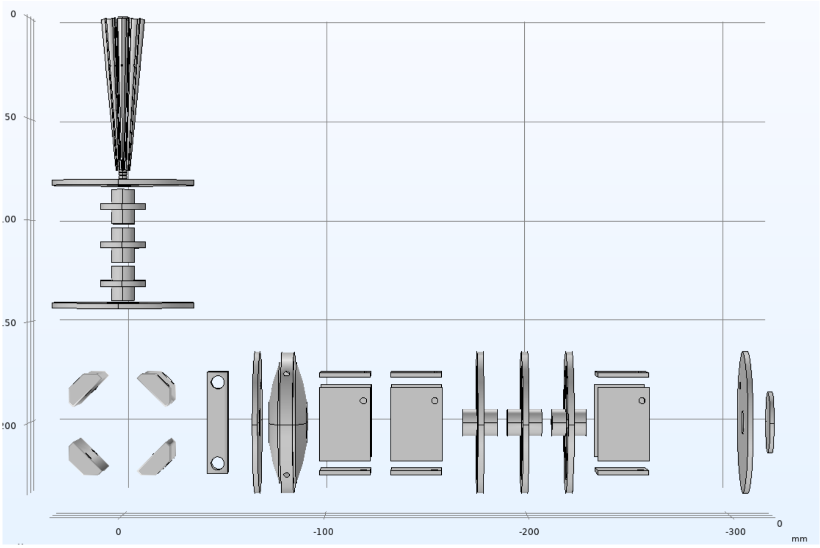

Figure 7.9: COMSOL geometric model of the new ion source.

Ion transport simulations

The ion optics design was determined based on ion transport simulations with the COMSOL multi-physics simulation package. Fig. 7.9 shows a rendering of the geometric model used in the COMSOL simulations.

To accelerate the charged particle tracing simulations, the presence of the gas in the octupole was firstly confirmed to improve the extraction and thermalization, leading to an extraction efficiency from the octupole of 90%, and was then stopped from subsequent simulations. The simulations thus demonstrated that the low-energy ion optics are sufficient to guide the ions to the acceleration region with a transport efficiency of at least 70%.

Construction and commissioning of the new CRIS ion source is planned for 2024.

Chapter 8

Summary and outlook

In this thesis, results of theoretical, experimental, and technical work on the intersection of nuclear and molecular physics are presented, focused on the spectroscopy of radioactive molecules that are of interest for future precision studies to search for signatures of new physics.

As elaborated in Chapter 1, precision tests of the SM based on searches for moments in the atomic nucleus and the electron that violate parity and time-reversal symmetries are being envisioned as a promising direction to search for new physics. Polar molecules that contain a nucleus with a high atomic number and static deformation are understood to be the most sensitive systems for these experiments. The majority of such nuclei, however, are short-lived, with the exception of a few primordial isotopes of thorium and uranium. As a result, even the preliminary spectroscopy of most radioactive molecules requires performing the experiment at RIB facilities.

This thesis presents theoretical work on the manifestation of the nuclear charge radius in molecular spectra (Chapter 3), the results of novel experiments on the spectroscopy of RaF (Chapters 4-5) and AcF (Chapter 6) using the CRIS technique at CERN-ISOLDE, and technical upgrades to the CRIS experiment for future molecular studies (Chapter 7).

The theoretical work on the intersection of nuclear and molecular physics focused on extending the King-plot analysis, which is well-established for atomic transitions, to diatomic molecules. This is an important step towards broadening our understanding of how nuclear effects manifest in molecular spectra, as precision molecular spectroscopy is receiving increasing attention as a probe for symmetry-violating nuclear moments. The work presented in Chapter 3 derived the King-plot analysis for simple diatomic molecules and demonstrated its validity using laser spectroscopy measurements in YbF and ZrO found in literature (Article 1).

In terms of experimental work, new results from the spectroscopy of RaF and AcF at CRIS are presented. RaF and AcF have been theoretically investigated for their sensitivity to the symmetry-violating electric dipole moments of the electron and the nucleus, which are key observables for precision tests of the SM. In RaF, following the first laser spectroscopy in 2018 [5, 4], a second CRIS experiment [176] was performed. I analyzed a significant part of the data set, which included – among other results – the measurement of 14 new and reassigned excited states (Article 2), a measurement of the lifetime of the $A\ ^2\Pi_{1/2}$ upper state in the proposed laser-cooling scheme, and measurements of the $A\ ^2\Pi_{1/2} \leftarrow X\ ^2\Sigma_{1/2}$ (0←0) transition in $^{210,212-214,226,227,230}$RaF, which are presented in Chapters 4-5.

Regarding AcF, Chapter 6 presents the first laser spectroscopy of this molecule, performed with the CRIS experiment. Despite a significantly more complicated electronic structure than RaF, which led to both experimental and computational challenges, a strong electronic transition was successfully identified that is suitable for an efficient detection scheme in future precision experiments.

Lastly, the technical component of the doctoral work was focused on improvements of the CRIS experiment that are necessary for performing molecular spectroscopy with faster scanning times and an improved signal-to-noise ratio. The developments presented are the design of a new ion source based on laser ablation in a buffer-gas-cooled octupole rf ion guide for the delivery of intense molecular beams with low emittance, and the implementation of voltage scanning for spectroscopy by Doppler-tuning (Article 3), which offers benefits over laser-frequency scanning for species not limited by a weak production rate, such as all stable and many radioactive molecules.

As discussed in Chapter 1, the motivation for the work covered by this thesis is the prospect of precision tests of the SM through the spectroscopy of radioactive molecules. As this field keeps growing, a lot more work on the topic of this thesis and beyond is to be expected.

In parallel with global plans for more studies with radioactive molecules [23], further experiments are currently in preparation at CRIS for RaF and AcF. A new proposal [177] was submitted to the ISOLDE facility at CERN for high-resolution measurements of the hyperfine structure of ^{223,225}RaF, written and defended by the author of this thesis and approved for 19 shifts (152 hours) of experimental work at ISOLDE. Additionally, 14 shifts (112 hours) of radioactive beam time at CRIS have been reserved for more measurements in AcF [157], aiming to complete the measurement of the lifetime of the excited state, measure the IP, and search for higher-lying excited states with a newly purchased continuously tunable OPO laser.

It is important to stress that the prospects of research on radioactive molecules are not limited to fundamental studies and tests of the SM. As elaborated in our Letter of Intent to the ISOLDE and nTOF Committee at CERN [22] and a recent white paper [23] submitted to *Reports on Progress in Physics*, the spectroscopy of radioactive molecules offers benefits for nuclear structure, nuclear astrophysics, quantum chemistry, and nuclear engineering beyond what can be investigated in radioactive atoms.

Drawing an example from this thesis, the excitation energies of the newly discovered states in RaF presented in Chapter 4 were compared with the predictions of coupled-cluster theory in Article 2 (Section 4.4). While knowledge of the level scheme is important for designing efficient and sensitive searches for new physics with RaF, these measurements simultaneously provide a strong benchmark of the predictive power of Fock-space relativistic coupled-cluster theory. RaF is an ideal system for such a benchmark, because Ra is heavy enough for relativistic effects to be crucial while the chemical bonding is simple enough to be tractable with existing computational tools.

As seen in Article 2, despite the apparent simplicity of the Ra-F bond, reproducing the experimental measurements is not trivial, and achieving the high computational accuracy presented in the article required the development of new computational tools by the theory collaborators. The challenge stemmed in part from the need to work in a fully relativistic formalism, which is not a strict requirement for the lighter homologues of RaF, such as the stable BaF, SrF, and CaF. This work is therefore an example of the cross-disciplinary benefits of research in radioactive molecules.

Similarly, studies of AcF also offer cross-disciplinary benefits. While its electronic structure is significantly more complicated than that of RaF, which makes fruitful benchmarks of quantum chemistry more complicated, AcF is of interest for the applied field of nuclear medicine. ^{225}Ac is a promising nuclide for targeted-α cancer therapy and its extraction in atomic form at ISOL facilities is under investigation as an efficient production pathway [178, 179]. The efficiency of the atomic extraction with the ISOL method is limited by the very low volatility of atomic Ac even at high temperatures and the efficiency limit of laser ionization [179]. The novel work by Mia Au (CERN, Switzerland and Johannes Gutenberg University Mainz, Germany) on the production of AcF$^+$ beams at ISOLDE for the purpose of the CRIS experiment also demonstrated that fluorination of the ISOL target leads to significantly improved high-temperature kinetics for Ac, which forms AcF$_x$ within the hot environment and effuses from the ISOL target much more easily than in atomic form. A publication is currently in preparation.

For research with radioactive molecules to attain its full potential as a field, further theoretical work on the manifestation of nuclear effects in molecular structure is also paramount.

Appendix A

Analysis code

The following snippets show the Python files used to import, clean, bin, and output the CRIS scans of RaF and AcF presented in this thesis. The main file is called hfs_analysis.py, which calls functions written in helpers.py. The code was written to also analyze hyperfine spectra from atomic spectroscopy at CRIS.

The code can be used by changing the parameters in lines 4-39 of hfs_analysis.py. Lines 4-14 define the analysis parameters needed to bin, select a subset of the time-of-flight profile, select the correct channel of the CRIS wavemeter, apply a frequency-summing factor, and choose a database file. Lines 16-26 define the atomic/molecular mass studied in a scan (also defined), the folder where the raw data is located, and whether a voltage scan or laser scan was performed. Finally, lines 28-39 specify what the user wants the code to perform with the raw data and the analysis parameters.

In the database files, 'spin' is set to 0 for all masses as the parameter should be used only for atomic hfs fitting with the satlas package.

```
1 from helpers import *
2 import helpers as h  # keep both lines
3
4 binsize = 3000  # MHz
5 binsize_volt = 1  # V
6 transition = 0 # in cm^-1. Nominal transition wn in
     reference isotope
```

```
spectroscopy_channel = ’4’ # channel on WS-U
freq_multiplier = 1  # for frequency mixing in the spectroscopy channel
tof_lower = 21   # for tof gate and banana plot
tof_upper = 24       # for tof gate and banana plot
tof_binsize = 0.02     # for tof binning
db_file = ’database_raf’   # database file with info. must be in \databases\ folder
# db_file = ’database_acf’   # database file with info. must be in \databases\ folder
# db_file = ’database_al’
#*****************#
DATA_FOLDER = "C:\\Users\\u0140952\\Desktop\\RaF\\RaF_2021_offline\\"
# DATA_FOLDER = "C:\\Users\\u0140952\\Desktop\\Al\\"
# DATA_FOLDER = ’C:\\Users\\u0140952\\Desktop\\AcF\\AcF_2022\\’
NOTE = "RaF"
MASS = 22619
SCANS = [3814,3815,3816,3817,3818,3819,3821]
V_SCAN = False
# save_trace_folder = "C:\\Users\\u0140952\\Desktop\\RaF\\Isotope-shift analysis\\"
save_trace_folder = "C:\\Users\\u0140952\\Desktop\\RaF\\Excited-state analysis\\"
# save_trace_folder = ’C:\\Users\\u0140952\\Desktop\\AcF\\AcF_2022\\’
# save_trace_folder = ’C:\\Users\\u0140952\\Desktop\\new_al\\’
#*****************#
show_count_evolution = False
show_fpi_centers = False
plot_tof = False
apply_tof_gate = False
export_tof_data = False # saves .csv with just the tof spectrum
slice_hist = False    # allows to remove regions in the frequency spectrum that you don’t want
banana_plot = False
conv_to_freq = False
plot_spectrum = True
fit_spectrum = False
save_trace = False  # saves trace of the binned spectrum
write_file = False  # saves fit results to a file
#*****************#

```

```python
# Import and clean the CRIS data
data = pd.DataFrame()
for SCAN in SCANS:
  imp_data = h.import_cris_dataset(ref_channel='wavenumber_2', data_folder=DATA_FOLDER, mass=MASS, scan=SCAN, note=NOTE, \
    apply_wavenumber_correction=False, voltage_scanning=V_SCAN)
  data = pd.concat([data, imp_data])

# plt.plot(data['events_per_bunch'])
# plt.show()
data = data[(data['events_per_bunch'] < 12)]

# data = h.import_cris_dataset(ref_channel='wavenumber_2', data_folder=DATA_FOLDER, mass=MASS, scan=SCAN, note=NOTE, apply_wavenumber_correction=False)
data, precise_mass = h.clean_cris_dataset(db_file, data, MASS, transition, ref_channel='wavenumber_2', voltage_scanning=V_SCAN)


# Make a plot of events_per_bunch by timestamp to check for sparks
if show_count_evolution:
  h.plot_counts_by_time(data)

# Make plot of fpi fitted centroids
if show_fpi_centers:
  h.extract_fpi(DATA_FOLDER, db_file)


# Bin the data
if not V_SCAN:
  tof_centers, tof_edges, tof, spectrum_centers, spectrum_edges, spectrum = h.bin_cris_dataset(db_file=db_file, scan=SCAN, mass=MASS, data=data, binsize=binsize, \
    spectrum_to_bin=spectroscopy_channel, frequency_multiplier=freq_multiplier, \
    pdl=False, tof_lower=tof_lower, tof_upper=tof_upper, tof_binsize=tof_binsize, \
    apply_tof_gate=apply_tof_gate, plot_tof=plot_tof, export_tof=export_tof_data, \
    voltage_scanning=V_SCAN, binsize_voltage=binsize_volt, precise_mass=precise_mass)
```

```
else:
  tof_centers, tof_edges, tof, df = h.bin_cris_dataset(db_file=db_file, scan=SCAN, mass=MASS, data=data, binsize=binsize, \
    spectrum_to_bin=spectroscopy_channel, frequency_multiplier=freq_multiplier, \
    pdl=False, tof_lower=tof_lower, tof_upper=tof_upper, tof_binsize=tof_binsize, \
    apply_tof_gate=apply_tof_gate, plot_tof=plot_tof, export_tof=export_tof_data, \
    voltage_scanning=V_SCAN, binsize_voltage=binsize_volt, precise_mass=precise_mass, transition_wavenumber=transition)
  fit_x = df['x'].to_numpy()
  fit_y = df['y'].to_numpy()
  fit_xerr = df['xerr'].to_numpy()
  fit_yerr = df['yerr'].to_numpy()

# optionally make a banana plot
if banana_plot:
  pcmesh_x, pcmesh_y, pcmesh_Z = h.create_banana_plot(data=data, binsize=binsize, \
    spectrum_to_bin=spectroscopy_channel, frequency_multiplier=freq_multiplier, \
    pdl=False, tof_lower=tof_lower, tof_upper=tof_upper, tof_binsize=tof_binsize, wavenumber_limit=200)

# convert histogram x and y arrays into arrays in MHz that can be used for SATLAS fitting
if not V_SCAN:
  fit_x, fit_y, fit_xerr, fit_yerr = h.create_fit_arrays(spectrum_centers, spectrum, transition, convert_to_frequency=conv_to_freq)

# if you want to slice the histogram and keep data only within a certain x interval
if slice_hist:
  fit_x, fit_y, fit_xerr, fit_yerr = h.slice_histogram(fit_x, fit_y, fit_xerr, fit_yerr, lower_lim=100, upper_lim=50000)

# create the base hfs model with SATLAS if it is asked to plot or fit the spectrum (otherwise skip to save time)
if plot_spectrum or fit_spectrum:
```

```python
  basemodel_gs, Igs = h.create_hyperfine_model(db_file, MASS, fit_x, fit_y, J_l=0.5, J_u=0.5, initial_centroid=-1600, fwhm=[150,400])

# Plot the test model with the hfs param predictions
if plot_spectrum:
  h.plot_hyperfine_spectrum(basemodel_gs, fit_x, fit_y, fit_xerr, fit_yerr, show_testmodel=True, note=NOTE, mass=MASS, scan=SCAN)

# Fit the hfs model
if fit_spectrum:
  h.fit_hyperfine_spectrum(basemodel_gs, fit_x, fit_y, fit_yerr=fit_yerr, I=Igs, note=NOTE, mass=MASS, scan=SCAN)

  # THIS IS HOW TO EXTRACT THE PARAMETER VALUES FROM THE FIT!
  if write_file:
    binsize_scan_file = 'C:\\Users\\u0140952\\Desktop\\Al_2022\\MAK cross analysis\\MAK_binsize_scan.txt'
    with open(binsize_scan_file, 'a') as file:
      file.write('Mass: '+str(MASS)+' - scan_'+str(SCAN)+': ')
      file.write('BINSIZE: '+str(binsize)+' MHz\n')
      for par in basemodel_gs.params.values():
        if par.name in ['TotalFWHM', 'Scale', 'Centroid', 'Background0']:
          file.write('{}: {} +/- {}\n'.format(par.name, par.value, par.stderr*np.sqrt(basemodel_gs.redchi_chi)))
      file.write('\n\n\n')

    for par in basemodel_gs.params.values():
      if par.name in ['TotalFWHM', 'Scale', 'Centroid', 'Background0']:
        print('{}: {} +/- {}'.format(par.name, par.value, par.stderr*np.sqrt(basemodel_gs.redchi_chi)))


if save_trace:
  trace_file = 'trace_'+NOTE+str(MASS)+'_scan_'+str(SCANS)+'_binsize_'+str(binsize)+'MHz'
  # with open(trace_file, 'a') as file:
  #   file.write('Note:', +str(NOTE), 'Mass: '+str(MASS)+' - scan_'+str(SCAN)+': ')
  #   file.write('BINSIZE: '+str(binsize)+' MHz\n')
```

```
  # if save_in_cm:
  #   df = pd.DataFrame([fit_x/29979.2458, fit_y, fit_xerr, fit_yerr]).T
  # else:
  df = pd.DataFrame([fit_x, fit_y, fit_xerr, fit_yerr]).T
  print(fit_x)
  df.to_csv(save_trace_folder+trace_file+’.csv’, index=False, header=False)
```

Listing A.1: hfs_analysis.py

```
    import numpy as np
import pandas as pd
import matplotlib.pyplot as plt
from scipy.constants import speed_of_light
from uncertainties import ufloat as uf
import uncertainties.umath as umath
import uncertainties.unumpy as unumpy
import os
import satlas as s
global precise_mass

def import_cris_dataset(ref_channel, data_folder, mass, scan, note=’’, voltage_scanning=False, \
  convert_to_rest_frame=True, apply_wavenumber_correction=True, \
  reference=’diode’, diode_wavenumber=12816.470353, hene_wavenumber=15798):

  ’’’
  ref_channel: channel in WS-U for referencing (diode or HeNe)
  data_folder: the folder that contains the mass folders with the cris data
  mass: mass number of the isotope
  scan: scan number to be analyzed
  note: add note on the plots
  convert_to_rest_frame: convert the wavenumbers to the rest frame
  apply_wavenumber_correction: correct for wavelength shifts
  reference: ’diode’ or ’hene’
  diode_wavenumber: wavenumber of locked diode laser
  hene_wavenumber: wavenumber of locked hene laser
  ’’’

  # define path for the scan
```

```python
PATH = data_folder + str(mass)+'\\' + "scan_"+str(scan) + "\\"

#*****************#
tagger_path = PATH + "tagger_ds.csv"
wavemeter_path = PATH + "wavemeter_ds.csv"
wavemeter_pdl_path = PATH + "wavemeter_pdl_ds.csv"
iscool_path = PATH + "iscool_ds.csv"
iscool2_path = PATH + "iscool2_ds.csv"
diodes_path = PATH + "diodes_ds.csv"
cec_voltage_path = PATH + "cec_voltage_ds.csv"

tagger_columns = ['timestamp', 'offset', 'bunch_no', 'events_per_bunch', 'channel', 'delta_t']
wavemeter_pdl_columns = ['timestamp', 'offset', 'wavenumber_pdl_1']
iscool_columns = ['timestamp', 'offset', 'iscool_voltage']
iscool2_columns = ['timestamp', 'offset', 'iscool2_voltage']
diodes_columns = ['timestamp', 'offset', 'photodiode_1', 'photodiode_2', 'photodiode_3', 'photodiode_4']
cec_voltage_columns = ['timestamp', 'offset', 'cec_measured_voltage', 'cec_set_voltage']

no_tagger, no_wavemeter, no_wavemeter_pdl, no_iscool, no_wavemeter_pdl, no_cec_voltage = False, False, False, False, False, False
try:
  tagger = pd.read_csv(tagger_path, sep=';', header=None, names=tagger_columns)
  # tagger.drop(labels=['offset', 'bunch_no'], axis=1, inplace=True) # I CHANGED THIS
  tagger.drop(labels=['offset'], axis=1, inplace=True)
  print('tagger files detected')
  no_tagger = False
except:
  no_tagger = True
  print('tagger files not detected')
try:
  with open(PATH+'metadata_wavemeter_ds.txt', 'r') as file:
    if ('mixed' in file.readlines()):
      wavemeter_columns = ['timestamp', 'offset', 'wavenumber_1', 'wavenumber_2', 'wavenumber_3', 'wavenumber_4', 'wavenumber_mixed']
      print('mixed found')
```

```
      else:
        wavemeter_columns = ['timestamp', 'offset', 'wavenumber_1', 'wavenumber_2', 'wavenumber_3', 'wavenumber_4']#, 'wavenumber_mixed']
        print('mixed not found')
    wavemeter = pd.read_csv(wavemeter_path, sep=';', header=None, names=wavemeter_columns)
    wavemeter.drop(labels=['offset'], axis=1, inplace=True)
    print('WS-U files detected')
    no_wavemeter = False
  except:
    no_wavemeter = True
    print('WS-U files not detected')
  try:
    wavemeter_pdl = pd.read_csv(wavemeter_pdl_path, sep=';', header=None, names=wavemeter_pdl_columns)
    wavemeter_pdl.drop(labels=['offset'], axis=1, inplace=True)
    print('WS-6 files detected')
    no_wavemeter_pdl = False
  except:
    no_wavemeter_pdl = True
    print('WS-6 files not detected')
  try:
    iscool = pd.read_csv(iscool_path, sep=';', header=None, names=iscool_columns)
    iscool.drop(labels=['offset'], axis=1, inplace=True)
    print('iscool files detected')
    no_iscool = False
  except:
    no_iscool = True
    print('iscool files not detected')
  try:
    iscool2 = pd.read_csv(iscool2_path, sep=';', header=None, names=iscool2_columns)
    iscool2 .drop(labels=['offset'], axis=1, inplace=True)
    print('iscool2 files detected')
    no_iscool2 = False
  except:
    no_iscool2 = True
    print('iscool2 files not detected')
  try:
    diodes = pd.read_csv(diodes_path, sep=';', header=None, names=diodes_columns)
    diodes.drop(labels=['offset'], axis=1, inplace=True)
    print('diodes file detected')
```

```
    no_diodes = False
  except:
    no_diodes = True
    print('diodes files not detected')
  try:
    cec_voltage = pd.read_csv(cec_voltage_path, sep=';', header=None, names=cec_voltage_columns)
    cec_voltage.drop(labels=['offset'], axis=1, inplace=True)
    print('cec_voltage files detected')
    no_cec_voltage = False
  except:
    no_cec_voltage = True
    print('cec_voltage files not detected')

  devices_to_concat = []
  if not no_tagger:
    devices_to_concat.append(tagger)
  if not no_wavemeter:
    devices_to_concat.append(wavemeter)
  if not no_wavemeter_pdl:
    devices_to_concat.append(wavemeter_pdl)
  if not no_iscool:
    devices_to_concat.append(iscool)
  if not no_iscool2:
    devices_to_concat.append(iscool2)
  if not no_diodes:
    devices_to_concat.append(diodes)
  if not no_cec_voltage:
    devices_to_concat.append(cec_voltage)


  data = pd.concat(devices_to_concat)
  # print(data['wavenumber_3'])
  # make a copy of the timestamp column before making it our index
  data['timestamp_copy'] = data['timestamp']
  data = data.set_index(['timestamp'])
  data = data.sort_index()

  ##########################

  # fill blank values in independent parameters and drop lines with blank values in counts
```

```python
for name in ['wavenumber_pdl_1', 'wavenumber_1', 'wavenumber_2', 'wavenumber_3', 'wavenumber_4', 'wavenumber_mixed', \
'iscool_voltage', 'iscool2_voltage', 'photodiode_1', 'photodiode_2', 'photodiode_3', 'photodiode_4', 'cec_measured_voltage', 'cec_set_voltage']:
  try:
    data[name] = data[name].fillna(method='ffill')
    data[name] = data[name].fillna(method='bfill')
  except Exception as e:
    print(e, 'couldnt front or back fill')
    pass
data = data.dropna()

# to calibrate iscool, multiply by 5963.39. This scale comes from the voltage divider
if not no_iscool:
  data['iscool_voltage'] = data['iscool_voltage'] * 5963.39 # ORIGINAL ONE FROM MICHALIS
if not no_iscool2:
  data['iscool2_voltage'] = data['iscool2_voltage'] * 10000 # ORIGINAL ONE FROM MICHALIS

# combine the voltages
try:
  if voltage_scanning:
    print('voltage scanning selected')
    data['voltage'] = data['iscool2_voltage'] - data['cec_measured_voltage'] * 1000 # this has to be minus, right? yes, also you can add a calibration factor, for silver this was * 1.005030
  else:
    data['voltage'] = data['iscool2_voltage']
except:
  try:
    # data['voltage'] = data['iscool2_voltage']
    data['voltage'] = data['iscool_voltage']
  except:
    print('NO ISCOOL VOLTAGE DETECTED')
    raise ValueError

if not no_tagger:
  data['delta_t'] = data['delta_t'] / 2000 # normalize the tof. The tagger has channels of 500 ps each. Convert to 1 us

```

```
  if apply_wavenumber_correction:
    print('Wavenumber correction: APPLIED')
    if reference == 'diode':
      print('Diode correction chosen')
      data['correction'] = data[ref_channel] - diode_wavenumber
    elif reference == 'hene':
      print('He:Ne correction chosen')
      data['correction'] = data[ref_channel] - hene_wavenumber
    else:
      data['correction'] = 0
      print('you did not choose a valid reference option')

    for name in ['wavenumber_1', 'wavenumber_2', 'wavenumber_3', 'wavenumber_4']:
      data[name] = data[name] - data['correction']

  return data


def clean_cris_dataset(db_file, data, mass, centroid, ref_channel, convert_to_rest_frame=True, voltage_scanning=False):
  '''
  data: dataframe that has been produced with import_cris_dataset()
  mass: mass of scan
  convert_to_rest_frame: convert all frequencies to rest frame
  centroid: expected centroid of the structure
  '''
  exec('from databases.'+db_file+' import *', globals()) # dynamically import the database file
  global precise_mass
  precise_mass = mass_data[mass]  # mass_data is the dictionary of mass data from AME, hosted in
  # print(precise_mass)

  for name in ['wavenumber_pdl_1', 'wavenumber_1', 'wavenumber_2', 'wavenumber_3', 'wavenumber_4']:
    try:
      data['observed_'+name] = data[name]
    except Exception as e:
      print(e)
      pass
```

```

  return data, precise_mass

##################

def plot_counts_by_time(data):
  ’’’
  plots the evolution of events_per_bunch as a function of timestamp.
  Very useful if you want to spot sparks.
  ’’’
  ts = data[’timestamp_copy’].to_numpy()
  counts = data[’events_per_bunch’].to_numpy()

  ts_bins = np.arange(ts.min(), ts.max()+1, 1)
  y, x_edges = np.histogram(ts, ts_bins, weights=counts)
  x = x_edges[:-1] + np.diff(x_edges)/2
  print(’average counts’, np.mean(y), ’std’, np.std(y))
  plt.plot(x, y)
  plt.xlabel(’Timestamp (s)’)
  plt.ylabel(’Events_per_bunch’)
  plt.show()
  return

#######################
# I CHANGED THIS, I ADDED MASS_DATA IN CASE YOU DONT HAVE A SUPPORTING DICT, AND A TRANSITION_WAVENUMBER TO GET THE RELATIVE FREQ
def bin_cris_dataset(db_file, scan, mass, data, binsize=50, spectrum_to_bin=1, frequency_multiplier=1, \
  pdl=False, wavenumber_limit=200, tof_lower=0, tof_upper=1000, tof_binsize=0.1, \
  apply_tof_gate= False, plot_tof=False, export_tof=False, voltage_scanning=False, binsize_voltage=1, precise_mass=None, mass_data = None, transition_wavenumber = 0):
  ’’’
  data: dataframe to bin
  binsize: binsize in MHz
  spectrum_to_bin: defines wavemeter channel to bin
  pdl: if True, binned spectrum is pdl_1
  wavenumber_limit: lower wavenumber that the bins can start from. used to prevent problems with wavemeter underexposure
  tof_lower: lower time of flight in us for the tof spectrum
  tof_upper: upper time of flight in us for the tof spectrum
  tof_binsize: binsize in us for the tof spectrum
```

```
'''

binsize_cm = binsize*0.0000334
if pdl:
  channel = 'pdl_1'
else:
  channel = str(spectrum_to_bin)

if apply_tof_gate:
  data = data[(data['delta_t'] < 0) | ( (data['delta_t'] >= tof_lower) & (data['delta_t'] < tof_upper) )] # I CHANGED THIS

# convert some quantities to np arrays because it's more useful
timestamp = data['timestamp_copy'].to_numpy()
# print('Total duration:', timestamp.max() - timestamp.min())
counts = data['events_per_bunch'].to_numpy()
delta_t = data['delta_t'].to_numpy()


# select spectroscopy channel
try:
  # I CHANGED THIS
  # if you want to keep the total_wn then you should add it to the dataframe, otherwise you cannot use the groupby stuff on it in the binning function
  # if channel == '99':
  #   # total wn is jyvis + grating + pdl
  #   total_wn = data['observed_wavenumber_1'] + data['observed_wavenumber_4'] + data['observed_wavenumber_pdl_1']
  #   wavenumber = total_wn.to_numpy() * frequency_multiplier
  # else:
  #   wavenumber = data['observed_wavenumber_'+str(channel)].to_numpy() * frequency_multiplier
  # valid_wn = np.where(wavenumber >= wavenumber_limit)

  data = data.loc[(data['observed_wavenumber_'+str(channel)] >= wavenumber_limit) & (data['observed_wavenumber_'+str(channel)] <= 40500)]
  wavenumber = data['observed_wavenumber_'+str(channel)].to_numpy() * frequency_multiplier
  spectrum_lower = wavenumber.min()
```

```
    spectrum_upper = wavenumber.max()
    spectrum_bins = np.arange(spectrum_lower, spectrum_upper+binsize_cm, binsize_cm)
  except Exception as e:
    print(e)
    pass

  ##########################

  # TOF SPECTRUM
  tof_bins = np.arange(tof_lower, tof_upper+tof_binsize, tof_binsize)
  tof, tof_edges = np.histogram(a=delta_t, bins=tof_bins)
  tof_centers = tof_edges[:-1] + np.diff(tof_edges)/2

  if plot_tof:
    fig = plt.gcf()
    plt.plot(tof_centers, tof, drawstyle='steps')
    plt.xlabel(r'Time of flight ($\mu$s)', size=24)
    plt.ylabel('Total counts', size=24)
    plt.xticks(size=20)
    plt.yticks(size=20)
    # plt.title('Time-of-flight profile of scan ' + str(scan), size=30)
    plt.title('Selected ToF region with ' + 'binsize: '+str(tof_binsize) + r' $\mu$s. '+'apply_tof_gate='+str(apply_tof_gate))
    plt.show()
    # fig.set_size_inches(10, 7)
    # fig.savefig('C:\\Users\\u0140952\\Desktop\\tof_scan'+str(scan)+'.svg', dpi=100)
    # fig.savefig('C:\\Users\\u0140952\\Desktop\\tof_scan'+str(scan)+'.pdf', dpi=100)

  if export_tof:
    df = pd.DataFrame()
    df['tof_x'] = tof_centers.tolist()
    df['tof_y'] = tof.tolist()
    fn = 'tofspec_scan'+str(scan) + '_mass' + str(mass) + '_tofbinsize' + str(1000*tof_binsize) + 'ns.csv'
    df.to_csv(fn, index=False)

  #######################
  # I CHANGED THIS

  if not voltage_scanning:
```

```
    voltage = (data['voltage']).to_numpy()
    beta = np.sqrt(1 - ( ((precise_mass*931.49410242*10**6)**2) / ( (voltage+(precise_mass*931.49410242*10**6))*(voltage+(precise_mass*931.49410242*10**6)) ) ))
    data['observed_wavenumber_'+str(channel)] = wavenumber * (1 - beta) / np.sqrt(1 - (beta*beta))
    spectrum_bins = np.arange(np.min(data['observed_wavenumber_'+str(channel)]), np.max(data['observed_wavenumber_'+str(channel)])+binsize_cm, binsize_cm)
    data['digit_index'] = np.digitize(data['observed_wavenumber_'+str(channel)], spectrum_bins)
    groups = data.groupby('digit_index')
    df = pd.DataFrame()
    df[['x','xerr']] = groups['observed_wavenumber_'+str(channel)].agg([np.mean,np.std])
    # df['x'] = (df['x'] - transition_wavenumber) * 29979.2458
    df['y'] = (groups.count()['bunch_no'] - groups['delta_t'].agg(lambda x: x.le(0).sum())) # minus the empty bunches, doesnt matter if you take bunch_no or smt else
    df['yerr'] = np.sqrt(df['y'])
    df['bunches'] = ([len(array) for array in list(groups['bunch_no'].unique())])
    df['yav'] = df['y'] / df['bunches']
    df['yerrav'] = df['yerr'] / df['bunches']
    df = df.sort_values(by = ['x']) # sort by x for convenience but it is not needed at all
    df['yerr'][df['yerr'] == 0] = 1/np.sqrt(np.array(df['bunches'][df['yerr'] == 0])) # to calculate the errors at 0 events recorded
    #
    y = df['yav'].to_numpy()
    x = df['x'].to_numpy()
    print('mean wn:', np.mean(x), 'std', np.std(x))
    xerr = df['xerr'].to_numpy()
    yerr = df['yerrav'].to_numpy()
    spectrum = unumpy.uarray(y, yerr)
    spectrum_centers = unumpy.uarray(x, xerr)
    spectrum_edges = spectrum_centers # whatever i just dont wanna break the whole code, this is meaningless
    return tof_centers, tof_edges, tof, spectrum_centers, spectrum_edges, spectrum

  else:
    voltage = (data['voltage']).to_numpy()
```

```
    # initialise the voltage bins, start and end voltage is -binsize_voltage/2 and +binsize_voltage/2, such that the measured voltages are in the middle of the bins
    voltage_bins = np.arange(voltage.min()-binsize_voltage/2, voltage.max()+binsize_voltage/2, binsize_voltage)
    # digitize voltages according to voltage bins
    data['digit_index'] = np.digitize(voltage, voltage_bins)

    # non-relativistic
    # beta = np.sqrt((2*voltage_bins[digitize_indices]*1.60218E-19)/((precise_mass)*1.6605418E-27)) / speed_of_light
    # relativistic
    beta = np.sqrt(1 - ( ((precise_mass*931.49410242*10**6)**2) / ( (voltage+(precise_mass*931.49410242*10**6))*(voltage+(precise_mass*931.49410242*10**6)) ) ))
    data['observed_wavenumber_'+str(channel)] = wavenumber * (1 - beta) / np.sqrt(1 - (beta*beta))

    # This is what actually bins the data according to the indices initialised by np.digitize
    groups = data.groupby('digit_index')
    # initialise the dataframe that will be returned
    df = pd.DataFrame()
    # put in the x and x errors
    df[['x','xerr']] = groups['observed_wavenumber_'+str(channel)].agg([np.mean,np.std])
    # subtract the transition wavenumber and convert it to MHz
    df['x'] = (df['x'] - transition_wavenumber) * 29979.2458
    # y = the amount of rows in the data that is provided ( = total amount of counts recorded + amount of empty bunches) - the amount of rows that have a delta_t < 0 (these are the empty bunches)
    df['y'] = (groups.count()['bunch_no'] - groups['delta_t'].agg(lambda x: x.le(0).sum())) # I put in 'bunch_no', but in principle you should be able to provided any column here
    # Since y in now total amount of counts, the error is just the sqrt
    df['yerr'] = np.sqrt(df['y'])
    # the amount of bunches = the amount of unique numbers in the column 'bunch_no'
    df['bunches'] = ([len(array) for array in list(groups['bunch_no'].unique())])
    # sort it by x
```

```
    df = df.sort_values(by = ['x']) # for convenience but it is not needed at all
    # if the yerr == 0, it means that this bin has no counts in it at all. So you need to calculate the error on it.
    # I do this by taking 1/sqrt(amount of bunches in that bin)
    df['yerr'][df['yerr'] == 0] = 1/np.sqrt(np.array(df['bunches'][df['yerr'] == 0])) # to calculate the errors at 0 events recorded

    return tof_centers, tof_edges, tof, df


##########################


def create_banana_plot(data, binsize=50, spectrum_to_bin=1, frequency_multiplier=1, \
  pdl=False, wavenumber_limit=200, tof_lower=0, tof_upper=1000, tof_binsize=0.1):
  '''
  creates banana plot and optionally applies correction
  #
  data: dataframe to bin
  binsize: binsize in MHz
  spectrum_to_bin: defines wavemeter channel to bin
  pdl: if True, binned spectrum is pdl_1
  wavenumber_limit: lower wavenumber that the bins can start from. used to prevent problems with wavemeter underexposure
  tof_lower: lower time of flight in us for the tof spectrum
  tof_upper: upper time of flight in us for the tof spectrum
  tof_binsize: binsize in us for the tof spectrum
  '''

  binsize_cm = binsize*0.0000334
  if pdl:
    channel = 'pdl_1'
  else:
    channel = str(spectrum_to_bin)

  try:
    if channel == '99':
      # total wn is jyvis + grating + pdl
```

```
      total_wn = data['observed_wavenumber_1'] + data['observed_wavenumber_4'] + data['observed_wavenumber_pdl_1']
      wavenumber = total_wn.to_numpy() * frequency_multiplier
    else:
      wavenumber = data['observed_wavenumber_'+str(channel)].to_numpy() * frequency_multiplier
    #
    valid_wn = np.where(wavenumber >= wavenumber_limit)
    spectrum_l = wavenumber[valid_wn].min()
    spectrum_u = wavenumber.max()
    spectrum_bins = np.arange(spectrum_l, spectrum_u+binsize_cm, binsize_cm)
  except Exception as e:
    print(e)
    pass

  tof_bins = np.arange(tof_lower, tof_upper+tof_binsize, tof_binsize)

  pcmesh_x = spectrum_bins
  pcmesh_y = tof_bins
  pcmesh_Z = []


  for i in range(len(tof_bins)-1):
    tof_l, tof_u = tof_bins[i], tof_bins[i+1]
    data_slice = data[(data['delta_t']>= tof_l) & (data['delta_t']<= tof_u)]

    ts_slice = data_slice['timestamp_copy'].to_numpy()
    counts_slice = data_slice['events_per_bunch'].to_numpy()
    dt_slice = data_slice['delta_t'].to_numpy()

    tof_slice_bins = np.arange(tof_l, tof_u + tof_binsize/10, tof_binsize/10)
    tof_slice, tof_slice_edges = np.histogram(a=dt_slice, bins=tof_slice_bins)
    tof_slice_centers = tof_slice_edges[:-1] + np.diff(tof_slice_edges)/2

    if channel == '99':
      # total wn is jyvis + grating + pdl
```

```
      total_wn = data_slice['observed_wavenumber_1'] + data_slice['observed_wavenumber_4'] + data_slice['observed_wavenumber_pdl_1']
      wavenumber_slice = total_wn.to_numpy() * frequency_multiplier
    else:
      wavenumber_slice = data_slice['observed_wavenumber_'+str(channel)].to_numpy() * frequency_multiplier

    # for the banana plot, we do not need count rate but just summing the counts in each bin
    y_slice, spectrum_slice_edges = np.histogram(wavenumber_slice, spectrum_bins)#, weights=counts_slice)
    y_slice = np.nan_to_num(y_slice, copy=False, nan=0.0)

    y_slice_og = y_slice
    spectrum_slice_centers = spectrum_slice_edges[:-1] + np.diff(spectrum_slice_edges)/2
    # spectrum_slice_centers, y_slice = spectrum_slice_centers[~unumpy.isnan(y_slice)],y_slice[~unumpy.isnan(y_slice)]
    spectrum_slice = y_slice

    pcmesh_Z.append(spectrum_slice)

  pcmesh_Z = np.asarray(pcmesh_Z)

  fig, ax = plt.subplots()
  ax.pcolormesh(pcmesh_x, pcmesh_y, pcmesh_Z, cmap=plt.colormaps['PiYG'])
  plt.show()


  return pcmesh_x, pcmesh_y, pcmesh_Z


#########################


def create_hyperfine_model(db_file, mass, fit_x, fit_y, fit_xerr=None, fit_yerr=None, J_l=0.5, \
  J_u=0.5, initial_centroid=0, fwhm=[100, 100]):

  # dynamically import the specified database file
  exec('from databases.'+db_file+' import *', globals())

```

```python
  # SATLAS model creation
  I = spin[mass]
  J = [J_l, J_u]
  ABC = hfs_factors[mass]
  FWHM = fwhm
  centroid = initial_centroid
  scale = fit_y.max() - fit_y.min()
  background = [fit_y.min()]

  # SATLAS model creation
  basemodel = s.HFSModel(I=I, J=J, ABC=ABC, centroid=centroid, scale=scale, fwhm=FWHM, background_params=background,use_racah=False,)

  return basemodel, I


########################


def create_fit_arrays(spectrum_x, spectrum_y, transition=0, convert_to_frequency=False):
  '''
  Takes the histogram x and y arrays from the spectrum and converts them to
  fit_x, fit_y, and fit_yerr numpy arrays that can be used for SATLAS hfs models

  The transition param should be given in /cm and corresponds to the nominal centerpoint
  of the transition wavenumber in the reference isotope
  '''
  try:
    fit_x = unumpy.nominal_values(spectrum_x)
    fit_xerr = unumpy.std_devs(spectrum_x)
  except:
    fit_x = spectrum_x
    fit_xerr = None
    pass

  try:
    if convert_to_frequency:
      fit_x = (fit_x - transition) * 29979.2458 # normalize and convert to frequency
      fit_xerr *= 29979.2458
    else:
```

```python
      fit_x = (fit_x - transition)

    fit_y = unumpy.nominal_values(spectrum_y)
    fit_yerr = unumpy.std_devs(spectrum_y)
  except Exception as e:
    print('cant use this spectroscopy set')
    print(e)
    raise ValueError

  return fit_x, fit_y, fit_xerr, fit_yerr


#####################

def slice_histogram(fit_x, fit_y, fit_xerr, fit_yerr, lower_lim, upper_lim):
  '''
  slices the fit arrays such that certain regions from the histogram are
  kept (anything between lower_lim and upper_lim) and the rest is omitted

  lower_lim and upper_lim must be given in MHz and correspond to regions in fit_x
  '''
  index_not_omit = [index for index, val in enumerate(fit_x) if (val < upper_lim) and (val > lower_lim)]
  fit_x = fit_x[index_not_omit]
  fit_y = fit_y[index_not_omit]
  fit_yerr = fit_yerr[index_not_omit]
  try:
    fit_xerr = fit_xerr[index_not_omit]
  except:
    pass


  return fit_x, fit_y, fit_xerr, fit_yerr

######################


def fit_hyperfine_spectrum(hfsmodel, fit_x, fit_y, fit_xerr=None, fit_yerr=None, I=0, note='', mass=0, scan=0, v_scan=False):
  if v_scan:
```

```
    success, message = s.chisquare_fit(hfsmodel, fit_x, fit_y, fit_yerr, fit_xerr)
  else:
    success, message = s.chisquare_fit(hfsmodel, fit_x, fit_y, fit_yerr)
  hfsmodel.display_chisquare_fit(show_correl=False)
  fig, ax = hfsmodel.plot(x=fit_x, y=fit_y, yerr=fit_yerr, show = False, plot_kws = {'legend':'I = ' + str(I), 'xlabel':'Observed frequency - transition frequency (MHz)', 'ylabel':'Countrate'})
  plt.legend()
  plt.title(str(note)+'-'+str(mass)+', scan '+str(scan))
  plt.show()
  return


#######################


def plot_hyperfine_spectrum(testmodel, fit_x, fit_y, fit_xerr=None, fit_yerr=None, show_testmodel=False, note='', mass=0, scan=0):
  '''
  Provides a plot of the data overlayed with a test hfs model to check how
  accurate the initial predictions of the hfs parameters are.
  '''
  # if fit_yerr != None:
  plt.errorbar(fit_x, fit_y, yerr=fit_yerr, drawstyle='steps', fmt='k-', label='Spectroscopy channel')
  # else:
  #   plt.plot(fit_x, fit_y, drawstyle='steps', color='magenta',label='Spectroscopy channel')

  freq_range = np.arange(min(fit_x), max(fit_x), 10)
  if show_testmodel:
    print('testmodel chosen')
    response_testmodel = testmodel(freq_range)
    plt.plot(freq_range, response_testmodel,'r-',label='Initial guess')
  plt.legend()
  plt.title('Test hfs model: ' + str(note)+'-'+str(mass)+', scan '+str(scan))
  plt.xlabel('Observed frequency - transition frequency')
  plt.show()
```

```

  return


########################


def extract_fpi(data_folder, db_file):#, scanning_channel=1, ref_channel=2, scanning_pd=1, ref_pd=2):
  ’’’
  data: dataframe to analyze
  scanning_channel: channel on the WS-U that records the laser that is used in the FPI
  ref_channel: WS-U measuring the reference laser for the FPI
  scanning_pd: photodiode signal for the scanning laser
  ref_pd: photodiode signal for the reference laser
  ’’’

  # INCOMPLETE -- UNDER DEVELOPMENT

  # dynamically import the specified database file
  exec(’from databases.’+db_file+’ import *’, globals())
  masses = mass_data.keys() # extract the valid masses

if __name__ == "__main__":
  print(’run hfs_analysis.py instead’)
```

Listing A.2: helpers.py

```
    mass_data = {
  20819: 208.001855012 + 18.99840316207,
  21019: 210.000475406 + 18.99840316207,
  21219: 211.999786619 + 18.99840316207,
  21319: 213.000370971 + 18.99840316207,
  21419: 214.000099560 + 18.99840316207,
  22319: 223.018500648 + 18.99840316207,
  22419: 224.020210361 + 18.99840316207,
  22519: 225.023610502 + 18.99840316207,
  22619: 226.025408186 + 18.99840316207,
  22719: 227.029176205 + 18.99840316207,
  23019: 230.037054776 + 18.99840316207,
  23219: 232.043475267 + 18.99840316207,
  23319: 233.047594570 +18.99840316207
}

spin = {
```

```
  20819: 0,
  21019: 0,
  21219: 0,
  21319: 0,
  21419: 0,
  22319: 0,
  22419: 0,
  22519: 0,
  22619: 0,
  22719: 0,
  23019: 0,
  23219: 0,
  23319: 0


}

hfs_factors = {
  20819: [0,0,0,0,0,0],
  21019: [0,0,0,0,0,0],
  21219: [0,0,0,0,0,0],
  21319: [0,0,0,0,0,0],
  21419: [0,0,0,0,0,0],
  22319: [0,0,0,0,0,0],
  22419: [0,0,0,0,0,0],
  22519: [0,0,0,0,0,0],
  22619: [0,0,0,0,0,0],
  22719: [0,0,0,0,0,0],
  23019: [0,0,0,0,0,0],
  23219: [0,0,0,0,0,0],
  23319: [0,0,0,0,0,0]
}
```

Listing A.3: database_raf.py

```
print('database_acf loaded')
mass_data = {
  22719: 227.027750594 + 18.99840316207
}

spin = {
  22719: 0
}

hfs_factors = {
  22719: [0,0,0,0,0,0]
```

```
}
```

Listing A.4: database_acf.py

Appendix B

RaF spectra

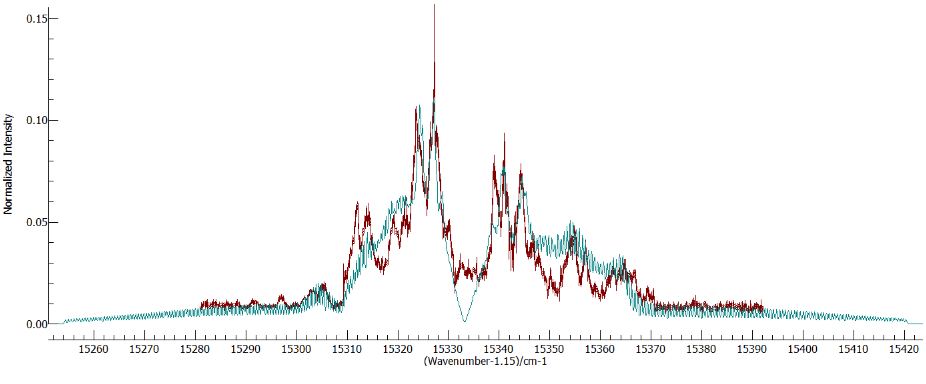

Figure B.1: Spectrum (red) and best-fit simulation (teal) for the $A\ ^2\Pi_{3/2} \leftarrow X\ ^2\Sigma_{1/2}$ $(v' = 0 \leftarrow v'' = 0)$ transition. The spectrum is complicated due to a non-uniform temperature distribution that creates sharp peaks in the structure. The excitation energy is defined by the location of the central gap, which is captured in a satisfactory manner as the rising edges around it are reproduced.

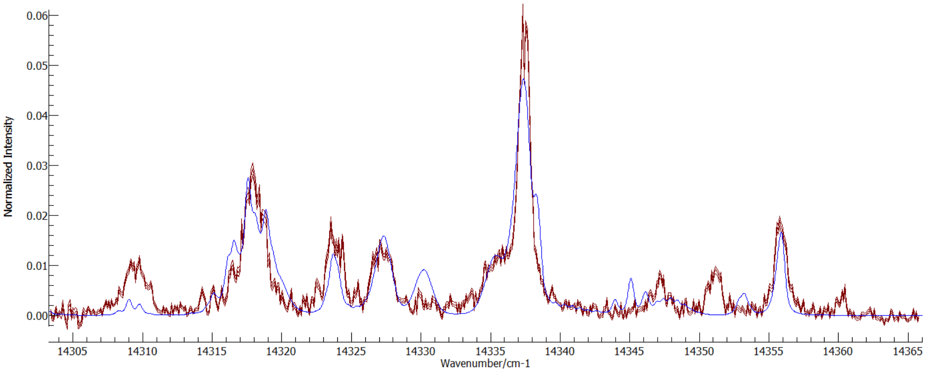

Figure B.2: Spectrum (red) and best-fit simulation (blue) for the $B\ ^2\Delta_{3/2} \leftarrow X\ ^2\Sigma_{1/2}$ $(v' = 0 \leftarrow v'' = 0)$ transition. The spectrum is complicated due to a non-uniform temperature distribution that creates sharp peaks in the structure.

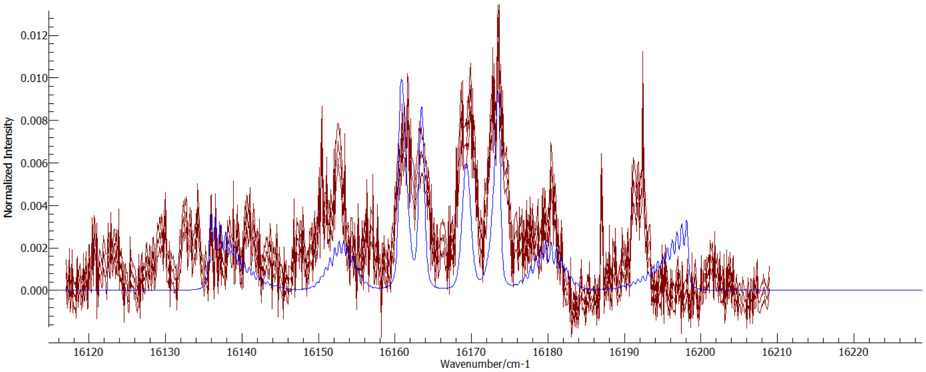

Figure B.3: Spectrum (red) and best-fit simulation (blue) for the $C\ ^2\Sigma_{1/2} \leftarrow X\ ^2\Sigma_{1/2}$ $(v' = 0 \leftarrow v'' = 1)$ transition. The spectrum is complicated due to a non-uniform temperature distribution that creates sharp peaks in the structure. Consequently, it was decided to not use the results of this fit to re-assign the $C\ ^2\Sigma_{1/2}$ state.

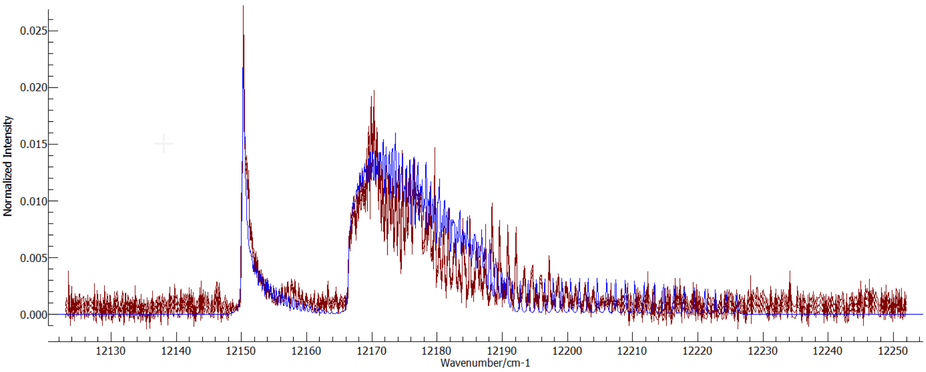

Figure B.4: Spectrum (red) and best-fit simulation (blue) for the $E\ ^2\Sigma_{1/2} \leftarrow A\ ^2\Pi_{1/2}$ $(v' = 0 \leftarrow v'' = 0)$ transition.

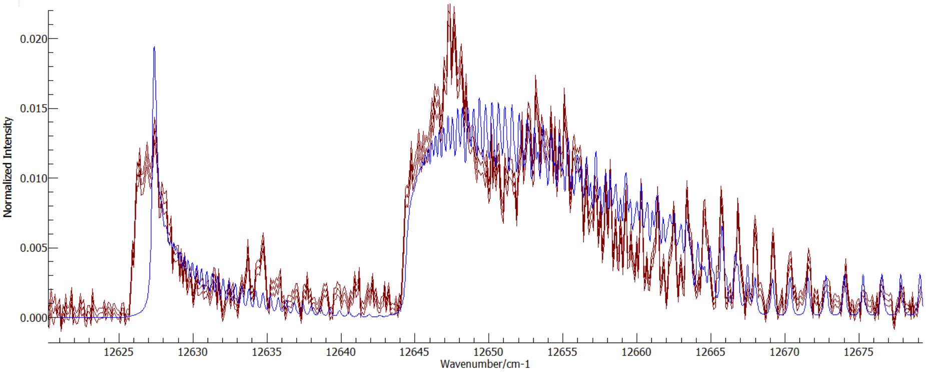

Figure B.5: Spectrum (red) and best-fit simulation (blue) for the $E\ ^2\Sigma_{1/2} \leftarrow A\ ^2\Pi_{1/2}$ $(v' = 1 \leftarrow v'' = 0)$ transition.

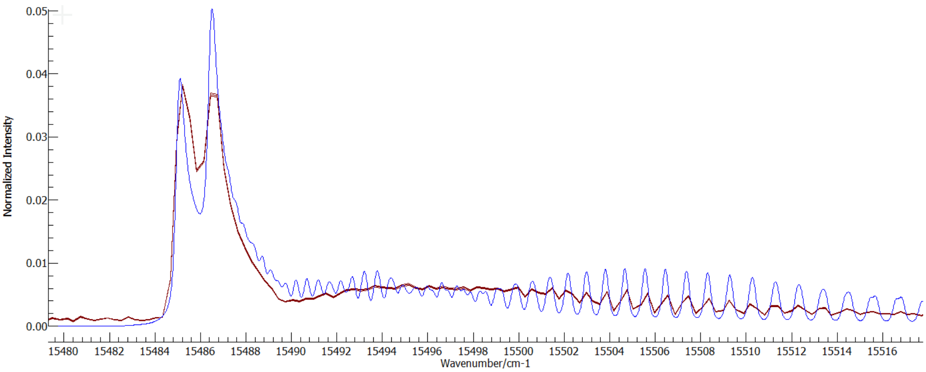

Figure B.6: Spectrum (red) and best-fit simulation (blue) for the $G\ ^2\Pi_{1/2} \leftarrow A\ ^2\Pi_{1/2}$ $(v' = 0 \leftarrow v'' = 0)$ transition.

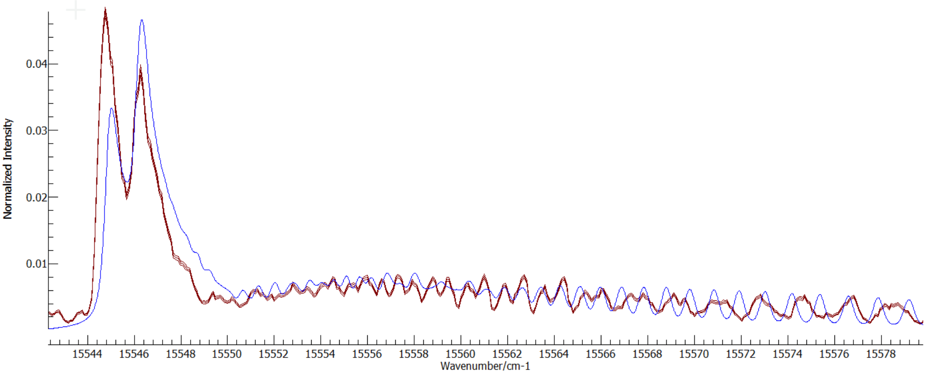

Figure B.7: Spectrum (red) and best-fit simulation (blue) for the $G\ ^2\Pi_{1/2} \leftarrow A\ ^2\Pi_{1/2}$ $(v' = 1 \leftarrow v'' = 1)$ transition.

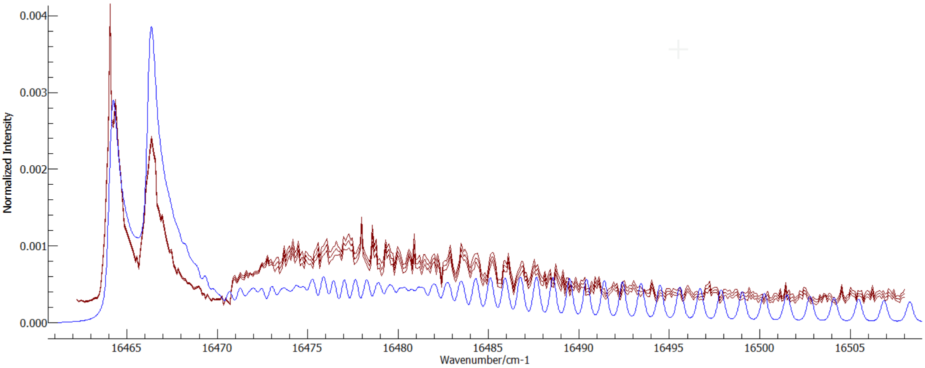

Figure B.8: Spectrum (red) and best-fit simulation (blue) for the $G\ ^2\Pi_{1/2} \leftarrow A\ ^2\Pi_{1/2}$ $(v' = 2 \leftarrow v'' = 0)$ transition. The assignment of the upper state in this transition is based on the difference in transition energy compared to the 0←0 line (Fig. B.6), which is approximately twice as much as the harmonic frequency in different RaF states has been measured to be ($\sim$ 400-500 cm^{-1}).

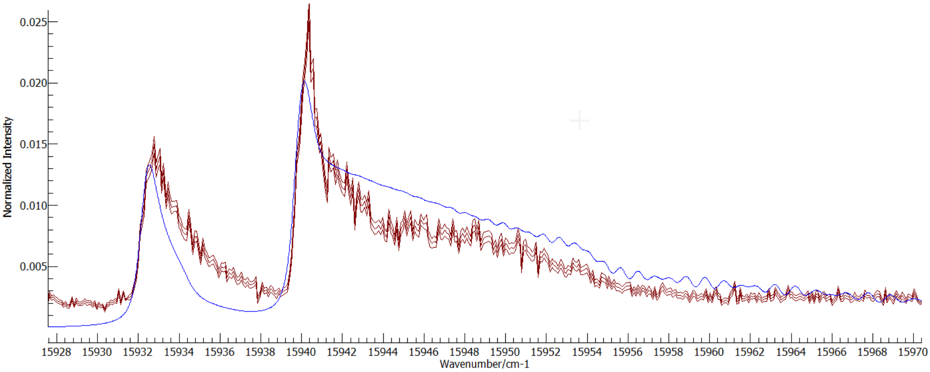

Figure B.9: Spectrum (red) and best-fit simulation (blue) for the $G\ ^2\Pi_{3/2} \leftarrow A\ ^2\Pi_{1/2}$ $(v' = 0 \leftarrow v'' = 0)$ transition.

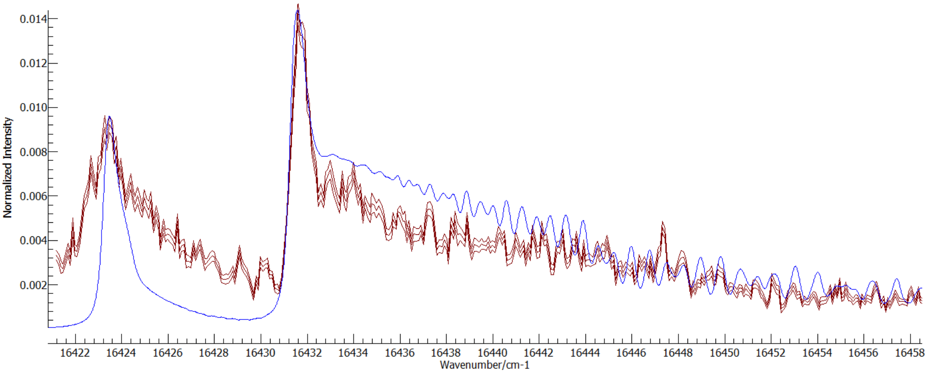

Figure B.10: Spectrum (red) and best-fit simulation (blue) for the $G\ ^2\Pi_{3/2} \leftarrow A\ ^2\Pi_{1/2}$ ($v' = 1 \leftarrow v'' = 0$) transition.

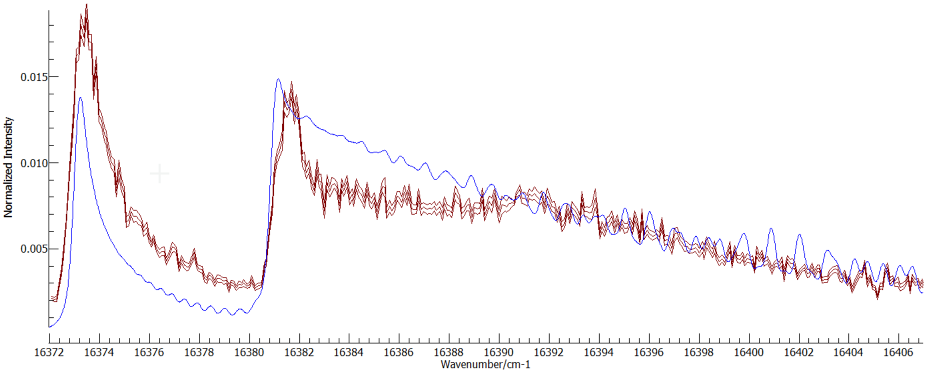

Figure B.11: Spectrum (red) and best-fit simulation (blue) for the $(H\ ^2\Sigma_{1/2})\ \leftarrow A\ ^2\Pi_{1/2}$ ($v' = 0 \leftarrow v'' = 0$) transition.

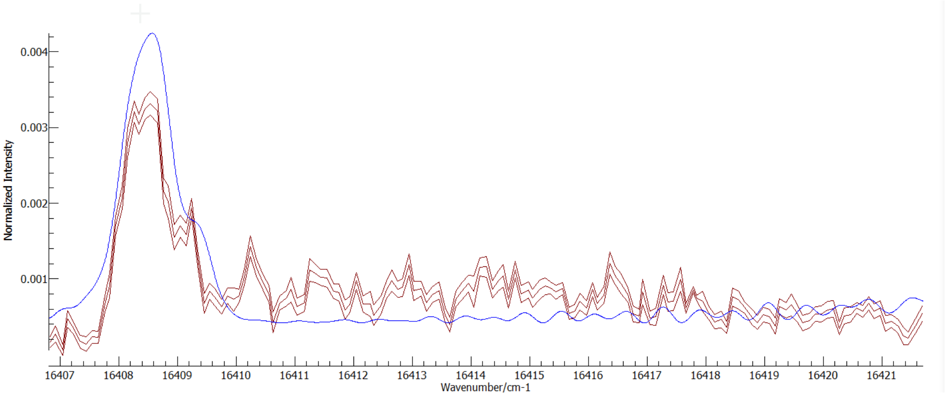

Figure B.12: Spectrum (red) and best-fit simulation (blue) for the $(I\ ^2\Delta_{3/2}) \leftarrow A\ ^2\Pi_{1/2}$ $(v' = 0 \leftarrow v'' = 0)$ transition. The upper state cannot be unambiguously assigned to $I\ ^2\Delta_{3/2}$ based on a comparison with the theoretical excitation energy, because the theoretical energies of the $I\ ^2\Delta_{3/2}$ and $H\ ^2\Sigma_{1/2}$ states are within uncertainties of each other. However, the profile of this spectrum resembles closely that of the spectrum in Fig. B.13, which can be assigned to $I\ ^2\Delta_{5/2}$ based on its excitation energy. Therefore, the upper state in this spectrum is interpreted as being of Δ character as well, and we thus tentatively assign it as $I\ ^2\Delta_{3/2}$.

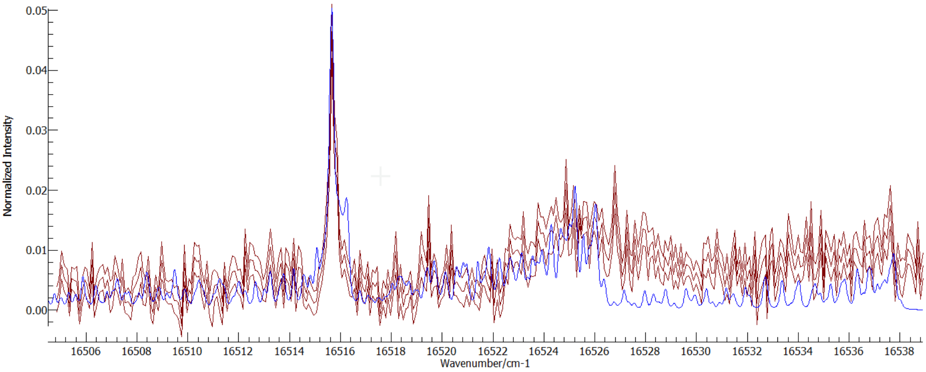

Figure B.13: Spectrum (red) and best-fit simulation (blue) for the $I\ ^2\Delta_{5/2} \leftarrow A\ ^2\Pi_{1/2}$ $(v' = 0 \leftarrow v'' = 0)$ transition.

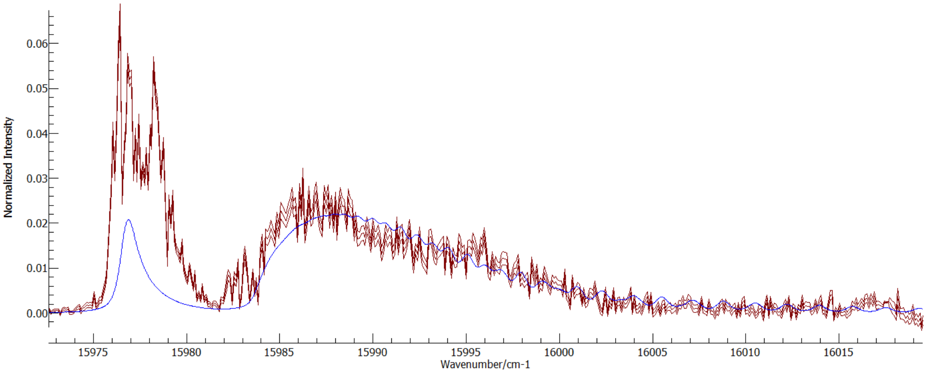

Figure B.14: Transition from the $A\ ^2\Pi_{1/2}$ $(v'' = 0)$ state to an unassigned upper state. Fitting the upper state as a $^2\Sigma_{1/2}$ state produced a reasonable fit. The excitation energy of the upper state is 29,268.38 (86)[26] cm^{-1}.

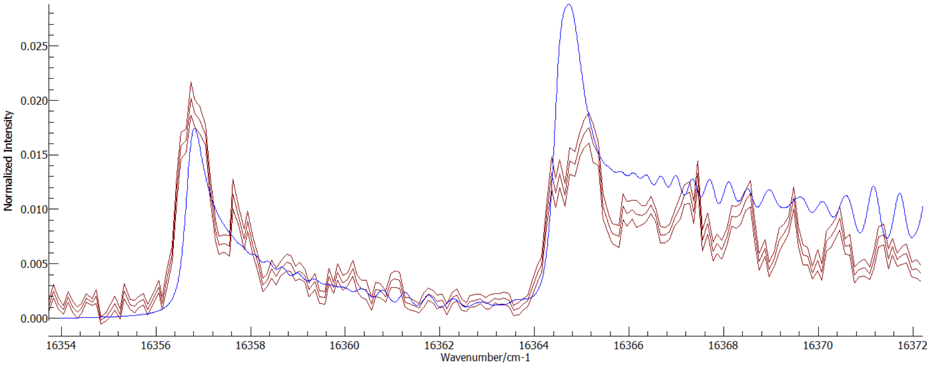

Figure B.15: Transition from the $A\ ^2\Pi_{1/2}$ $(v'' = 0)$ state to an unassigned upper state. The upper state was fitted as a Σ state, as the spectral profile resembles that in Fig. B.11. The excitation energy of the upper state is 29,649.53(7)[35] cm^{-1}.

Appendix C

Article 4: On the Feasibility of Rovibrational Laser Cooling of Radioactive RaF$^+$ and RaH$^+$ Cations

atoms

MDPI

Article

On the Feasibility of Rovibrational Laser Cooling of Radioactive RaF$^+$ and RaH$^+$ Cations

Timur A. Isaev [1,*], Shane G. Wilkins [2] and Michail Athanasakis-Kaklamanakis [3,4]

[1] National Research Center “Kurchatov Institute”, Petersburg Nuclear Physics Institute, Orlova Roscha 1, 188300 Gatchina, Russia
[2] Laboratory for Nuclear Science, Massachusetts Institute of Technology, Cambridge, MA 02139, USA; wilkinss@mit.edu
[3] Experimental Physics Department, CERN, CH-1211 Geneva, Switzerland; m.athkak@cern.ch
[4] Instituut voor Kern- en Stralingsfysica, KU Leuven, B-3001 Leuven, Belgium
* Correspondence: isaev_ta@pnpi.nrcki.ru

Abstract: Polar radioactive molecules have been suggested to be exceptionally sensitive systems in the search for signatures of symmetry-violating effects in their structure. Radium monofluoride (RaF) possesses an especially attractive electronic structure for such searches, as the diagonality of its Franck-Condon matrix enables the implementation of direct laser cooling for precision experiments. To maximize the sensitivity of experiments with short-lived RaF isotopologues, the molecular beam needs to be cooled to the rovibrational ground state. Due to the high kinetic energies and internal temperature of extracted beams at radioactive ion beam (RIB) facilities, in-flight rovibrational cooling would be restricted by a limited interaction timescale. Instead, cooling techniques implemented on ions trapped within a radiofrequency quadrupole cooler-buncher can be highly efficient due to the much longer interaction times (up to seconds). In this work, the feasibility of rovibrationally cooling trapped RaF$^+$ and RaH$^+$ cations with repeated laser excitation is investigated. Due to the highly diagonal nature between the ionic ground state and states in the neutral system, any reduction of the internal temperature of the molecular ions would largely persist through charge-exchange without requiring the use of cryogenic buffer gas cooling. Quasirelativistic X2C and scalar-relativistic ECP calculations were performed to calculate the transition energies to excited electronic states and to study the nature of chemical bonding for both RaF$^+$ and RaH$^+$. The results indicate that optical manipulation of the rovibrational distribution of trapped RaF$^+$ and RaH$^+$ is unfeasible due to the high electronic transition energies, which lie beyond the capabilities of modern laser technology. However, more detailed calculations of the structure of RaH$^+$ might reveal possible laser-cooling pathways.

Keywords: molecular electronic structure; radioactive molecules; molecular spectroscopy

PACS: 31.30.-i; 37.10.Mn; 12.15.Mm; 21.10.Ky

check for updates

Citation: Isaev, T.A.; Wilkins, S.G.; Athanasakis-Kaklamanakis, M. On the Feasibility of Rovibrational Laser Cooling of Radioactive RaF$^+$ and RaH$^+$ Cations. *Atoms* **2021**, *9*, 101. https://doi.org/10.3390/atoms9040101

Academic Editor: Ulrich D. Jentschura

Received: 16 August 2021
Accepted: 21 November 2021
Published: 26 November 2021

1. Introduction

In recent decades, the high-precision spectroscopy of atomic and molecular beams within reverting electromagnetic fields has emerged as a highly sensitive technique to search for physics beyond the Standard Model, potentially probing energy scales a few orders of magnitude greater than the capabilities of state-of-the-art particle colliders [1].

The structure of the diatomic RaF molecule has been proposed as especially attractive for tabletop experiments that probe the extent of fundamental symmetry violations in the universe [2,3], owing to its enhanced sensitivity to symmetry-violating effects within the radium nucleus [4,5] and the highly diagonal Franck-Condon matrix for vibronic transitions between the ground and low-lying excited electronic states that allow for direct laser cooling [6].

Recently, a milestone in the study of compounds of short-lived nuclei was achieved, with the first laser-spectroscopic study of RaF molecules containing different isotopes of Ra [6]. The technique of Isotope Separation On-Line (ISOL) at the ISOLDE radioactive ion beam (RIB) facility at CERN was combined with Collinear Resonance Ionization Spectroscopy (CRIS) [7] to measure the vibronic spectra of short-lived $^{223-226,228}$RaF molecules. The successful laser-spectroscopic campaign on isotopically pure molecular beams of RaF at the CRIS experiment paves the way for designing experiments to measure the extent of symmetry-violating effects in their spectra and other systems which can be produced at RIB facilities.

To maximize the precision of such experiments, the most developed of which are searching for small variations in the coherent precession of electrons within the internal molecular fields, the molecular beam should exist entirely in a single rovibrational state. In this case, the experimental count rate is maximized without needing to compromise the spectroscopic resolution.

However, through the ISOL technique, the radioactive molecules are extracted from solid targets as ionic species, which at the later stage have to be neutralised, at temperatures typically above 2000 °C, and accelerated to kinetic energies of 30–60 keV upon extraction [8]. The elevated target temperature is required to enhance the diffusion of short-lived species of interest from the interior of the target, while the high kinetic energy is a prerequisite for the efficient operation of the isotopic separation of the ionized beam. As a result, experiments aiming to perform high-precision searches for symmetry-violating effects in the extracted molecular beams need to compensate for the translational and rovibrational energy of the molecules in a reliable and efficient manner.

One of the important features of RaF (RaF$^+$) molecules is the quasidiagonality of the Franck-Condon matrix for neutralisation transitions $^0\Sigma \rightarrow {}^2\Sigma$ between the electronic ground state of the RaF$^+$ cation and the electronic ground state of neutral RaF. Thus, given the highly diagonal nature of transitions between the ionic ground state and low-lying states in the neutral system, any reduction in the vibrational temperature of the RaF$^+$ can be expected to persist through charge-exchange, yielding an improved spectroscopic sensitivity.

In this work, the electronic structure of the ground and lowest-lying excited electronic states of the RaF$^+$ cation is investigated to assess the prospect of rovibrational cooling through spectrally shaped femtosecond optical pumping with commercially available laser systems. The electronic transition energies of RaF$^+$ are also compared to those of the RaH$^+$ cation.

2. Current Prospects for Experiments on RaF

In addition to searches for *P,T*-violating effects, the systematic study of isotopologue shifts in the transition frequencies of RaF has demonstrated that the molecular electronic structure can be exceptionally sensitive to differences in the nuclear size between isotopes [9]. Therefore, particularly for unstable isotopes that either cannot be extracted from the ISOL target in atomic form, or whose study is significantly hindered by isobaric contamination, a possible experimental pathway for extending the current limits of laser spectroscopy for nuclear structure may utilize molecular beams to study nuclear size effects.

However, for the study of isotopes far from nuclear stability, which may be produced at rates significantly below 10^3 nuclei per second, the percentage of molecules that are initially at a common lower rovibronic state becomes the main limitation for performing laser spectroscopy to extract nuclear structure observables. The CRIS experiment at ISOLDE has successfully studied atomic species with production yields as low as 20 nuclei per second in the past [10]. Even at room temperature however, which the molecules can reach after being trapped for a few milliseconds in a buffer-gas-cooled ion trap, the vibrational state distribution of RaF would result in less than than 70% of the molecular ion beam in the vibronic ground state. Within this, the molecules are further distributed across numerous rotational states. As a result, without additional rovibrational cooling, the capability of performing high-resolution molecular spectroscopy of RaF at RIB facilities would be reached for isotopologues with production yields considerably higher than the limit for atomic systems.

Rovibrationally cooling the molecular beam results in the compression of the energy state distribution of the molecules to only the lowest levels, increasing the population fraction that shares a common lower state during laser excitation. At RIB facilities, the implementation of rovibrational cooling of molecular beams faces additional challenges compared to non-radioactive laboratories. Firstly, efficient rovibrational cooling of radioactive molecules can require timescales that can be comparable to the radioactive half-life of the beam. In typical collinear laser spectroscopy experiments at RIB facilities, isotopes with half-lives as low as a few milliseconds can be studied [11]. Secondly, the beam properties and high kinetic energy of the ion beam must be preserved to ensure the efficient transmission and separation of radioactive molecules with low production yields.

While in-flight rovibrational cooling techniques would have very limited interaction times at these kinetic energies (typically 30–60 keV), such facilities often also incorporate a radiofrequency quadrupole trap that provides cooling and bunching of the radioactive beams using a room-temperature, inert buffer gas and quadrupole oscillating fields [12–14], with the possibility of laser access in the trap [15]. As the cooling and bunching of the ion beams of interest takes place on timescales of up to seconds, conditioning the molecular beams within the RFQ trap could provide a pathway for rovibrational cooling.

Rovibrational cooling via collisions with a cryogenic buffer gas [16] and via optical pumping with a spectrally shaped femtosecond laser [17] are techniques compatible with the requirements of RIB facilities and which can take advantage of the cooler-buncher in a straight-forward manner. Rovibrational cooling in a cryogenic buffer-gas cell is a state-of-the-art technique with widespread usage in molecular spectroscopy, in which a slow molecular beam flies through a cell filled with cryogenic helium or neon, or the beam is directly created within the cell, most often through laser ablation. In-flight cooling in a gas cell, however, is incompatible with the typical kinetic energies of delivered radioactive beams at RIB facilities. Instead, efficient cryogenic buffer-gas cooling must be done within a cryogenic cooler-buncher, in lieu of the typically room-temperature cooler-bunchers currently in use at the various RIB facilities, or by adding a deceleration region and a cryogenic buffer gas cell following the room-temperature RFQ.

An alternative route to reducing the internal energy of molecules produced at RIB facilities relies on directly manipulating the vibrational population using laser light. This technique was first experimentally realized on photo-associated Cs_2 molecules [18]. Assembly of molecules from ultracold atoms often leaves the resulting molecules in a number of vibrational states of the electronic ground state, despite the ensemble being translationally cold. In this approach, a broadband laser is used to selectively excite an electronic transition that, after a number of excitation-deexcitation cycles, optically pumps a large fraction of the population to the vibrational ground state. This is achieved by spectrally shaping the frequency output of the laser to exclude the wavelengths that would lead to excitations from the vibrational ground state, which therefore acts as a dark state where all the molecules eventually accumulate. The technique was later extended to allow efficient transfer of Cs_2 molecules to an arbitrary vibrational state of the electronic ground state [19]. Due to its relative simplicity, the technique has been applied to different systems (a review of which can be found in [20]). Once the molecules have been transferred to the vibrational ground state, the internal temperature can be further reduced by selectively exciting P-branch rotational transitions using similar spectral filtering techniques [21].

Realizing these techniques requires a tunable broadband laser, often a femtosecond titanium-sapphire system, with a frequency output that is sufficiently wide to encompass the necessary components of the molecular structure (typically tens of cm^{-1}). The spectral density of such systems is inevitably poor and therefore requires long interaction times (milliseconds to seconds) to achieve a significant population transfer. The majority of these studies have therefore taken place in a trap. However, one study was able to significantly rovibrationally cool a supersonic beam of BaF in less than 500 μs, owing to the development of custom laser systems that deliver a higher spectral density in the wavelength regions of interest. As RaF($^+$) is a significantly heavier system, its rotational and vibrational constants scale favourably when considering its potential for rovibrational cooling with laser light.

A future experiment aiming to search for signatures of an electron electric dipole moment (eEDM) in RaF may utilize either optical-cycling or buffer-gas cooling. While cryogenic buffer-gas cooling is an established technique in molecular eEDM searches [22–24], the technical developments required for substituting a room-temperature cooler-buncher at an RIB facility to a cryogenic one raise the necessity for a detailed investigation into whether optical pumping with spectral shaping can be pursued instead.

3. Computational Methods

Two sets of calculations were performed for both RaF$^+$ and RaH$^+$; 1) two-component all-electron calculations within the molecular-mean-field X2C quasirelativistic framework (see [25,26] for details on the X2C approach) 2) scalar-relativistic calculations using 78-electron energy-consistent ECP on Ra and 2-electron ECP on F [27]. The scalar-relativistic calculations were performed using the MOLPRO 2019.2.0 program package, while the X2C calculations were performed using the DIRAC19 program package [28].

3.1. X2C Quasirelativistic Calculations

In the X2C calculations, the basis set [28s26p18d12f], analogous to the one used in Refs. [29,30], was used for Ra, while the uncontracted ANO-RCC basis set [14s9p4d] by Roos and co-authors was used for F and the correlation-consistent basis set cc-pVTZ [5s2p1d] by Dunning, contracted to [3s2p1d], was used for H. A Gaussian nuclear model was employed in all calculations, with nuclear Gaussian exponents 1.310×10^8 (Ra), 5.355×10^8 (F) and 21.25×10^8 (H).

Firstly, DHF calculations of the lowest-by-energy closed-shell configuration of the singly charged cations RaF$^+$ and RaH$^+$ were performed. Afterwards, Kramers-restricted generalised active space CI (GAS-CI) calculations (for details on the GAS-CI scheme see Ref. [31]) were performed, accounting for correlations of 16 electrons in RaF$^+$ and 10 electrons in RaH$^+$. In the GAS-CI calculations, only single and double excitations were allowed from the ground-state closed-shell configuration to the space of virtual spinors which included for RaF$^+$ 120 Kramers pairs and for RaH$^+$ 150 Kramers pairs. Molecular symmetry $C_{\infty v}$ was used in all the calculations; 3, 2 and 2 roots were calculated in the $C_{\infty v}$ irreps corresponding to projections of total electron angular momenta Ω = 0, 1 and 2.

3.2. Scalar-Relativistic ECP Calculations

For the scalar-relativistic ECP calculations, basis sets supplied with energy-consistent ECPs were used for both Ra (78 inner-core electrons are simulated by ECP) and F (2 inner-core electrons are included in ECP), while the basis set for F was also augmented by *d*-functions from the def2-QZVP basis set from MOLPRO basis set library. For H, *s*- and *p*-functions were taken from the def2-QZVP basis set from the MOLPRO basis set library.

As a result, the basis sets [$15s14p8d4f$], [$4s5p3d$] and [$7s3p$] were taken for Ra, F and H, respectively, in the ECP calculations. In all calculations, we started from DFT calculations with the B3LYP exchange-correlation potential of the closed-shell ground-state configuration of RaF$^+$ and RaH$^+$. Molecular symmetry in all calculations was set to C_1; the initial internuclear distance between Ra and F was taken to be equal to 4.0 a_0 and 4.38 a_0 for Ra and H. After the DFT calculations, a CASSCF calculation was performed, where the average energy of the two lowest singlet electronic states was minimized. For RaF$^+$ correlations between 6 valence electrons are accounted for by MCSCF method, while 10 electrons on the lowest energy MOs are frozen after the SCF/DFT step. Six valence electrons can occupy higher by energy four MOs (energetically following frozen 5 MOs), without restrictions to possible configurations, thus realizing minimal CASSCF scheme which allows us to capture in calculation excited electronic energies. An analogous scheme of electron distribution over active MOs is used for RaH^+, where correlations between 10 valence electrons are accounted for (none of the electrons are frozen). In the last step, multireference internally contracted CI (micCI) calculations (as implemented in the MOLPRO package [32]) were performed. In the micCI calculations of RaF^+, the internal space consisted of 16 natural molecular orbitals with the greatest occupation numbers obtained from the CASSCF calculations, while for RaH^+, the internal CI space included 11 natural orbitals.

4. Results and Discussion

Single-point X2C/GAS-CI calculations of RaF^+ and RaH^+ were firstly performed to estimate the relative energies of excited molecular levels and the positions of singlet and triplet states. In these calculations, the internuclear distances were taken to be approximately equal to the equilibrium internuclear distances of the ground electronic states of RaF^+ and RaH^+. The results of the calculations are presented in Table 1. It can be seen that the properties of the excited states in RaF^+ and RaH^+ are distinctly different. In particular, the vertical excitation energies in RaF^+ are almost two times higher than those in RaH^+, being in the range of 10^5 cm^{-1}. Such high transition frequencies indicate that laser-cooling techniques are inapplicable to both RaF^+ and RaH^+, even in the case of quasidiagonal FC-matrices for vibronic transitions between electronic states, as they lay far beyond the reach of state-of-the-art laser technology.

To elucidate the nature of chemical bonding in RaF^+ and RaH^+, molecular geometry optimisation in the framework of the scalar-relativistic ECP approach was performed for both RaF^+ and RaH^+; the results are presented in Table 2. The data corroborate that chemical bonding is essentially different for RaF^+ and RaH^+. It is worth noting that a number of scalar-relativistic correlation calculations of the electronic structure exists for lighter homologues of RaH^+, including SrH^+ and BaH^+ [33,34], and our previous experience with calculations of neutral RaF [3,30] show that, for the purpose of estimation of quality of calculation, the comparison of molecular parameters with the corresponding parameters in lighter homologues is justified.

The results of the scalar-relativistic calculations of RaF^+ indicate that the excited states lie at about 70×10^3 cm^{-1} over the ground electronic state, while in RaH^+ the situation resembles that of the lighter homologues BaH^+ and SrH^+, where electronic excitation energies are in the optical range. Additionally, the potential energy curves (PEC) of the excited electronic states are crucially different in the two cations. For RaH^+, the PEC of the first excited singlet state looks similar to the PEC of the ground state, having a well-defined minimum and harmonic vibrational quanta in the order of a few hundred cm^{-1}, thus having the typical characteristics of a chemical bond. For RaF^+, the first excited singlet state is quasi-dissociative and resembles the bonding situation in a charge-neutral van der Waals complex. It must be emphasized, however, that the scalar-relativistic calculations for both RaF^+ and RaH^+ show considerably lower transition frequencies compared to the two-component X2C calculations.

The structure of the bonding molecular orbitals for the ground and excited electronic states in both RaF^+ and RaH^+ were also studied; the results are presented in Table 3.

The highest occupied molecular orbitals (HOMOs) in the ground electronic states of RaF^+ (8.1) and RaH^+ (5.1) are quite different. For RaF^+ the HOMO is in fact the atomic fluorine orbital, which is expected for a strong ionic bond. In the case of the bond in RaH^+, which has a rather covalent character, the HOMO is distributed over both Ra and H. In the excited electronic state of RaH^+, averaged natural orbitals show that the electronic charge distribution remains similar to that in the electronic ground state. In the case of RaF^+, the charge distribution changes considerably from being centered on the fluorine atom into a covalent-type distribution. These points are also supported by Mulliken analyses of charge distribution on H and F, when going from the ground to excited electronic states: (1) in RaH^+, the charge on H in the ground electronic state is -0.28, and it becomes -0.21 in excited electronic state (2) in RaF^+ ,the corresponding charges on F change from −0.59 to −0.36. Thus, a remarkable charge transfer takes place.

Table 1. Values of GAS-CI/X2C vertical excitation energies and projections of electronic orbital angular momentum on the internuclear axis l_z and electronic spin s_z for RaF^+ and RaH^+ for the internuclear distances $4.16a_0$ and $4.38a_0$ for Ra-F and Ra-H, respectively. Values of T_0 are rounded to thousands of cm^{-1} to emphasize the suggested accuracy of the calculations.

	RaF^+				**RaH^+**		
Ω	**T_0**	**l_z**	**s_z**	**Ω**	**T_0**	**l_z**	**s_z**
0	0	−0.0002	0.0002	0	0	0.0023	−0.0023
0	114×10^3	−0.0243	0.0243	0	55×10^3	−0.0119	0.0119
1	114×10^3	0.9768	0.0232	1	55×10^3	0.0103	0.9897
0	114×10^3	0.0236	−0.0236	0	58×10^3	0.0163	−0.0163
2	118×10^3	0.9998	1.0002	2	64×10^3	1.0055	0.9945
1	118×10^3	0.0003	0.9997	2	66×10^3	2.0030	−0.0030
2	125×10^3	−0.0215	2.0215	1	66×10^3	1.2694	−0.2694

Table 2. Results of the molecular geometry optimisation for the ground and excited electronic states for RaF^+ and RaH^+ in scalar-relativistic ECP calculations. The equilibrium distance R_e is in Å, adiabatic transition energies T_e and harmonic vibrational quanta are in cm^{-1}. For comparison, the data from [33,34] for molecular constants of SrH^+ and BaH^+ are provided.

	RaF^+		**RaH^+**		**SrH^+**		**BaH^+**	
State	$X(^1\Sigma)$	$A(^1\Sigma)$	$X(^1\Sigma)$	$A(^1\Sigma)$	$X(^1\Sigma)$	$A(^1\Sigma)$	$X(^1\Sigma)$	$A(^1\Sigma)$
R_e	2.20	17.98	2.32	2.98	2.073 [1]	2.608 [1]	2.177 [1]	2.913 [1]
					1.97 [2]	2.47 [2]	2.079 [2]	2.719 [2]
ω_e			1251	542	1264 [1]	678 [1]	1353 [1]	515 [1]
T_e				21,791		24,027 [1]		23,365 [1]
						23,972 [2]		

[1] data from [33]; [2] data from [34].

Table 3. MO-LCAO expansion of the averaged natural molecular orbitals in ground and excited $^1\Sigma$ states of RaF^+ and RaH^+, with the corresponding occupation numbers. Only expansion coefficients larger than 0.3 are provided.

State	**N**	**Occ**	**RaF^+**	**N**	**Occ**	**RaH^+**
X ($^1\Sigma$)	8.1	2.0	$(0.44482p_z + 0.43291p_z)$(F)	5.1	2.0	$(-0.34524s + 0.32983s)$(Ra) +$(0.31941s)$(H)
A ($^1\Sigma$)	8.1	1.5	$(0.26669p_z)$(Ra) + $(0.46247p_z + 0.46855p_z)$(F)	5.1	1.5	$(0.42396s)$(H)
	9.1	0.5	$(0.34216s - 0.32604s - 0.60611s + 0.98934s)$(Ra)	6.1	0.5	$(0.32950s - 0.31464s - 0.56286s + 0.99801s)$(Ra)

5. Conclusions

An investigation of the electronic structure of the RaF^+ and RaH^+ molecular cations was performed to explore the prospect of direct rovibrational laser cooling. Additionally, the nature of chemical bonding in both compounds was studied for the ground and excited electronic states. It is concluded that for both RaF^+ and RaH^+, the application of direct laser-cooling techniques appears unfeasible due to the high transition energies that lie beyond the capability of modern state-of-the-art laser technology. However, according to the data from the Table 2 we see a trend in scalar-relativistic calculations in series of (Sr- > Ba- > Ra)H^+ compounds, that excitation energies of X- > A transitions are gradually decreasing. However, X2C calculations, where spin-orbit effects are accounted for, show higher excitation energies than these in scalar-relativistic calculations for RaH^+. Thus, more sophisticated calculations of the electronic structure of RaH^+ utilizing a basis set extended to higher harmonics and a larger spinor space for electron excitation in MRCI would be of interest, especially combined with similar calculations of neutral RaH. In the latter case, it would be interesting to see deviation from simple "one-electron-over-closed-shell" picture, as possible low-lying states connected with excitation with electron from closed shell could be rather close in energy to the states generated by excitation of the valence electron.

Author Contributions: Formal analysis, S.G.W.; Investigation, T.A.I., S.G.W. and M.A.-K.; Validation, T.A.I.; Writing—original draft, T.A.I., S.G.W. and M.A.-K. All authors have read and agreed to the published version of the manuscript.

Funding: This research was funded by Russian Science Foundation grant number 21-42-04411.

Institutional Review Board Statement: Not applicable.

Informed Consent Statement: Not applicable.

Acknowledgments: The authors are grateful for discussions with R. Berger and other members of the CRIS collaboration at ISOLDE. This work was supported financially by RSF grant 21-42-04411.

Conflicts of Interest: The authors declare no conflict of interest. The funders had no role in the design of the study; in the collection, analyses, or interpretation of data; in the writing of the manuscript, or in the decision to publish the results.

References

1. Safronova, M.S.; Budker, D.; DeMille, D. Search for new physics with atoms and molecules. *Phys. Mod. Phys.* **2018**, *90*, 025008. [CrossRef]
2. Isaev, T.A.; Hoekstra, S.; Berger, R. Laser-cooled RaF as a promising candidate to measure molecular parity violation. *Phys. Rev. A* **2010**, *82*, 052521. [CrossRef]
3. Isaev, T.A.; Berger, R. Electron correlation and nuclear charge dependence of parity-violating properties in open-shell diatomic molecules. *Phys. Rev. A* **2012**, *86*, 062515. [CrossRef]
4. Auerbach, N.; Flambaum, V.V.; Spevak, V. Collective T- and P-odd electromagnetic moments in nuclei with octupole deformations. *Phys. Rev. Lett.* **1996**, *76*, 4316–4319. [CrossRef] [PubMed]
5. Gaffney, L.P.; Butler, P.A.; Scheck, M.; Hayes, A.B.; Wenander, F.; Albers, M.; Bastin, B.; Bauer, C.; Blazhev, A.; Bönig, S.; et al. Studies of pear-shaped nuclei using accelerated radioactive beams. *Nature* **2013**, *497*, 199–204. [CrossRef]
6. Garcia Ruiz, R.F.; Berger, R.; Billowes, J.; Binnersley, C.L.; Bissell, M.L.; Breier, A.A.; Brinson, A.J.; Chrysalidis, K.; Cocolios, T.E.; Cooper, B.S.; et al. Spectroscopy of short-lived radioactive molecules. *Nature* **2020**, *581*, 396–400. [CrossRef]
7. Flanagan, K.T.; Lynch, K.M.; Billowes, J.; Bissell, M.L.; Budinčević, I.; Cocolios, T.E.; de Groote, R.P.; De Schepper, S.; Fedosseev, V.N.; Franchoo, S.; et al. Collinear Resonance Ionization Spectroscopy of Neutron-Deficient Francium Isotopes. *Phys. Rev. Lett.* **2013**, *111*, 212501. [CrossRef]
8. Catherall, R.; Andreazza, W.; Breitenfeldt, M.; Dorsival, A.; Focker, G.J.; Gharsa, T.P.; Giles, T.J.; Grenard, J.L.; Locci, F.; et al. The ISOLDE facility. *J. Phys. Nucl. Part. Phys.* **2017**, *44*, 094002. [CrossRef]
9. Udrescu, S.; Brinson, A.; Ruiz, R.G.; Gaul, K.; Berger, R.; Billowes, J.; Binnersley, C.; Bissell, M.; Breier, A.; Chrysalidis, K.; et al. Isotope Shifts of Radium Monofluoride Molecules. *Phys. Rev. Lett.* **2021**, *127*, 033001. [CrossRef]
10. de Groote, R.P.; Billowes, J.; Binnersley, C.L.; Bissell, M.L.; Cocolios, T.E.; Goodacre, T.D.; Farooq-Smith, G.J.; Fedorov, D.V.; Flanagan, K.T.; Franchoo, S.; et al. Measurement and microscopic description of odd–even staggering of charge radii of exotic copper isotopes. *Nat. Phys.* **2020**, *16*, 620–624. [CrossRef]
11. Campbell, P.; Moore, I.; Pearson, M. Laser spectroscopy for nuclear structure physics. *Prog. Part. Nucl. Phys.* **2016**, *86*, 127–180. [CrossRef]
12. Mané, E.; Billowes, J.; Blaum, K.; Campbell, P.; Cheal, B.; Delahaye, P.; Flanagan, K.T.; Forest, D.H.; Franberg, H.; Geppert, C.; et al. An ion cooler-buncher for high-sensitivity collinear laser spectroscopy at ISOLDE. *Eur. Phys. J.* **2009**, *42*, 503–507. [CrossRef]
13. Nieminen, A.; Huikari, J.; Jokinen, A.; Äystö, J.; Campbell, P.; Cochrane, E. Beam cooler for low-energy radioactive ions. *Nucl. Instrum. Methods Phys. Res. Sect. Accel. Spectrom. Detect. Assoc. Equip.* **2001**, *469*, 244–253. [CrossRef]
14. Barquest, B.; Bollen, G.; Mantica, P.; Minamisono, K.; Ringle, R.; Schwarz, S.; Sumithrarachchi, C. RFQ beam cooler and buncher for collinear laser spectroscopy of rare isotopes. *Nucl. Instrum. Methods Phys. Res. Sect. Accel. Spectrom. Detect. Assoc. Equip.* **2017**, *866*, 18–28. [CrossRef]
15. Fedosseev, V.; Chrysalidis, K.; Goodacre, T.D.; Marsh, B.; Rothe, S.; Seiffert, C.; Wendt, K. Ion beam production and study of radioactive isotopes with the laser ion source at ISOLDE. *J. Phys. Nucl. Part. Phys.* **2017**, *44*, 084006. [CrossRef]
16. Hutzler, N.R.; Lu, H.I.; Doyle, J.M. The Buffer Gas Beam: An Intense, Cold, and Slow Source for Atoms and Molecules. *Chem. Rev.* **2012**, *112*, 4803–4827. [CrossRef] [PubMed]
17. Manai, I.; Horchani, R.; Lignier, H.; Pillet, P.; Comparat, D.; Fioretti, A.; Allegrini, M. Rovibrational Cooling of Molecules by Optical Pumping. *Phys. Rev. Lett.* **2012**, *109*, 183001. [CrossRef] [PubMed]

18. Viteau, M.; Chotia, A.; Allegrini, M.; Bouloufa, N.; Dulieu, O.; Comparat, D.; Pillet, P. Optical Pumping and Vibrational Cooling of Molecules. *Science* **2008**, *321*, 232–234. [CrossRef] [PubMed]
19. Sofikitis, D.; Weber, S.; Fioretti, A.; Horchani, R.; Allegrini, M.; Chatel, B.; Comparat, D.; Pillet, P. Molecular vibrational cooling by optical pumping with shaped femtosecond pulses. *New J. Phys.* **2009**, *11*, 055037. [CrossRef]
20. Hamamda, M.; Pillet, P.; Lignier, H.; Comparat, D. Ro-vibrational cooling of molecules and prospects. *J. Phys. At. Mol. Opt. Phys.* **2015**, *48*, 182001. [CrossRef]
21. Stollenwerk, P.R.; Antonov, I.O.; Venkataramanababu, S.; Lin, Y.W.; Odom, B.C. Cooling of a Zero-Nuclear-Spin Molecular Ion to a Selected Rotational State. *Phys. Rev. Lett.* **2020**, *125*, 113201. [CrossRef]
22. Tarbutt, M.R.; Sauer, B.E.; Hudson, J.J.; Hinds, E.A. Design for a fountain of YbF molecules to measure the electron's electric dipole moment. *New J. Phys.* **2013**, *15*, 053034. [CrossRef]
23. Baron, J.; Campbell, W.C.; DeMille, D.; Doyle, J.M.; Gabrielse, G.; Gurevich, Y.V.; Hess, P.W.; Hutzler, N.R.; Kirilov, E.; Kozyryev, I.; et al. Order of Magnitude Smaller Limit on the Electric Dipole Moment of the Electron. *Science* **2013**, *343*, 269–272. [CrossRef] [PubMed]
24. Andreev, V.; Ang, D.G.; DeMille, D.; Doyle, J.M.; Gabrielse, G.; Haefner, J.; Hutzler, N.R.; Lasner, Z.; Meisenhelder, C.; O'Leary, B.R.; et al. Improved limit on the electric dipole moment of the electron. *Nature* **2018**, *562*, 355–360. [CrossRef]
25. Liu, W. Ideas of relativistic quantum chemistry. *Mol. Phys.* **2010**, *108*, 1679–1706. [CrossRef]
26. Saue, T. Relativistic Hamiltonians for Chemistry: A Primer. *ChemPhysChem* **2011**, *12*, 3077–3094. [CrossRef]
27. Lim, I.; Stoll, H.; Schwerdtfeger, P. Relativistic small-core energy-consistent pseudopotentials for the alkaline-earth elements from Ca to Ra. *J. Chem. Phys.* **2006**, *124*, 034107. [CrossRef]
28. Saue, T.; Bast, R.; Gomes, A.S.P.; Jensen, H.J.A.; Visscher, L.; Aucar, I.A.; Remigio, R.D.; Dyall, K.G.; Eliav, E.; Fasshauer, E.; et al. The DIRAC code for relativistic molecular calculations. *J. Chem. Phys.* **2020**, *152*, 204104. [CrossRef]
29. Isaev, T.A.; Hoekstra, S.; Willmann, L.; Berger, R. Ion neutralisation mass-spectrometry route to radium monofluoride (RaF). *arXiv* **2013**, arXiv:1310.1511.
30. Isaev, T.A.; Berger, R. Lasercooled radium monofluoride: A molecular all-in-one probe for new physics. *arXiv* **2013**, arXiv:1302.5682.
31. Fleig, T.; Olsen, J.; Visscher, L. The generalized active space concept for the relativistic treatment of electron correlation. II. Large-scale configuration interaction implementation based on relativistic 2- and 4-spinors and its application. *J. Chem. Phys.* **2003**, *119*, 2963–2971. [CrossRef]
32. Werner, H.; Knowles, P. An efficient internally contracted multiconfiguration reference configuration-interaction method. *J. Chem. Phys.* **1988**, *89*, 5803–5814. [CrossRef]
33. Abu el Kher, N.; Zeid, I.; El-Kork, N.; Korek, M. Electronic structure of the SrH^+ and BaH^+ molecules with dipole moment and rovibrational calculations. *J. Comput. Sci.* **2021**, *51*, 101264. [CrossRef]
34. Aymar, M.; Dulieu, O. The electronic structure of the alkaline-earth-atom (Ca, Sr, Ba) hydride molecular ions. *J. Phys. At. Mol. Opt. Phys.* **2012**, *45*, 215103. [CrossRef]

Bibliography

[1] A Koszorús, J Billowes, C L Binnersley, M L Bissell, T E Cocolios, B S Cooper, R P de Groote, G J Farooq-Smith, V N Fedosseev, K T Flanagan, S Franchoo, R F Garcia Ruiz, W Gins, K M Lynch, G Neyens, F P Gustafsson, C Ricketts, H H Stroke, A Vernon, S G Wilkins, and X F Yang. Resonance ionization schemes for high resolution and high efficiency studies of exotic nuclei at the CRIS experiment. *Nuclear Instruments and Methods in Physics Research Section B: Beam Interactions with Materials and Atoms*, 463:398–402, 2020.

[2] S. M. Udrescu, S. G. Wilkins, A. A. Breier, R. F. Garcia Ruiz, M. Athanasakis-Kaklamanakis, M. Au, R. Berger, I. Belosevic, M. L. Bissell, K. Chrysalidis, T. E. Cocolios, R. P. de Groote, A. Dorne, K. T. Flanagan, S. Franchoo, K. Gaul, S. Geldhof, T. F. Giesen, D. Hanstorp, R. Heinke, A. Koszorús, S. Kujanpää, L. Lalanne, G. Neyens, M. Nichols, H. A. Perrett, J. R. Reilly, S. Rothe, B. van den Borne, Q. Wang, J. Wessolek, X. F. Yang, and K. Zülch. Precision spectroscopy and laser cooling scheme of a radium-containing molecule. *Under review*, 2023.

[3] L W Wansbeek, S Schlesser, B K Sahoo, A E L Dieperink, C J G Onderwater, and R G E Timmermans. Charge radii of radium isotopes. *Physical Review C*, 86(1):15503, 7 2012.

[4] S. M. Udrescu, A. J. Brinson, R. F. Garcia Ruiz, K. Gaul, R. Berger, J. Billowes, C. L. Binnersley, M. L. Bissell, A. A. Breier, K. Chrysalidis, T. E. Cocolios, B. S. Cooper, K. T. Flanagan, T. F. Giesen, R. P. de Groote, S. Franchoo, F. P. Gustafsson, T. A. Isaev,

A. Koszorus, G. Neyens, H. A. Perrett, C. M. Ricketts, S. Rothe, A. R. Vernon, K. D. A. Wendt, F. Wienholtz, S G. Wilkins, and X. F. Yang. Isotope Shifts of Radium Monofluoride Molecules. *Physical Review Letters*, 127(3):033001, 2021.

[5] R. F. Garcia Ruiz, R. Berger, J. Billowes, C. L. Binnersley, M. L. Bissell, A. A. Breier, A. J. Brinson, K. Crysalidis, T. E. Cocolios, B. S. Cooper, K. T. Flanagan, T. F. Giesen, R. P. de Groote, S. Franchoo, F. P. Gustafsson, T. A. Isaev, A. Koszorus, G. Neyens, H. A. Perrett, C. M. Ricketts, S. Rothe, L. Schweikhard, A. R. Vernon, K. D. A. Wendt, F. Weinholtz, S. G. Wilkins, and X. F. Yang. Spectroscopy of short-lived radioactive molecules. *Nature*, 581(May):396–400, 2020.

[6] Leonid V Skripnikov, Alexander V Oleynichenko, Andréi Zaitsevskii, Nikolai S Mosyagin, Michail Athanasakis-Kaklamanakis, Mia Au, and Gerda Neyens. Ab initio study of electronic states and radiative properties of the AcF molecule. *arXiv:2305.06932*, 2023.

[7] X F Yang, S J Wang, S G Wilkins, and R F Garcia Ruiz. Laser spectroscopy for the study of exotic nuclei. *Progress in Particle and Nuclear Physics*, 129:104005, 2023.

[8] P Campbell, I D Moore, and M R Pearson. Laser spectroscopy for nuclear structure physics. *Progress in Particle and Nuclear Physics*, 86:127–180, 2016.

[9] M. S. Safronova, D. Budker, D. DeMille, D. F. J. Kimball, A. Derevianko, and C. W. Clark. Search for new physics with atoms and molecules. *Reviews of Modern Physics*, 90(2), 2018.

[10] Andrei D Sakharov. Violation of CP invariance, C asymmetry, and baryon asymmetry of the universe. *Soviet Physics Uspekhi*, 34(5):392, 1991.

[11] Cari Cesarotti, Qianshu Lu, Yuichiro Nakai, Aditya Parikh, and Matthew Reece. Interpreting the electron EDM constraint. *Journal of High Energy Physics*, 2019(5):59, 2019.

[12] T. E. Chupp, P. Fierlinger, M. J. Ramsey-Musolf, and J. T. Singh. Electric dipole moments of atoms, molecules, nuclei, and particles. *Reviews of Modern Physics*, 91(1):15001, 1 2019.

[13] V. V. Flambaum and J. S.M. Ginges. Nuclear Schiff moment and time-invariance violation in atoms. *Physical Review A*, 65(3):9, 2002.

[14] N. J. Fitch, J. Lim, E. A. Hinds, B. E. Sauer, and M. R. Tarbutt. Methods for measuring the electron's electric dipole moment using ultracold YbF molecules. *Quantum Science and Technology*, 6(1), 1 2021.

[15] L. P. Gaffney, P. A. Butler, M. Scheck, A. B. Hayes, F. Wenander, M. Albers, B. Bastin, C. Bauer, A. Blazhev, S. Bönig, N. Bree, J. Cederkäll, T. Chupp, D. Cline, T. E. Cocolios, T. Davinson, H. De Witte, J. Diriken, T. Grahn, A. Herzan, M. Huyse, D. G. Jenkins, D. T. Joss, N. Kesteloot, J. Konki, M. Kowalczyk, Th Kröll, E. Kwan, R. Lutter, K. Moschner, P. Napiorkowski, J. Pakarinen, M. Pfeiffer, D. Radeck, P. Reiter, K. Reynders, S. V. Rigby, L. M. Robledo, M. Rudigier, S. Sambi, M. Seidlitz, B. Siebeck, T. Stora, P. Thoele, P. Van Duppen, M. J. Vermeulen, M. Von Schmid, D. Voulot, N. Warr, K. Wimmer, K. Wrzosek-Lipska, C. Y. Wu, and M. Zielinska. Studies of pear-shaped nuclei using accelerated radioactive beams. *Nature*, 497(7448):199–204, 2013.

[16] Brady G Butler, Scott C Middlemas, Eric M Klier, James D Paramore, Daniel T Casem, and Kevin J Hemker. Effect of Boron on Microstructure and Fracture of Sintered Ultrafine-Grained Tungsten. *JOM*, 70(11):2537–2543, 2018.

[17] E. Verstraelen, A. Teigelhöfer, W. Ryssens, F. Ames, A. Barzakh, M. Bender, R. Ferrer, S. Goriely, P. H. Heenen, M. Huyse, P. Kunz, J. Lassen, V. Manea, S. Raeder, and P. Van Duppen. Search for octupole-deformed actinium isotopes using resonance ionization spectroscopy. *Physical Review C*, 100(4):44321, 2019.

[18] N Auerbach, V V Flambaum, and V Spevak. Collective T- and P-Odd Electromagnetic Moments in Nuclei with Octupole Deformations. *Physical Review Letters*, 76(23):4316–4319, 6 1996.

[19] J. Dobaczewski and J. Engel. Nuclear Time-Reversal Violation and the Schiff Moment of 225Ra. *Physical Review Letters*, 94(23):232502, 6 2005.

[20] V. V. Flambaum and V. A. Dzuba. Electric dipole moments of atoms and molecules produced by enhanced nuclear Schiff moments. *Physical Review A*, 101:042504, 4 2020.

[21] V V Flambaum and A J Mansour. Enhanced magnetic quadrupole moments in nuclei with octupole deformation and their CP-violating effects in molecules. *Physical Review C*, 105(6):65503, 6 2022.

[22] M. Athanasakis, S. G. Wilkins, T. E. Cocolios, K. T. Flanagan, R. F. Garcia Ruiz, G. Neyens, X. F. Yang, M. Au, R. Berger, M. L. Bissell, A. Borschevsky, A. A. Breier, A. J. Brinson, R. P. de Groote, Ch. E. Duellmann, K. Gaul, S. Geldhof, T. F. Giesen, F. P. Gustafsson, J. Karthein, A. Koszorús, S. Lechner, S. Malbrunot-Ettenauer, S. Rothe, S. Sels, J. Stohner, S. M. Udrescu, P. Van Duppen, A. R. Vernon, and M. Vilén. Radioactive molecules at ISOLDE. Technical report, CERN, 2021.

[23] Gordon Arrowsmith-Kron, Michail Athanasakis-Kaklamanakis, Mia Au, Jochen Ballof, Robert Berger, Anastasia Borschevsky, Alexander A Breier, Fritz Buchinger, Dmitry Budker, Luke Caldwell, Christopher Charles, Nike Dattani, Ruben P de Groote, David DeMille, Timo Dickel, Jacek Dobaczewski, Christoph E Düllmann, Ephraim Eliav, Jon Engel, Mingyu Fan, Victor Flambaum, Kieran T Flanagan, Alyssa Gaiser, Ronald Garcia Ruiz, Konstantin Gaul, Thomas F Giesen, Jacinda Ginges, Alexander Gottberg, Gerald Gwinner, Reinhard Heinke, Steven Hoekstra, Jason D Holt, Nicholas R Hutzler, Andrew Jayich, Jonas Karthein, Kyle G Leach, Kirk Madison, Stephan Malbrunot-Ettenauer, Takayuki Miyagi, Iain D Moore, Scott Moroch, Petr Navrátil, Witold Nazarewicz, Gerda Neyens, Eric Norrgard, Nicholas Nusgart, Lukáš F Pašteka, Alexander N Petrov, Wolfgang Plass, Roy A Ready, Moritz Pascal Reiter, Mikael Reponen, Sebastian Rothe, Marianna Safronova, Christoph Scheidenberger, Andrea Shindler, Jaideep T Singh, Leonid V Skripnikov, Anatoly V

Titov, Silviu-Marian Udrescu, Shane G Wilkins, and Xiaofei Yang. Opportunities for Fundamental Physics Research with Radioactive Molecules. *arXiv*, 2302.02165, 2023.

[24] A Koszorús, X F Yang, W G Jiang, S J Novario, S W Bai, J Billowes, C L Binnersley, M L Bissell, T E Cocolios, B S Cooper, R P de Groote, A Ekström, K T Flanagan, C Forssén, S Franchoo, R F Garcia Ruiz, F P Gustafsson, G Hagen, G R Jansen, A Kanellakopoulos, M Kortelainen, W Nazarewicz, G Neyens, T Papenbrock, P.-G. Reinhard, C M Ricketts, B K Sahoo, A R Vernon, and S G Wilkins. Charge radii of exotic potassium isotopes challenge nuclear theory and the magic character of N = 32. *Nature Physics*, 2021.

[25] R. P. de Groote, J. Billowes, C. L. Binnersley, M. L. Bissell, T. E. Cocolios, T. Day Goodacre, G. J. Farooq-Smith, D. V. Fedorov, K. T. Flanagan, S. Franchoo, R. F. Garcia Ruiz, W. Gins, J. D. Holt, Koszorús, K. M. Lynch, T. Miyagi, W. Nazarewicz, G. Neyens, P. G. Reinhard, S. Rothe, H. H. Stroke, A. R. Vernon, K. D.A. Wendt, S. G. Wilkins, Z. Y. Xu, and X. F. Yang. Measurement and microscopic description of odd–even staggering of charge radii of exotic copper isotopes. *Nature Physics*, 16(6):620–624, 2020.

[26] A J Miller, K Minamisono, A Klose, D Garand, C Kujawa, J D Lantis, Y Liu, B Maaß, P F Mantica, W Nazarewicz, W Nörtershäuser, S V Pineda, P.-G. Reinhard, D M Rossi, F Sommer, C Sumithrarachchi, A Teigelhöfer, and J Watkins. Proton superfluidity and charge radii in proton-rich calcium isotopes. *Nature Physics*, 15(5):432–436, 2019.

[27] G. Hagen, M. Hjorth-Jensen, G. R. Jansen, R. Machleidt, and T. Papenbrock. Continuum Effects and Three-Nucleon Forces in Neutron-Rich Oxygen Isotopes. *Phys. Rev. Lett.*, 108(24):242501, 6 2012.

[28] G. Neyens. Nuclear magnetic and quadrupole moments for nuclear structure research on exotic nuclei. *Reports on Progress in Physics*, 66(4):633–689, 2003.

[29] T. Q. Teodoro, R. L. A. Haiduke, and L. Visscher. Nuclear electric quadrupole moment of potassium from the molecular method. *Physical Review A*, 91(3):1–4, 2015.

[30] P. Pyykkö. Year-2017 nuclear quadrupole moments. *Molecular Physics*, 116(10):1328–1338, 2018.

[31] U. Köster, P. Carbonez, A. Dorsival, J. Dvorak, R. Eichler, S. Fernandes, H. Frånberg, J. Neuhausen, Z. Novackova, R. Wilfinger, and A. Yakushev. (Im-) possible ISOL beams. *European Physical Journal: Special Topics*, 150(1):285–291, 2007.

[32] Jochen Ballof. *Radioactive Molecular Beams at CERN-ISOLDE*. PhD thesis, JGU Mainz, 2021.

[33] Mia Au and Jochen Ballof. Molecular sidebands for radioactive ion beam extraction, 7 2022.

[34] Dongqi Wang, Wilfred F van Gunsteren, and Zhifang Chai. Recent advances in computational actinoid chemistry. *Chemical Society Reviews*, 41(17):5836–5865, 2012.

[35] Attila Kovács, Rudy J.M. Konings, John K. Gibson, Ivan Infante, and Laura Gagliardi. Quantum chemical calculations and experimental investigations of molecular actinide oxides. *Chemical Reviews*, 115(4):1725–1759, 2015.

[36] T Vitova, I Pidchenko, D Fellhauer, P S Bagus, Y Joly, T Pruessmann, S Bahl, E Gonzalez-Robles, J Rothe, M Altmaier, M A Denecke, and H Geckeis. The role of the 5f valence orbitals of early actinides in chemical bonding. *Nature Communications*, 8(1):16053, 2017.

[37] Michael L Neidig, David L Clark, and Richard L Martin. Covalency in f-element complexes. *Coordination Chemistry Reviews*, 257(2):394–406, 2013.

[38] Melanie. Pepper and Bruce E Bursten. The electronic structure of actinide-containing molecules: a challenge to applied quantum chemistry. *Chemical Reviews*, 91(5):719–741, 7 1991.

[39] Brett A McGuire. 2021 Census of Interstellar, Circumstellar, Extragalactic, Protoplanetary Disk, and Exoplanetary Molecules. *The Astrophysical Journal Supplement Series*, 259(2):30, 2022.

[40] R. De Nutte, L. Decin, H. Olofsson, R. Lombaert, A. de Koter, A. Karakas, S. Milam, S. Ramstedt, R. J. Stancliffe, W. Homan, and M. Van de Sande. Nucleosynthesis in AGB stars traced by oxygen isotopic ratios. *Astronomy & Astrophysics*, 600:A71, 4 2017.

[41] D. R. Schmidt, N. J. Woolf, T. J. Zega, and L. M. Ziurys. Extreme 13C,15N and 17O isotopic enrichment in the young planetary nebula K4-47. *Nature*, 564(7736):378–381, 2018.

[42] G. R. Adande and L. M. Ziurys. MILLIMETER-WAVE OBSERVATIONS OF CN AND HNC AND THEIR 15N ISOTOPOLOGUES: A NEW EVALUATION OF THE 14N/15N RATIO ACROSS THE GALAXY. *The Astrophysical Journal*, 744(2):194, 1 2012.

[43] Tomasz Kamiński, Romuald Tylenda, Karl M Menten, Amanda Karakas, Jan Martin Winters, Alexander A Breier, Ka Tat Wong, Thomas F Giesen, and Nimesh A Patel. Astronomical detection of radioactive molecule 26AlF in the remnant of an ancient explosion. *Nature Astronomy*, 2(10):778–783, 2018.

[44] Alexander A Breier. *HIGH-RESOLUTION MICROWAVE SPECTROSCOPY OF RADIOACTIVE MOLECULES: Mass-independent studies of AlF, AlH, AlO, AlS, TiO, and FeO*. PhD thesis, University of Kassel, 2019.

[45] Alexander A Breier, Björn Waßmuth, Guido W Fuchs, Jürgen Gauss, and Thomas F Giesen. Mass-independent analysis of the stable isotopologues of gas-phase titanium monoxide – TiO. *Journal of Molecular Spectroscopy*, 355:46–58, 2019.

[46] R Neugart, J Billowes, M L Bissell, K Blaum, B Cheal, K T Flanagan, G Neyens, W Nörtershäuser, and D T Yordanov. Collinear laser spectroscopy at ISOLDE: new methods and highlights. *Journal of Physics G: Nuclear and Particle Physics*, 44(6):064002, 6 2017.

[47] B A Marsh, B Andel, A N Andreyev, S Antalic, D Atanasov, A E Barzakh, B Bastin, Ch. Borgmann, L Capponi, T E Cocolios, T Day Goodacre, M Dehairs, X Derkx, H De Witte, D V Fedorov, V N Fedosseev, G J Focker, D A Fink, K T Flanagan, S Franchoo, L Ghys, M Huyse, N Imai, Z Kalaninova, U Köster, S Kreim, N Kesteloot, Yu. Kudryavtsev, J Lane, N Lecesne, V Liberati, D Lunney, K M Lynch, V Manea, P L Molkanov, T Nicol, D Pauwels, L Popescu, D Radulov, E Rapisarda, M Rosenbusch, R E Rossel, S Rothe, L Schweikhard, M D Seliverstov, S Sels, A M Sjödin, V Truesdale, C Van Beveren, P Van Duppen, K Wendt, F Wienholtz, R N Wolf, and S G Zemlyanoy. New developments of the in-source spectroscopy method at RILIS/ISOLDE. *Nuclear Instruments and Methods in Physics Research Section B: Beam Interactions with Materials and Atoms*, 317:550–556, 2013.

[48] B. A. Marsh, T. Day Goodacre, S. Sels, Y. Tsunoda, B. Andel, A. N. Andreyev, N. A. Althubiti, D. Atanasov, A. E. Barzakh, J. Billowes, K. Blaum, T. E. Cocolios, J. G. Cubiss, J. Dobaczewski, G. J. Farooq-Smith, D. V. Fedorov, V. N. Fedosseev, K. T. Flanagan, L. P. Gaffney, L. Ghys, M. Huyse, S. Kreim, D. Lunney, K. M. Lynch, V. Manea, Y. Martinez Palenzuela, P. L. Molkanov, T. Otsuka, A. Pastore, M. Rosenbusch, R. E. Rossel, S. Rothe, L. Schweikhard, M. D. Seliverstov, P. Spagnoletti, C. Van Beveren, P. Van Duppen, M. Veinhard, E. Verstraelen, A. Welker, K. Wendt, F. Wienholtz, R. N. Wolf, A. Zadvornaya, and K. Zuber. Characterization of the shape-staggering effect in mercury nuclei. *Nature Physics*, 14(12):1163–1167, 2018.

[49] R P de Groote, J Billowes, C L Binnersley, M L Bissell, T E Cocolios, T Day Goodacre, G J Farooq-Smith, D V Fedorov, K T Flanagan, S Franchoo, R F Garcia Ruiz, A Koszorús, K M Lynch, G Neyens, F Nowacki, T Otsuka, S Rothe, H H Stroke, Y Tsunoda, A R Vernon, K D A Wendt, S G Wilkins, Z Y Xu, and X F Yang. Dipole and quadrupole moments of 73-78Cu as a test of the robustness of the Z=28 shell closure near 78Ni. *Physical Review C*, 96(4):41302, 10 2017.

[50] N. R. Hutzler, A. Borschevsky, D. Budker, D. DeMille, V. V. Flambaum, G. Gabrielse, R. F. Garcia Ruiz, A. M. Jayich, L. A.

Orozco, M. Ramsey-Musolf, M. Reece, M. S. Safronova, J. T. Singh, M. R. Tarbutt, and T. Zelevinsky. Searches for new sources of CP violation using molecules as quantum sensors. *arXiv*, 2010.08709(2010.08709):1–5, 2020.

[51] E Caurier, G Martínez-Pinedo, F Nowacki, A Poves, and A P Zuker. The shell model as a unified view of nuclear structure. *Reviews of Modern Physics*, 77(2):427–488, 6 2005.

[52] Kenneth S Krane. *Introductory nuclear physics*. John Wiley & Sons, 1991.

[53] Maria Goeppert Mayer. The shell model. *Science*, 145(3636):999–1006, 1964.

[54] Takaharu Otsuka, Alexandra Gade, Olivier Sorlin, Toshio Suzuki, and Yutaka Utsuno. Evolution of shell structure in exotic nuclei. *Reviews of Modern Physics*, 92(1), 3 2020.

[55] V Paar. A parabolic rule for the energy dependence on x = I(I + 1) for proton-neutron multiplets in odd-odd nuclei. *Nuclear Physics A*, 331(1):16–28, 1979.

[56] R P de Groote, S Kujanpää, A Koszorús, J G Li, and I D Moore. Magnetic octupole moment of 173Yb using collinear laser spectroscopy. *Physical Review A*, 103(3):32826, 3 2021.

[57] R P de Groote, J Moreno, J Dobaczewski, A Koszorús, I Moore, M Reponen, B K Sahoo, and C Yuan. Precision measurement of the magnetic octupole moment in 45Sc as a test for state-of-the-art atomic- and nuclear-structure theory. *Physics Letters B*, 827:136930, 2022.

[58] Wouter Ryssens, Giuliano Giacalone, Björn Schenke, and Chun Shen. Evidence of Hexadecapole Deformation in Uranium-238 at the Relativistic Heavy Ion Collider. *Physical Review Letters*, 130(21):212302, 5 2023.

[59] Richard F Casten. *Nuclear structure from a simple perspective*, volume 23. Oxford University Press on Demand, 2000.

[60] R Neugart and G Neyens. Nuclear moments. *The Euroschool Lectures on Physics with Exotic Beams, Vol. II*, pages 135–189, 2006.

[61] P. A. Butler, L. P. Gaffney, P. Spagnoletti, K. Abrahams, M. Bowry, J. Cederkäll, G. de Angelis, H. De Witte, P. E. Garrett, A. Goldkuhle, C. Henrich, A. Illana, K. Johnston, D. T. Joss, J. M. Keatings, N. A. Kelly, M. Komorowska, J. Konki, T. Kröll, M. Lozano, B. S. Nara Singh, D. O'Donnell, J. Ojala, R. D. Page, L. G. Pedersen, C. Raison, P. Reiter, J. A. Rodriguez, D. Rosiak, S. Rothe, M. Scheck, M. Seidlitz, T. M. Shneidman, B. Siebeck, J. Sinclair, J. F. Smith, M. Stryjczyk, P. Van Duppen, S. Vinals, V. Virtanen, N. Warr, K. Wrzosek-Lipska, and M. Zielińska. Evolution of Octupole Deformation in Radium Nuclei from Coulomb Excitation of Radioactive 222Ra and 228Ra Beams. *Physical Review Letters*, 124(4):42503, 1 2020.

[62] P A Butler. Octupole collectivity in nuclei. *Journal of Physics G: Nuclear and Particle Physics*, 43(7):073002, 2016.

[63] H J Wollersheim, H Emling, H Grein, R Kulessa, R S Simon, C Fleischmann, J de Boer, E Hauber, C Lauterbach, C Schandera, P A Butler, and T Czosnyka. Coulomb excitation of 226Ra. *Nuclear Physics A*, 556(2):261–280, 1993.

[64] M M R Chishti, D O'Donnell, G Battaglia, M Bowry, D A Jaroszynski, B S Nara Singh, M Scheck, P Spagnoletti, and J F Smith. Direct measurement of the intrinsic electric dipole moment in pear-shaped thorium-228. *Nature Physics*, 16(8):853–856, 2020.

[65] C S Wu, E Ambler, R W Hayward, D D Hoppes, and R P Hudson. Experimental Test of Parity Conservation in Beta Decay. *Physical Review*, 105(4):1413–1415, 2 1957.

[66] Jonathan Engel, Michael J Ramsey-Musolf, and U van Kolck. Electric dipole moments of nucleons, nuclei, and atoms: The Standard Model and beyond. *Progress in Particle and Nuclear Physics*, 71:21–74, 2013.

[67] C. Abel, S. Afach, N. J. Ayres, C. A. Baker, G. Ban, G. Bison, K. Bodek, V. Bondar, M. Burghoff, E. Chanel, Z. Chowdhuri, P.-J.

Chiu, B. Clement, C. B. Crawford, M. Daum, S. Emmenegger, L. Ferraris-Bouchez, M. Fertl, P. Flaux, B. Franke, A. Fratangelo, P. Geltenbort, K. Green, W. C. Griffith, M. van der Grinten, Z. D. Grujić, P. G. Harris, L. Hayen, W. Heil, R. Henneck, V. Hélaine, N. Hild, Z. Hodge, M. Horras, P. Iaydjiev, S. N. Ivanov, M. Kasprzak, Y. Kermaidic, K. Kirch, A. Knecht, P. Knowles, H.-C. Koch, P. A. Koss, S. Komposch, A. Kozela, A. Kraft, J. Krempel, M. Kuźniak, B. Lauss, T. Lefort, Y. Lemière, A. Leredde, P. Mohanmurthy, A. Mtchedlishvili, M. Musgrave, O. Naviliat-Cuncic, D. Pais, F. M. Piegsa, E. Pierre, G. Pignol, C. Plonka-Spehr, P. N. Prashanth, G. Quéméner, M. Rawlik, D. Rebreyend, I. Rienäcker, D. Ries, S. Roccia, G. Rogel, D. Rozpedzik, A. Schnabel, P. Schmidt-Wellenburg, N. Severijns, D. Shiers, R. Tavakoli Dinani, J. A. Thorne, R. Virot, J. Voigt, A. Weis, E. Wursten, G. Wyszynski, J. Zejma, J. Zenner, and G. Zsigmond. Measurement of the Permanent Electric Dipole Moment of the Neutron. *Physical Review Letters*, 124(8):81803, 2 2020.

[68] Andrzej Czarnecki and Bernd Krause. Neutron Electric Dipole Moment in the Standard Model: Complete Three-Loop Calculation of the Valence Quark Contributions. *Physical Review Letters*, 78(23):4339–4342, 6 1997.

[69] V. Andreev, D. G. Ang, D. DeMille, J. M. Doyle, G. Gabrielse, J. Haefner, N. R. Hutzler, Z. Lasner, C. Meisenhelder, B. R. O'Leary, C. D. Panda, A. D. West, E. P. West, and X. Wu. Improved limit on the electric dipole moment of the electron. *Nature*, 562(7727):355–360, 2018.

[70] Tanya S Roussy, Luke Caldwell, Trevor Wright, William B Cairncross, Yuval Shagam, Kia Boon Ng, Noah Schlossberger, Sun Yool Park, Anzhou Wang, Jun Ye, and Eric A Cornell. An improved bound on the electron's electric dipole moment. *Science*, 381(6653):46–50, 7 2023.

[71] Maxim Pospelov and Adam Ritz. Electric dipole moments as probes of new physics. *Annals of Physics*, 318(1):119–169, 2005.

[72] L. I. Schiff. Measurability of nuclear electric dipole moments. *Physical Review*, 132(5):2194–2200, 1963.

[73] J. Dobaczewski, J. Engel, M. Kortelainen, and P. Becker. Correlating Schiff Moments in the Light Actinides with Octupole Moments. *Physical Review Letters*, 121(23):232501, 2018.

[74] C M Maekawa, E Mereghetti, J de Vries, and U van Kolck. The time-reversal- and parity-violating nuclear potential in chiral effective theory. *Nuclear Physics A*, 872(1):117–160, 2011.

[75] E B Norrgard, D S Barker, S Eckel, J A Fedchak, N N Klimov, and J Scherschligt. Nuclear-spin dependent parity violation in optically trapped polyatomic molecules. *Communications Physics*, 2(1):77, 2019.

[76] Yongliang Hao, Petr Navrátil, Eric B Norrgard, Miroslav Iliaš, Ephraim Eliav, Rob G E Timmermans, Victor V Flambaum, and Anastasia Borschevsky. Nuclear spin-dependent parity-violating effects in light polyatomic molecules. *Physical Review A*, 102(5):52828, 11 2020.

[77] Bruce R Barrett, Petr Navrátil, and James P Vary. Ab initio no core shell model. *Progress in Particle and Nuclear Physics*, 69:131–181, 2013.

[78] K Beloy, A Derevianko, and W R Johnson. Hyperfine structure of the metastable 3P2 state of alkaline-earth-metal atoms as an accurate probe of nuclear magnetic octupole moments. *Physical Review A*, 77(1):12512, 1 2008.

[79] W. H. King. *Isotope shifts in atomic spectra.* Springer Science & Business Media, 2013.

[80] Gleb Penyazkov, Sergey D Prosnyak, Anatoly E Barzakh, and Leonid V Skripnikov. Refined theoretical values of field and mass isotope shifts in thallium to extract charge radii of Tl isotopes. *The Journal of Chemical Physics*, 158(11):114110, 3 2023.

[81] P Aufmuth, K Heilig, and A Steudel. Changes in mean-square nuclear charge radii from optical isotope shifts. *Atomic Data and Nuclear Data Tables*, 37(3):455–490, 1987.

[82] Anna V Viatkina, Vladimir A Yerokhin, and Andrey Surzhykov. Calculation of isotope shifts and King plot nonlinearities in Ca+, 2023.

[83] Joonseok Hur, Diana P. L. Aude Craik, Ian Counts, Eugene Knyazev, Luke Caldwell, Calvin Leung, Swadha Pandey, Julian C Berengut, Amy Geddes, Witold Nazarewicz, Paul-Gerhard Reinhard, Akio Kawasaki, Honggi Jeon, Wonho Jhe, and Vladan Vuletić. Evidence of Two-Source King Plot Nonlinearity in Spectroscopic Search for New Boson. *Physical Review Letters*, 128(16):163201, 4 2022.

[84] Ian Counts, Joonseok Hur, Diana P L Aude Craik, Honggi Jeon, Calvin Leung, Julian C Berengut, Amy Geddes, Akio Kawasaki, Wonho Jhe, and Vladan Vuletić. Evidence for Nonlinear Isotope Shift in Yb+ Search for New Boson. *Physical Review Letters*, 125(12):123002, 9 2020.

[85] Julian C. Berengut, Dmitry Budker, Cédric Delaunay, Victor V. Flambaum, Claudia Frugiuele, Elina Fuchs, Christophe Grojean, Roni Harnik, Roee Ozeri, Gilad Perez, and Yotam Soreq. Probing New Long-Range Interactions by Isotope Shift Spectroscopy. *Physical Review Letters*, 120(9):1–7, 2018.

[86] Julian C Berengut, Cédric Delaunay, Amy Geddes, and Yotam Soreq. Generalized King linearity and new physics searches with isotope shifts. *Physical Review Research*, 2(4):43444, 12 2020.

[87] G. Herzberg. *Molecular spectra and molecular structure.* D. van Nostrand, 1945.

[88] Linus Pauling and E Bright Wilson. *Introduction to quantum mechanics with applications to chemistry.* Courier Corporation, 2012.

[89] John M Brown and Alan Carrington. *Rotational Spectroscopy of Diatomic Molecules.* Cambridge University Press, Cambridge, 2003.

[90] Friedrich Hund. Allgemeine Quantenmechanik des Atom- und Molekelbaues. In H Bethe, F Hund, N F Mott, W Pauli,

A Rubinowicz, G Wentzel, and A Smekal, editors, *Quantentheorie*, pages 561–694. Springer Berlin Heidelberg, Berlin, Heidelberg, 1933.

[91] J K G Watson. The isotope dependence of diatomic Dunham coefficients. *Journal of Molecular Spectroscopy*, 80(2):411–421, 1980.

[92] H Knöckel and E Tiemann. Isotopic field shift in the transition A 0+—X $1\Sigma+$ of PbS. *Chemical Physics*, 68(1):13–19, 1982.

[93] J Schlembach and E Tiemann. Isotopic field shift of the rotational energy of the Pb-chalcogenides and Tl-Halides. *Chemical Physics*, 68(1):21–28, 1982.

[94] H Knöckel and E Tiemann. Isotope shift of the transition A 0+-X $1\Sigma+$ of PbO. *Chemical Physics Letters*, 104(1):83–86, 1984.

[95] H Knöckel, T Kröckertskothen, and E Tiemann. Molecular-beam-laser studies of the states $X1\Sigma+$ and A0+ of PbS. *Chemical Physics*, 93(2):349–358, 1985.

[96] S A Cooke, M C L Gerry, D J Brugh, and R D Suenram. The rotational spectrum, nuclear field shift effects, 195Pt nuclear spin–rotation constant, and electric dipole moment of PtSi. *Journal of Molecular Spectroscopy*, 223(2):185–194, 2004.

[97] Stephen A Cooke and Michael C L Gerry. Internuclear distance and effects of Born–Oppenheimer breakdown for PtS, determined from its pure rotational spectrum. *The Journal of Chemical Physics*, 121(8):3486–3494, 8 2004.

[98] Stephen A Cooke and Michael C L Gerry. The influence of nuclear volume and electronic structure on the rotational energy of platinum monoxide, PtO. *Physical Chemistry Chemical Physics*, 7(12):2453–2459, 2005.

[99] Jack C Harms, Leah C O'Brien, and James J O'Brien. Mass-independent Dunham analysis of the known electronic states of platinum sulfide, PtS, and analysis of the electronic field-shift effect. *The Journal of Chemical Physics*, 151(9):094303, 9 2019.

[100] Jack C Harms, Ji Wu, Shahzan Mian, Leah C O'Brien, and James J O'Brien. Mass-independent Dunham analysis of the [13.8] transition of platinum monochloride, PtCl, observed by intracavity laser spectroscopy. *Journal of Molecular Spectroscopy*, 359:6–15, 2019.

[101] J L Dunham. The Energy Levels of a Rotating Vibrator. *Phys. Rev.*, 41(6):721–731, 9 1932.

[102] Stefan Knecht and Trond Saue. Nuclear size effects in rotational spectra: A tale with a twist. *Chemical Physics*, 401:103–112, 2012.

[103] Maria J G Borge and Björn Jonson. ISOLDE past, present and future. *Journal of Physics G: Nuclear and Particle Physics*, 44(4):44011, 2017.

[104] R Catherall, W Andreazza, M Breitenfeldt, A Dorsival, G J Focker, T P Gharsa, Giles T J, J-L Grenard, F Locci, P Martins, S Marzari, J Schipper, A Shornikov, and T Stora. The ISOLDE facility. *Journal of Physics G: Nuclear and Particle Physics*, 44(9):094002, 2017.

[105] K T Flanagan, K M Lynch, J Billowes, M L Bissell, I Budinčević, T E Cocolios, R P de Groote, S De Schepper, V N Fedosseev, S Franchoo, R F Garcia Ruiz, H Heylen, B A Marsh, G Neyens, T J Procter, R E Rossel, S Rothe, I Strashnov, H H Stroke, and K D A Wendt. Collinear Resonance Ionization Spectroscopy of Neutron-Deficient Francium Isotopes. *Physical Review Letters*, 111(21):212501, 11 2013.

[106] R. P. de Groote, I Budincevic, J Billowes, M. L. Bissell, T. E. Cocolios, G. J. Farooq-Smith, V. N. Fedosseev, K. T. Flanagan, S Franchoo, R F Garcia Ruiz, H Heylen, R Li, K. M. Lynch, B. A. Marsh, G Neyens, R. E. Rossel, S Rothe, H. H. Stroke, K. D. A. Wendt, S. G. Wilkins, and X Yang. Use of a Continuous Wave Laser and Pockels Cell for Sensitive High-Resolution Collinear Resonance Ionization Spectroscopy. *Physical Review Letters*, 115(13):132501, 9 2015.

[107] K. M. Lynch, J. Billowes, M. L. Bissell, I. Budincevic, T. E. Cocolios, R. P. De Groote, S. De Schepper, V. N. Fedosseev, K. T.

Flanagan, S. Franchoo, R. F. Garcia Ruiz, H. Heylen, B. A. Marsh, G. Neyens, T. J. Procter, R. E. Rossel, S. Rothe, I. Strashnov, H. H. Stroke, and K. D. A. Wendt. Decay-Assisted Laser Spectroscopy of Neutron-Deficient Francium. *Phys. Rev. X*, 4(1):11055, 3 2014.

[108] Ruben Pieter de Groote and Pierre Lassegues. Characterization of the atomic 6D-states in neutral francium using collinear resonance ionization spectroscopy, CERN-INTC-2023-035, INTC-P-664. Technical report, CERN, Geneva, 2023.

[109] M Nichols, M Athanasakis-Kaklamanakis, A Borschevsky, T E Cocolios, R Crosa-Rossa, R P de Groote, K T Flanagan, R F Garcia Ruiz, S Geldhof, D Hanstorp, A Koszorús, L Lalanne, D Leimbach, G Neyens, J Reilly, S Rothe, S G Wilkins, and X F Yang. Investigating radioactive negative ion production via double electron capture. *Nuclear Instruments and Methods in Physics Research Section B: Beam Interactions with Materials and Atoms*, 541:264–267, 2023.

[110] M Reponen, R P de Groote, L Al Ayoubi, O Beliuskina, M L Bissell, P Campbell, L Cañete, B Cheal, K Chrysalidis, C Delafosse, A de Roubin, C S Devlin, T Eronen, R F Garcia Ruiz, S Geldhof, W Gins, M Hukkanen, P Imgram, A Kankainen, M Kortelainen, A Koszorús, S Kujanpää, R Mathieson, D A Nesterenko, I Pohjalainen, M Vilén, A Zadvornaya, and I D Moore. Evidence of a sudden increase in the nuclear size of proton-rich silver-96. *Nature Communications*, 12(1):4596, 2021.

[111] D. A. Fink, T. E. Cocolios, A. N. Andreyev, S Antalic, A. E. Barzakh, B Bastin, D. V. Fedorov, V. N. Fedosseev, K. T. Flanagan, L Ghys, A Gottberg, M Huyse, N Imai, T Kron, N Lecesne, K. M. Lynch, B. A. Marsh, D Pauwels, E Rapisarda, S. D. Richter, R. E. Rossel, S Rothe, M. D. Seliverstov, A. M. Sjödin, C Van Beveren, P Van Duppen, and K. D. A. Wendt. In-Source Laser Spectroscopy with the Laser Ion Source and Trap: First Direct Study of the Ground-State Properties of 217,219Po. *Physical Review X*, 5(1):11018, 2 2015.

[112] R Heinke, T Kron, S Raeder, T Reich, P Schönberg, M Trümper, C Weichhold, and K Wendt. High-resolution in-source laser

spectroscopy in perpendicular geometry. *Hyperfine Interactions*, 238(1):6, 2016.

[113] Reinhard Heinke, Mia Au, Cyril Bernerd, Katerina Chrysalidis, Thomas E Cocolios, Valentin N Fedosseev, Isabel Hendriks, Asar A H Jaradat, Magdalena Kaja, Tom Kieck, Tobias Kron, Ralitsa Mancheva, Bruce A Marsh, Stefano Marzari, Sebastian Raeder, Sebastian Rothe, Dominik Studer, Felix Weber, and Klaus Wendt. First on-line application of the high-resolution spectroscopy laser ion source PI-LIST at ISOLDE. *Nuclear Instruments and Methods in Physics Research Section B: Beam Interactions with Materials and Atoms*, 541:8–12, 2023.

[114] E Mané, J Billowes, K Blaum, P Campbell, B Cheal, P Delahaye, K T Flanagan, D H Forest, H Franberg, C Geppert, T Giles, A Jokinen, M Kowalska, R Neugart, G Neyens, W Nörtershäuser, I Podadera, G Tungate, P Vingerhoets, and D T Yordanov. An ion cooler-buncher for high-sensitivity collinear laser spectroscopy at ISOLDE. *The European Physical Journal A*, 42(3):503–507, 2009.

[115] V Sonnenschein, I D Moore, S Raeder, M Reponen, H Tomita, and K Wendt. Characterization of a pulsed injection-locked Ti:sapphire laser and its application to high resolution resonance ionization spectroscopy of copper. *Laser Physics*, 27(8):085701, 2017.

[116] B Cheal, T E Cocolios, and S Fritzsche. Laser spectroscopy of radioactive isotopes: Role and limitations of accurate isotope-shift calculations. *Physical Review A*, 86(4):42501, 10 2012.

[117] Robert J Le Roy. Improved Parameterization for Combined Isotopomer Analysis of Diatomic Spectra and Its Application to HF and DF. *Journal of Molecular Spectroscopy*, 194(2):189–196, 1999.

[118] Adel Almoukhalalati, Avijit Shee, and Trond Saue. Nuclear size effects in vibrational spectra. *Phys. Chem. Chem. Phys.*, 18(22):15406–15417, 2016.

[119] A. D. Kudashov, A. N. Petrov, L. V. Skripnikov, N. S. Mosyagin, T. A. Isaev, R. Berger, and A. V. Titov. Ab initio study of radium

monofluoride (RaF) as a candidate to search for parity- and time-and-parity-violation effects. *Physical Review A - Atomic, Molecular, and Optical Physics*, 90(5):1–5, 2014.

[120] T. A. Isaev, S. Hoekstra, and R. Berger. Laser-cooled RaF as a promising candidate to measure molecular parity violation. *Physical Review A - Atomic, Molecular, and Optical Physics*, 82(5):1–5, 2010.

[121] Sudip Sasmal, Himadri Pathak, Malaya K Nayak, Nayana Vaval, and Sourav Pal. Relativistic coupled-cluster study of RaF as a candidate for the parity- and time-reversal-violating interaction. *Physical Review A*, 93(6):62506, 6 2016.

[122] Konstantin Gaul and Robert Berger. Zeroth order regular approximation approach to electric dipole moment interactions of the electron. *The Journal of Chemical Physics*, 147(1):14109, 7 2017.

[123] Chaoqun Zhang, Xuechen Zheng, and Lan Cheng. Calculations of time-reversal-symmetry-violation sensitivity parameters based on analytic relativistic coupled-cluster gradient theory. *Physical Review A*, 104(1):12814, 7 2021.

[124] V. V. Flambaum and H. Feldmeier. Enhanced nuclear Schiff moment in stable and metastable nuclei. *Physical Review C*, 101(1):1–11, 2020.

[125] C S Wood, S C Bennett, D Cho, B P Masterson, J L Roberts, C E Tanner, and C E Wieman. Measurement of Parity Nonconservation and an Anapole Moment in Cesium. *Science*, 275(5307):1759–1763, 3 1997.

[126] V. A. Dzuba, V. V. Flambaum, J. S.M. Ginges, and M. G. Kozlov. Electric dipole moments of Hg, Xe, Rn, Ra, Pu, and TlF induced by the nuclear Schiff moment and limits on time-reversal violating interactions. *Physical Review A*, 66(1):7, 2002.

[127] S G Porsev, K Beloy, and A Derevianko. Precision determination of weak charge of `$^{133}\mathrm{Cs}$` from atomic parity violation. *Physical Review D*, 82(3):36008, 8 2010.

[128] V A Dzuba, J C Berengut, V V Flambaum, and B Roberts. Revisiting Parity Nonconservation in Cesium. *Physical Review Letters*, 109(20):203003, 11 2012.

[129] B M Roberts, V A Dzuba, and V V Flambaum. Double-core-polarization contribution to atomic parity-nonconservation and electric-dipole-moment calculations. *Physical Review A*, 88(4):42507, 10 2013.

[130] B. K. Sahoo, B. P. Das, and H Spiesberger. New physics constraints from atomic parity violation in $ˆ{133}\mathrm{Cs}$. *Physical Review D*, 103(11):L111303, 6 2021.

[131] B. M. Roberts and J. S. M. Ginges. Comment on “New physics constraints from atomic parity violation in $ˆ{133}\mathrm{Cs}$”. *Physical Review D*, 105(1):18301, 1 2022.

[132] Colin M Western. PGOPHER: A program for simulating rotational, vibrational and electronic spectra. *Journal of Quantitative Spectroscopy and Radiative Transfer*, 186:221–242, 2017.

[133] Ruben Pieter De Groote. *High resolution collinear resonance ionization spectroscopy of neutron-rich 76,77,78Cu isotopes.* PhD thesis, KU Leuven, Leuven, Belgium, 2017.

[134] Peter Atkins and Julio de Paula. *Atkins' Physical Chemistry.* Oxford University Press, 2014.

[135] Carlos M. Fajardo Zambrano. Broadband laser spectroscopy of RaF, Master's thesis, KU Leuven, 2023.

[136] K. M. Lynch, S. G. Wilkins, J. Billowes, C. L. Binnersley, M. L. Bissell, K. Chrysalidis, T. E. Cocolios, T. Day Goodacre, R. P. De Groote, G. J. Farooq-Smith, D. V. Fedorov, V. N. Fedosseev, K. T. Flanagan, S. Franchoo, R. F. Garcia Ruiz, W. Gins, R. Heinke, Koszorús, B. A. Marsh, P. L. Molkanov, P. Naubereit, G. Neyens, C. M. Ricketts, S. Rothe, C. Seiffert, M. D. Seliverstov, H. H. Stroke, D. Studer, A. R. Vernon, K. D.A. Wendt, and X. F. Yang. Laser-spectroscopy studies of the nuclear structure of neutron-rich radium. *Physical Review C*, 97(2):1–9, 2018.

[137] Shane Gary Wilkins. *Collinear resonance ionization spectroscopy of exotic francium and radium isotopes.* PhD thesis, The University of Manchester, Manchester, 2018.

[138] K Wendt, S A Ahmad, W Klempt, R Neugart, E W Otten, and H H Stroke. On the hyperfine structure and isotope shift of radium. *Zeitschrift für Physik D Atoms, Molecules and Clusters*, 4(3):227–241, 1987.

[139] L V Skripnikov. Combined 4-component and relativistic pseudopotential study of ThO for the electron electric dipole moment search. *The Journal of Chemical Physics*, 145(21):214301, 12 2016.

[140] L V Skripnikov. Communication: Theoretical study of HfF+ cation to search for the T,P-odd interactions. *The Journal of Chemical Physics*, 147(2):21101, 7 2017.

[141] M. G. Kozlov and L. N. Labzowsky. Parity violation effects in diatomics. *Journal of Physics B: Atomic, Molecular and Optical Physics*, 28(10):1933–1961, 1995.

[142] R A Frosch and H M Foley. Magnetic Hyperfine Structure in Diatomic Molecules. *Physical Review*, 88(6):1337–1349, 12 1952.

[143] Timur A Isaev, Shane G Wilkins, and Michail Athanasakis-Kaklamanakis. On the Feasibility of Rovibrational Laser Cooling of Radioactive RaF+ and RaH+ Cations. *Atoms*, 9(4), 2021.

[144] Matthieu Viteau, Amodsen Chotia, Maria Allegrini, Nadia Bouloufa, Olivier Dulieu, Daniel Comparat, and Pierre Pillet. Optical Pumping and Vibrational Cooling of Molecules. *Science*, 321(5886):232–234, 7 2008.

[145] I. Manai, R. Horchani, H. Lignier, P. Pillet, D. Comparat, A. Fioretti, and M. Allegrini. Rovibrational Cooling of Molecules by Optical Pumping. *Physical Review Letters*, 109(18):183001, 10 2012.

[146] Mehdi Hamamda, Pierre Pillet, Hans Lignier, and Daniel Comparat. Ro-vibrational cooling of molecules and prospects. *Journal of*

Physics B: Atomic, Molecular and Optical Physics, 48(18):182001, 2015.

[147] P. R. Stollenwerk, I. O. Antonov, S. Venkataramanababu, Y. W. Lin, and B. C. Odom. Cooling of a Zero-Nuclear-Spin Molecular Ion to a Selected Rotational State. *Physical Review Letters*, 125(11):113201, 2020.

[148] N. R. Hutzler, M. F. Parsons, Y. V. Gurevich, P. W. Hess, E. Petrik, B. Spaun, A. C. Vutha, D. DeMille, G. Gabrielse, and J. M. Doyle. A cryogenic beam of refractory, chemically reactive molecules with expansion cooling. *Physical Chemistry Chemical Physics*, 13(42):18976–18985, 2011.

[149] F Dalton, V V Flambaum, and A J Mansour. Enhanced Schiff and magnetic quadrupole moments in deformed nuclei and their connection to the search for axion dark matter. *Physical Review C*, 107(3):35502, 3 2023.

[150] Alexander V Oleynichenko, Leonid V Skripnikov, Andréi V Zaitsevskii, and Victor V Flambaum. Laser-coolable ${\mathrm{AcOH}}^{+}$ ion for $\mathcal{CP}$-violation searches. *Physical Review A*, 105(2):22825, 2 2022.

[151] L. V. Skripnikov, N. S. Mosyagin, A. V. Titov, and V. V. Flambaum. Actinide and lanthanide molecules to search for strong CP-violation. *Physical Chemistry Chemical Physics*, 22(33):18374–18380, 2020.

[152] D. Cho, K. Sangster, and E. A. Hinds. Search for time-reversal-symmetry violation in thallium fluoride using a jet source. *Physical Review A*, 44(5):164–164, 1991.

[153] R Eder, H Grawe, E Hagebø, P Hoff, E Kugler, H L Ravn, and K Steffensen. The production yields of radioactive ion-beams from fluorinated targets at the ISOLDE on-line mass separator. *Nuclear Instruments and Methods in Physics Research Section B: Beam Interactions with Materials and Atoms*, 62(4):535–540, 1992.

[154] J. Ballof, C. Seiffert, B. Crepieux, Ch. E. Düllmann, M. Delonca, M. Gai, A. Gottberg, T. Kröll, R. Lica, M. Madurga Flores,

Y. Martinez Palenzuela, T. M. Mendonca, M. Owen, J. P. Ramos, S. Rothe, T. Stora, O. Tengblad, and F. Wienholtz. Radioactive boron beams produced by isotope online mass separation at CERN-ISOLDE. *The European Physical Journal A*, 55(5):65, 2019.

[155] M Au, M Athanasakis-Kaklamanakis, L Nies, J Ballof, R Berger, K Chrysalidis, P Fischer, R Heinke, J Johnson, U Köster, D Leimbach, B Marsh, M Mougeot, J Reilly, E Reis, M Schlaich, Ch. Schweiger, L Schweikhard, S Stegemann, J Wessolek, F Wienholtz, S G Wilkins, W Wojtaczka, Ch. E Düllmann, and S Rothe. In-source and in-trap formation of molecular ions in the actinide mass range at CERN-ISOLDE. *arXiv*, (2303.12215), 2023.

[156] Alfred Morgenstern, Christos Apostolidis, and Frank Bruchertseifer. Supply and Clinical Application of Actinium-225 and Bismuth-213. *Seminars in Nuclear Medicine*, 50(2):119–123, 2020.

[157] M. Athanasakis-Kaklamanakis, S. G. Wilkins, M. Au, R. Berger, A. Borschevsky, K. Chrysalidis, T. E. Cocolios, R. P. de Groote, Ch. E. Duellmann, K. T. Flanagan, R. F. Garcia Ruiz, S. Geldhof, R. Heinke, T. A. Isaev, J. Johnson, A. Kiuberis, A. Koszorús, L. Lalanne, M. Mougeot, G. Neyens, L. Nies, J. Reilly, S. Rothe, L. Schweikhard, A. R. Vernon, and X. F. Yang. Laser ionization spectroscopy of AcF, CERN-INTC-2021-053, INTC-P-615. Technical report, CERN, 2021.

[158] L Penescu, R Catherall, J Lettry, and T Stora. Development of high efficiency Versatile Arc Discharge Ion Source at CERN ISOLDEa). *Review of Scientific Instruments*, 81(2):02A906, 2 2010.

[159] C J Ho, J Lim, B E Sauer, and M R Tarbutt. Measuring the nuclear magnetic quadrupole moment in heavy polar molecules. *Frontiers in Physics*, 11, 2023.

[160] Tanya S Roussy, Luke Caldwell, Trevor Wright, William B Cairncross, Yuval Shagam, Kia Boon Ng, Noah Schlossberger, Sun Yool Park, Anzhou Wang, Jun Ye, and Eric A Cornell. A new bound on the electron's electric dipole moment. *arXiv*, 2212.11841, 2022.

[161] K B MacAdam, N L S Martin, D B Smith, R G Rolfes, and D Richards. Electron loss from Na Rydberg atoms by ion impact. *Physical Review A*, 34(6):4661–4668, 12 1986.

[162] K B MacAdam, J C Day, J C Aguilar, D M Homan, A D MacKellar, and M J Cavagnero. Transient Molecular-Ion Formation in Rydberg-Electron Capture. *Physical Review Letters*, 75(9):1723–1726, 8 1995.

[163] B D DePaola, M.-T. Huang, S Winecki, M P Stöckli, Y Kanai, S R Lundeen, C W Fehrenbach, and S A Arko. Absolute cross sections for charge capture from Rydberg targets by slow highly charged ions. *Physical Review A*, 52(3):2136–2140, 9 1995.

[164] S B Hansen, T Ehrenreich, E Horsdal-Pedersen, K B MacAdam, and L J Dubé. Electron capture from circular Rydberg atoms. *Physical Review Letters*, 71(10):1522–1525, 9 1993.

[165] Kieran T. Flanagan. Recent Advances in Laser Spectroscopy at ISOLDE. *Acta Physica Polonica B*, 44(3):627–637, 2013.

[166] Thomas John Procter. *New Techniques of Laser Spectroscopy on Exotic Isotopes of Gallium and Francium*. PhD thesis, The University of Manchester, Manchester, 2013.

[167] W Gins, R D Harding, M Baranowski, M L Bissell, R F Garcia Ruiz, M Kowalska, G Neyens, S Pallada, N Severijns, Ph. Velten, F Wienholtz, Z Y Xu, X F Yang, and D Zakoucky. A new beamline for laser spin-polarization at ISOLDE. *Nuclear Instruments and Methods in Physics Research Section A: Accelerators, Spectrometers, Detectors and Associated Equipment*, 925:24–32, 2019.

[168] Michail Athanasakis-Kaklamanakis, Jordan R Reilly, Agota Koszorús, Shane G Wilkins, Louis Lalanne, Sarina Geldhof, Miranda Nichols, Quanjun Wang, Bram van den Borne, David Chorlton, Thomas E Cocolios, Kieran T Flanagan, Ronald F Garcia Ruiz, Ruben de Groote, Dag Hanstorp, Gerda Neyens, Andrew J Smith, Adam R Vernon, and Xiaofei F Yang. Voltage scanning and technical upgrades at the Collinear Resonance

Ionization Spectroscopy experiment. *Nuclear Instruments and Methods in Physics Research Section B: Beam Interactions with Materials and Atoms*, 541:86–89, 2023.

[169] Agota Koszorús. *Collinear Resonance Ionization Spectroscopy of potassium isotopes: crossing N=32.* PhD thesis, KU Leuven, Leuven, 9 2019.

[170] R. F. Garcia Ruiz, A. R. Vernon, C. L. Binnersley, B. K. Sahoo, M Bissell, J Billowes, T. E. Cocolios, W Gins, R. P. de Groote, K. T. Flanagan, A Koszorus, K. M. Lynch, G Neyens, C. M. Ricketts, K. D. A. Wendt, S. G. Wilkins, and X. F. Yang. High-Precision Multiphoton Ionization of Accelerated Laser-Ablated Species. *Physical Review X*, 8(4):41005, 10 2018.

[171] B K Sahoo, A R Vernon, R F Garcia Ruiz, C L Binnersley, J Billowes, M L Bissell, T E Cocolios, G J Farooq-Smith, K T Flanagan, W Gins, R P de Groote, A Koszorús, G Neyens, K M Lynch, F Parnefjord-Gustafsson, C M Ricketts, K D A Wendt, S G Wilkins, and X F Yang. Analytic response relativistic coupled-cluster theory: the first application to indium isotope shifts. *New Journal of Physics*, 22(1):12001, 2020.

[172] A R Vernon, R P de Groote, J Billowes, C L Binnersley, T E Cocolios, G J Farooq-Smith, K T Flanagan, R F Garcia Ruiz, W Gins, A Koszorús, G Neyens, C M Ricketts, A J Smith, S G Wilkins, and X F Yang. Optimising the Collinear Resonance Ionisation Spectroscopy (CRIS) experiment at CERN-ISOLDE. *Nuclear Instruments and Methods in Physics Research Section B: Beam Interactions with Materials and Atoms*, 463:384–389, 2020.

[173] John C Miller. *Laser ablation: principles and applications*, volume 28. Springer Science \& Business Media, 2013.

[174] Dima Egorov, Jonathan D Weinstein, David Patterson, Bretislav Friedrich, and John M Doyle. Spectroscopy of laser-ablated buffer-gas-cooled PbO at 4 K and the prospects for measuring the electric dipole moment of the electron. *Phys. Rev. A*, 63(3):30501, 2 2001.

[175] Jinha Kim, Bretislav Friedrich, Daniel P Katz, David Patterson, Jonathan D Weinstein, Robert DeCarvalho, and John M Doyle.

Buffer-Gas Loading and Magnetic Trapping of Atomic Europium. *Phys. Rev. Lett.*, 78(19):3665–3668, 5 1997.

[176] R. F. Garcia Ruiz and S. G. Wilkins. Rotational and Hyperfine Structure of RaF Molecules, INTC-P-555. Technical report, 2020.

[177] Michail Athanasakis-Kaklamanakis, Ronald Fernando Garcia Ruiz, and Shane Gary Wilkins. IS663: Rotational and Hyperfine Structure of RaF Molecules, CERN-INTC-2023-037, INTC-P-555-ADD-1. Technical report, CERN, Geneva, 2023.

[178] A. K. H. Robertson, C. F. Ramogida, P. Schaffer, and V. Radchenko. Development of 225Ac Radiopharmaceuticals: TRIUMF Perspectives and Experiences. *Current Radiopharmaceuticals*, 11(3):156–172, 2018.

[179] Jake D. Johnson, Michael Heines, Frank Bruchertseifer, Eric Chevallay, Thomas E. Cocolios, Kristof Dockx, Charlotte Duchemin, Stephan Heinitz, Reinhard Heinke, Sophie Hurier, Laura Lambert, Benji Leenders, Hanna Skliarova, Thierry Stora, and Wiktoria Wojtaczka. Resonant laser ionization and mass separation of 225Ac. *Scientific Reports*, 13(1), 12 2023.

FACULTY OF SCIENCE
DEPARTMENT OF PHYSICS AND ASTRONOMY
NUCLEAR MOMENTS
Office 26/1-007, CERN, 1 Esplanade des Particules, Meyrin 1217, Switzerland
B-3001 Leuven
m.athkak@cern.ch
https://fys.kuleuven.be/iks/nm